INTERPLAY BETWEEN SHEAR LAYER DYNAMICS AND CAVITATION IN TURBULENT FLOWS ON MICROFLUIDIC CHIPS: A NUMERICAL AND EXPERIMENTAL STUDY

by

MOHAMMADAMIN MALEKI

Submitted to the Graduate School of Engineering and Natural Sciences in partial fulfilment of the requirements of for the degree of Doctor of Philosophy in Mechatronics Engineering

Sabancı University
June 2025

MOHAMMADAMIN MALEKI ©

All Rights Reserved

ABSTRACT

INTERPLAY BETWEEN SHEAR LAYER DYNAMICS AND CAVITATION IN TURBULENT FLOWS ON MICROFLUIDIC CHIPS: A NUMERICAL AND EXPERIMENTAL STUDY

MOHAMMADAMIN MALEKI
Mechatronics Engineering, PhD, June 2025

Thesis Supervisor: Asst. Prof. MORTEZ GHORBANI
Thesis Co-advisor: Prof. ALİ KOŞAR

Keywords: Cavitation, Microscale Flows, Computational Fluid Dynamics (CFD), BFS, Large Eddy Simulation (LES), Compressible Multiphase Flow, Experimental Fluid Dynamics

Cavitation, the local evaporation and re-condensation of liquids due to pressure drops, significantly impacts engineering systems, necessitating a deep understanding for reliable design. This thesis presents a comprehensive investigation into the complex interaction of compressible cavitating flows with turbulent shear layers in microscale BFS configurations. Our methodology integrates advanced computational fluid dynamics with experimental analysis. We employed a custom three-dimensional fully compressible cavitation solver within a Large Eddy Simulation (LES) framework. This solver, leveraging an all-Mach Riemann approximation-based scheme to accurately capture complex density, pressure wave dynamics, and phase change across varying Mach number regimes. We utilized both functional (WALES) and advanced mixed Subgrid-Scale (SGS) models to robustly simulate turbulence across scales. Key findings reveal that cavitation profoundly alters turbulent flow, reducing shear layer growth, delaying reattachment, and modifying Reynolds stresses and pressure fluctuations through vapor collapse. We identified dominant low-frequency modes associated with reattachment displacement and distinct vapor transport mechanisms. Furthermore, riblet-equipped surfaces control incoming turbulence: they shift Turbulence Kinetic Energy (TKE) transport, modify Reynolds stress anisotropy, and promote larger, slower coherent structures. These riblet-induced turbulent changes directly affect cavitation dynamics and characteristics. Experimentally, the study provides the first insights into shear cavitation in a microscale BFS. We observed unique microscale shedding modes influenced by vortex strength and pressure waves. This thesis advances the understanding of turbulent cavitating flows, demonstrating that comprehensive numerical and experimental approaches are essential for designing and optimizing microfluidic and energy systems.

ÖZET

MİKROAKIŞKAN ÇİPLERDEKİ TÜRBÜLANSÇI AKIŞLARDA KESME TABAKASI DİNAMİĞİ İLE KAVİTASYON ARASINDAKİ ETKİLEŞİM: SAYISAL VE DENEYSEL BİR ÇALIŞMA

MOHAMMADAMIN MALEKI
Mekatronik Mühendisliği, Doktora Tezi, Haziran 2025

Danışmanı: Dr. Öğr. Üyesi. MORTEZA GHORBANI
Yardımcı Danışman: Prof. Dr. ALİ KOŞAR

Anahtar Kelimeler: Kavitasyon, Mikro Ölçekli Akışlar, Hesaplamalı Akışkanlar Dinamiği (HAD), Geriye Dönük Basamak (GDB), Büyük Girdap Benzetimi (BGB), Sıkıştırılabilir Çok Fazlı Akış, Deneysel Akışkanlar Dinamiği

Kavitasyon, sıvıların basınç düşüşleri nedeniyle yerel buharlaşması ve yeniden yoğunlaşması olarak tanımlanır, mühendislik sistemlerini önemli ölçüde etkiler ve güvenilir tasarım için derinlemesine bir anlayış gerektirir. Bu tez, mikro ölçekli geri basamak (BFS) konfigürasyonlarında sıkıştırılabilir kavitasyonlu akışların türbülanslı kesme tabakalarıyla karmaşık etkileşimine dair kapsamlı bir araştırma sunmaktadır. Metodolojimiz, gelişmiş hesaplamalı akışkanlar dinamiğini deneysel analizle birleştirmektedir. Büyük Girdap Benzetimi (BGB) çerçevesinde özel olarak geliştirilmiş üç boyutlu tam sıkıştırılabilir bir kavitasyon çözücü kullandık. Bu çözücü, farklı Mach sayısı rejimlerinde karmaşık yoğunluk, basınç dalgası dinamikleri ve faz değişimini doğru bir şekilde yakalamak için tüm-Mach Riemann yaklaşımına dayalı bir şemadan faydalanmaktadır. Türbülansı farklı ölçeklerde sağlam bir şekilde simüle etmek için hem fonksiyonel (WALES) hem de gelişmiş karmaşık Alt-Izgara Ölçeği (AİÖ) modellerini kullandık. Temel bulgularımız, kavitasyonun türbülanslı akışı derinden değiştirdiğini, kesme tabakası büyümesini azalttığını, yeniden tutunmayı geciktirdiğini ve buhar çökmesi yoluyla Reynolds gerilmelerini ve basınç dalgalanmalarını değiştirdiğini ortaya koymaktadır. Yeniden tutunma yer değiştirmesiyle ilişkili baskın düşük frekanslı modlar ve belirgin buhar taşınım mekanizmaları tespit ettik. Ayrıca, riblet donanımlı yüzeyler gelen türbülansı kontrol etmektedir: Türbülans Kinetik Enerjisi (TKE) taşınımını değiştirir, Reynolds gerilimi anizotropisini modifiye eder ve daha büyük, daha yavaş uyumlu yapılar oluşumunu teşvik ederler. Bu riblet kaynaklı türbülanslı değişimler, kavitasyon dinamiğini ve özelliklerini doğrudan etkilemektedir. Deneysel olarak, bu çalışma mikro ölçekli bir BFS'deki kesme kavitasyonuna dair ilk içgörüleri sunmaktadır. Girdap gücü ve basınç dalgalarından etkilenen benzersiz mikro ölçekli kopma (shedding) modları gözlemledik. Bu tez, türbülanslı kavitasyonlu akışlar hakkındaki anlayışı ilerletmekte, mikroakışkan ve enerji sistemlerinin tasarımı ve optimizasyonu için kapsamlı sayısal ve deneysel yaklaşımların vazgeçilmez olduğunu göstermektedir.

Acknowledgements

I want to express my deepest gratitude to the many individuals and organizations who supported me throughout my doctoral journey. This thesis, and indeed my growth as a researcher, wouldn't have been possible without their invaluable contributions.

First and foremost, I extend my profound appreciation to my supervisor, Dr. Morteza Ghorbani. His exceptional guidance, unwavering support, and insightful mentorship have been the cornerstone of my Ph.D. study. From the initial conceptualization of research ideas to the intricate details of analysis and writing, Dr. Ghorbani's profound expertise, meticulous feedback, and boundless patience continually challenged me to push the boundaries of my understanding and refine my scientific approach. He fostered an environment of intellectual curiosity and critical thinking that was truly inspiring.

I am also immensely grateful to my co-advisor, Prof. Ali Kosar. His profound knowledge, particularly in experimental microfluidics and cavitation, provided an essential complementary perspective to my research. Prof. Kosar's encouragement, practical advice, and willingness to share his extensive experience were invaluable, especially in bridging the gap between numerical simulations and experimental realities. His insights were crucial in shaping the interdisciplinary nature of this thesis.

My sincerest thanks also go to my colleagues and fellow researchers at Microscale Cavitation Research Group in Sabancı University. The collaborative atmosphere, stimulating discussions, and shared challenges made the journey far more enriching and enjoyable. I am particularly thankful to Dr. Farzad Rokhsar Talabazar for his insightful discussions and support.

I also want to acknowledge the crucial financial support that made this research possible. The Scientific and Technological Research Council of Türkiye (TUBITAK, Project number: 5230100) provided the funding for this Ph.D. project. This support was indispensable for conducting the extensive computational work and experimental investigations presented in this thesis.

Finally, to my family and friends, your unwavering love, encouragement, and understanding have been my greatest source of strength. Thank you for your patience and belief in me throughout this challenging yet rewarding endeavor.

TABLE OF CONTENTS

LIST OF TABLES

LIST OF FIGURES

Nomenclature

A_b	reversed flow
c	speed of sound
C_v	specific heat
e	specific internal energy
f	frequency
h	step size
k	Thermal conductivity
L_R	length of the reattachment
$\dot{m}$	phase change mass transfer rate
p	pressure field
$\bar{p}$	ensemble mean of pressure
p'_{rms}	root mean square of pressure fluctuations
$\mathbf{F_s}$	Surface tension stress
q	heat flux
Q	Q – criteria
R	ideal gas constant
R_B	nuclei radius
R_c	radius of the curvature
Re_h	Reynolds number based on step size
s	entropy
S_{ij}	antisymmetric parts of the velocity gradient
St_h	Strouhal number based on step size
$\mathbf{S}$	stress tensor
$\mathbf{S_\tau}$	strain tensor
t	time
$\tilde{t}$	normalized time
T	Temperature field
u	streamwise velocity fluctuations
u_τ	friction velocity
$\overline{uu}, \langle uu \rangle$	Reynolds streamwise normal stress
α^{th}	mixture of thermal diffusivity
μ	dynamic viscosity
ν	kinematic viscosity
δ_ω	vorticity thickness
κ	interface curvature
ρ	density
$\hat{\rho}$	Favre filtered value of density
$\bar{\rho}$	ensemble mean of density
σ	surface tension
σ_c	cavitation number
$\boldsymbol{\tau}$	viscous stress tensor
θ	local momentum thickness
γ	backflow coefficient
γ_i	isentropic expansion factor
ψ	compressibility coefficient
Ω_{ij}	antisymmetric parts of the velocity gradient

Subscripts/ Superscripts

0	reference value
ref	reference value
c	critical value
l	liquid phase
v	vapor phase
w	bottom wall
sat	saturation
sgs	subgrid scale

Abbreviations

Large Eddy Simulation (LES)

Root Mean Square (RMS)

Power Spectral Densities (PSDs)

Turbulent Separation Bubble (TSB)

Spectral Proper Orthogonal Decomposition (SPOD)

$\overline{uv}$ $\langle uv \rangle$, Reynolds shear stress

U streamwise velocity

U_e steamwise velocity at boundary layer edge

$\bar{U}$ ensemble mean of streamwise velocity

U velocity vector field

v wall-normal velocity fluctuations

$\overline{vv}, \langle vv \rangle$ Reynolds cross-streamwise normal stress

V wall-normal velocity

$\bar{V}$ ensemble mean of wall-normal velocity

w spanwise velocity fluctuations

$\overline{ww}, \langle ww \rangle$ Reynolds spanwise normal stress

W spanwise velocity

$\bar{W}$ ensemble mean of spanwise velocity

$W(x)$ local width of the channel

$\tilde{x}$ x-coordinate normalized by step size

y^+ dimensionless wall distance

$\tilde{y}$ y-coordinate normalized by step size

z^* z-coordinate normalized by half depth

Greek Symbols

α volume fraction

α_{nuc} volume fraction of initial nuclei

n_0 initial nuclei concentration

Geometry-Induced Separation Bubble (GISB)

Turbulent Boundary Layer (TBL)

BFS

Quasi-Streamwise Vortices (QSVs)

Volume of Fraction (VOF)

Multidimensional Universal Limiter with Explicit Solution (MULES)

Sub-Grid Scales (SGS)

Wall Adaptive Large Eddy (WALE)

Equations of State (EOS)

Kelvin Helmholtz (KH)

Recirculation Region Interface (RRI)

Expansion Ratio (ER)

Turbulent Kinetic Energy (TKE)

RMS (Root Mean Square)

Low Frequency (LF)

Medium Frequency (MF)

Adverse Pressure Gradient (APG)

Favorable Pressure Gradient (FPG)

1 INTRODUCTION

The dynamics of separated flows play a crucial role in various industrial/engineering applications encompassing a wide range of systems such as bluff bodies, diffusors, streamlined bodies, combustion chambers, turbines, and pipelines(Stella, 2017). A separation bubble is typically generated when there is a geometric discontinuity in an immersed body, which is referred as a geometry-induced separation bubble (GISB)(DIWAN and RAMESH, 2009). In many applications, turbulent separation bubble (TSB) (Kiya and Sasaki, 1983; Simpson, 1989) is of prime interest where the fluid flowing over a solid surface contains a turbulent boundary layer (TBL). Separation and reattachment in TSB give rise to unsteadiness across a broad range of frequencies which have significant implications for systems involving flow. Unsteadiness can appear as statistically stationary fluctuations in velocity, pressure, and other flow variables arising from hydrodynamic instabilities like Kelvin-Helmholtz, triggered by specific flow conditions and channel geometry. These instabilities are inherent to turbulent shear flows and contribute to the observed unsteadiness. Pressure fluctuations arising from the turbulent shear layer can potentially induce phase change and cavitation, even at high average pressures. Phase transition can significantly alter the dynamics of coherent structures and events such as vortex shedding and breathing mechanism within the TSB, which results in intricate interactions between the shear layer and cavitation (Arndt, 2002). Understanding and analyzing the behavior of the shear layer in separating flows in the presence of phase transition and cavitation is of great importance to have an accurate prediction of the relevant fluidic systems to harness its advantages for flow control and other applications.

Comprehensive investigations on the dynamics of TSB in single-phase flows were made to elucidate the fundamental principles related to spatial and temporal fluctuations in the pressure, void fraction, and velocity fields within separating flows (Abe, 2017; CHOU et

al., 2005; Eaton and Johnston, 1981; Kiya and Sasaki, 1983; Le Floc'h et al., 2020a; Mohammed-Taifour and Weiss, 2016; NA and MOIN, 1998; Nadge and Govardhan, 2014; Stella, 2017). Previous studies have extensively investigated separated flows using backward-facing steps (BFS) due to their ability to capture complex flow features despite their simplicity (Berk et al., 2017; Hickel et al., 2021; Hu et al., 2019; LE et al., 1997; Nadge and Govardhan, 2014; Pires Araujo and Tenório Rezende, 2017; Shehadi, 2018). BFS flows exhibit a fixed separation point followed by shear layer roll-up, leading to large-scale vortices similar to mixing layers (Browand and Troutt, 1985). This separated shear layer grows, reattaches downstream, and slowly recovers the boundary layer due to the persistence of turbulent structures from the separated shear layer (Simpson, 1989; Song and Eaton, 2004).

While some studies explored the fundamental mechanisms governing various dynamics in separating flows TSBs, studies on related dynamics in the presence of phase transition and cavitation are still scarce. Consequently, further investigations are needed to attain a more profound comprehension of the intricate bidirectional coupling between phase transition and separating flow dynamics. Studies on cavitation in turbulent shear layer were conducted to accomplish two objectives. First group of studies focused on exploring the inception mechanism within the shear flows (Agarwal et al., 2023; Arndt and George, 1979; Katz and Liu, 2013; Katz and O'Hern, 1986), while the second group, investigated unsteady behavior of the turbulent shear flow in the presence of cavitation as well as cavitation dynamics in TSBs (Arndt, 2002; Barbaca et al., 2019; Bhatt et al., 2021a; Iyer and Ceccio, 2002).

Studies on cavitation inception in shear flows focus on the interplay between pressure fluctuations, turbulent structures, and the inception mechanism. Pioneering works by (Arndt and George, 1979) established that larger nuclei are more responsive to high-frequency pressure fluctuations, thus increasing the likelihood of cavitation inception. (Katz and O'Hern, 1986) investigated the relationship between the structure of the turbulent shear layer and cavitation inception using a sharp-edged plate geometry. Their study concluded that streamwise vortices act as preferential sites for cavitation due to lower average pressure, while spanwise vortices play a lesser role. Recent investigations using BFS configurations consistently link cavitation inception to pressure minima within quasi-streamwise vortices (QSVs) (Agarwal et al., 2018; Allan et al., 2023; Brandao and Mahesh, 2022). Allan et al. (Arndt and George, 1979) experimentally observed

microbubbles trapped in the recirculation zone of a BFS shear layer act as preferential sites for re-nucleation and subsequent cavitation, highlighting the role of pre-existing nuclei in the inception process. Similarly, (Agarwal et al., 2023) investigated the development of pressure field fluctuates and placement of initiating bubbles within and in the vicinity of QSVs. Their results highlighted a consistent relationship between the cavity size and shape in intermittent low-pressure regions preceded by stretching along the streamwise direction (aligned with quasi-streamwise vortices) and followed by contraction. Their study linked cavity size and shape to the low-pressure regions within QSVs, explaining the observed decrease in QSV diameter and pressure minima with increasing Reynolds number (Re) due to reduced viscous diffusion in the vortex core. This finding aligns with the Re trends reported earlier by (Arndt and George, 1979).

An increase in vapor generation within the shear layer influences the vorticity structures in the shear layer, and vapor can start to fill the separated region of the flow(Bhatt et al., 2021a). Several studies examined the effect of developed cavitation on the dynamics of large scale structures such as vortex morphology, shedding mechanisms and convection of spanwise structures. In a related study**,** Iyer and Ceccio(Iyer and Ceccio, 2002) conducted an experimental study on a turbulent shear layer, observing minimal changes in the initiation, development, and transport of primary and secondary vortices due to cavitation. Notably, their study found a significant increase in turbulent fluctuations within the cavitating flow. In another experimental investigation by Aeschlimann et al.(Aeschlimann et al., 2011a), behavior of a 2D mixing layer flow with and without cavitation was compared to gain insights into the effects of cavitation on 2D free mixing layer flow dynamics. The findings of their study revealed that the vaporization and collapse of bubbles introduced additional fluctuations, predominantly in the longitudinal direction of density (due to the phase change) and velocity. Additionally, they observed that vapor generation changed the size of coherent vortices while the thickness of the mixing area remained unchanged.

Some studies dealt with shear layer cavitation dynamics in BFS configurations. One of the initial studies on cavitation in BFS was an experimental study by Maurice et al.(Maurice et al., 2014), where the effect of cavitation on the mean and fluctuating velocity field was investigated. Their results showed that the mean velocity field experienced a meaningful change only after the shear layer was fully saturated with vapor. According to their results, remarkable vapor generation within the shear layer resulted in

a decline in the shear layer (thickness) growth rate while elongating the reattachment length. They also observed decreases in the size of the vortical structures, their shedding frequency and the coherence of shear layer vortices. In a numerical study by Ohta et al.(OHTA et al., 2011), flows in a turbulent cavitating shear layer were studied to examine the effect of cavitation on vortex dynamics within shear layer.

Focusing on BFS configurations, Maurice et al. (Maurice et al., 2014) experimentally investigated the impact of cavitation on the velocity field within the shear layer. They observed significant changes only after full vapor saturation. Remarkably, vapor generation reduced the growth rate of the shear layer thickness and extended the reattachment length. Additionally, they found a decrease in vortex size, shedding frequency, and vortex coherence. Ohta et al. (OHTA et al., 2011) conducted a numerical study on vortex dynamics within cavitating shear layers. Their work, however, requires further exploration alongside experimental studies like Maurice et al. (Maurice et al., 2014) for a more comprehensive understanding. According to their results, cavitation inception occurred in spanwise and streamwise vortices. They also observed that the frequency of vortex shedding increased in the upstream region, which was attributed this tendency to the disturbance induced by the strong instability of the cavitating flow field. In a recent study by Bhatt et al.(Bhatt et al., 2021a)**,** dynamics of cavitation in the BFS configuration was explored using X-ray densitometry and high-speed cinematography. The authors examined the influence of Reynolds number (Re) on various cavity properties and behavior of shear layer in the presence of a significant vapor void fraction. They reported that mean cavity lengths had a dependence on Re. Their study demonstrated a cavity filling mechanism behind the step controlled by vortex-pair interaction. They also observed adverse flow front in the form of a shockwave, which moved towards the step and eventually diminished the cavity. In another study by Li et al.(Li and Carrica, 2023), an incompressible polydisperse cavitation model was implemented to numerically evaluate the cavitation dynamics under the same physical conditions and domain provided in the experimental study of Bhatt et al.(Bhatt et al., 2021a). In their study, dynamics of cavitation behind the backward step and effect of the condensation front pressure wave on cavitation shedding were investigated. Although an incompressible model was used for each individual phase (liquid and vapor) in their study, the significant density changes during phase transition (condensation/evaporation) introduced compressibility effects. The authors defined a condensation front as a moving interface

associated with substantial condensation. Importantly, they focused on cases with very low-pressure differences across the front (within a few kPa). Under these conditions, the influence of weak pressure waves associated with condensation could be captured while neglecting the effects of large pressure jumps and high sound speeds. Their results showed that vortex formation in the wake of the step was responsible for condensation front movement to the upstream location. While the Li and Carrica (Li and Carrica, 2023) model offers valuable insights into cavitating flows, it is important to acknowledge that its incompressible nature limits its ability to capture shock waves. Shock waves, as potentially observed in the study of Bhatt et al (Bhatt et al., 2021a), are a high-speed phenomenon associated with unsteady cavitating flows. These shock waves can trigger condensation with characteristics distinct from those caused by weak pressure waves, as demonstrated in the study by Zhang (Zhang et al., 2022). Therefore, the Li and Carrica (Li and Carrica, 2023) model might not fully capture the condensation dynamics observed in the study of Bhatt et al (Bhatt et al., 2021a) due to its focus on weak pressure wave effects. Recently, Mourice et al.(Maurice et al., 2021) studied cavitation dynamics within a BFS test section. The high-speed x-ray attenuation technique, which was synchronized with pressure fluctuation measurements, was exploited to characterize the effects of void fraction dynamics on wall pressure fluctuations and vortex dynamics in different cavitation intensities. It was observed that the pressure waves generated by extreme events led to a remarkable change in the flow signature and topology after hitting the step wall.

Despite the existing studies on cavitation and shear layer dynamics, there are still several important questions that remain open. There are a limited number of numerical studies in this topic, most of which have not considered the compressibility effect of pure phases and the effect of shock waves in the presence of cavitation(Brandao and Mahesh, 2022; Li and Carrica, 2023; OHTA et al., 2011). Moreover, it is crucial to conduct more studies using both numerical and experimental perspectives to explore the impact of vapor generation, transport, and condensation on the unsteadiness of turbulent separating flow, which includes low/medium/high frequency dynamic, and underlying mechanisms. Another critical, yet underexplored, aspect is the influence of the incoming turbulent boundary layer and roughness-induced perturbations on cavitating flow characteristics and dynamics. This Ph.D. thesis presents a multi-faceted investigation into the complex interplay between turbulence, cavitation, and geometric modifications in microscale

separated flows, primarily focusing on BFS configurations. The thesis integrates advanced computational fluid dynamics (CFD) with novel experimental analyses to provide a comprehensive understanding of these phenomena across varying flow conditions and surface treatments.

Methodologically, this thesis employs a sophisticated framework. This includes a customized three-dimensional fully compressible cavitation flow solver, built upon OpenFOAM's rhoCentralFoam with integrated HZDR's SGS model for Large Eddy Simulation (LES). This solver, capable of handling low Mach number compressible flow physics and thermodynamic non-equilibrium through a vapor volume fraction transport equation, accurately captures effects such as shock waves and baroclinic vortex dynamics. Temporal advancement utilizes a second-order, four-stage low-storage Runge-Kutta technique with an adaptive Courant-Friedrichs-Lewey (CFL) criterion. Complementing the computational work, the thesis also presents the first experimental analysis of shear cavitation in a microscale BFS configuration, employing high-speed imaging to analyze cavitation patterns and vortex dynamics across various flow regimes.

Key findings reveal significant insights into the influence of cavitation on turbulent flow characteristics. Cavitation actively hinders the mean growth of the shear layer and retards its reattachment. The generation and condensation of vapor structures critically affect how turbulence is dissipated and produced, leading to increased mean pressure and pressure fluctuations near the reattachment. Spectral analysis identifies two dominant low-frequency modes associated with reattachment point displacement, which exhibit smaller frequencies in the presence of cavitation, each linked to specific vapor transport mechanisms. Moreover, cavitation enhances the spectral energy of high-frequency fluctuations in the reattachment region due to frequent bubble collapses. Spectral Proper Orthogonal Decomposition (SPOD) provides valuable insights into coherent structures and their dynamics under cavitating conditions.

This thesis further explores the profound impact of riblet-equipped surfaces (quantified by Blockage Ratio, BR) on turbulent flow and cavitation. Riblets fundamentally alter the flow field by shifting Turbulence Kinetic Energy (TKE) transport from local production/dissipation to enhanced turbulent diffusion and convection, particularly within the shear layer. Reynolds stress anisotropy is significantly modified near the wall, indicating altered turbulent mixing. Coherent structures become notably larger and

slower, and Dynamic Mode Decomposition (DMD) highlights the formation of dominant low-frequency vortices near rib crests, directly impacting the downstream flow. These riblet-induced turbulent modifications profoundly influence cavitation, leading to the formation of larger and more intense cavitation packets that correlate directly with the underlying coherent structure strength. The channel's downstream region ultimately transitions into a supercavitation regime, with varying void fraction distributions dependent on BR.

Experimentally, the thesis highlights critical differences between microscale and macroscale shear cavitation. Surface forces are found to play a dominant role in nuclei distribution and vapor formation. Distinct timescales are identified for phenomena like shedding and shockwave propagation, with vortex strength in the shear layer hypothesized to be crucial for cavity shedding during upstream shockwave propagation. Increased pressure significantly elevates the mean thickness, length, and intensity of cavitation within the shear layer. Two vortex modes (shedding and wake) at the reattachment zone are identified, affecting cavitation shedding frequency and downstream penetration, with the stronger, lower-frequency wake mode transporting cavities deeper into the channel.

Collectively, this thesis advances the understanding of turbulent separated flows and cavitation in microscale environments, elucidating the complex, multi-scale interactions between fluid dynamics, phase change, and geometric factors. The findings provide critical insights for the design and optimization of microfluidic devices and energy systems operating under cavitating conditions.

Thesis Objectives

This thesis undertakes a comprehensive investigation into the intricate interplay of cavitation, TSB, and TBL. Specifically, the research aims to:

- Thoroughly examine the influence of cavitation and associated phase transition phenomena (vapor generation and condensation) on the dynamics and characteristics of TSBs. This includes a detailed analysis of the impact of vapor packets within the shear layer and the role of condensation shockwaves in the reattachment region.
- Systematically study the effect of the incoming TBL—specifically, when controlled using riblets—on the overall dynamics and characteristics of the TSB.

- Investigate the specific impact of the incoming TBL on cavitating flow conditions.
- Experimentally characterize the dynamics and characteristics of cavitating flow in separating and reattaching flows across various flow regimes.

Novel Aspects of This Research

This thesis introduces several novel contributions to the field:

- Development and integration of a custom, full Mach number cavitating flow solver within the OpenFOAM platform, uniquely coupled with mixed Large Eddy Simulation (LES) capabilities.
- Execution of a pioneering experimental study focusing on microscale separating and reattaching cavitating flows.
- Synergistic application of the developed custom solver and the experimental setup to provide a comprehensive understanding of the complex interplay between phase transition, TSBs, and TBLs in separating and reattaching cavitating flows.

Research Plan

To achieve the stated objectives, the research will follow a structured plan encompassing both numerical and experimental methodologies, complemented by advanced data analysis techniques:

- Numerical Solver Customization: Developing and refining a numerical solver specifically designed to accurately simulate both shockwaves and turbulent structures, capturing their effects with high fidelity.
- Experimental Setup Implementation: Establishing a robust experimental setup that serves a dual purpose: validating the numerical results and enabling the extension of the study to a wide range of flow conditions.
- Extensive Post-processing and Data Analysis: Employing advanced post-processing and data analysis techniques—including, but not limited to, statistical analysis, modal analysis, and turbulent analysis—to comprehensively characterize the statistics and dynamics of the flow, thereby facilitating an in-depth understanding of underlying mechanisms and their effects.

Building upon this foundation, the primary objective of this PhD thesis is to comprehensively investigate the complex interplay between turbulent shear layer

dynamics and cavitation in microscale BFS configurations. This is achieved through a dual numerical and experimental approach, specifically aiming to:

Customize and validate a fully compressible cavitation solver capable of accurately capturing collapse shock waves and turbulent structures and effects.

Provide a detailed understanding of how cavitation profoundly affects the turbulent characteristics and dynamics of separating-reattaching flows, including its influence on the TSB characteristics and dynamics, the effect of phase transition on the shear layer, the impact of collapse on reattachment, the turbulent energy cascade, and the relation of vortex dynamics with vapor generation and condensation, utilizing modal analysis to identify coherent structures and their dynamics, as well as dominant motions and unsteadiness.

Explore the control of cavitation within the TSB by strategically modifying the incoming TBL using riblets, and to analyze how these modifications impact downstream turbulent characteristics of both the TBL and TSB, and their subsequent influence on cavitation and condensation phenomena.

Ultimately, this work seeks to significantly advance fundamental knowledge critical for the design and optimization of microfluidic and energy systems operating under cavitating conditions.

2 METHODS: COMPRESSIBLE CAVITATING FLOW SOLVER-PART 1

2.1 Introduction

The computational models are solved using OpenFOAM-2012, an open-source C++ library from the OpenFOAM Foundation ("OpenFoam. The Open Source CFD Toolbox openfoam foundation," 2023). The characteristics and dynamics of compressible cavitating flows are explored through the application of the existing compressible cavitation solver and the newly proposed physical models. Within this cavitation solver, a cell-centered, co-located finite-volume approach (FVM) is employed for spatial discretization, coupled with a multistep temporal scheme to solve the compressible Navier-Stokes equations pertinent to unsteady cavitating flows. The solver employs a homogenous equilibrium model to account for phase transition, along with corresponding appropriate equation of states. Moreover, the effect of non-condensable gases is considered with adding a third phase to the conservative equations. Details of the numeric are provided in the work(Jasak, 1996). Detailed information about the solution procedure and discretization are presented in the following sections.

The newly developed numerical model was successfully applied to simulate previously obtained experimental results, demonstrating its effectiveness in capturing the complex dynamics of compressible cavitating flows. This model offers several key advantages, including its ability to incorporate the impact of non-condensable gases on cavitation dynamics, consider the effects of pressure fluctuations in the phase transition formula, accurately predict shock waves and their influence on bubble collapse through the use of a nonlinear model for mixture compressibility, account for thermal effects by incorporating an energy equation and corresponding equation of state, and consider thermodynamic disequilibrium between phases (finite rates of evaporation and condensation) by employing separate transport equations for each phase.

2.2 Physical Description and Governing Equations

2.2.1 Phase Equation

The cavitating flow was modeled using an Eulerian single-fluid approach, assuming mechanical equilibrium between all phases (no slip velocity). This approach treated the flow as a mixture of phases, with the volume of fraction (VOF)(Hirt and Nichols, 1981) method employed to capture the interface between them. In the VOF framework, the phase fractions of each phase were accounted for by incorporating additional phase transport equations into the governing equations.

While typical cavitation models consider only liquid and vapor phases, this study introduced a noncondensable gas as an additional phase to investigate its influence on cavitating flows. To account for phase transition, the transport equation for each phase was expressed as follows:

$$\frac{\partial(\rho_l \alpha_l)}{\partial t} + \nabla \cdot (\rho_l \alpha_l \mathbf{U}) = \dot{m} \tag{2.1}$$

$$\frac{\partial(\rho_v \alpha_v)}{\partial t} + \nabla \cdot (\rho_v \alpha_v \mathbf{U}) = -\dot{m} \tag{2.2}$$

$$\frac{\partial(\rho_{ng} \alpha_{ng})}{\partial t} + \nabla \cdot (\rho_{ng} \alpha_{ng} \mathbf{U}) = \dot{0} \tag{2.3}$$

$$\alpha_l + \alpha_v + \alpha_{ng} = 1 \tag{2.4}$$

where $\rho, \alpha, \mathbf{U}$ and $\dot{m}$ represent density, phase fraction, velocity, and phase change mass transfer rate, respectively. Subscripts $l, v,$ and ng stand for liquid, vapor, and noncondensable gas phases. The source term showing mass transfer is given by:

$$\dot{m} = \dot{m}^+ + \dot{m}^- \tag{2.5}$$

where $\dot{m}^+$ and $\dot{m}^-$ are the rate of condensation and vaporization on the phase interface.

Then the compressible and incompressible parts of the equations will be decoupled by expanding the convective terms and doing some mathematical manipulations as follow:

$$\begin{cases} \dfrac{\partial \alpha_l}{\partial t} + \nabla \cdot (\alpha_l \mathbf{U}) = -\dfrac{\alpha_l}{\rho_l}\left[\dfrac{D\rho_l}{Dt}\right] + \dfrac{\dot{m}}{\rho_l} \\ \dfrac{\partial \alpha_v}{\partial t} + \nabla \cdot (\alpha_v \mathbf{U}) = -\dfrac{\alpha_v}{\rho_v}\left[\dfrac{D\rho_v}{Dt}\right] - \dfrac{\dot{m}}{\rho_v} \\ \dfrac{\partial \alpha_{ng}}{\partial t} + \nabla \cdot \left(\alpha_{ng} \mathbf{U}\right) = -\dfrac{\alpha_{ng}}{\rho_{ng}}\left[\dfrac{D\rho_{ng}}{Dt}\right] \end{cases} \tag{2.6}$$

where $\frac{D}{Dt}$ is the material derivative. With the addition of all the equations in (6) the divergence of the velocity field will be as follows:

$$\nabla \cdot \mathbf{U} = -\left(\frac{\alpha_l}{\rho_l}\left[\frac{D\rho_l}{Dt}\right] + \frac{\alpha_v}{\rho_v}\left[\frac{D\rho_v}{Dt}\right] + \frac{\alpha_{ng}}{\rho_{ng}}\left[\frac{D\rho_{ng}}{Dt}\right]\right) + \dot{m}\left(\frac{1}{\rho_l} - \frac{1}{\rho_v}\right) \tag{2.7}$$

An artificial counter-gradient compression term(HG Weller, 2008) $\nabla \cdot \Big(\alpha_l \alpha_v (\mathbf{U}_l - \mathbf{U}_v) + \alpha_l \alpha_{ng}\big(\mathbf{U}_l - \mathbf{U}_{ng}\big)\Big)$ is used in equations to maintain the liquid-gas interface sharpness. By replacing the divergence term from the equation (7) and adding the artificial compression, the final form of the transport equation compromising the phase transition is given by:

$$\begin{cases} \dfrac{\partial \alpha_l}{\partial t} + \nabla \cdot (\alpha_l \mathbf{U}) + \nabla \cdot \Big(\alpha_l \alpha_v (\mathbf{U}_l - \mathbf{U}_v) + \alpha_l \alpha_{ng}\big(\mathbf{U}_l - \mathbf{U}_{ng}\big)\Big) \\ \quad = -\dfrac{\alpha_l}{\rho_l}\left[\dfrac{D\rho_l}{Dt}\right](1 - \alpha_l) + \alpha_l(\nabla \cdot \mathbf{U}) + \\ \quad \alpha_l\left[\dfrac{\alpha_v}{\rho_v}\left[\dfrac{D\rho_v}{Dt}\right] + \dfrac{\alpha_{ng}}{\rho_{ng}}\left[\dfrac{D\rho_{ng}}{Dt}\right]\right] + \dot{m}\left(\dfrac{1}{\rho_l} - \alpha_l\left(\dfrac{1}{\rho_l} - \dfrac{1}{\rho_v}\right)\right) \\ \dfrac{\partial \alpha_v}{\partial t} + \nabla \cdot (\alpha_v \mathbf{U}) + \nabla \cdot \Big(\alpha_v \alpha_l (\mathbf{U}_v - \mathbf{U}_l) + \alpha_v \alpha_{ng}\big(\mathbf{U}_v - \mathbf{U}_{ng}\big)\Big) \\ \quad = -\dfrac{\alpha_v}{\rho_v}\left[\dfrac{D\rho_v}{Dt}\right](1 - \alpha_v) + \alpha_v(\nabla \cdot \mathbf{U}) + \\ \quad \alpha_v\left[\dfrac{\alpha_l}{\rho_l}\left[\dfrac{D\rho_l}{Dt}\right] + \dfrac{\alpha_{ng}}{\rho_{ng}}\left[\dfrac{D\rho_{ng}}{Dt}\right]\right] - \dot{m}\left(\dfrac{1}{\rho_v} - \alpha_v\left(\dfrac{1}{\rho_l} - \dfrac{1}{\rho_v}\right)\right) \\ \dfrac{\partial \alpha_{ng}}{\partial t} + \nabla \cdot \left(\alpha_{ng} \mathbf{U}\right) + \nabla \cdot \Big(\alpha_{ng} \alpha_l \big(\mathbf{U}_{ng} - \mathbf{U}_\mathbf{l}\big) + \alpha_{ng} \alpha_v \big(\mathbf{U}_{ng} - \mathbf{U}_v\big)\Big) \\ \quad = -\dfrac{\alpha_{ng}}{\rho_{ng}}\left[\dfrac{D\rho_{ng}}{Dt}\right]\big(1 - \alpha_{ng}\big) + \alpha_{ng}(\nabla \cdot \mathbf{U}) + \\ \quad \alpha_{ng}\left[\dfrac{\alpha_l}{\rho_l}\left[\dfrac{D\rho_l}{Dt}\right] + \dfrac{\alpha_v}{\rho_v}\left[\dfrac{D\rho_v}{Dt}\right]\right] + \dot{m}\alpha_{ng}\left(\dfrac{1}{\rho_l} - \dfrac{1}{\rho_v}\right) \end{cases} \tag{2.8}$$

The artificial compression is only active in the interface region where $\alpha_l \alpha_v$ and $\alpha_l \alpha_{ng}$ are nonzero. To make sure that the compression is applied normally to the interface the relative velocity between any two phases is expressed as:

$$\mathbf{U}_c = c_a|\mathbf{U}|\frac{\nabla\alpha}{|\nabla\alpha|} \tag{2.9}$$

The compression rate is regulated by c_a. Large values of c_a can lead to numerical instabilities, therefore the value in the order of unity is suggested for this parameter(HG Weller, 2008). In the system of phase-fraction equations (9), the first terms on the right-hand side (RHS) show the effect of the compressibility on the mass distribution, and the third terms show the effect of the phase transition on the mass exchange and generation.

The system of phase fraction equations was discretized using the Multidimensional Universal Limiter with Explicit Solution (MULES) method which warrant consistency and boundedness even in the presence of flow phase transition(Zalesak, 1979). Due to the sharp interface between non-miscible phases, the discretization of the convective term in the VOF method poses a challenge in preserving solution boundedness and consistency near interfaces. First-order schemes can lead to interface smearing due to false diffusion, while high-order schemes may be unstable and cause numerical oscillations. Limiters address this issue by reducing the flux near sharp interfaces.

In the MULES method, the convective term is discretized using a combination of high-order and low-order flux approximations. An anti-diffusion flux is then defined to mitigate the numerical diffusion introduced by the low-order flux. A flux-limiting technique is employed to decrease the contribution of the anti-diffusion flux in regions with sharp interfaces, thereby preventing overshoot and undershoot of the phase fraction.

2.2.2 Mass and Momentum Equations

As it was mentioned earlier in this section, the single fluid approach is adopted in this study for modeling the multiphase flow. Therefore, one set of equations is used for the mass and the momentum conservation of the three-phase mixture flow, which is given by (Yu et al., 2017):

$$\frac{\partial(\rho)}{\partial t} + \nabla\cdot(\rho\mathbf{U}) = 0 \tag{2.10}$$

$$\frac{\partial(\rho\mathbf{U})}{\partial t} + \nabla\cdot(\rho\mathbf{U}\otimes\mathbf{U}) = -\nabla p + \nabla\cdot\mathbf{S} + \mathbf{F_s} \tag{2.11}$$

In the above equations, ρ represents the mixture density which is estimated by $\rho = \rho_l\alpha_l + \rho_v\alpha_v + \rho_{ng}\alpha_{ng}$, $\mathbf{S}$ is the stress tensor, and $\mathbf{F_s}$ denotes the surface tension stress.

To account for pressure fluctuations that have a remarkable influence on the cavitation dynamics Large Eddy Simulation (LES) is employed(Garnier et al., n.d.). In the LES method, large energetic scales associated with large eddies are resolved while small scales (Sub-Grid scales (SGS)) are modeled. For this purpose, the filtered form of governing equations is used(Bensow and Bark, 2010). Therefore, $\mathbf{S}$ in equation (11) is formed from two terms of viscous stress tensor ($\boldsymbol{\tau} = 2\mu\mathbf{S}_\tau, \mathbf{S}_\tau$ is strain tensor, and μ is the mixture dynamic viscosity given by: $\mu = \mu_l\alpha_l + \mu_v\alpha_v + \mu_{ng}\alpha_{ng}$), and SGS stress ($\boldsymbol{\tau^{sgs}}$).

The most commonly used LES models are subgrid viscosity models which assume the energy transfer mechanism from the resolved to the subgrid scales resembles a molecular mechanism represented by the diffusion term, $\boldsymbol{\tau^{sgs}} = 2\mu^{sgs}\mathbf{S}_\tau$, where μ^{sgs} is subgrid scale viscosity. In this study Wall Adaptive Large Eddy (WALE) is implemented(Nicoud and Ducros, 1999). WALE model is an algebraic subgrid viscosity model that enables correct prediction of SGS viscosity close to the wall without resorting to a transport-like equation or adding a damping wall function.

The surface tension is calculated as $\mathbf{F_s} = \sigma\kappa\nabla\alpha_l$, where σ shows the surface tension coefficient and κ shows the interface curvature which is obtained as $\kappa = \nabla\alpha_l/|\nabla\alpha_l|$.

In this study, a pressure-based solver is implemented. To drive the pressure equation the momentum equation is partially discretized(Jasak, 1996) (Demirdžić et al., 1993):

$$\mathbf{U}_p = \frac{H(\mathbf{U})}{a_p} - \frac{\nabla p}{a_p} \tag{2.12}$$

Where $H(\mathbf{U})$ includes the influence of the transport terms of neighboring cells and the source part of transients and the surface tension force effect. Accordingly, the divergence of the predicted velocity is given by:

$$\nabla \cdot \mathbf{U}_p = \nabla \cdot \left(\frac{H(\mathbf{U})}{a_p}\right) - \nabla \cdot \left(\frac{\nabla p}{a_p}\right) \tag{2.13}$$

Using equations (1), (10), and (13), and considering the pressure-density relation ($\frac{D\rho}{Dt} = \psi\frac{Dp}{Dt}$, ψ is the compressibility coefficient) the final form of the mixture pressure equation is the compromise of incompressible and compressible parts(Yu et al., 2017):

$$\begin{cases} \underbrace{\frac{\alpha_l}{\rho_l}\left[\psi_l \frac{\partial p}{\partial t} + \mathbf{U}\cdot\nabla(\rho_l)\right] + \frac{\alpha_v}{\rho_v}\left[\psi_v \frac{\partial p}{\partial t} + \mathbf{U}\cdot\nabla(\rho_v)\right] + \frac{\alpha_{ng}}{\rho_{ng}}\left[\psi_{ng} \frac{\partial p}{\partial t} + \mathbf{U}\cdot\nabla(\rho_{ng})\right]}_{compressble} + \\ \underbrace{\nabla\cdot\mathbf{U} - \dot{m}\left(\frac{1}{\rho_l} - \frac{1}{\rho_v}\right)}_{incompressble} = 0 \end{cases} \tag{2.14}$$

2.2.3 Energy Equation

The energy equation of the mixture is given by (Wang et al., 2021):

$$\frac{\partial}{\partial t}\left[\rho\left(\frac{1}{2}|\mathbf{U}|^2 + e\right)\right] + \nabla\cdot\left[\rho\mathbf{U}\left(\frac{1}{2}|\mathbf{U}|^2 + e\right)\right] = -\nabla\cdot q - \nabla\cdot(p\mathbf{U}) \tag{2.15}$$

where, e shows the specific internal energy, and q is the heat flux. To express the energy equation based on temperature, the internal energy and the heat flux can be replaced by $e = C_{v,m}T$ and $q = -\alpha^{th}C_{v,m}\nabla T$, respectively:

$$\begin{aligned} &\frac{\partial}{\partial t}\left(\rho C_{v,m}T\right) + \nabla\cdot\left(\rho C_{v,m}T\mathbf{U}\right) - \nabla\cdot(\alpha^{th}C_{v,m}\nabla T) \\ &\qquad = -\nabla\cdot(p\mathbf{U}) - \frac{\partial}{\partial t}(\rho k) + \nabla\cdot(\rho k\mathbf{U}) \end{aligned} \tag{2.16}$$

where $C_{v,m}$ represents the mixture-specific heat and α^{th} is the mixture of thermal diffusivity, which is given by:

$$\alpha^{th} = \frac{\alpha_l k_l}{C_{v,l}} + \frac{\alpha_v k_v}{C_{v,v}} + \frac{\alpha_{ng} k_{ng}}{C_{v,ng}} \tag{2.17}$$

here k denotes the thermal conductivity.

2.2.4 Thermodynamic Equation of State

The physics model includes the Equation of State (EoS) for water, vapor, and noncondensable gas. This allows it to capture compressibility effects within cavitating flows, where density variations are essential for understanding cavity behavior. The EOS for each pure phase and the mixture is presented in the following.

In the pure water region where $\alpha_l = 1$, modified Tait EOS is applied as follow(Aitken and Foulc, 2019):

$$\frac{p_l + B}{p_{l,sat} + B} = \left(\frac{\rho_l}{\rho_{l,sat}}\right)^N \tag{2.18}$$

Where B and N are empirical parameters, and subscript sat stands for vapor saturation state.

For the pure vapor and noncondensable gas, ideal gas EOS is utilized to estimate the density based on the pressure and the temperature:

$$\begin{aligned} p_v &= \rho_v R_v T_v, \\ p_{ng} &= \rho_{ng} R_{ng} T_{ng} \end{aligned} \tag{2.19}$$

where R shows the gas constant.

In addition, the internal energy for each pure phase is given as:

$$e = C_{v,i}(T - T_0) + e_{i,0} \tag{2.20}$$

where i can be substituted by $l, v,$ and ng. Also, T_0 and $e_{i,0}$ denote the reference temperature and internal energy for the i_{th} phase.

Accordingly, the compressibility of each phase is calculated as follows:

$$\begin{aligned} \psi_l &= \frac{d\rho_l}{dp} = \frac{\rho_l}{(\rho_l/\rho_{l,sat})^N N\left(p_{l,sat} + B\right)} \\ \psi_i &= \frac{d\rho_i}{dp} = \frac{1}{R_i T} \quad i = v, ng \end{aligned} \tag{2.21}$$

In the mixture region, the specific internal energy is given by:

$$e = \left(\alpha_l C_{v,l} + \alpha_v C_{v,v} + \alpha_{ng} C_{v,ng}\right)(T - T_0) + e_0 \tag{2.22}$$

Saturation pressure can be expressed as a polynomial function of temperature. For water, the saturation pressure is estimated based on Wagner's equation as follows(Saul and Wagner, 1987):

$$\ln\left(\frac{p_{sat}}{p_c}\right) = (a_1 t + a_2 t^{1.5} + a_3 t^3 + a_4 t^{3.5} + a_5 t^4 + a_6 t^{7.5})\frac{T_c}{T} \tag{2.23}$$

where p_c is critical pressure, T_c is the temperature of the water, and $t = 1 - \frac{T}{T_c}$. a_i for i=1_7 are constant coefficients. Based on the homogenous mixture assumption,

the internal energy (e) and density (ρ) of the mixture can be used to estimate the thermodynamical state of the fluid.

The speed of sound in the mixture is approximated using the frozen sound speed assumption. Accordingly, the sound speed in the mixture will be given by(Yu et al., 2017):

$$\frac{1}{\rho c^2} = \frac{\alpha_l}{\rho_l c_l^2} + \frac{\alpha_v}{\rho_v c_v^2} + \frac{\alpha_{ng}}{\rho_{ng} c_{ng}^2} \tag{2.24}$$

where c is the speed of sound. According to this nonlinear equation, the acoustic characteristics of the fluid are strongly altered in the water-vapor mixture, and the speed of sound in the bubbly mixture reduced by around two orders- of magnitude compared to the speed of sound in the pure phases. Consequently, due to the small sound speed in the mixture, shock waves occur even in low flow velocities which can have a significant effect on the cavitation dynamics and collapses(Wang et al., 2021).

2.2.5 Phase Transition Model

The phase transition model that is used in the current study is based on the cavitation model developed by F.Giussani et al.(Giussani et al., 2020a) which considered the effect of the third term in the phase transition term. Consequently, the mass transfer rate $\dot{m}$ in phase fraction equations (Eqs (8)) is calculated as:

$$\dot{m} = \begin{cases} -\dfrac{3\alpha_v \left(\dfrac{\rho_v \rho_l}{\rho + \alpha_{nc}\left(\rho_l - \rho_{nc}\right)}\right) \max\left(p - p_{sat}, 0\right) \sqrt{\dfrac{2}{3}\dfrac{1}{\rho_l \left|p - p_{sat}\right|}}}{R + R^4 \dfrac{4}{3}\pi n_0 \left[\dfrac{\rho + \alpha_{nc}\left(\rho_v - \rho_{nc}\right)}{\rho + \alpha_{nc}\left(\rho_l - \rho_{nc}\right)}\right]} & if\ p > p_{sat} \\ -\dfrac{4\pi\alpha_l n_0 R^2 \left(\dfrac{\rho_v \rho_l}{\rho + \alpha_{nc}\left(\rho_l - \rho_{nc}\right)}\right) \min\left(p - p_{sat}, 0\right) \sqrt{\dfrac{2}{3}\dfrac{1}{\rho_l \left|p - p_{sat}\right|}}}{1 + R^3 \dfrac{4}{3}\pi n_0 \left[\dfrac{\rho + \alpha_{nc}\left(\rho_v - \rho_{nc}\right)}{\rho + \alpha_{nc}\left(\rho_l - \rho_{nc}\right)}\right]} & if\ p < p_{sat} \end{cases} \tag{2.25}$$

$$R = \sqrt[3]{\frac{3}{4\pi n_0}\frac{1 + \alpha_{nuc} - \alpha_l - \alpha_{nc}}{\alpha_l}} \tag{2.26}$$

where α_{nuc}, and n_0 represent the volume fraction of the initial nuclei and initial nuclei concentration. This model accounts for homogenous nucleation and is developed based on the work of Schnerr et al.(Schnerr et al., 2008).

2.3 Solution Procedure and Discretization

The unknown field variables include phase fractions ($\alpha_l, \alpha_v,$ and α_{ng}), densities ($\rho_l, \rho_v,$ and ρ_{ng}), velocity field (**U**), pressure field (p), and temperature field (T). The treatment mechanism of field variables is similar to the study of Koch et al.(Koch et al., 2016). During the solution process, the phase fraction fields were updated using the system of phase fraction equations (8). The momentum equation was employed to solve for the velocity field, while the pressure equation (14) was used to determine the pressure field. The temperature field was calculated from the energy equation (16). Finally, the velocity, pressure, temperature, density, and internal energy fields were computed using the equations of state (EOS) (equations 18, 19, and 20). The coupling between the velocity and pressure fields is solved by using the PIMPLE algorithm. PIMPLE is a combination of SIMPLE(Patankar and Spalding, 1972) and PISO algorithms(Issa, 1986) in which the inner PISO loop is completed by the outer SIMPLE loop and possibly under the relaxation of variables. The transient term was discretized using the first-order implicit Euler scheme. The Laplacian term was approximated using the second-order Gauss linear scheme. The van Leer TVD scheme was employed for the discretization of the convection term. To control the boundedness and consistency of the solution, the MULES scheme, previously discussed for phase fractions, was utilized. Artificial compression terms were evaluated using a conservative interface compression scheme (CICSAM) to ensure a sharp liquid-gas interface(Markatos, 1986). For the vapor-gas mixture, the compression factor in the CICSAM scheme is set to 0 to account for diffusion at their interface. Considering $n + 1$, n, and $*$, as indicators as the current, preceding timestep, and prior iteration values, the overall solution procedure in the implemented three-phase compressible cavitation model is as follows:

1) Phase fractions are updated using equation (8), and then the surface curvature κ is obtained using the calculated phase fractions,

2) The SGS model is solved to update the SGS stresses,
3) Momentum predicter (12) is solved to obtain $\mathbf{U}^*$,
4) Energy equation (16) is solved to calculate the new temperature field T^{n+1}, and fluid properties are updated accordingly (such as p_{sat} in equation (23))
5) Calculate the new pressure field p^{n+1} using equation (14), and use it to calculate the new velocity $\mathbf{U}^{\boldsymbol{n+1}}$,
6) New temperature and pressure fields are used in EOS (18, 19, 20) to calculate the new density and internal energy of pure phases,
7) Equation (21) is used to update the compressibility of pure phases,
8) Mixture properties including density, viscosity, and sound speed, are updated using the related mixture models,
9) Return to step (1) and solve for the next time step.

Implementation

The flowchart of the pressure-based solver is shown in Figure1.

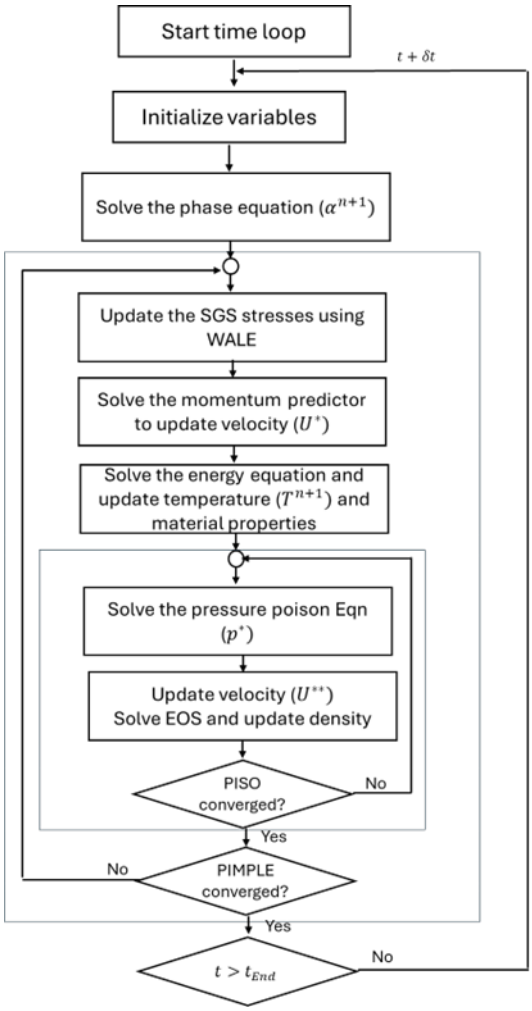

Figure 2.1 Flowchart of the customized three-phase pressure-based solver.

2.4 Validation

2.4.1 BFS Microchannel Experiments

In this section, experimental results are presented for comparison with the numerical solutions. Since temporal resolution in our experiment was orders of magnitude lower than the required resolution to capture dominant dynamics of TSB, we were not able to use the current experimental results for quantitative evaluation of void fraction dynamics. Figure 1 presents 4 sequential snapshots of calculated void fraction in our experiments, where the snapshots of void fraction were obtained starting from an arbitrary start time with the same time intervals as in the numerical simulations. Considering uncertainties in

the experiments (including uncertainties in the measurements, as well as those associated with the device and surface defects), as well as, stochastic nature of turbulence and cavitation, some differences between the instantaneous results of experiments and numerical studies are expected. Nonetheless, an acceptable agreement can be seen in the evolution of the void fraction for instantaneous results within the given time period. For example, the region associated with vapors within the shear layer and also reattachments agree well for all time sequences. Furthermore, from displacement of the reattachment it can be seen that the expansion and contraction of TSB could be correctly captured which proves the capability of the model in accurately capturing TSB dynamics (from top in 1st and 4th rows the reattachment is around $\tilde{x} = 5.5$, and in 2nd and 3rd rows around $\tilde{x} = 6.5$).

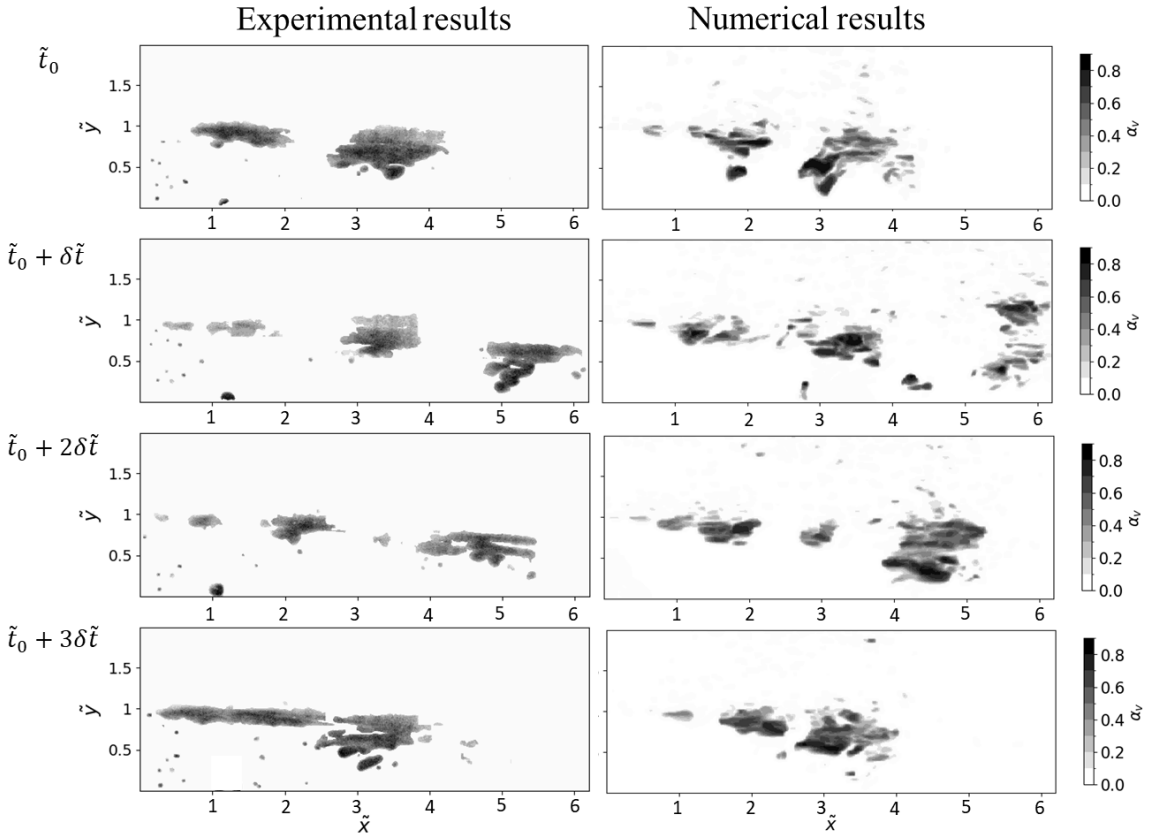

Figure 2.2 Comparison between experimental and numerical results of void fraction distribution in several sequential time instances.

In addition to instantaneous results, some statistical evaluations were made to have a more concrete conclusion about the deviation of the numerical results from the experimental results. Figure 2.3 shows the mean value ($\bar{\alpha}_v$) and Root Mean Square (RMS) of the fluctuations ($\alpha'_{v\,rms}$) of void fraction field regarding the experimental results and

numerical simulations. Due to the limitations in measurements in the field of view in the experiments, the channel area for $\tilde{x} > 6.2$ is not included in the results. The results indicate that $\bar{\alpha}_v$ and $\alpha'_{v\,rms}$ are mostly concentrated within the shear layer which aligns with recent studies(Agarwal et al., 2023; Bhatt et al., 2021a). These results support that cavitation generation and transport mostly occur within the shear layer. Mitigation in the mean void fraction value can be observed around $\tilde{x} = 6$ for both experimental and numerical results indicating a strong mean pressure recovery in this region associated with shear layer impingement. Moreover, there is a good agreement in the RMSof fluctuations in void fraction between both results. The results of $\alpha'_{v\,rms}$ prove the highly fluctuating nature of cavitation within the shear layer where vapor packets are generated, transported, and collapse at various locations along the shear layer. The main difference between the numerical and experimental results lies in a larger spreading of the vapor packets towards the bottom wall at $\tilde{x} \approx 4$.

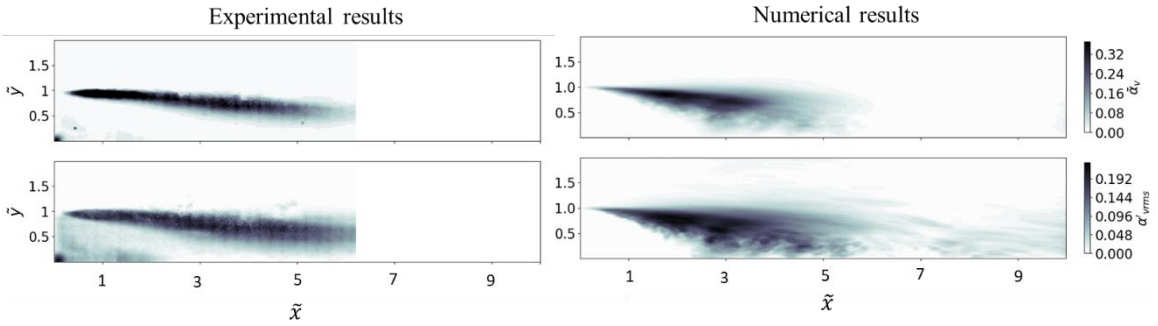

Figure 2.3 Comparison in mean and RMSvoid fraction fields between experimental and numerical results.

2.4.2 Numerical Replication of Experimental Study of Winklhofer et al.(Winklhofer et al., 2001)

We further validated our numerical model using experimental study of Winklhofer et al.(Winklhofer et al., 2001) since that study provides quantitative data related to the pressure and velocity distribution and was used as a benchmark example in many numerical studies such as Yu et al.(Yu et al., 2017). The computational domain was selected based on the experimental conditions and also previous numerical studies(Yu et al., 2017). The numerical domain (Figure 2.4) consists of three main parts: inlet extension,

microchannel and outlet extension (the dimensions are provided in Table S.2). The inlet is located on the left side in Figure 3 where constant pressure of 10 MPa is applied. On the other side of the channel various values of pressures ranging from 2 to 6 MPa are applied by imposing a non-reflective boundary condition for this area. In the non-slip and adiabatic wall boundary conditions were imposed with zero gradient for hydrodynamic parameters. Related information about the fluid properties is provided in Table S.3.

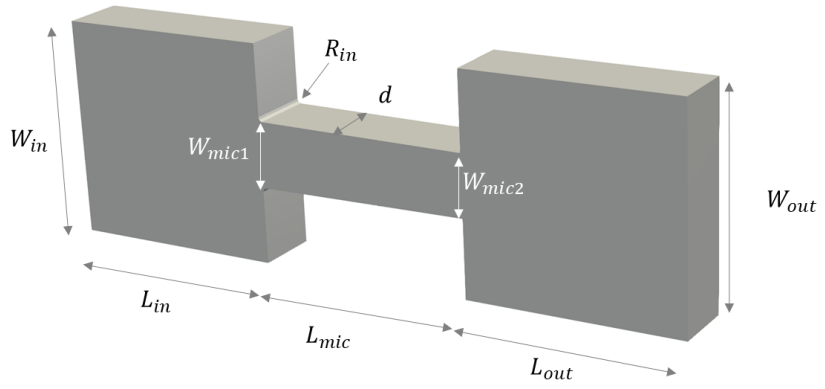

Figure 2.4 Computational domain related to the experimental study by Winklhofer et al[56].

Table 2.1 Dimensions related to the computational domain represented in Figure

W_{in} $[\mu m]$	W_{mic1} $[\mu m]$	W_{mic2} $[\mu m]$	W_{out} $[\mu m]$	R_{in} $[\mu m]$	d $[\mu m]$	L_{in} $[\mu m]$	L_{mic} $[\mu m]$	L_{out} $[\mu m]$
1000	301	284	1000	20	300	1000	1000	1000

Table 2.2 Fluid properties related to the experimental study by Winklhofer et al(Winklhofer et al., 2001).

p_{in} $[MPa]$	ρ_f $\left[\frac{kg}{m^3}\right]$	ρ_{fv} $\left[\frac{kg}{m^3}\right]$	p_{sat} $[Pa]$	μ_v $\left[\frac{Ns}{m^2}\right]$	μ_{fv} $\left[\frac{Ns}{m^2}\right]$	σ $\left[\frac{N}{m}\right]$	p_{amb} $[MPa]$	T_{amb} $[K]$

10	832	0.136	2000	6.5e-3	5.9e-6	0.03	2-7	304

Our computational findings align well with the experimental data of Winklhofer et al(Winklhofer et al., 2001) as well as the numerical results provided by Yu et al(Yu et al., 2017). The results for the mean values of the pressure field and void fraction field in three different outlet pressures are provided in Figure 2.5. It is observed that the model accurately captured the cavitation inception and development, as well as the pressure field prior to the inception regime. In addition, the pressure field along the centerline for the cavitation regime is provided in Figure 2.6. which shows a good agreement between our numerical results and the experimental results of Winklhofer et al(Winklhofer et al., 2001).

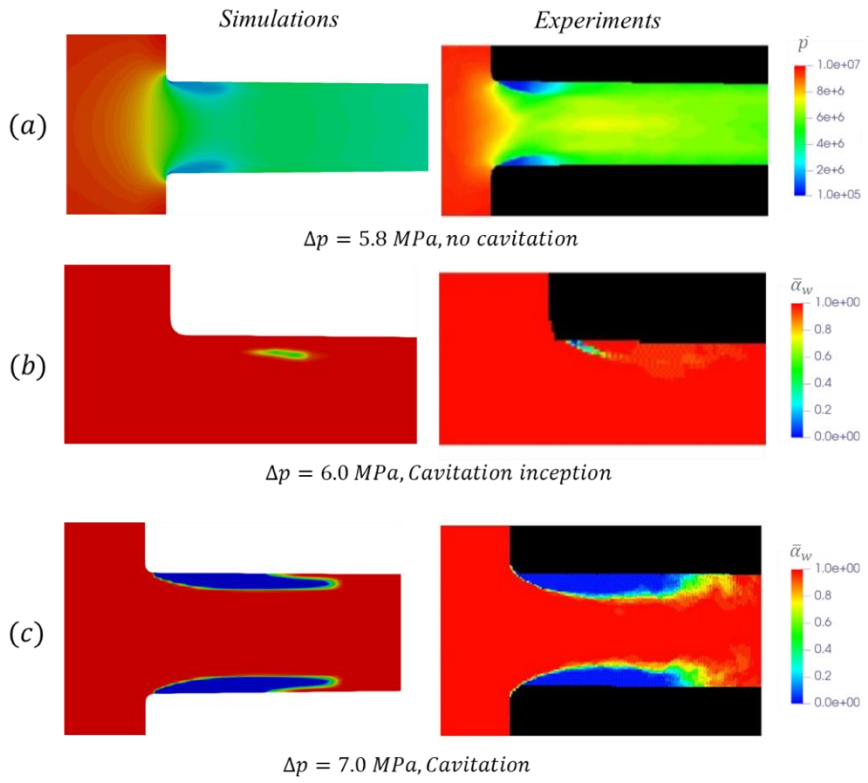

Figure 2.5 Average contour plots of (a) the pressure field for Δp=5.8 MPa, and (b) the void fraction field for Δp=6.0 MPa, at cavitation inception regime (c) the void fraction field for Δp=7.0 MPa, at cavitation regime.

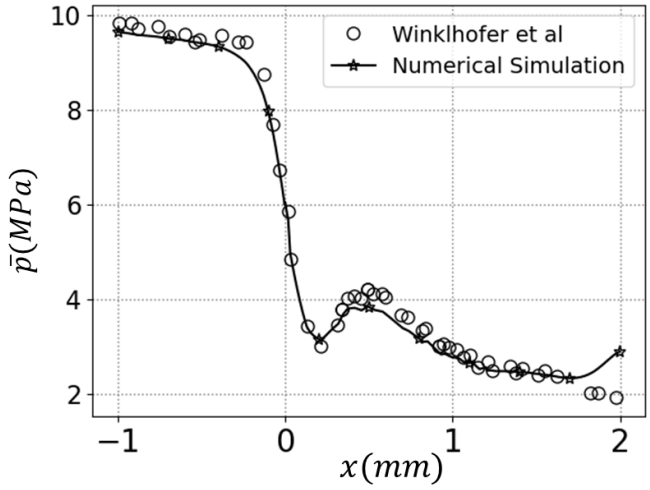

Figure 2.6 Comparison of mean pressure distribution along the channel centerline for cavitation regime (Δp=7.0 MPa) between the results of Winklhofer et al[56] and the numerical simulation.

3 METHODS: COMPRESSIBLE CAVITATING FLOW SOLVER-PART 2

3.1 Introduction

Cavitation is driven by two key phenomena: shockwaves and low-pressure zones within turbulent structures, both of which can initiate phase transitions. In cavitating flows, the Mach number varies significantly both spatially and temporally. The highest compressibility effects are observed in the bubbly mixture zones, while pure phases (especially the liquid phase) show the lowest susceptibility to these effects. To obtain stable and accurate solutions for these complex compressibility effects, specialized all-Mach number flux reconstruction schemes have recently been developed. These schemes are adept at accurately capturing shockwave effects within cavitating flows. In this study, the Schmidt all-Mach scheme (Schmidt, 2015) is integrated with a mixed Subgrid Scale (SGS) turbulent model. This approach enables the accurate simulation of both the influence of turbulent structures on cavitation initiation and the generation of shockwaves due by bubble collapses—two of the most critical aspects of cavitating flows.

3.2 Physical Model

3.2.1 Governing Equations

Three-dimensional fully compressible form of conservative governing equations can be written as follows(Trummler, 2021):

$$\partial_t \boldsymbol{U} + \nabla \cdot \boldsymbol{F}(\boldsymbol{U}) = 0 \tag{3.1}$$

Where U represents the state vectors and $F(U)$ stands for nonlinear fluxes. F can be further splits to three parts, namely the convective part ($\boldsymbol{F^c}$), the diffusive parts ($\boldsymbol{F^d}$), and the part encompassing the contribution of the pressure and surfaces forces ($\boldsymbol{F^p}$):

$$\partial_t \boldsymbol{U} + \nabla \cdot [\boldsymbol{F^c}(\boldsymbol{U}) + \boldsymbol{F^d}(\boldsymbol{U}) + \boldsymbol{F^p}(\boldsymbol{U})] = 0 \tag{3.2}$$

Where the state vector and fluxes can be shown as:

$$\boldsymbol{U} = \begin{bmatrix} \rho \\ \rho \boldsymbol{u} \\ \rho E \end{bmatrix} \quad \boldsymbol{C}(\boldsymbol{U}) = \boldsymbol{u} \begin{bmatrix} \rho \\ \rho \boldsymbol{u} \\ \rho E + p \end{bmatrix} \quad \boldsymbol{P}(\boldsymbol{U}) = \begin{bmatrix} 0 \\ pI - \sigma\kappa\alpha I \\ 0 \end{bmatrix} \quad D(U) = \begin{bmatrix} 0 \\ -\tau \\ \boldsymbol{q} \end{bmatrix} \tag{3.3}$$

The above transport equations solve for mass, momentum and total energy. The primitive variables (p and T) along with vapor volume are estimated using appropriate equations of state and caloric equations along with iterative algorithms. The surface tension force is calculated with $\sigma\kappa\mathbf{n}\delta_s$, which can be rewritten as $\sigma\kappa\nabla\alpha$ (Abu-Al-Saud et al., 2018). Where σ shows the surface tension coefficient, κ is the surface curvature, **n** is the surface normal vector and α is the vapor volume fractions. The viscos stress tensor, τ is written as:

$$\tau = \nabla \cdot \mu \left(\nabla u + (\nabla \mathrm{u})^T - \frac{2}{3}(\nabla \cdot u) I \right) \tag{3.4}$$

The total energy is formed from the kinetic energy (k) and the internal energy (e):

$$E = e + \frac{1}{2}||u||^2 \tag{3.5}$$

The heat flux is given as: $q = \lambda \nabla T$

Where λ is thermal diffusivity and is obtained using $\lambda = \nu/Pr$.

3.2.2 Single Fluid Model

As it is discussed in (Mihatsch, 2017), cavitation occurs in a broad range of length scales and the cavitation length scale characteristic (ψ_{cav}) can varies from nuclei sizes ($O < 10^{-4} m$), to the length scales of the flow. On the other hand, the scales that can be resolved within the flow simulation depends on the grid length (ψ_{grid}). In the cases of a very large cavity characteristics length to the grid size ratio ($\frac{\psi_{cav}}{\psi_{grid}} \gg 1$), the cavitation

can be fully resolved allowing for the usage of approaches such as sharp interface methods where the phase boundary is calculated explicitly. These models consider one set of mass, momentum, and energy for each phase and the interaction between phases is modeled with considering exchange rate between phases explicitly. On the other side, when this ration is very small, $\frac{\psi_{cav}}{\psi_{grid}} \ll 1$, bubbly flow models are utilized where the liquid phase is treated as a continuum phase and cavity bubbles are treated as Lagrangian particles. In this case, the dynamics of the cavity bubbles are typically estimated using the Rayleight-Plesset model and its extensions.

In cases where the characteristics length scales of the cavitation are in the same orders of the grid size ($\frac{\psi_{cav}}{\psi_{grid}} \approx 1$), a special treatment of vapor phase is required. Under these conditions cavity structures with sizes larger than the grid size can be resolved ($\psi_{cav} > \psi_{grid}$), while resolving all the scales, including all the bubbles in cloud cavities with $\psi_{cav} \ll \psi_{grid}$ would be computationally very expensive and for cavities smaller than the grid a model needs to be used to approximate their effects.

A common approach to overcome this issue is so called homogenous mixture or single-fluid model. In this model the information regarding the variations in length scales smaller than ψ_{grid} is lost and the properties of each phase that is smaller than the grid is averaged over the grid.

The volume and the mass fraction of phase I is defined as:

$$\alpha_i = \frac{V_i}{V},\ \beta_i = \frac{m_i}{m},\quad \text{with}\ \sum_i \alpha_i = \sum_i \beta_i = 1 \tag{3.6}$$

Then the conservative variables over each control volume (the mixture values) are approximated as:

$$\rho_{mix} = \frac{1}{\Omega}\int_\Omega \rho d\Omega,\quad (\rho \boldsymbol{u})_{mix} = \frac{1}{\Omega}\int_\Omega \rho \boldsymbol{u} d\Omega,\quad (\rho \boldsymbol{E})_{mix} = \frac{1}{\Omega}\int_\Omega \rho \boldsymbol{E} d\Omega \tag{3.7}$$

In this approach the pressure, temperature and velocity is considered to be identical for all the components within each cell, which implies a mechanical, thermal and kinetic equilibrium of phases. Additionally, the density of the mixture is calculated from each component density and the volume fraction as follows:

$$\rho_{mix} = \sum_i \alpha_i \rho_i \tag{3.8}$$

3.2.3 Thermodynamic Closures and Transport Properties

To close the governing equations there is a need to calculate the primitive parameters from the caloric equations and equations of states. The following section covers the details regarding the relevant equations used for the liquid and the vapor phases.

Liquid phase

For the liquid phase modified Tait equation of state is utilized which is expressed as follows(Koop, 2008):

$$p_l(\rho_l, T_l) = B\left[\left(\frac{\rho_l}{\rho_{sat,l}(T_l)}\right)^N - 1\right] + p_{sat,l}(T_l) \tag{3.9}$$

Where subscript l shows the liquid phase and the parameters B and N take the constant values of 3.3×10^8 Pa and 7.15, respectively. Also, the relation between the internal energy and temperature can be expressed based on the caloric equation as follows:

$$e_l(T_l) = C_{vl}(T_l - T_0) + e_{l0} \tag{3.10}$$

Where C_{vl} shows the specific heat at a constant volume and $T0$ and $el0$ show the reference temperature and the reference internal energy of the liquid component respectively (for water $C_{vl} = 4180\, Jkg^{-1}K^{-1}, T_0 = 273.15\, K, e_{l0} = 617.0$).

Vapor phase

For the gas phase the ideal gas phase equation of state is considered:

$$p_v(\rho_v, e_v) = (\gamma_g - 1)\rho_v e_v \tag{3.11}$$

Where γ_g is the specific heat ration and can be expressed as $\gamma_g = \frac{RT_v}{e_v}$ with R being the specific gas constant (for vapor $\gamma = 1.327$ and $R = 461.6\, Jkg^1K^{-1}$). The caloric equation corresponds to the gas phase can be written as:

$$e_v(T_v) = C_{vv}(T_v - T_0) + L_v(T_0) + e_{l0} \tag{3.12}$$

Where Lv shows the laten heat of the vaporization with $Lv(T_0) = 2.3753 \times 10^6$, $C_{vv} = 1410.8\, Jkg^{-1}K^{-1}, T_0 = 273.15\, K$.

Mixture

With the assumption of thermal and mechanical equilibrium in the mixture, the pressure and the temperature in the mixture are given as:

$$p_l = p_v = p = p_{sat}(T), \quad T_l = T_v = T \tag{3.13}$$

The density and internal energy of the mixture are given:

$$\rho = \alpha\rho_{v,sat}(T) + (1-\alpha)\rho_{l,sat}(T) \tag{3.14}$$

$$\rho e = \alpha\rho_{v,sat}(T)e_v(T) + (1-\alpha)\rho_{l,sat}(T)l(T) \tag{3.15}$$

The void fraction value of the vapor α is updated as:

$$\alpha = \frac{\rho - \rho_{v,sat}(T)}{\rho_{l,sat}(T) - \rho_{v,sat}(T)} \tag{3.16}$$

The saturation values for densities and pressure are given based on analytical relations provided as(Schmidt and Grigull, 1989):

$$\ln\left(\frac{p_{sat}(T)}{p_c}\right) = \frac{T_c}{T}\sum_{i=1} a_i\theta^{\hat{a}_i}\ , \qquad \frac{\rho_{l,sat}(T)}{\rho_c} = \sum_{i=1} b_i\theta^{\hat{b}_i}\ , \qquad \ln\left(\frac{p_{sat}(T)}{p_c}\right) = \frac{T_c}{T}\sum_{i=1} c_i\theta^{\hat{c}_i}$$

$$T\epsilon[T_{ref}, T_c] \tag{3.17}$$

Where $\theta = 1 - T/T_c$ and the coefficients $a_i, b_i, c_i, \hat{a}_i, \hat{b}_i, and\ \hat{c}_i$ can be found in(Schmidt and Grigull, 1989). The critical values for the water are $T_c = 647.16\ K, p_c = 22.12 \times 10^6 Pa, and\ \rho_c = 332\ kgm^{-3}$.

With considering the thermodynamic equilibrium for the mixture, the speed of sound for the mixture is estimated based on the Wallis relationship:

$$\frac{1}{\rho c^2} = \frac{\alpha}{\rho_l c_l^2} + \frac{(1-\alpha)}{\rho_v c_v^2} \tag{3.18}$$

Numerical Flux Reconstruction for Fully Compressible Flow

The integral (weak form) of the governing equations can be written as follows:

$$\partial_t \int_\Omega \boldsymbol{U}(x,t)dV + \int_{\partial\Omega} \boldsymbol{F}(\boldsymbol{U},x,t)dA = 0 \tag{3.19}$$

Where the control volume and the boundaries are denoted by Ω and $\partial\Omega$.

The computational domain is discretized into N grid cells i with a control volume and volume of Ω_i and V_i respectively. The volume average of the field over the grid cell is calculated as:

$$\overline{U}_i(t) = \frac{1}{V_i}\int_{\Omega_i} \boldsymbol{U_i}(x,t)dV_i \tag{3.20}$$

The flux terms are split over the cell boundaries j with the area of A_j and normal vector of $\boldsymbol{n_j}$. The numerical approximation of the fluxes over the faces of each cell is then calculated as:

$$\int_{\partial\Omega_i} \boldsymbol{F}(\boldsymbol{U},x,t)dA = \sum_{\boldsymbol{j}} \overline{\overline{F}}_j n_j \tag{3.21}$$

Where $\overline{\overline{F}}_j$ represents the numerical approximation of the physical flux passing through the face j. The consistency and conservativeness of the numerical flux is met with the following conditions:

After applying the discretization, the final form of the governing equations will be:

$$\partial_t \overline{U}_i(t) + \sum_{\boldsymbol{j}} \overline{\overline{F}}_j n_j = 0 \tag{3.22}$$

At each time step $t = t^k$ the constant piecewise estimation of the vector state $\overline{U}_i(t_k)$ is calculated by solving the above equations.

3.2.4 Riemann Problem

To reconstruct the convective fluxes across the cell interfaces, in the fully compressible cases approximate Riemann solvers can be employed. In approximate Riemann solvers, the numerical flux on every cell interface f_{ij} is defined based on adopting Riemann problem. With exploiting the rotational invariance property of the Euler equations, the fluxes can be calculated on cell normal directions. With considering a local coordinate on the centroid of the interface ($\boldsymbol{x'}_f$), the initial condition for the Riemann problem would be as Follows:

$$\boldsymbol{U}'(\boldsymbol{x}', t^n) = \begin{cases} \boldsymbol{U'}_L^n = \boldsymbol{T}\boldsymbol{U}_L^n \\ \boldsymbol{U'}_R^n = \boldsymbol{T}\boldsymbol{U}_R^n \end{cases} \tag{3.23}$$

Where T shows the rotational tensor and the superscript " ' " represents the variable in the cells interface coordinates. For small time intervals $t - t^n$, the solution of the Reimann problem remains constant along the characteristic plane manifold $\frac{x'}{t-t^n} = const$. A potential solution of a Reimann problem on a cell interface is shown below. In Figure 3.1

two nonlinear waves are represented by S_R and S_L across which all the primitive variables experience an abrupt change. S_* corresponds to the three linear waves, one of which corresponds to the contact wave across which the density is changed, and two others are shear waves with different tangential velocities across them. The star-regions containing two states $\boldsymbol{U}_R'^n$ and $\boldsymbol{U}_L'^n$ are located between nonlinear and linear waves. The pressure and the normal velocity in this region are constant, i.e. $p_L^* = p_R^*$ and $\boldsymbol{u}_L'^* = \boldsymbol{u}'^*_R$.

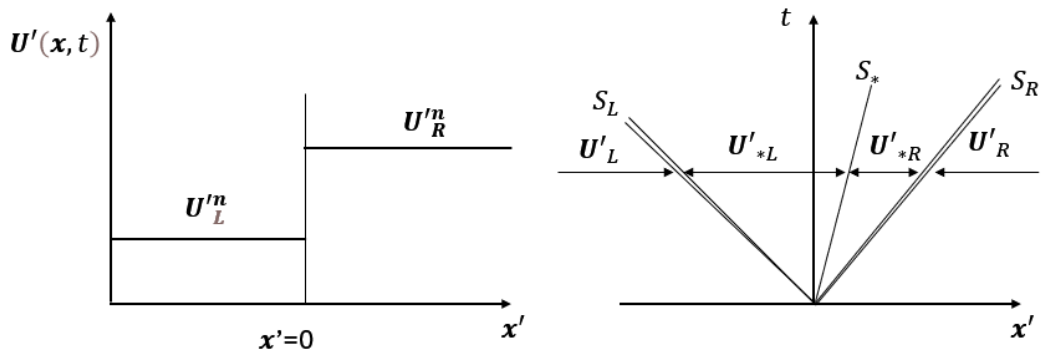

Figure 3.1 Reiman problem (left) the interface located at sequential cells interface, corresponding to x'=0 at t = t^k, and (right) Reimann fan including four states and three characteristics lines.

Flux reconstruction methods which are developed based on Reimann solution are called Godunov type methods(Toro, 2009)**.** The first version of these methods that was used for a nonlinear hyperbolic system was developed by Godunov. The original work of the Godunov(Toro, 2009) was based on the exact solution of the Reimann problem which is very difficult to implement in most of the cases. To overcome these difficulties the approximate Reimann solvers, which are the extended version of the original Godunov method were introduced. The most well-known approximate Reimann solvers in the literature are HLL-based methods and AUSM family. The idea of HLL method was introduced by Harten, Lax and van Leer(Harten et al., 1983), to solve the Godunov flux using a Reimann approximate solver. In this approach the solution space of the cell interfaces is divided into three constant regions using two characteristics waves. The major shortcoming of this approach is its inability to consider shear and contact waves in the solution, so it only works for the condition where two sets of hyperbolic equations are used, such as shallow waters. To overcome this drawback an extended version of the HLL, so called HLLC(Toro, 1992) technique was developed which was able to consider

both shear and contact waves with considering two star regions. HLL mothed are further modified with other researchers to reduce the dissipation (Minoshima and Miyoshi, 2021) and incorporate turbulence in the solution(Fleischmann et al., 2020).

AUSM (Advection Upstream Splitting Method) approach was developed by(Liou and Steffen, 1993) , which combine features from flux vector splitting approaches and Godunov methods. This approach is solved for time dependent Euler equations where the flux is split into the convection and pressure terms. This method is upwind depending on the sign of Mach number in the cell interface, where the cell interface Mach number is estimated from the neighboring cells characteristics speed with considering convection and pressure splitting. Different extensions of AUSM scheme are developed such as AUSM+ (Liou, 1996) which has some positive features such as damping spurious pressure oscillations around slow moving shock and positivity preserving of scalar quantities such as the density.

Most of the Reimann approximate solvers are useful for single phase compressible flows and only High Mach number flow conditions. In the case of cavitating flow due to a significant compressibility variation across the flow domain which almost no compressibility in the liquid regions and very large compressibility (up to *O(1)* in high pressure injection regions) in the mixture regions strong variations in Mach number exist. In these cases, most of the classical approximate Reimann solvers fail to replicate the physical conditions due to an inconsistent asymptotic behavior of the dissipative part of the flux computations(Schmidt, 2015). For this reason, the low-Mach consistent approach suggested by Schmidt was used here which employes a uniformly consistent numerical flux function in low Mach number leading to a stable time accurate simulation. The details of the scheme can be found in (Schmidt, 2015; Sezal, 2009), where the approach was used for the Euler system of equations and neglect diffusion terms. Here, the major features of this approach will be summarized for a flux reconstruction in one direction utilizing a 4-point stencil shown in the below Figure. The unit normal vector of the cell face is shown as n_i and the corresponding cell face is shown as f_i. The numerical Flux $\breve{F}$ at the cell face is calculated by reconstruction of fluxes $\breve{F}^C, \breve{F}^P, and\ \breve{F}^D$. For the face + the fluxes $\breve{F}_+^C\ and\ \breve{F}_+^P$ can be shown as:

$$\breve{F}_+^C = u^* U^+ = u^* \begin{bmatrix} \rho^+ \\ (\rho u)^+ \\ \left(\rho e + \frac{1}{2}\rho u^2 + p^*\right)^+ \end{bmatrix} \quad \breve{F}_+^P = p^* \begin{bmatrix} 0 \\ n \\ 0 \end{bmatrix} \tag{3.23}$$

Where u^{*+} is the numerical transport velocity and p^{*+} is the interface pressure. The upwind biased scheme is used to reconstruct u^{*+} and p^{*+} along with variables $\phi = \{\rho^+, u^+, v^+, w^+, (\rho e)^+\}$ as described in the following.

As illustrated in the stencil schematic, adjacent cells are marked by superscript "--, -, +, ++" for field ϕ. The Favre filtered velocity field (details in LES section) $\widetilde{\boldsymbol{u}} = \frac{\overline{\rho \boldsymbol{u}}}{\bar{\rho}}$ is decomposed into the cell face normal $\widetilde{\boldsymbol{u}}_{\perp} = \widetilde{\boldsymbol{u}} \cdot \boldsymbol{n}$ and tangential $\widetilde{\boldsymbol{u}}_{\parallel} = \widetilde{\boldsymbol{u}} - \widetilde{\boldsymbol{u}} \cdot \boldsymbol{n}$ components. For reconstruction of the velocity at the cell interface the general flux limiter form of the reconstruction scheme is give as $\phi = \{\widetilde{\boldsymbol{u}}_{\perp},\ \widetilde{\boldsymbol{u}}_{\parallel}\}$:

$$\phi^{*-} = \phi^{-} + \frac{1}{2}\psi(r_f^{-})(\phi^{+} - \phi^{-}) \tag{3.24}$$

$$\phi^{*+} = \phi^{+} - \frac{1}{2}\psi(r_f^{+})(\phi^{+} - \phi^{-}) \tag{3.25}$$

Where ψ is the flux limiter function and the r_f is the gradient ratio of ϕ at face *f*. ϕ^{*-} and ϕ^{*+} show the left and right interpolated values on the cell interface. The r_f can be expressed as follows:

$$r_f^{-} = \frac{\Delta x^*}{\Delta x^-}\frac{\phi^- - \phi^{--}}{\phi^+ - \phi^-},\ r_f^{+} = \frac{\Delta x^*}{\Delta x^+}\frac{\phi^{++} - \phi^+}{\phi^+ - \phi^-} \tag{3.26}$$

In our case the velocity at the interface is reconstructed based on the recent Reconstruction Operators on Unified Normalized-variable Diagram (ROUND)(Deng, 2023a, 2023b) scheme which provides a high-resolution structure-preserving convection solution. More specifically, the flux limiter form of the ROUND A scheme was utilized in this work. Also, the second order form of r_f was used which is given follows(Jasak, 1996):

$$r_f^{-} = \frac{2(\nabla\phi^-)\Delta x^*}{\phi^+ - \phi^-} - 1 \tag{3.27}$$

Where the gradient is calculated explicitly based on the neighbors' cell old values ($\phi^{--} and\ \phi^{++}$). The $\psi(r_f)$ for ROUND A scheme is defined as follows:

$$\psi_{rf} = \begin{cases} min\left(\dfrac{A(2 - 5r_f) + 6r_f B^2}{3B^2}, 2r_f\right) & 0 < rf \le 1 \\ min\left(\dfrac{6\beta_2(1-\lambda)(-1 + r_f)^4 C + 256A(2 + r_f)}{3B^D}, 2 - 2\lambda\right) & 1 < rf \\ 0 & rf \le 0 \end{cases}$$

$$\phi_r = \begin{cases} min\left(\frac{A(2-5r)+6rB^2}{3B^2}, 2r\right) & 0 < r \leq 1 \\ min\left(\frac{6\beta_2(1-\lambda)(-1+r)^4C+256A(2+r)}{3B^D}, 2-2\lambda\right) & 1 < r \\ 0 & r \leq 0 \end{cases}$$

$$A = (1+rf)^8, B = (\beta_1(0.5-0.5rf)^4 + (1+rf)^4)$$

$$C = (\beta_2(1-rf)^4 + 32(1+rf)^4) \quad ,$$
$$D = (\beta_2(1-rf)^4 + 16(1+rf)^4) \quad (3.28)$$

With parameters $\beta_1 = 500,\ \beta_2 = 1000, and\ \lambda = 0.25.$

Where $\Delta x^* = x^+ - x^-$, $\Delta x^- = x^- - x^{--}$, and $\Delta x^+ = x^{++} - x^+$ indicate the distances between the cell centers. The advection velocity u^* is calculated as follows:

$$\tilde{u}^* = \frac{I^+\tilde{u}_\perp^{*+} + I^-\tilde{u}_\perp^{*-}}{\bar{I}^+ + \bar{I}^-} - \frac{\bar{p}^+ - \bar{p}^-}{\bar{I}^+ + \bar{I}^-} \quad (3.29)$$

In the above equation $I^{\mp}$ denote the left and right acoustic impedance:

$$\bar{I}^- = \frac{1}{4}(3\bar{\rho}^- + \bar{\rho}^+)c_{max},\ \bar{I}^+ = \frac{1}{4}(\bar{\rho}^- + 3\bar{\rho}^+)c_{max} \quad (3.40)$$

The c_{max} is the maximum speed of sound in the adjacent cells. In the current scheme, the reconstructed velocity is selected based on the sign of the advection velocity $sgn(u^*)$ and for $\phi = \{\tilde{\boldsymbol{u}}_\perp,\ \tilde{\boldsymbol{u}}_\parallel\}$:

$$\phi^* = \frac{1}{2}[(1 + sgn(\tilde{u}^*))\phi^{*-} + (1 - sgn(\tilde{u}^*))\phi^{*+}] \quad (3.41)$$

To ensure the low Mach consistency the following centered approximation of the pressure is used:

$$p^* = \frac{1}{2}(\bar{p}^+ + \bar{p}^-) \quad (3.42)$$

The diffusivity flux $\breve{F}^D$ term was discretized using a second order linear central scheme.

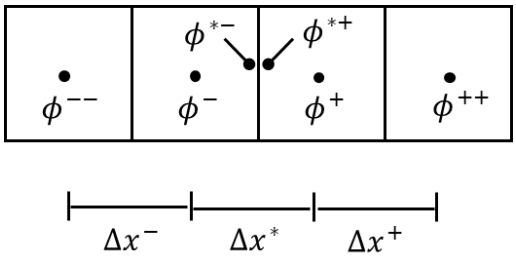

Figure 3.2 Schematic of the 1D stencil.

Sensor Functional

Two sensor functions were adopted to detect discontinuity within the domain. The vorticity dilation sensor proposed by Ducros et al. which is used to detect the shock and expansion waves (Nicoud and Ducros, 1999):

$$\theta^d = \frac{(\nabla \cdot u)^2}{(\nabla \cdot u)^2 + (\nabla \times u)^2 + \epsilon} \tag{3.43}$$

ϵ is a very small value to avoid division by zero.

The other senor is used to detect the pseudo phase boundary through the variations of vapor volume fraction:

$$\theta^\alpha = \max\left(\left\|\alpha_c - \alpha_f\right\|\right) \tag{3.44}$$

Where subscript *c* denotes the cell center, and *f* denotes the cell faces.

Time Integration

The advance of the solution from time t^n to t^{n+1} was achieved by using second-order four-stage low storage Runge-Kutta time integration technique(Cooper and Verner, 1972).

Considering a simplified version of the system of equations:

$$\partial_t \bar{U} = \Re(\bar{U}) \tag{3.45}$$

With $L(\bar{U})$ being the right-hand side of the equations a multi-time step integration is done as follows:

$$\bar{U}_i^{n+1} = \bar{U}_i^n + C_k \Delta t \Re_i\left(\bar{U}_i^{n+1,k-1}\right), \qquad k = 1, \dots, N_k$$

$$\bar{U}_i^{n+1,0} = \bar{U}_i^n \; and \; \bar{U}_i^{n+1} = \bar{U}_i^{n+1,N_k} \tag{3.46}$$

Where $N_k = 4$ and coefficients are $C_1 = 0.11, C_2 = 0.2766, C_3 = 0.5, and\ C_4 = 1.$

Furthermore, adaptive time marching was utilized based on Courant-Friedrichs-Lewey (CFL) criterion:

$$\Delta t = \min\left(CFL\left(\frac{\Delta x_i}{|u_i|+c_i} + \frac{\Delta x_i^2}{2(v_i+v_{t,i})}\right)\right) \tag{3.47}$$

Where Δx_i shows the characteristic cell length divided by the dimension ($\Delta x_i = l_i/Nd$), u_i is the characteristic velocity, c_i is the speed of sound, v_i is the kinematic viscosity, and $v_{t,i}$ is the unresolved viscosity, CFL was selected to be =1.

3.2.5 Large Eddy Simulation Modeling

Turbulent flows contain motions in a wide range of scales, where large-scale motions hold the majority of the energy, are usually anisotropic, and are primarily responsible for transport. Conversely, small-scale motions are mainly dissipative. In most of the cases (except at low Reynolds numbers), It is impossible to resolve all the scales of the flow. In these cases, LES method is very beneficial in replicating the complex physical conditions with reasonable resources. LES methods attempt to resolve large scale motions and model the effect of small unresolved scale motions (so called subgrid scale (SGS)) using appropriate closure model and based on the information provided from the resolved scales(BARDINA et al., 1980).

LES models are mainly classified into two main categories, functional models, and structural models("Structural Modeling," 2006). Functional models have two main assumptions regarding the small-scale motions. One assumption is that these small-scale motions are isotropic throughout the flow, and the other assumptions is equilibrium between the resolved and subgrid scales. Previous studies(Mestayer, 1982) have shown that the first assumption is only valid if the cut-off width of the filter is in the orders of Kolmogorov scales, $KL_\epsilon > 50$, where K shows the wave number and L_ϵ shows the dissipative integral length scale. Also, the second assumption is invalidated momentarily, when the flow is influenced by non-steady external forces in the cases of having impulsive accelerations, such as those appears in shear flows(O'NEIL and MENEVEAU, 1997).

Among functional LES models, eddy viscosity models are the most famous in which it is assumed that the energy transfer mechanism from the resolved to the subgrid scales is similar to how molecular diffusion works. eddy viscosity models, the energy cascade is represented by a specific mathematical term. This term essentially mimics the dissipative nature of molecular viscosity but on a much larger, turbulent scale. where the molecular viscosity is substituted by a subgrid viscosity shown by ν_{sgs}. The Boussinesq mathematical form of the subgrid model is represented as:

$$-\nabla \cdot \tau^{*} = \nabla \cdot \left(\nu_{sgs}(\nabla\overline{u} + \nabla^{\mathrm{T}}\overline{u})\right) \tag{3.48}$$

Where (*) denotes deviatoric part of the tensor:

$$\tau_{ij}^{*} = \tau_{ij} - \frac{1}{3}\tau_{kk}\delta_{ij} \tag{3.49}$$

Subgrid-viscosity based LES models produce alignment between the eigenvectors of the resolved strain rate tensor and subgrid-scale tensor, while previous studies have shown that Tao et al.(TAO et al., 2002) have shown that this alignment is unphysical.

Structural LES models overcome some of the shortcomings of the Functional LES models, including the assumptions of isotropic small scale motions and alignment between SGS-stress tensor with strain-rate tensor. Structural models have different subcategories such as scale similarity models (SSM), deconvolution approximation models, mixed models among others.

Scale similarity approaches assume statistical structures of the subgrid scale motions are similar to their equivalents in the smallest scale motions(BARDINA et al., 1980). First proposed SSM model corresponds to the study by Bardina (BSS), where the model employed filtering to approximate the SGS velocity ($u_i' = u_i - \bar{u}_i$) from the approximated filtered fluctuating velocity (approximate $\overline{u_\iota - \bar{u}_\iota}$ as $\bar{u}_i - \bar{\bar{u}}_i$). This model considers approximation of decomposed SGS stress, including approximate sum of Reynolds and cross stresses as $\bar{u}_i\bar{u}_j - \bar{\bar{u}}_i\bar{\bar{u}}_j$ and Leonard stress which leads to a final form of the stress tensor as follows:

$$\tau_{ij}^{BSS} = L_{ij} - \frac{1}{3}L_{kk}\delta_{ij} = \overline{\bar{u}_\iota\bar{u}_j} - \bar{\bar{u}}_i\bar{\bar{u}}_j \tag{3.50}$$

In a priori study of decaying homogenous isotropic turbulence and sheared homogenous turbulence BSS show a significant improvement in predication of the SGS fields. Moreover, another noted benefit of the similarity model was its ability to predict SGS

stress with eigenvectors unaligned with those of the mean strain rate, thus allowing for the possibility of reverse energy transfer. By approximating the filter using a Taylor series in SSM such as BSS, tensor-diffusivity (gradient based) LES models can be derived. One of the famous tensor diffusivity models was derived by Clark and Ferziger(Clark et al., 1979) which was derived as the term of Taylor expansion of modified Leonard term $\overline{\bar{u}_i \bar{u}_j} - \bar{\bar{u}}_i \bar{\bar{u}}_j$.

Major drawback of SSM is its deficiency in dissipation. This deficiency is also applied tensor-diffusivity model as they also lack the ability to properly account for aspects of energy transfer. Anderson and Domaradzki(Anderson and Domaradzki, 2012) showed that this deficiency is due to the model failure in predictions of unresolved small scales turbulence effects on the reception and dissipation of the kinetic energy.

Mixed models(BARDINA et al., 1980; Vreman et al., 1995) were developed to overcome deficiencies of SSM models with combining SSM models with an eddy viscosity models. Therefore, Mixed models benefit from dissipations of eddy viscosity models while still maintaining the correlation with real stresses. The general formulations of stress tensor in mixed models are as follows:

$$\tau_{ij}^{*} = \tau_{ij} - \frac{1}{3}\tau_{kk}\delta_{ij} = -2\nu_{SGS}\bar{S}_{ij} + L_{ij} - \frac{1}{3}L_{kk}\delta_{ij} \tag{3.51}$$

Where ν_{SGS} is calculated from the EV models and L_{ij} tensor is calculated from the structural models("Structural Modeling," 2006). Several innovative approaches were developed to combine advantages of functional and structural approaches. In a study by Abe(Abe, 2013), Bardina scale similarity model was mixed with an eddy viscosity model to provide an anisotropy resolving SGS scheme, where the eddy viscosity term affects SGS energy transfer and the Bardina term affects the SGS forces. The stress tensor in the Abe study(Abe, 2013) was developed by combining the isotropic part of eddy viscosity SGS model with anisotropic effect of the scale similarity model as follows (notice here τ_{ij}^{*} shows the deviatoric part):

$$\tau_{ij}^{*} = -2v_{SGS}S_{ij} + 2k_{SGS}b_{ij}^{SGS} \tag{3.52}$$

With anisotropy tensor $b_{ij}^{SGS} = \frac{\tau'_{ij} - (-2v'S_{ij})}{\tau'_{kk} - (-2v'S_{kk})} - \frac{1}{3}\delta_{ij}$, and τ'_{ij} showing the stress tensor in the scale similarity model. The term $-2v'S_{ij}$ can be considered as the isotropic approximation of the original model. Considering this issue, further simplification of the

model leads to the anisotropy tensor $b_{ij}^{SGS} = \frac{\tau'^{*}_{ij} - (-2v'S_{ij})}{\tau'_{kk}} = \frac{R_{ij}}{\tau'_{kk}}$, where $\tau^{*'}_{ij}$ shows the deviatoric part of the Bardina model tensor and R_{ij} is the SGS-stress anisotropy term calculated by subtracting the eddy viscosity isotropic approximation from the Bardina model (Abe, 2013). Following this model, Kobayashi et al (Kobayashi, 2018) proposed a new scale similarity approach with Clark term. The model consisted of Clark term with only forward energy transfer and Clark term combined with Subgrid kinetic energy, where the second term only affects the SGS forces. The SGS tensor in the Kobayashi (Kobayashi, 2018) model was given as:

$$\tau_{ij}^{*} = \frac{-L_{ab}\bar{S}_{ab} + |-L_{ab}\bar{S}_{ab}|}{-L_{ab}\bar{S}_{ab}} L_{ij}^{*} + \frac{2k_{SGS}}{L_{kk}}\left(L_{ij}^{*} + \frac{-L_{ab}^{*}\bar{S}_{ab}}{\bar{S}_{ab}\bar{S}_{ab}}\bar{S}_{ij}\right) \tag{3.53}$$

$$L_{ij} = \frac{\bar{\Delta}_k^2}{12}\frac{\partial \bar{u}_i}{\partial x_k}\frac{\partial \bar{u}_j}{\partial x_k}$$

Where L_{ij} shows the Clark stress term(Clark et al., 1979). And the second term modifies the Clark stress term based on the concept in the Abe study(Inagaki, 2011), and only contributes to the SGS forces.

While these models show good predictions of turbulent channel flows even for coarse grids, they need solving a separate transport equation to calculate SGS kinetic energy based on Inagaki (2011)(Inagaki, 2011) model, which requires using empirical parameters. Following these two studies, Klein et al (Klein et al., 2020) proposed a new parameter mixed model. Similar to the Abe and Kobayashi model, their model includes an anisotropy part, which in the forward scatter equals to the baseline structural model, and in the backscatter, is projected into a tensor to only affect SGS forces. The stress tensor in this model is given as (here τ_{ij}^{KKK2} shows the whole tensor):

$$\tau_{ij}^{KKK2} = \tau_{ij}^{SSM} - 2v'^{\bar{S}_{ij}} \tag{3.54}$$

Where τ_{ij}^{SSM} could be any arbitrary scale similarity stress tensor and the viscosity v' is given as:

$$v' = \frac{1}{2}\max\left\{\frac{\tau_{ij}^{SSM}\bar{S}_{ij}}{\bar{S}_{ij}\bar{S}_{ij}}\right\} \tag{3.55}$$

In the current study the mixed model proposed by Klein is implemented along with Ketterl (Clark) gradient-based model for a more accurate prediction of SGS effects in low Reynolds multiphase shear flow.

The Favre filtered conservative equations for the density, momentum, and total energy in the case of compressible flow is given as:

$$\frac{\partial \bar{\rho}}{\partial t} + \frac{\partial \bar{\rho}\tilde{u}}{\partial x_j} = 0 \tag{3.56}$$

$$\frac{\partial \bar{\rho}\tilde{u}_i}{\partial t} + \frac{\partial \bar{\rho}\tilde{u}_i\tilde{u}_j}{\partial x_j} =$$

$$-\frac{\partial \hat{p}}{\partial x_i} + \frac{\partial}{\partial x_j}\bar{\mu}\left(\frac{\partial \tilde{u}_i}{\partial x_j} + \frac{\partial \tilde{u}_j}{\partial x_i} - \frac{2}{3}\frac{\partial \tilde{u}_k}{\partial x_k}\delta_{ij}\right) + \sigma\bar{k}\bar{n}_i\bar{\delta}_s + \tau_{nn,i} - \frac{\partial}{\partial x_j}\tau_{\rho uu,ij} \tag{3.57}$$

$$\frac{\partial \bar{\rho}\tilde{E}}{\partial t} + \frac{\partial \bar{\rho}\tilde{E}\tilde{u}_j}{\partial x_j} = -\frac{\partial \hat{p}\tilde{u}_j}{\partial x_i} - \frac{\partial}{\partial x_j}(\bar{\lambda} + \bar{\lambda}_t)\left(\frac{\partial \hat{e}}{\partial x_j}\right) \tag{3.58}$$

$$\tilde{E} = \frac{1}{2}\tilde{u}_j\tilde{u}_j + \hat{e},\ \bar{\lambda} = \frac{\bar{\rho}\nu}{Prt}, \bar{\lambda}_t = \frac{\bar{\rho}\nu_t}{Prt} \tag{3.59}$$

λ_t is the turbulent thermal diffusion coefficient, $\lambda = \nu/Pr$. The effect of subgrid scale surface tension is typically ignored in multiphase studies. In our cases here we ignore SGS surface tensions for two reasons, 1st our weber number is of order of 10^4, which is large enough to ignore these effects. Secondly, the critical scales for bubble growth, and collapse are larger than the SGS filter scale in LES simulations of cavitating turbulence, placing the dominant surface tension effects within the resolved scales.

Implementation

The flowchart of the density-based solver is shown in Figure1. This solver was implemented in OpenFOAM 2306. Turbulent mixed SGS model Helmholtz-Zentrum Dresden-Rossendorf e.V. (HZDR) software("https://www.hzdr.de/db/Cms?pNid=0," 2024) was used with modifications to be adopted in OpenFOAM 2306.

Figure 1 shows the flowchart of the solver, while Figure 2 shows the file/folder structure.

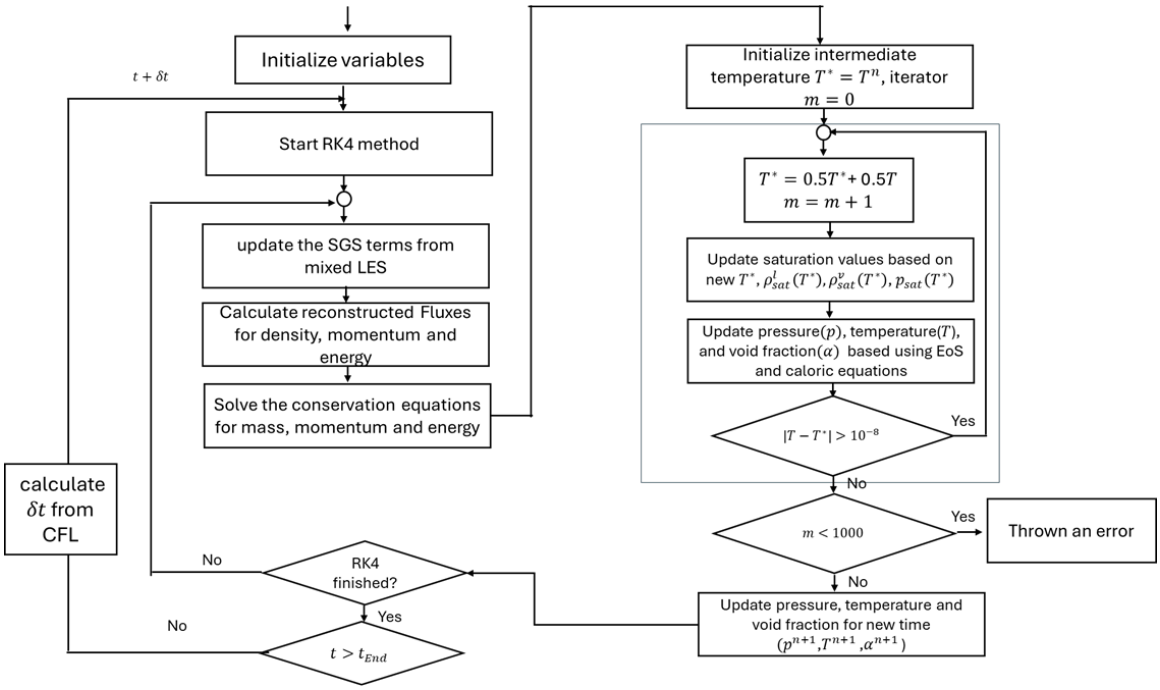

Figure 3.3 Flowchart of the customized Density-Based Cavitation solver.

3.3 Validation

Three different validations, one dimensional two-phase shock tube, turbulent channel flow, and Cavitating turbulent mixing layer, were performed to evaluate the performance of the cavitation solver in compressibility, cavitation, and turbulence prediction.

3.3.1 Case 1: Two-Phase Shock Tube

The first validation case corresponding to one dimensional two-phase shock tube was performed to evaluate the performance of the solver in capturing the shock/expansions waves and phase transition. The below schematic represents the initial and boundary conditions of this problem where two symmetric expansion waves move in opposite directions toward the boundaries(Egerer et al., 2016).

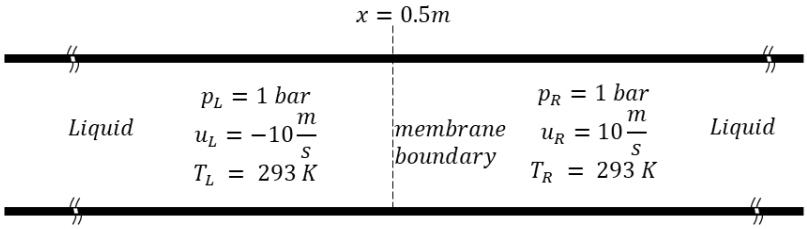

Figure 3.4 Schematic of the 1D shock tube.

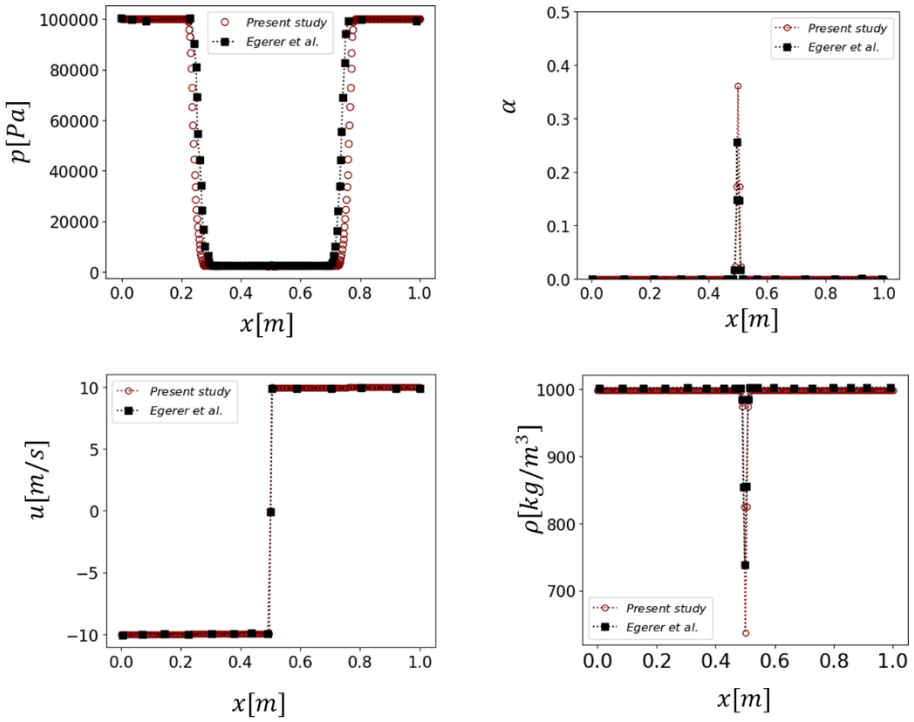

Figure 3.5 Distribution of pressure field, void fraction, velocity field, and density after dt, comparison with Egerer et al study.

3.3.2 Case 2: Turbulent Channel Flow

Second validation was done on the turbulent channel flow, where the results were compared with the DNS dataset provided by Moser(Moser and Zandonade, 2004). In this case, a Newtonian fluid between two infinite parallel plates is driven by a constant mean pressure gradient. The turbulent channel flow problem has been investigated for different friction Reynolds number, in current study we validated our results against DNS dataset for friction Reynolds number of 395. The friction Reynolds number is defined as $Re_\tau = u_\tau H/\nu$, where H is the half channel height and $u_\tau = \tau_w^{1/2}$is the friction velocity, and τ_w

shows the wall shear stress. The computational domain for the channel flow has dimensions of ($L \times 2H \times W = 4\pi \times 2 \times 4/3\pi$). After achieving to the statistically stationary condition, the simulation was first conducted for 30 flow through time ($FFT = U_b/L$, U_b is the mean bulk streamwise velocity) using the WALE LES model(Nicoud and Ducros, 1999), and the rest 70 *FFT* using both the mixed LES model and WALE LES model. The statistical results in the following Figure were calculated based on the ensemble averaging of the last 70 *FFT* time steps and spatial averaging over x and z directions. The results of the mixed Kobayashi-Clark model are compared with DNS data and results obtained from the WALE model.

The posteriori-tests results are represented in Figure 5, including the statistical values of the normal Reynolds stresses and mean velocity distribution. The results for of the mixed SGS model show a good agreement with the DNS results, and also improvement compared to the WALE simulation results. Particularly, in the case of streamwise Reynolds stress component a remarkable improvement in the mixed SGS results is observed compared to the overestimated WALE results. This improvement should be the result of the accurate estimation of the backscattering (backward cascade of energy from SGS to the GS scale) in the mixed Kobayashi-Clark model, which cannot be achieved by typical functional models.

6

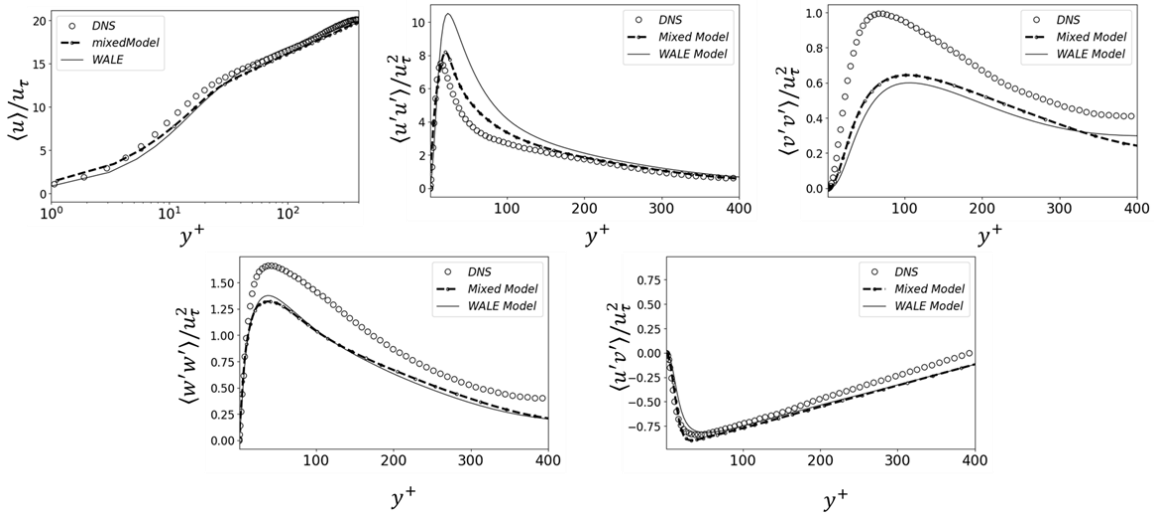

Figure 3.6 Validation of the mixed SGS model against DNS channel flow benchmark, for normalized values of (a) mean streamwise velocity (b) streamwise Reynolds

stresses (b) cross streamwise Reynolds stress, (c) spanwise Reynolds stress and, (d) Reynolds

3.3.3 Case 3: Evolving Turbulent Cavitating Mixing Layer

To further validate the presented density-based cavitation solver a three-dimensional numerical simulation of evolving cavitating mixing layer was conducted. A LES of turbulent cavitating mixing layer was done for the three different cavitation numbers ($\sigma_c = \frac{p_\infty - p_{sat}}{\frac{1}{2}\rho_\infty (\Delta U)^2}$), the details of which are provided in the table I. The simulation results are validated against the experimental data of Aeschlimann et al(Aeschlimann et al., 2011a; Egerer et al., 2016), as well as the numerical results of Egerer eta al study(Aeschlimann et al., 2011a) . The schematic of the computational domain and corresponding flow condition are represented in Figure 5. In the experimental setup of Aeschlimann study(Aeschlimann et al., 2011a), a splitter plate separated the high U_1 and U_2 low speed flows in the experimental study. According to the results of this study, the Reynolds number $Re_{\delta_\omega} = \frac{\rho_\infty \Delta U \delta_\omega}{\mu_\infty}$ at the beginning of the self-similar region was 1.5×10^5 with subscript ∞ showing the reference values and $\delta_\omega = \Delta U / \partial\langle u \rangle|_{max}$ ($\langle\,\rangle$ show spanwise average). In the simulation, $\delta_{\omega,0}$ was selected to have the same Reynolds number at the beginning of the self-similar region. The mean inlet velocity was determined using the function $\bar{u}_{in} = U_C + \Delta U \tanh(-2y/\delta_{\omega,0})$, where $\Delta U = U_1 - U_2$, $U_C = (U_1 + U_2)/2$, and $\delta_{\omega,0}$ shows the initial vorticity thickness. In the inlet, 3D velocity fluctuations restricted to the shear layer using a damping function $exp(-y^2/(2\delta_{\omega,0}))$. Th fluid properties and flow conditions are shown in the table 1 (only the 1st case was considered p=50.046e5 pa). in the spanwise and cross-streamwise directions a periodic boundary condition was considered. Moreover, a nonreflective (wave-transmissive) boundary condition (Poinsot and Lelef, 1992) was considered in the outlet of the domain. To reduce the computational costs, a barotropic condition (fixed temperature) condition was considered for this problem.

The whole computational domain is a rectangular box with dimensions of $L_x \times L_y \times L_z = 450 \times 240 \times 75$ and $N_x \times N_y \times N_z = 576 \times 278 \times 96$ number of grid cells. The

constant spacing of the grids in the spanwise and streamwise directions were considered, while in the cross-stream the grid size is doubled form centers to the sidewalls.

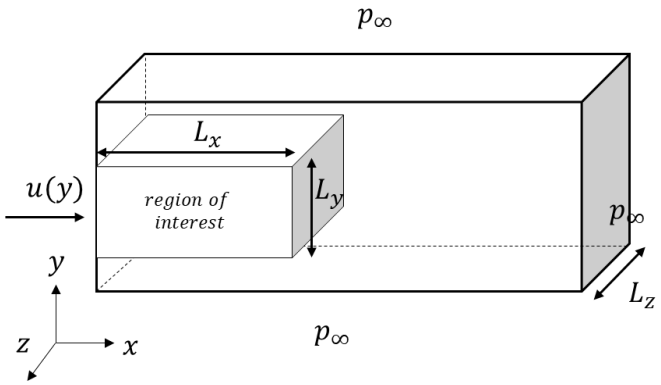

Figure 3.7 Schematic of the computational domain for cavitating free mixing layer.

Table 3.1 Cavitation number and flow properties of the cavitating mixing layer in the Aeschlimann experiments

$\boldsymbol{\sigma_c}$	$\boldsymbol{\Delta U(m/s)}$	$\boldsymbol{U_c(m/s)}$	$\boldsymbol{\rho_\infty(kg/m^3)}$	$\boldsymbol{p_\infty(MPa)}$	$\boldsymbol{\delta_{\theta,0}(\times 10^{-4}m)}$	$\boldsymbol{\delta_{\omega,0}(\times 10^{-4}m)}$
1.0	100	75	1000.44	50.46	0.5	2.0
0.167	100	75	998.54	8.361	0.5	2.0
0.1	100	75	998.39	5.015	0.5	2.0

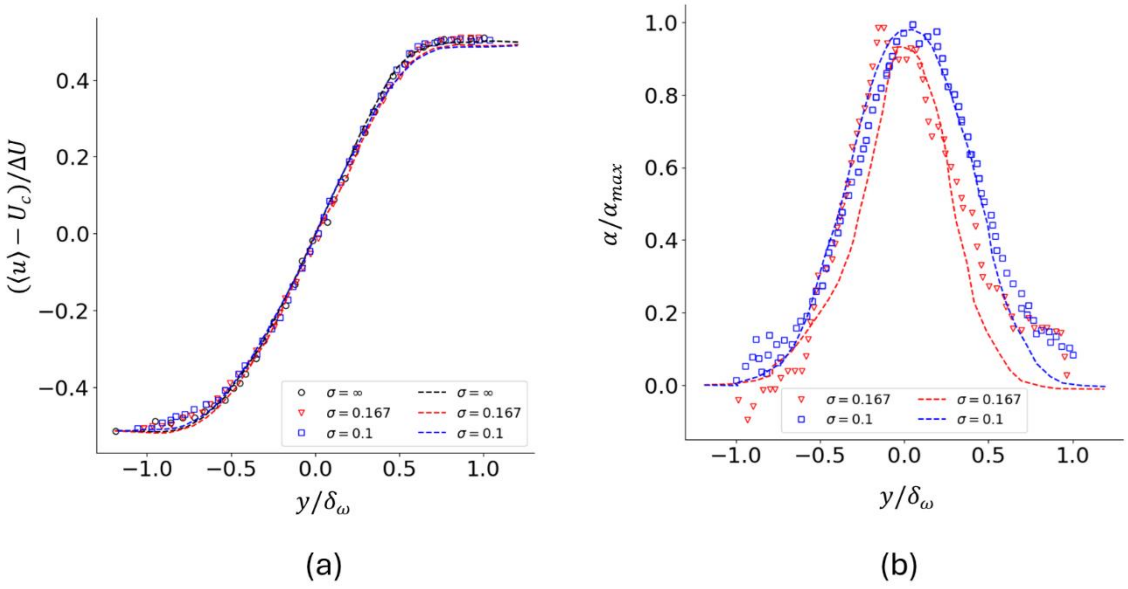

Figure 3.8 Cavitating mixing layer, comparison between LES (lines) and experimental study(Aeschlimann et al., 2011b) (symbols) of (a) normalized velocity (b) and normalized void fraction.

4 SPATIO-TEMPORAL DYNAMICS OF CAVITATING TURBULENT SHEAR FLOW OVER A MICROSCALE BFS: A NUMERICAL STUDY

4.1 Introduction

This study thoroughly examined how cavitation affects the average properties and fluctuating nature of turbulent separated flows. The investigation was conducted using a microscale backward-facing step configuration at a Reynolds number (Re_D) of 7440. Our computational methodology incorporated both compressibility and finite mass transfer (thermodynamic non-equilibrium). This comprehensive approach aimed to precisely capture the impacts of shock waves and the influence of baroclinic phenomena on vortex dynamics within the turbulent separated flow. Compressibility effects were managed by employing suitable equations of state for each phase and for the mixture. We accounted for phase-change through a transport equation for the vapor volume fraction, which allowed for contributions from finite mass transfer. Additionally, a wall-adaptive Large Eddy Simulation (LES) technique was used to model the turbulent structures and their effects. The results indicate that vapor formation reduces the average growth rate of the shear layer and delays its reattachment, moving it further from the step. Analysis of Reynolds normal and shear stresses, along with the Root Mean Square (RMS) of pressure fluctuations, further reveals that the creation and collapse of vapor packets significantly alter turbulence decay and production in the latter half of the shear layer and at the reattachment point. We also observed an increase in both mean pressure and pressure fluctuations near the reattachment region when cavitation was present, a phenomenon attributed to condensation and collapse events. Spectral analysis identified the presence of two prominent low-frequency modes, which are linked to the shifting of the reattachment point. Each of these detected low frequencies was linked to a distinct vapor transport mechanism within the turbulent separated bubble (TSB). Moreover, the presence of cavitation resulted in significantly higher spectral energy for high-frequency

fluctuations within the reattachment zone, compared to non-cavitating conditions. This phenomenon is likely due to the frequent collapse of bubbles in that area. Finally, we utilized Spectral Proper Orthogonal Decomposition (SPOD) for modal analysis. This technique provides valuable insights into the coherent structures and their associated frequencies in both cavitating and non-cavitating scenarios, thereby deepening our understanding of cavitation's impact on these structures and their dynamics.

4.1.1 Flow Configuration and Grid Study

The computational domain and grid distribution are shown in Figure 4.1. The domain compromises two main parts including the interior port (cylindrical section), which was designed in parallel with experiments, and the BFS configuration. In our experiments, the device was designed based on the fabrication limitations in microscales and the capability of the device to reproduce the desired phenomena (turbulent and intense cavitation) within an affordable flow condition, and the computational domain was adopted accordingly (Figure 4.1(a)). The interior port acts as a turbulent generator which significantly affects the flow topology and turbulence level within the channel. Therefore, consideration of the interior port was required for an accurate replication of our experimental results. This helped us to avoid using any artificial turbulent generator boundary condition in our numerical simulations. Regarding the boundary conditions, a uniform total pressure boundary condition was applied to the inlet, and a simplistic non-reflective boundary condition (wave transmissive) pressure was considered for outlet("OpenFoam. The Open Source CFD Toolbox openfoam foundation," 2023; Poinsot and Lelef, 1992). In addition, all walls were treated as no slip adiabatic walls. For timesteps, an automatic adjustable technique based on Courant and acoustic Courant numbers was utilized so that these numbers did not exceed 0.5 and 50, respectively, with maximum time steps limitation of 1e-7 seconds. The write time of 0.5 μs for the solution was utilized to capture a wide range of frequencies while avoiding storage problems.

The initial turbulence level at the inlet port is zero, as no perturbations are introduced to the flow. Upstream of the backward-facing step ($\tilde{x} = -5$), the turbulence intensity is estimated to be around 0.0737 based on the study of Teng and Piomelli (Teng and Piomelli, 2022). This study does not account for dissolved gas. In Case I (cavitating flow),

the number density and diameter of cavitation nuclei are set to 1.5×10^{15} m^{-3} and 1.5 μm, respectively, based on the study of Giussani et al. (Giussani et al., 2020b). In this study, a single Reynolds and cavitation number were chosen to isolate the fundamental impact of phase transition on TSB dynamics. This approach simplifies the analysis and isolates the influence of phase transition without introducing additional complexities associated with variations in flow conditions. Consequently, Case II (non-cavitating flow) differs from Case I only in the number density of cavitation nuclei, which is set to zero. The Reynolds number and cavitation number in both cases are Re_D = 7440 and σ_c=1.58, respectively. This approach allows for variations in cavitation inception and dynamics without altering the overall flow conditions (velocity and pressure). However, for real-world applications, it is crucial to investigate how these findings translate across a broader Re range.

Previous studies such as (Bhatt et al., 2021b; Maurice et al., 2021) explored cavitation in BFS configurations across different Reynolds and cavitation regimes. Bhatt et al. (Bhatt et al., 2021b) studied three distinct cavitation regimes and reported minimal variations in the mean characteristics and dominant frequencies of different Reynolds numbers for each regime. It is crucial to recognize that Reynolds significantly influences turbulent separation bubble characteristics and dynamics in single-phase flow scenarios. Numerous studies focusing on the characteristics and dynamics of TSB in single-phase flows underscored the significant influence of Reynolds number on various properties such as pressure fluctuations, dominant frequencies, and instabilities within the TSB. For instance, in the study by Abe et al. (Abe, 2017), the effect of Reynolds number (defined based on the momentum thickness) on RMS values of pressure fluctuations, frequency/power spectra of prms, and instantaneous pressure fields in the presence of adverse pressure gradient (APG)-induced separation bubble was investigated. Their findings revealed that an increase in Reynolds' number resulted in variations in mean flow characteristics, including separation bubble size and separation/reattachment locations, as well as pressure fluctuations and dominant frequencies (manifested by a significant decrease in p'_{rms} in the separation region due to the Reynolds number dependence of an incoming turbulent boundary layer). Furthermore, they reported a significant impact of Reynolds number on the development of large-scale streamwise structures downstream of reattachment, significantly impacting wall pressure. Such

observations highlight the intricate link between Reynolds number variations and evolution of coherent structures within the TSB.

Since cavitation inception, condensation, and overall dynamics are highly sensitive to pressure fluctuations, dominant frequencies of pressure fluctuations and characteristics of coherent structures within the TSB, it is reasonable to expect remarkable consequences regarding cavitation dynamics within separated flows at varying Reynolds numbers. Future detailed investigations are necessary to comprehensively explore this interaction within a broader Reynolds range. Such efforts would significantly contribute to the understanding of the complex interplay between Reynolds number variations and cavitation dynamics in separated flows.

More details regarding the fluid properties and flow conditions are provided in Table 4.1.

Table 4.1 Fluid properties and flow conditions of the current study.

$p_{inlet}[MPa]$	$\rho_w\left[\frac{kg}{m^3}\right]$	$\rho_v\left[\frac{kg}{m^3}\right]$	$p_{sat}[Pa]$	$\mu_w\left[\frac{Ns}{m^2}\right]$	$\mu_v\left[\frac{Ns}{m^2}\right]$	$\sigma\left[\frac{N}{m}\right]$	$p_{outlet}[kPa]$	$T_{ambient}[K]$
5.06	998.2	0.55	2340	0.9e-3	0.74e-6	0.07	100	293.16

Grid generation was accomplished using block-based local refinement, close to the walls and TSB regions. Grid resolution was adjusted in such a way that the value of dimensionless wall distance ($y^+ = yu_\tau/\nu$, where u_τ is the friction velocity) close to the walls did not exceed 0.9 for the single-phase case and 1.2 for the cavitating case, which enabled appropriate resolving of the wall shear stress.

The results for grid convergence study are presented in Figure 4.2 which includes the mean streamwise velocity profile in the absence of cavitation along the channel. Comparisons between coarse, fine, and finer grids, with 2,520,000; 5,051,000; and 6,146,000 mesh numbers respectively, show minor differences between fine and finer grids implying a grid convergence at fine grid which was accordingly considered for this study.

It can be observed there is a local minimum in the velocity profile around the centerline of the channel, which was alleviated by moving downstream. A similar flow profile at the

throttle entrance was reported in previous studies(Winklhofer et al., 2001). Figure 4.2b presents the mean velocity distribution close to the channel bottom (2 micrometers above the wall), streamlines entering the channel cross-section, and distribution of the streamwise velocity and pressure fields within several cross-sectional planes located at various streamwise distances. It is evident that in the entry region of the channel, there exists a separation and reattachment phenomenon similar to that observed in previous studies of forward-facing step configurations (Barbosa-Saldaña and Anand, 2007). The symmetric velocity distribution on the bottom wall exhibits maximum and minimum spreading of reversed flow at the centerline of the channel and close to the wall, respectively.

The streamwise velocity and pressure distribution on cross-sectional planes offer insightful information about the development of crossflow instabilities downstream of the contraction. Downstream of the contraction (I), similar to a forward-facing step channel, near the bottom wall adverse pressure gradient derives flow separation. Moreover, as the flow converges towards the upper central region of the channel, flow impingment to the top wall leads to an increase in the static pressure in this area. Consequently, fluid particles deflect towards the low-pressure regions near the side walls. Simultaneously, fluid particles near the side walls deflect towards the lower central region, resulting in the creation of two pair of symmetrical streamwise vortices near the channel's bottom center (II).

When moving to the downstream location, the pressure field within the yz cross-section becomes increasingly uniform, characterized by lower pressure in the central region and higher pressures near the side walls. This leads to a deflection of fluid particles towards the side walls, triggering the formation of vortices on both the top and side walls (III). As a consequence, two pairs of central streamwise vortices become more compact within the central region, facilitating the exchange of momentum between the lower and upper regions and leading to a more uniform pressure and momentum distribution. Under this condition, the flow within the two lateral vortices has the highest streamwise velocity, as they are predominantly fed with high-momentum fluid particles originating from the upper central region upstream of the channel. The exchange of mass and momentum between the lateral and central regions through the streamwise vortices gradually leads to a uniform distribution of mean velocity and pressure across yz cross-section, except near the walls where the no-slip boundary condition exists (IV).

The reattachment point in the flow can be determined by identifying the streamwise location where the velocity near the bottom wall shifts from negative (reverse flow) to positive values. This transition aligns with the location where the wall shear stress (τ_w) and $\partial U/\partial y$ change from a negative to a positive value, following the no-slip boundary condition. Utilizing the profile depicted in Figure 4.2a (which considers the velocity profile at the channel mid-depth), the reattachment point in this plane can be approximated to be $\tilde{x} = 5$.

The temporal averages of velocity components at {x, y, z} directions are expressed as $\{\overline{U}, \overline{V}, \overline{W}\}$, while the fluctuating part are presented as {u, v, w}. The RMS is presented using the subscript rms. p′stands for the fluctuating part of the pressure field.

The variables are nondimensionalized with respect to the step height h, reference streamwise velocity U_0, and reference density ρ_0. In general, the variables with units of [Pa] and [m/s] are nondimensionalized using $\rho_0 U_0^2$ and U_0. The reference velocity and density are determined as the maximum streamwise velocity (peak velocity) and average density over the y and z directions at $\tilde{x} = -5$.

The dimensionless numbers are obtained based on the step height and reference parameters (Bhatt and Mahesh, 2021). Reynolds number is calculated based on the hydraulic diameter (D_h) of the channel as $Re_D = U_0 D_h/\nu$. The Strouhal number, Str,

which is used for quantification of unsteady characteristics, is calculated as fh/U_0. Finally, the cavitation number is expressed as $\sigma = (p_0 - p_{sat})/(\frac{1}{2}\rho_0 U_0^2)$.

We used the results from our experiments as well as existing literature(Winklhofer et al., 2001) for evaluation and validation of our numerical model. The results of the validation are presented in supplementary material.

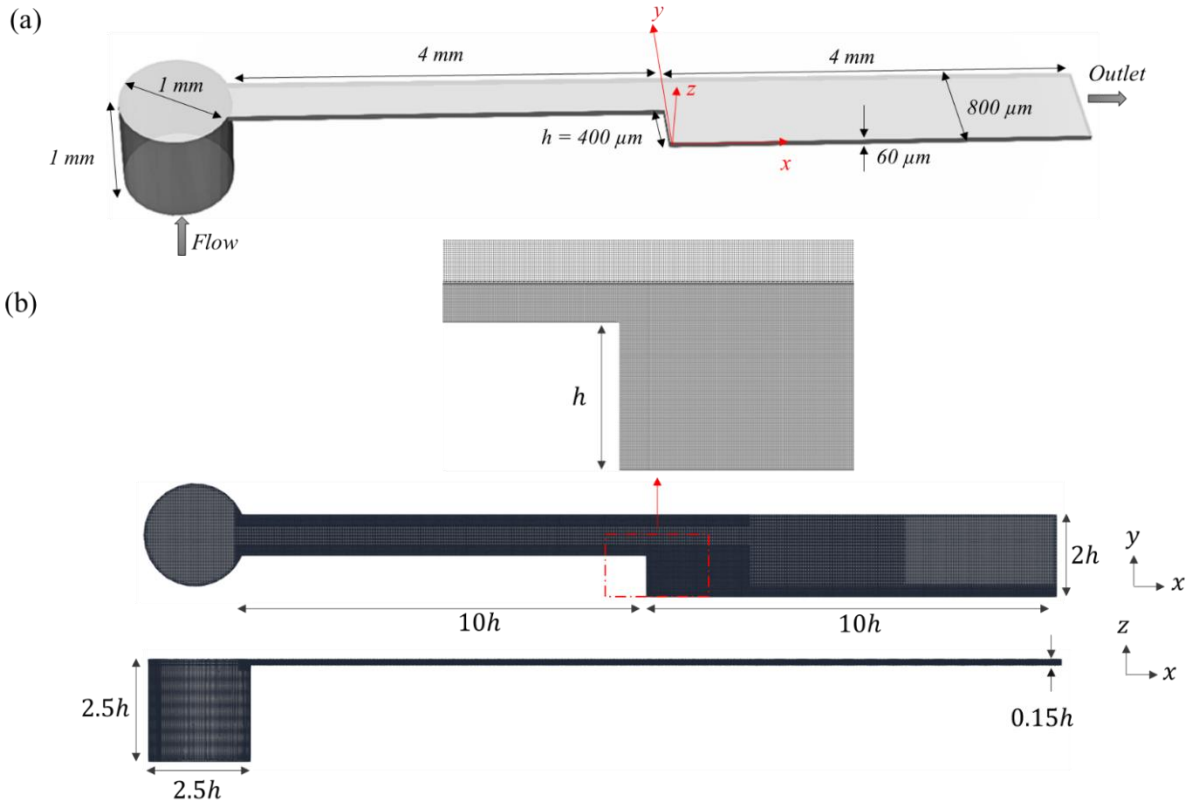

Figure 4.1. The computational domain (a) and grid configuration inside the domain (b).

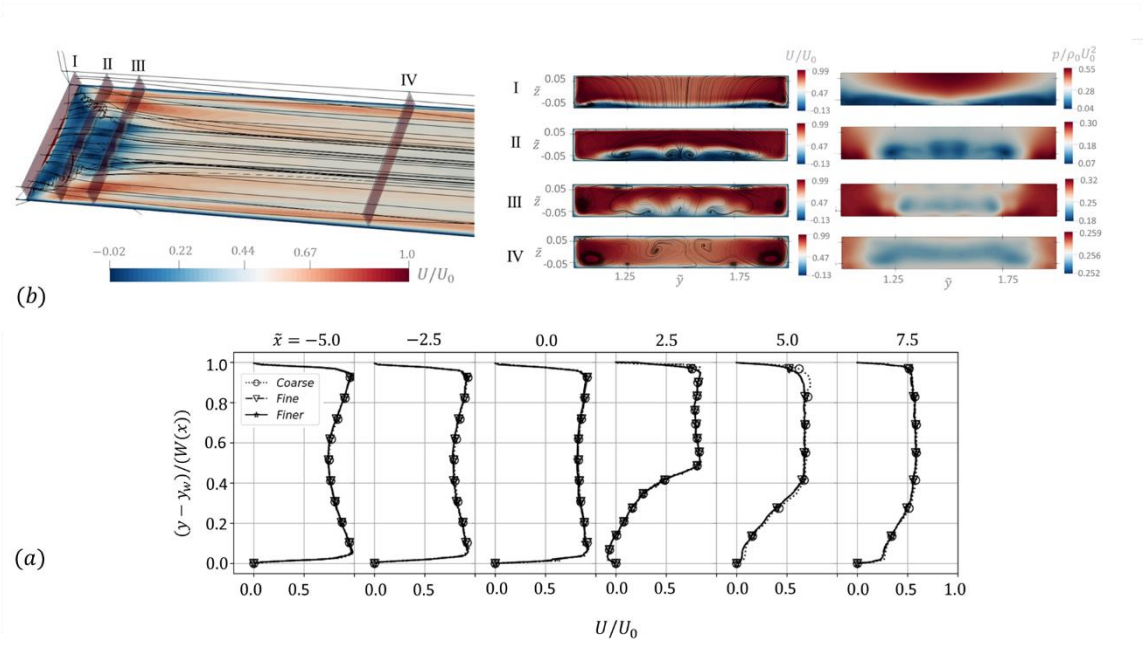

Figure 4.2. (a) Mean streamwise velocity profile at the center of spanwise direction and along different distances from the step for dashed. The vertical axis shows the local normalized width y coordinate where $\boldsymbol{y_w}$ is the distance from the bottom wall and, W(x) is the local width of the channel. Dotted line with circular marker: coarse mesh, solid line with triangular marker: fine mesh, and dashed line with star marker: finer mesh. (b) streamlines and contours of the mean streamwise velocity along with the cross-sectional mean streamwise velocity and pressure fields at different streamwise locations (I) $\tilde{\boldsymbol{x}} = -\mathbf{9.75}$, (II) $\tilde{\boldsymbol{x}} = -\mathbf{9.5}$, (III) $\tilde{\boldsymbol{x}} = -\mathbf{9.25}$ (IV) $\tilde{\boldsymbol{x}} = -\mathbf{4.75}$.

4.2 Results and Discussions

4.2.1 Vortex Structure in BFS

Figure 4.3(a) represents the instantaneous vortex structures within the channel in the presence of cavitation. For more clarity and better representation of the structures, some parts of the channel are enlarged. The instantaneous vortical structures for Case II

(non-cavitating flow) are not presented for several reasons. First, due to the inherent turbulence of the flow, the distribution and intensity of these structures exhibit significant variations across different time steps. This variation makes direct visual comparison between the challenging cases. Furthermore, given that both cases share identical boundary conditions, and differ only in the presence of cavitation in Case I, the distinctions in coherent structures are not sufficiently pronounced in the instantaneous results. Furthermore, while useful for visualization, instantaneous results have limitations in capturing the remarkable differences in both the dynamics and characteristics of vortical structures between Case I and Case II. These variations, encompassing the time-dependent behavior and inherent properties of the structures, are crucial for a complete understanding of the flow. To address these limitations and gain a more comprehensive perspective statistical, dynamical, and modal analysis techniques are employed in later sections. The Q-criterion, introduced by Chong et al. (Chong et al., 1990), is a commonly employed technique for detecting three-dimensional flow structures. It is mathematically defined as the second invariant of the velocity gradient tensor:

$$Q = -\frac{\partial u_j}{\partial x_i}\frac{\partial u_i}{\partial x_j} = \frac{1}{2}(\Omega_{ij}\Omega_{ij} - S_{ij}S_{ij})$$

where Ω_{ij} and S_{ij} correspond to the velocity gradient's antisymmetric and symmetric portions, respectively. Thresholding the Q-criterion to positive values helps in identifying rotation-dominated regions of the flow, which typically correspond to vortices. Conversely, negative values of Q indicate straining regions within the flow. These interpretations are supported by critical point analysis of the velocity gradient tensor, as detailed by (Chong et al., 1990). As mentioned above, we considered the inlet port as the physical domain for consistency of our results with our experimental tests (chapter 2 (Figures 2.2-2.3)). The presence of the inlet port has a remarkable contribution to the vortex generation within the channel, upstream of the step. Cascade of events can be observed in the enlarged view of the inlet region (Figure 4.1). The extreme contraction in the channel inlet leads to a formation of a shear layer in $x - z$ plane within the interior part of the channel. Downstream of contraction, spanwise Kelvin Helmholtz (KH) structures are formed. Upon moving downstream, the secondary streamwise instabilities distort the shape of the KH structures to wavy shape structures, which transform into $\Lambda -$ shaped vortices after moving along a distance from the contraction(Hu et al., 2019). Due to the momentum difference between head and tails, $\Lambda -$ shaped vortices keep stretching

as they move through the channel (Bottaro et al., 2011). Consequently, stretching of $\Lambda-$ shaped vortices lead to the formation of hairpin-like structures. As the flow evolves, $\Lambda-$ shaped and hairpin-like vortical structures break down to smaller fluctuations. The unique channel geometry upstream of the step confines the turbulent structures within the boundary layers near the top and bottom walls at $\tilde{x} = -5$. This localized clustering intensifies the turbulence within these layers, which results in significantly higher turbulence intensity compared to the bulk flow. Some studies, such as (Smeltzer et al., 2023), utilized the Ensemble-averaged enstrophy as an indicator of the turbulence intensification. The normalized mean value of enstrophy ($\bar{\zeta}/\bar{\zeta}_{\max}$, where $\zeta = 0.5|\nabla \times \mathbf{U}|^2$) distribution on the xz plane close to the bottom wall (at y=2μm) is depicted in Figure 4.3(b), which illustrates turbulence intensification and distribution downstream of the contraction. Additionally, the contour of U=0 on this plane is overlaid on the enstrophy distribution, representing points of detachment and reattachment on this plane. It can be observed that away from the side walls, the maximum enstrophy coincides with the reattachment region. A similar observation was reported by other studies, such as Eppink et al. (Eppink, 2020), where it was shown that the a sharp rise in fluctuation intensity occurring after reattachment was attributed to the vortex-shedding mechanism (region of large wall normal shear stresses associated with shedding). Similarly, the turbulence intensification close to the reattachment in this study should be associated with vortex breakdown and shedding of the vortices from the separation bubble. Furthermore, when moving along the channel, the enstrophy gradually spreads in the spanwise direction, while it is mostly concentrated and intensified close to the side walls, which is more significant for $-7 \leq \tilde{x} \leq -3$. A similar observation was provided in (Eppink, 2020), where a thin band of intense fluctuations was observed along both sides of the separation bubble. It seems that the gain in enstrophy caused by the unsteadiness, which is generated with the vortex breakdown downstream of the shear layer, spreads to the sidewall regions. As demonstrated in Figure 4.2, downstream of reattachment, the flow is mainly focused close to the sidewalls, suggesting that the turbulence structures generated at reattachment are mainly transported to the side wall by mean flow.

Moreover, a thin layer of large enstrophy can be seen close to the side wall. This observation is consistent with the results of previous studies (Bechlars and Sandberg,

2017; Wang and Lu, 2012) where large values of enstrophy were reported within the viscous sublayer.

Our primary focus in this study is the second region of the channel, which encompasses the BFS (image of channel with labeled regions and BFS). This region attracts particular interest due to the presence of cavitation within its turbulent shear layer. The combined influence of the step size and flow conditions here causes the generation of significantly larger turbulent structures compared to other regions. Identifying these structures, however, necessitates the utilization of a smaller Q in the analysis.

Unfortunately, employing overly small Q presents a challenge. While they successfully can capture the larger structures of interest, they also encompass numerous smaller-scale fluctuations. This results in cluttered images where individual structures become indistinguishable. Therefore, for visual clarity, we primarily presented structures identified with $Q \geq 2e11\ s^{-1}$. We subsequently employed alternative methods such as modal analysis in later sections to identify and characterize larger coherent structures.

Downstream of the step, turbulent shear layer forms, which is fed by the upcoming TBL. The KH instability leads to the formation of KH spanwise structures ($x - y$ plane). While these structures may not be directly identifiable by the given Q, their influence manifests as undulations in the interface between high and low fluctuating regions. In addition, secondary QSVs, which typically appear between sequential spanwise vortices, are visualized and shown in the enlarged section (Figure 4.3(a)). Quasi-Streamwise Vortices (QSVs) are frequently observed turbulent structures within separated flows. They typically appear as counter-rotating vortex pairs inclined between adjacent primary spanwise vortices(Katz and O'Hern, 1986). Their aspect ratio (length-to-diameter) is around 5, with strengths ranging from 10% to 40% of the primary structures(Katz and O'Hern, 1986). Several studies, including (Jimenez, 1983), extensively documented their formation and characteristics. Notably, despite their lower strength, QSVs are particularly susceptible to cavitation inception due to the significant pressure drop (Agarwal et al.,

2023). Impingement of turbulent structures to the bottom wall marks the shear layer reattachment, where elongated hairpin-like turbulent structures can be detected.

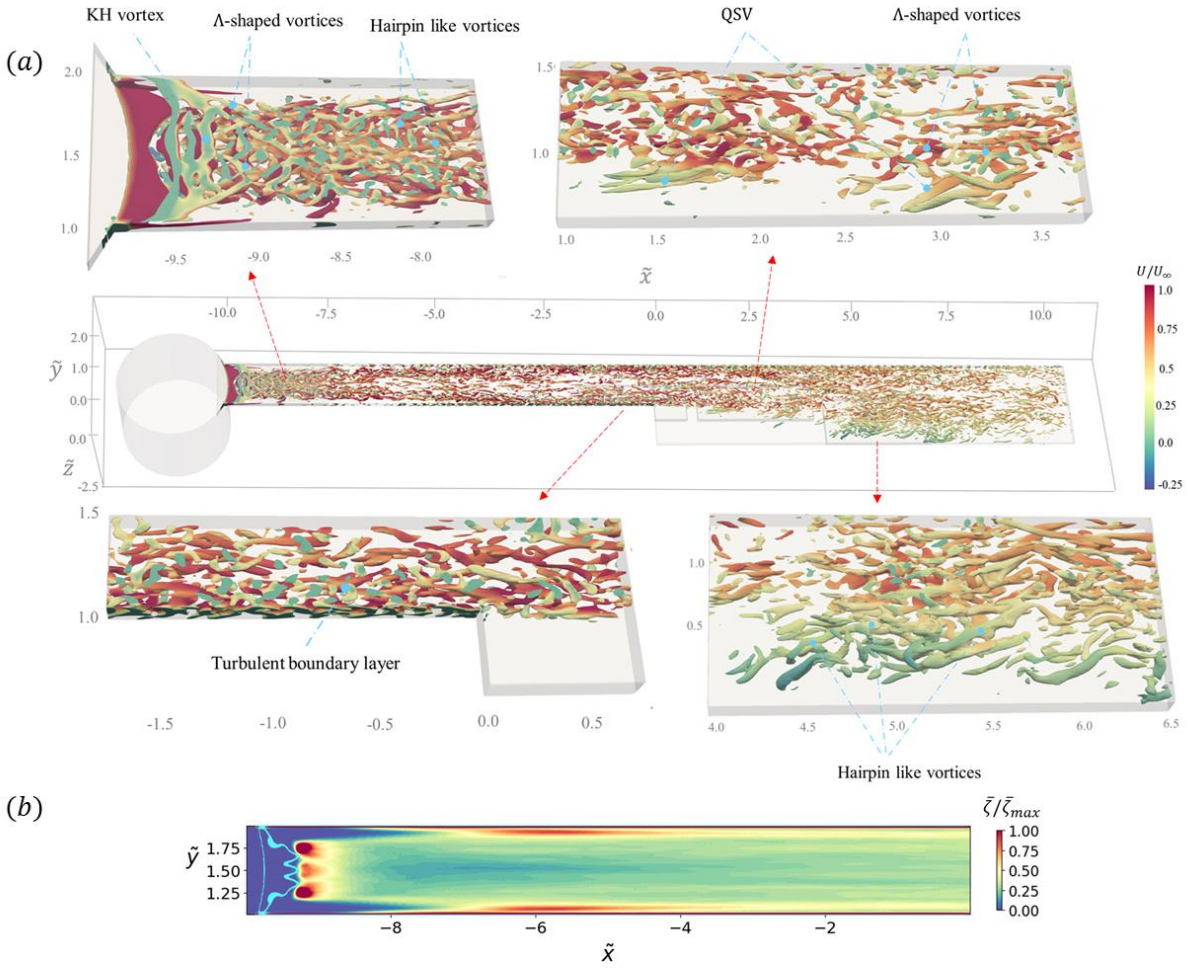

Figure 4.3. (a) Schematic of the BFS configuration. The figure represents the time instance of vortex structures in the presence of cavitation. Vortex structures were calculated using $\boldsymbol{Q-criteria}$ with $\boldsymbol{Q \geq 2e11}$ (Magnified regions are outlined in gray in the Figure). (b) The mean value of enstrophy distribution on the xz plane close to the bottom wall (at y=2μm) superimposed by contour of U=0 (light blue color).

4.2.2 Three Dimensional Effects

Considering the small depth of the channel, a significant portion of the channel is affected by three dimensional dynamics. Previous studies(Bouriga et al., 2015; Bradshaw, 1987; Le Floc'h et al., 2020a) reported that the three-dimensional effects could be caused due to the formation of large longitudinal secondary vortices close to the side walls. In this section, we provide some details on the three-dimensionality of the backward facing step flow in the presence of cavitation, similar to the case provided in the study by Floc'h et al.(Le Floc'h et al., 2020a) . Figure 4.4(a) represents the streamlines of the velocity field close to the side wall of the channel along with the cross-sectional view of mean spanwise velocity and mean pressure fields along the channel. The signature of longitudinal corner vortices can be observed in the streamlines passing over the step (Bouriga et al., 2015; Le Floc'h et al., 2020a). These vortices are associated with the lateral pressure gradient (in y direction) caused by the degree of curvature exhibited by streamlines in the potential flow region(Le Floc'h et al., 2020a). Downstream of the step, the degree of curvature exhibited by streamlines in the potential flow region induces a positive lateral pressure gradient ($\partial p/\partial y$) (Bouriga et al., 2015; Le Floc'h et al., 2020a). This pressure gradient exerts a strong deflection on the near wall streamlines due to their lower momentum. Consequently, fluid particles near the side walls are directed towards the bottom wall (negative y), as depicted in Figure 4.4(a). This deflection results in an inflection point, after which the streamlines bend back towards positive y, which leads to the formation of two longitudinal vortices extending from downstream of the step up to the reattachment point.

Figure 4.4(b) displays spanwise variations in the normalized RMS of pressure fluctuations, p'_{rms}, along the dividing streamline (z^* represents the spanwise coordinate normalized by the half depth of the channel). The normalization of p'_{rms} with the maximum Reynolds stresses within the TSB is based on established findings from previous studies. For example, the study of Ji and Wang (Ji and Wang, 2012) demonstrated that in the backward-facing step, p'rms scales with the local maximum Reynolds shear stress in the adverse pressure gradient (APG) region, while it scales well with the local maximum wall-normal Reynolds stress near reattachment. The results exhibit a similar collapse of p'_{rms} with Reynolds stresses, particularly the Reynolds shear stress, indicating that the scaling law holds across the spanwise direction of the channel.

The variations in these variables are utilized in Figure 4.6(a) and (b) to illustrate that the unsteady nature of the TSBs and scaling of pressure fluctuations remain relatively unaffected, despite strong distortions caused by corner effects on the average flow. As can be seen, the distribution of p'_{rms} is almost symmetrical with respect to the channel centerline for all distances from the step. A notable variation in p'_{rms} value can be observed close to the side wall for $x/L_R = 0.33$ and $x/L_R = 0.67$ (L_R is the length of the reattachment, which is shown to be around 6h for Case I in the next sections), caused by the growth of the longitudinal vortices in these regions.

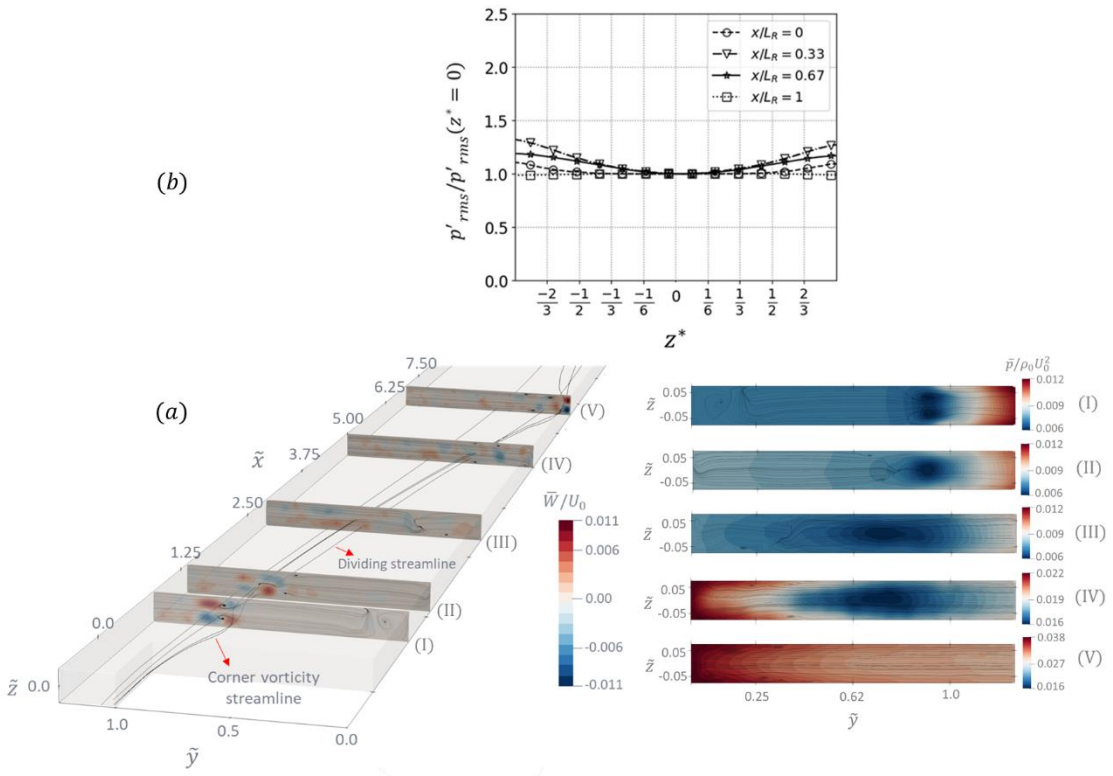

Figure 4.4. (a) Streamlines of the mean velocity field showing the effect of the corner flow along with cross-sectional contours mean spanwise velocity and mean pressure fields (b) Normalized root mean pressure fluctuations along the spanwise direction and at different longitudinal distances on the dividing streamline.

Dividing streamlines into different spanwise depths of the channel are shown in Figure 4.5 to provide more details about the three-dimensional nature in the flow. A strong variation in dividing streamline topology is observed at $z^* = 2/3$. Close to the side walls,

the streamlines in the initial region after separation are more inclined downwards compared to the central streamlines (Figure 4.5(b)). This inclination is primarily caused by the corner vortices, which also contribute to the observed increase in pressure fluctuations near the wall (Figure 4.5(a)). However, downstream of the reattachment point, the streamlines near the walls become more horizontal and flattened. This can be caused by the existence of slender vortices running parallel to the flow, positioned close to the side and bottom boundaries in this region, as observed in Figure 4.5(b).

Variations in p'_{rms} and Reynolds normal stresses ($\overline{vv}$ and $\overline{uv}$) with respect to the spanwise direction at $x/L_R = 0.5$ and y of the middle plane streamline are presented in Figure 4.6(a), which show a rise in fluctuation level upon a decrease in the distance from the wall. A similar trend in pressure and turbulent fluctuations is apparent across the spanwise direction. Scaled values of p'_{rms} with respect to Reynolds stresses are depicted in Figure 4.6(b). The small variations in scaled p'_{rms} (particularly $p'_{rms}/\rho\overline{vv}$) suggest that the unsteady character of the flow changes slightly in spanwise direction(Le Floc'h et al., 2020a).

It should be noted that in this study, spanwise averaging was done for $|z^*| \leq \frac{1}{3}$, where the three-dimensional effects of the flow are minor, and fluctuations have negligible spanwise variations.

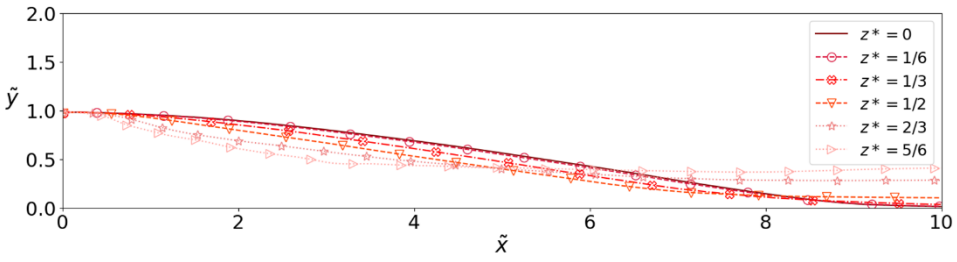

Figure 4.5. Dividing streamline $\boldsymbol{\psi = 0}$ at different spanwise depths of the channel.

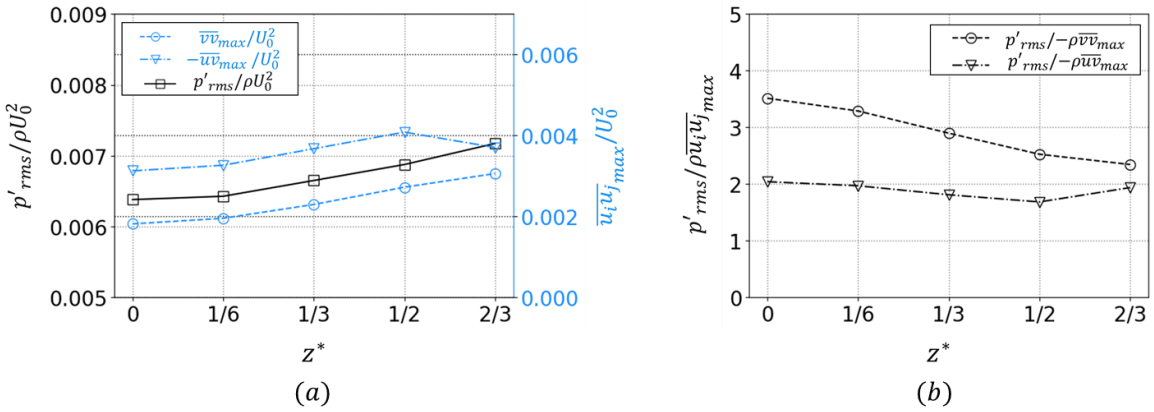

Figure 4.6. (a) Variations in normalized $\boldsymbol{p'_{rms}}$ and Re stresses, and (b) scaled values of $\boldsymbol{p'_{rms}}$, in spanwise direction on the dividing streamline at $\boldsymbol{x/L_R = 0.5}$.

Separated flow generally shows fluctuations over many different time scales and frequencies (Cherry et al., 1984; Eaton and Johnston, 1981; Kiya and Sasaki, 1983; LE et al., 1997; NA and MOIN, 1998; W. Wu et al., 2020). These unsteady modes can dominate the dynamics of the separation bubble. Generally, three distinguishable modes -low, medium and high frequencies- are associated with separated flows. In the following sections, first the effect of phase transition (cavitation and condensation) on the mean flow characteristics is presented, which is followed by a dynamic analysis of low and medium frequency modes. Finally, a modal analysis of coherent structures is covered. Information regarding data processing and data analysis techniques used in the Results section is provided in Appendix A. The details on the supplementary results can be found in the Supplementary materials section.

4.2.3 Characteristics of the Mean Flow

The incoming boundary layer separates due to the abrupt expansion of the test section (Figure 4.3). Beyond this separation point, the flow displays a significant average recirculation zone where the streamwise velocity is negative. This recirculation region extends until the reattachment, where the detached shear layer strikes the surface. Two crucial parameters of separated flow are the reattachment length (L_R) and the thickness of the shear layer (δ_ω). These parameters are influenced by various mechanisms,

including adverse pressure gradient, backstep height, interior TBL, and mass/momentum entrainment(Stella, 2017). TSB is typically characterized by the Recirculation Region Interface (RRI), which specifies the lower boundary of the shear layer, marking the point at which the shear layer separates from the reversed flow region. Moreover, the length of TSB is determined as the streamwise length spanning from the separation point (the RRI's initial boundary) to the reattachment point (the RRI's final boundary).

In this study, the mean flow RRI is identified by either the isoline U=0 on the mean streamwise velocity field or the set of points where the backflow coefficient γ is equal to 0.5 (γ being defined as the fraction of time during which the flow moves downstream)(Stella, 2017; Stella et al., 2017). Figure 4.7(a) depicts the contour of the streamwise mean velocity overlaid with the $U = 0$ streamline for two cases: with cavitation (case I) and without cavitation (case II)(Berk et al., 2017). Figure 4.7(b) also displays the forward-flow fraction. The 50% forward-flow fraction isopleth (shown as blue dashed lines) follows a specific path: it starts from either the leading or trailing edge of the step, goes through the center of the separating bubble, and ends on the wall very near the reattachment points. This pattern aligns with observations from Djilali & Gartshore(Djilali et al., 1991) and Mohammed-Taifour & Weiss(Mohammed-Taifour and Weiss, 2016).

Two distinct separation bubbles can be observed in Figures 4.7(a) and (b): The small bubble in the corner around $\tilde{x} = x/h \approx 2.8$ and the large separation bubble behind the step(Fang and Tachie, 2019). The large separation bubble has two interfaces: one with the shear layer and another with the smaller separation bubble and bottom wall. The streamwise extent of the reversed flow region for $y = 0$, i.e., the location at which the interface between the large separation bubble and shear layer reaches the x-axis (cross sign in Figure 4.7(b)), coincides with the average length of TSB (the distance between the mean detachment and mean reattachment)(Berk et al., 2017; Mohammed-Taifour and Weiss, 2016). According to Figure 4.7, it can be recognized that in the case of cavitating flow, the reattachment length increases by around 8% compared to the case without phase change. The main reason for larger TSB in case I compared to case II should be the phase transition and vapor generation within the shear layer which changes the mean characteristics of the flow. More details on this issue are provided in the following sections where our results show that the vapor generation within the shear layer results in longitudinal stretching of the spanwise vortical structures (longer and thinner) and a

decline in the shear layer growth rate compared to the case II. Moreover, we observed that the mean convective velocity is almost the same for both cases. Some studies(Berk et al., 2017; Stella et al., 2017) reported that the reattachment length has an inverse relation with momentum entrainment so that it can be concluded that the increase in L_R for case I is attributed to the decrease in the momentum entrainment due to the vapor generation within the shear layer.

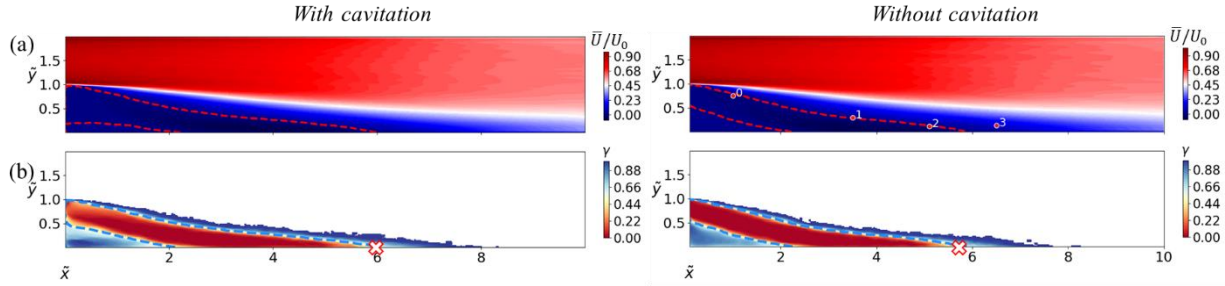

Figure 4.7 Mean value of RRI characterized by (a) isoline of the streamwise vlocity field and (b) $\boldsymbol{\gamma}$parameter (cross signs represent the reattachment point).

To further investigate the impact of the phase change on the mean characteristics of the shear layer, the vorticity thickness (δ_ω, Appendix A), which serves as an indicator of shear layer growth, is obtained for both cases. The vorticity thickness has been widely used in various studies to describe the expansion of the shear layer in separating flows(Stella et al., 2017). Related studies revealed that the development of δ_ω (vorticity thickness) in the first half of the TSB (x/L_R<0.5) closely resembles that of the free mixing layer(Fang and Tachie, 2019; Stella et al., 2017). Specifically, these studies highlighted a linear increase in the vorticity thickness along the streamwise direction with a slope of $d\delta\omega/dx$ ranging from 0.15 to 0.22. This linear trend is valid for both the free mixing layer and the first half of the separated shear flow(Cherry et al., 1984; Djilali et al., 1991; Fang and Tachie, 2019; Kiya and Sasaki, 1983).

Figure 4.8(a) illustrates the evolution of δ_ω in the streamwise direction ($\tilde{x}$). In addition, Figure 4.8(b) provides the estimation of the mean shear layer by combining the vorticity thickness with the mean RRI(Aeschlimann et al., 2011a; Stella, 2017). It can be seen that for both cases (I and II), in the first half of the shear layer (which is shown by s_1), the vortex thickness grows linearly in streamwise direction with a slope of 0.154. This growth rate of the mean shear layer is consistent with those reported in the existing

literature(Maurice et al., 2014), which suggests similar dynamics of the shear layer and free mixing layer in this region. In the second half of the shear layer (s_2, $x/L_R > 0.5$), the growth trend of the shear layer deviates from that of the free mixing layer, and the slope of the growth rate decreases for both cases(Stella, 2017; W. Wu et al., 2020). Notably, a remarkable difference in the shear layer development between cases I and II can be observed in the second half of the shear layer. Except for the final parts (near the reattachment point), the mean shear layer thickness is larger for case II compared to case I throughout the second half of the shear layer. This finding is in agreement with previous studies(Maurice et al., 2014) that presented similar behavior for both shear layer thickness and reattachment length.

The development of the shear layer is primarily influenced by entrainment and expansion ratio across the step. Previous studies (Stella et al., 2017) demonstrated that shear layer spreading in the second half exhibits a strong correlation with pressure recovery in the reattachment region (a higher pressure recovery results in lower spreading). They concluded that in reattachment region, the expansion ratio played a notable role in the shear layer growth rate. Moreover, the growth rate ($d\delta/dx$) has an inverse relation with the reattachment length (L_R)(Adams and Johnston, 1988). Case I exhibits a stronger mean pressure recovery (Figures 4.9(a) and 4.11(a)) in the reattachment, which is associated with a larger reattachment length (Figure 4.7) and a smaller shear layer thickness in the second half (Figure 4.8). Therefore, in the presence of phase change, in addition to the expansion ratio (ER), there should be another mechanism that control the pressure recovery in the reattachment region, and consequently, the reattachment points and shear layer thickness in the second half.

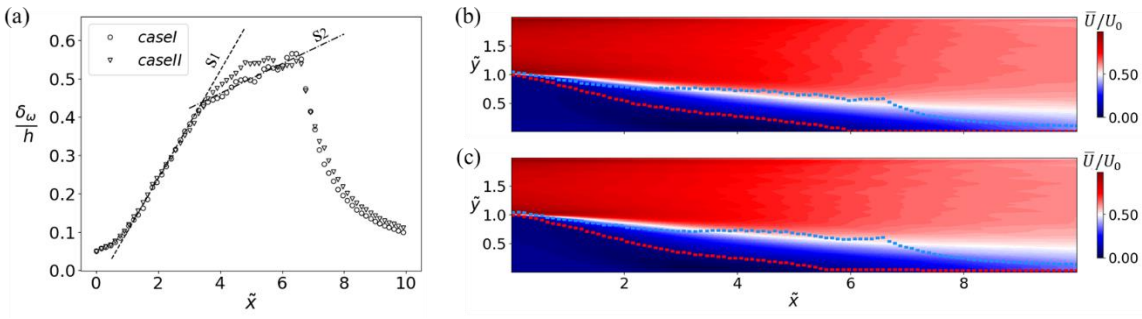

Figure 4.8 Shear layer growth. (a) vorticity thickness δ_ω. Mean separated flow superimposed on velocity field (b) case I (with cavitation), and (c) case II (without cavitation).

The contours of the mean pressure $\bar{p}$, and RMS value of the pressure fluctuations p'_{rms} are presented in Figure 4.9. The values were averaged over spanwise direction and were nondimensionalized by $\rho_0 U_0^2$, where the subscript 0 indicates the conditions in the free flow upstream of the step (around $\tilde{x} \approx -5$). According to Figure 4.9(a), the spanwise average value of $\bar{p}$ is significantly larger for the case I (with cavitation) than that for the case II (without cavitation) in the reattachment region ($5.5 < \tilde{x} < 8.5$, also see Figure 4.10(a)), while the reattachment point is located around 0.5h farther away from the step for case I (Figure 4.2). Similar changes are present for the streamwise mean pressure distribution along the bottom wall of the channel behind the step ($\bar{p}_w$) in Figure 4.10 (a). For both cases, $\bar{p}_w$ initially decreases smoothly until it reaches a local minimum value at $\tilde{x} \approx 3$ (middle of the shear layer), beyond which the mean pressure increases rapidly and reaches its maximum at around $\tilde{x} \approx 7$ (slightly downstream of reattachment point)(Kourta et al., 2015). In addition, $\bar{p}_w$ is smaller for case I than that for case II at the initial part of the channel ($\tilde{x} < 5.5$). This difference can be attributed to the convection of vapor to the recirculation region which changes the dynamics of the vorticities within the recirculation region(Bhatt et al., 2021a; Le et al., 1993). Vapor formation leads to a local increase in the volume of the flowing fluid, particularly in the second half or the recirculation region. This increase in the volume can locally raise the flow velocity (particularly when it is convected to the recirculation region) and decreases the static pressure of the flow. As the shear layer is mainly associated with vapor generation, it can be concluded that the vapor formation is the main contributor to the difference in $\bar{p}$ in this section of the channel. Conversely, at $\tilde{x} > 5.5$, $\bar{p}_w$ is higher for case I versus case II. This finding suggests a stronger impingement for case I versus case II. While several parameters such as the incoming TBL(Stella, 2017), Reynolds number, and geometrical features (such as the expansion ratio over the step)(Ji and Wang, 2012), can influence the impingement mechanism and pressure recovery in the reattachment region, the shockwave induced by bubble collapses appears to play a significant role in the stronger pressure recovery after impingement for case I versus case II (discussed in the next section). When cavitation occurs near flow separation, bubble collapse during impingement can trigger the reattachment shockwave(Bhatt et al., 2021a), which leads to a stronger pressure recovery after reattachment(Akhilesh et al., 2022).

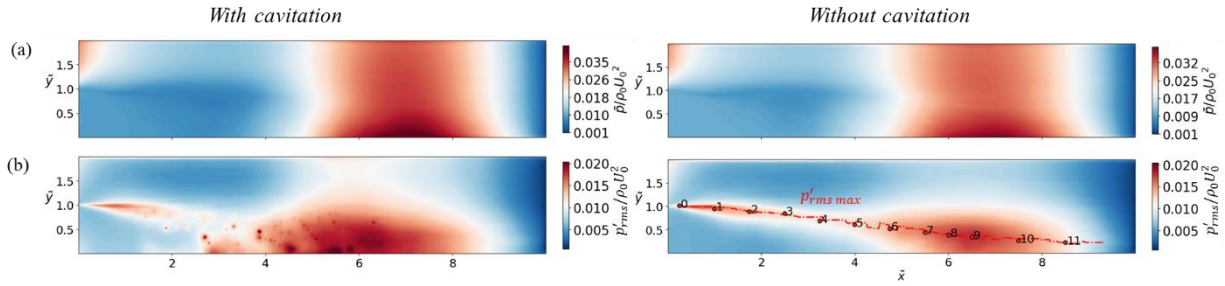

Figure 4.9 Contours of spanwise average value of (a) $\frac{\bar{p}}{\rho_0 U_0^2}$, and (b) $\frac{p'_{rms}}{\rho_0 U_0^2}$ for case I (the left column) and case II (the right column).

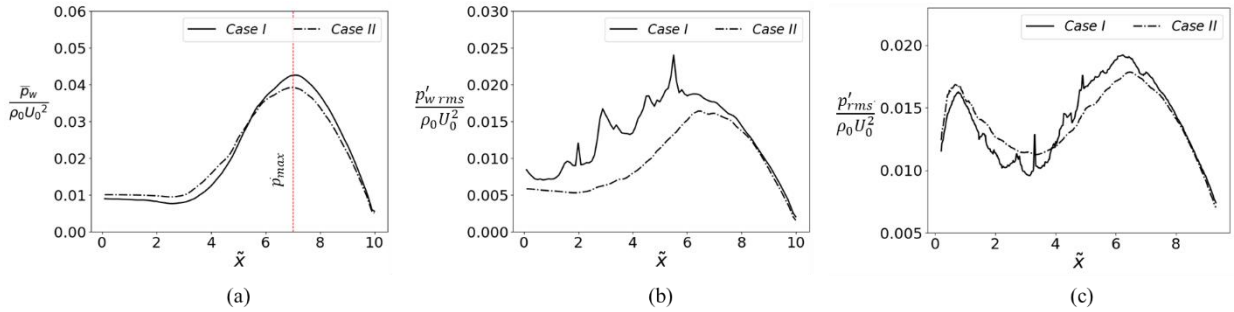

Figure 4.10 Distribution of spanwise average value of (a) $\frac{\bar{p}_w}{\rho_0 U_0^2}$, (b) $\frac{p'_{w\,rms}}{\rho_0 U_0^2}$ along the bottom wall of the channel, and (c) $\frac{p'_{rms}}{\rho_0 U_0^2}$ along the streamwise pathway of maximum RMS pressure fluctuations for case II.

Regarding RMS pressure fluctuations (p'_{rms}) (Figure 4.9(b)), both cases I and II show a similar trend besides some significant differences. Consistent with previous studies(Abe, 2017), p'_{rms} within the shear layer is primarily influenced by Reynolds shear stress, $\overline{uv}$, while it is mainly associated with cross-streamwise (mostly $\overline{vv}$) and streamwise ($\overline{uu}$) Reynolds normal stresses in the reattachment region. In accordance with prior research(Ji and Wang, 2012; MOIN and NA, 1998), the current findings indicate that a significant level of p'_{rms} is produced in the initial section of the separated shear layer ($\tilde{x} = 1$), This value then decreases in the middle of the shear layer but spikes again after reattachment (Figures 4.9(b) and 4.11(c)) for both cases. The pressure fluctuations within the shear layer and upstream of the reattachment points are primarily influenced by vortical

structures that are carried along by the flow. Na and Moin (1998b)(MOIN and NA, 1998) observed that these vortical structures, particularly those within the detached shear layer overlying the separation bubble, act as significant sources of pressure fluctuations. The movement of these vortical structures plays a crucial role in generating pressure fluctuations within the shear layer. The pattern of pressure fluctuations within the shear layer and upstream of the reattachment point is similar to that of turbulence intensities and local maximum Reynolds shear stress (Figures 4.10(c) and 4.12(c)). Therefore, it can be inferred that local maximum Reynolds shear stresses, which are primarily generated by vortical structures, are the main contributors to pressure fluctuations within the shear layer. This aligns with the findings of the Na and Moin study(MOIN and NA, 1998). Another notable trend observed in this study is the decrease in p'_{rms} within the shear layer beyond an initial growth phase (Figures 4.9(b) and 4.10(c)). This decline can be attributed to the phenomenon of vortex pairing and the subsequent reduction in the intensity of $\overline{uv}$ within the shear layer (Figures 4.11(c) and 4.12(c)).

In the second half of the shear layer, between the two peaks visible in the p'_{rms} and $\overline{uv}$ plots, a more significant drop in p'_{rms} and $\overline{uv}$ can be seen for case I (with cavitation) compared to case II (without cavitation). In the same region within the shear layer, large mean vapor fractions exist for case I (as shown in chapter 2 Figure 2.3.). Previous studies(Aeschlimann et al., 2011a; Iyer and Ceccio, 2002; Ji and Wang, 2012) reported that vapor generation and increase in compressibility within the vortical structures attenuate p'_{rms}fluctuation and $\overline{uv}$, which agrees well with our findings.

In addition, as reported in the previous studies(Belahadji et al., 1995; Iyer and Ceccio, 2002)**,** the decline in cross-stream fluctuations and Reynolds stresses can be linked to the effect of cavitation on the decoupling between streamwise and cross-stream velocity fluctuations within the vortices. Furthermore, it was suggested by Aeschlimann et al.(Aeschlimann et al., 2011a) that cavitation development continuously reduces turbulence production which is proportional to $\overline{uv}$, and converts it to turbulent kinetic energy (TKE). This explanation is in line with our findings (Figures 2.11 and 2.12(a) and (c)), where it is illustrated that the vapor generation within the shear layer (particularly its 2nd half) is associated with the decrease in $\overline{uv}$ and increase in TKE level.

After reaching minimum RMS pressure fluctuations at $\tilde{x} \approx 4$, the pressure fluctuations gradually recover and reach the maximum value slightly downstream of the reattachment

point (almost the same place as $\bar{p}_{max}$ (Figure 2.11(c)). Previous studies (Abe, 2017; Ji and Wang, 2012) showed that RMS pressure fluctuations in the reattachment region are mainly regulated with convection and increase in normal Reynolds stresses. Ji and Wang(Ji and Wang, 2012) indicated that for a step height remarkably larger than the upstream turbulent boundary layer, the RMS pressure fluctuation scales with the local maximum cross-stream Reynolds normal stress $\overline{vv}$. Our results (Figure 2.10(b) and 2.12(b)) highlight that $\overline{vv}$ reaches its highest value in the reattachment region and has a remarkable contribution on RMS fluctuation pressure in this region. Nonetheless, we can observe that $\overline{uu}$ has an equivalent importance. The TKE (Figure 2.12(a)) and $\overline{uu}$ level are significantly larger for case I than case II in the reattachment region ($5 < \tilde{x} < 7$), which is in harmony with the p'_{rms} behavior (Figures 2.10(c) and 2.12(a)) in this region and shows the major impact of the pressure shock waves generated by bubble collapses on streamwise Reynolds stresses. By moving vapor structures within the shear layer towards the high pressure reattachment region and considering their collapses and condensation in this region, one can expect the increase in the turbulence and pressure fluctuation level(CECCIO and LABERTEAUX, 2001; Iyer and Ceccio, 2002). This is accompanied with spike pressure pulses in the shear layer for case I (Figure 2.9(b) and 2.10(b)) which are related to the shock waves generated by the bubble collapses in reattachment and at a slightly upstream location of the reattachment. More discussion will be provided on shock wave generation and propagation for case I in the next section.

Furthermore, Figure 2.9(b) shows that, for case I, a substantial region near the wall surface is subjected to an augmented p'_{rms} (also see Figure 2.10(b)). Additionally, circular regions of high fluctuations are randomly distributed throughout the second half of the shear layer and reattachment region. These regions are indicative of shockwaves arising from bubble collapses in these areas. Distribution of streamwise RMS of fluctuating wall pressure ($p'_{w\,rms}$) is provided in Figure 2.10(b) for cases I and II. In the front part of the separation bubble, due to a remarkable distance between the shear layer and wall surface, the effect of fluctuations within the shear layer on $p'_{w\,rms}$ is minimal. Thus, close to the step, $p'_{w\,rms}$ is largely influenced by slow and large vortices within the recirculation region and near the wall. As we move along the channel and get closer to the reattachment region, the shear layer becomes closer to the wall and the influence of the shear-layer-generated vortical structures on the $p'_{w\,rms}$ becomes more dominant(Ji and Wang, 2012). The results of RMS of fluctuating pressure on the bottom wall surface

show that $p'_{w\,rms}$ of case I is in general larger than that of the case II (except at the end of the channel ($8.5 < \tilde{x} < 10$), where two results converge), with several spikes at the upstream location of the reattachment points, which illustrate the effect of bubble collapses and shock waves on wall pressure fluctuations in this region. To offer better understanding of pressure fluctuations within the shear layer, p'_{rms} is represented along the pathway of maximum fluctuations for case II (the pathway is shown in Figure 2.8(b) case II) in Figure 2.11 (c). It can be seen that similar to the $\bar{p}$, in the initial part of the shear layer (particularly in the middle of the shear layer), case II has a larger p'_{rms}, while the pressure fluctuations are dominant for case I at locations closer to the reattachment ($4 < \tilde{x}$). Throughout the bottom wall, $p'_{w\,rms}$ is significantly larger for case I than that of case II, while the values converge to each other around one step after reattachment ($\tilde{x} \sim 8$), where there is no effect of condensation and vapor generation. As mentioned earlier, the spike pulses on p'_{rms} distribution demonstrate the effect of shock waves due to bubble collapses which are more pronounced near the wall surface and distributed in a remarkable portion of the channel (Also see Figure 2.9(b)) ($3 < \tilde{x} < 6$). From these results it can be inferred that the suppressed mean pressure and pressure fluctuations within the shear layer for case I are linked to the vapor generation and increase in compressibility. Meanwhile, frequent bubble collapse and condensation wave propagation near the wall around the reattachment point appear to drive the opposite trend, i.e., an increase in both mean and fluctuating pressure parameters in the reattachment region.

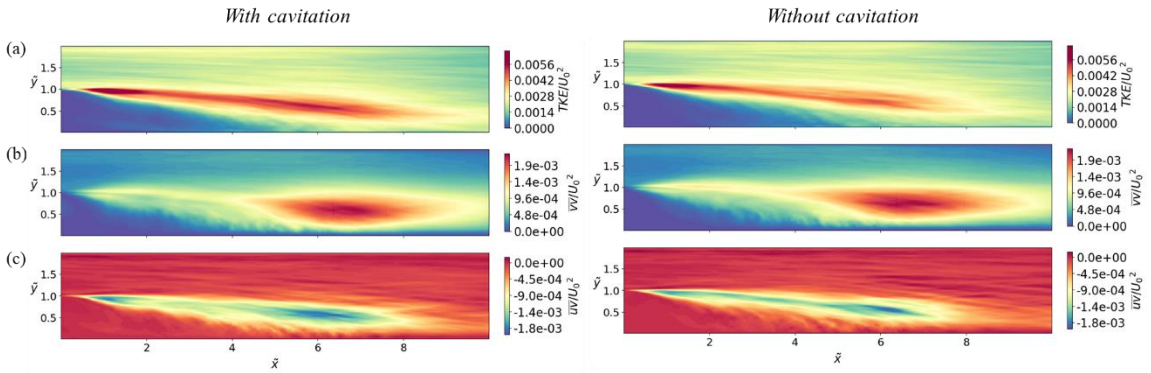

Figure 4.11 Contours of spanwise average value of (a) $\frac{TKE}{U_0^2}$, (b) $\frac{\overline{vv}}{U_0^2}$, and (c) $\frac{\overline{uv}}{U_0^2}$ for case I (left column) and case II right column.

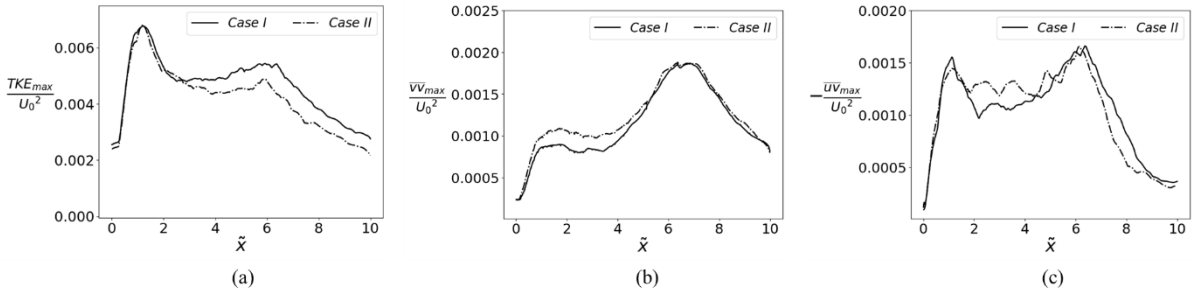

Figure 4.12 Streamwise distribution of spanwise average value of (a) $\frac{\boldsymbol{TKE_{max}}}{\boldsymbol{U_0^2}}$, (b) $\frac{\boldsymbol{\overline{vv}_{max}}}{\boldsymbol{U_0^2}}$, and (c) $\frac{\boldsymbol{\overline{uv}_{max}}}{\boldsymbol{U_0^2}}$.

One important aspect in the shape, size and distribution of the spanwise vortical structures within the shear layer. To examine the effect of cavitation on the mean characteristics of KH vorticities, two-point autocorrelation (R_{xx}, Appendix A) can be employed. The autocorrelation contours for streamwise and cross-streamwise components of velocity are shown in Figure 4.13. It can be observed that spanwise structures are elongated and have an elliptical shape within the shear layer (before reattachment) while autocorrelation of both velocity components has the same size showing almost spherical shape of vortices after the reattachment. From the comparisons between the autocorrelation components for cases I and II, it is evident that the vortices within the shear layer are thinner and more stretched for case I compared to those for case II. Still, the vortices after the reattachment have almost the same size. These results suggest that vapor generation within the vortical structures has a dominant impact on their topology, particularly in the second part of TSB. This region is characterized by a large fraction of vapor, which appears to significantly drive the observed morphological changes. Previous studies similarly reported the significance of compressibility(Arun et al., 2019; Belahadji et al., 1995) and phase transition(Belahadji et al., 1995) on the morphology of the vortical structures. From our results in Figure 4.13, it is apparent that in the case of cavitation, the spanwise vortical structures are elongated within the region with large vapor fraction (second part of TSB) in direction of the shear layer (apparent from the streamwise velocity autocorrelation), which is accompanied by contraction in the width of the structures (cross-streamwise velocity fluctuations). These observations align with the results of the Reynolds stresses, where it was observed that vapor generation leads to a remarkable increase in streamwise

Reynolds normal stress while significantly reducing the cross-streamwise Reynolds normal stress (Figure 4.12). In the case of cavitation, a significant variation in density exists across the vortical structures, with the lowest density within the two-phase mixture and highest density within the surrounding liquid phase. It seems that, upon a sudden decrease in the vortex density, the velocity field within the vortex is more influenced by the momentum transfer across its boundaries with the high-density surrounding flow so that vortices become more stretched in the direction of streamlines. In addition, phase change leads to an increase in the volume of the vortices as evident from Figure 4.13.

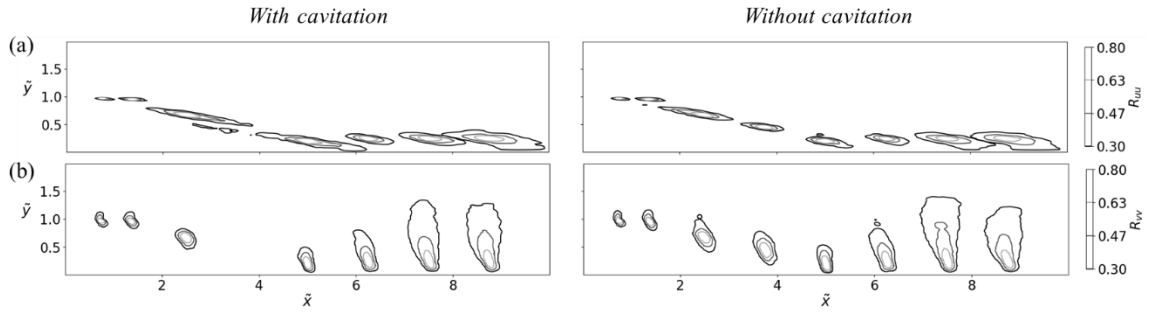

Figure 4.13 Contours of two-point correlation for (a) streamwise velocity, and (b) cross streamwise velocity.

4.2.4 Spectral Analysis

Frequency characteristics of TBS are provided by pre-multiplied power spectral density (PSD) at selected streamwise locations along the maximum p'_{rms} streamwise pathway(Ji and Wang, 2012) region (probe placements are shown with circular markers in Figure 4.9(b), right column). The sampling interval was $\tilde{t} = \frac{tU_0}{h} = 288$ with a sampling rate of $\frac{f_s h}{U_0} = 10.67$. Details regarding Data treatment and processing for power spectral density (PSD) calculations are provided in Appendix A. Pre-multiplied PSD values for two cases, with and without cavitation, are presented in Figures 4.14(a) and (b), respectively. Notably, due to the significant difference in PSD levels between cases I and II within the high frequency ranges, distinct limits for PSD values are employed on x axis for each case (4e-6 to 2e-4 for case I and 0.5e-6 to 2e-4 for case II). This differentiation facilitates a clearer understanding of the variations across the frequencies. Furthermore, three distinct dashed lines (in blue, black, and red) corresponding to the dominant frequencies

for each case ($St_h \approx 0.045, 0.11,$ and 1.4 for case I and $St_h \approx 0.065, 0.16,$ and 1.4 for case II) across the streamwise pathway are illustrated to aid in the comparison between two cases (For brevity, the three frequencies will be referred as First Low Frequency (LF1), Second Low Frequency (LF2), and Medium Frequency (MF) throughout the rest of the study). Accordingly, downstream of the step, a broad spectrum of frequencies can be observed. For both cases, the shear layer behind the step exhibits two initial peaks in the energy spectrum: one high frequency peak centered around $St_h \sim 1.4$, and a low frequency peak centered around $St_h \sim 0.11$ for case I and $St_h \sim 0.08$ for case II. When moving along the maximum ${p'}_{rms}$ pathway, the high frequency peak continuously shifts towards the lower frequencies, indicated by a red flash ($St_h = 0.11 \sim 1.4$ and $0.16 \sim 1.4$, for cases I and II, respectively). Previous studies demonstrated that this continuous decrease in the peak frequency is linked to the pairing of spanwise vortices(Barbaca et al., 2019; Hudy et al., 2007; W. Wu et al., 2020). This frequency converges to a constant value after reattachment, which should correspond to the shedding mechanism at this stage. Close to the reattachment point, the spanwise vortical structures grow to their maximum size and exhibit a constant frequency highly dependent on the step size and Re number(Hudy et al., 2007; Ji and Wang, 2012). For case I, the energy spectrum deviates from the characteristic logarithmic decay at high frequencies, which is evident for case II. Instead, a notable energy level persists at high frequencies throughout the second half of the shear layer and reattachment regions, which further corroborates the effect of bubble collapses on intensifying the turbulence level within the flow(Iyer and Ceccio, 2002).

The smallest frequency peak is likely linked to the TSB breathing mechanism for both cases (Hudy et al., 2007; Ji and Wang, 2012; W. Wu et al., 2020). For case I, the smallest frequency peak emerges at $\tilde{x} = 2.5$, and is dominated after the reattachment. For case II, the smallest frequency peak can be observed in the initial segment of the shear layer and contains a smaller energy compared to case I, which implies less frequent occurrence or a smaller amplitude. Various mechanisms were proposed in the literature to explain this low-frequency dynamic, including Gortler vortices(Hickel et al., 2021; W. Wu et al., 2020). Additionally, it can be observed that while the high-frequency peak is nearly identical for cases I and II, the low frequencies are slightly larger for case II.

Furthermore, spectral analysis was performed (Figure 4.14(c)) to reveal the effects of pressure fluctuations on vapor dynamics within the shear layer and beyond it in the

reattachment region. A similar trend is apparent for vapor fluctuations within the shear layer where vapor fluctuations exhibit a dominant PSD level at high and low frequencies (local maxima in $St_h \sim 1.4$ and $St_h \sim 0.11$) at $\tilde{x} = 0.25$. This peak in PSD shifts towards smaller frequencies when moving away from the step (similar to pressure PSD). This behavior shows that the fluctuations of void fraction are in harmony with those of the pressure within the initial part of the shear layer, which suggests that the growth and transport of vapor packets occur within the coherent structures and spanwise vortices of the shear layer (Agarwal et al., 2023; Bhatt et al., 2021a; W. Wu et al., 2020). Furthermore, except for the initial part of the channel (first half of the shear layer), high frequencies exhibit a small PSD level for vapor fluctuations, which indicates that the fluctuations induced by the bubble collapses have a minimal impact on vapor transport. Beyond $\tilde{x} \sim 6$, most of vapor are condensed (primarily due to the high pressure after impingement) and a few of them survive, for which a broad range of frequencies centered around a peak at $St_h \sim 1$ can be observed. This implies that the transport of vapor packets is controlled with random high frequency turbulent structures in this region.

According to the results, major differences in pressure spectral content for cases I and II are due to the presence of high frequency pressure fluctuations with large PSD levels near the reattachment for case I, as well as differences between cases I and II in their dominant low frequencies. The differences in PSD distribution between cases I and II within the shear layer and reattachment regions can be attributed to several factors. These include changes in the dynamics of vortical structures in the shear layer, recirculation due to vapor formation and convection, altered dynamics of the reentrant jet, and effects of bubble collapse and propagation of condensation shock waves. In the next section, we will examine some of the important flow parameters to elucidate the sources of dominant frequencies and differences between the cases(Barbaca et al., 2019).

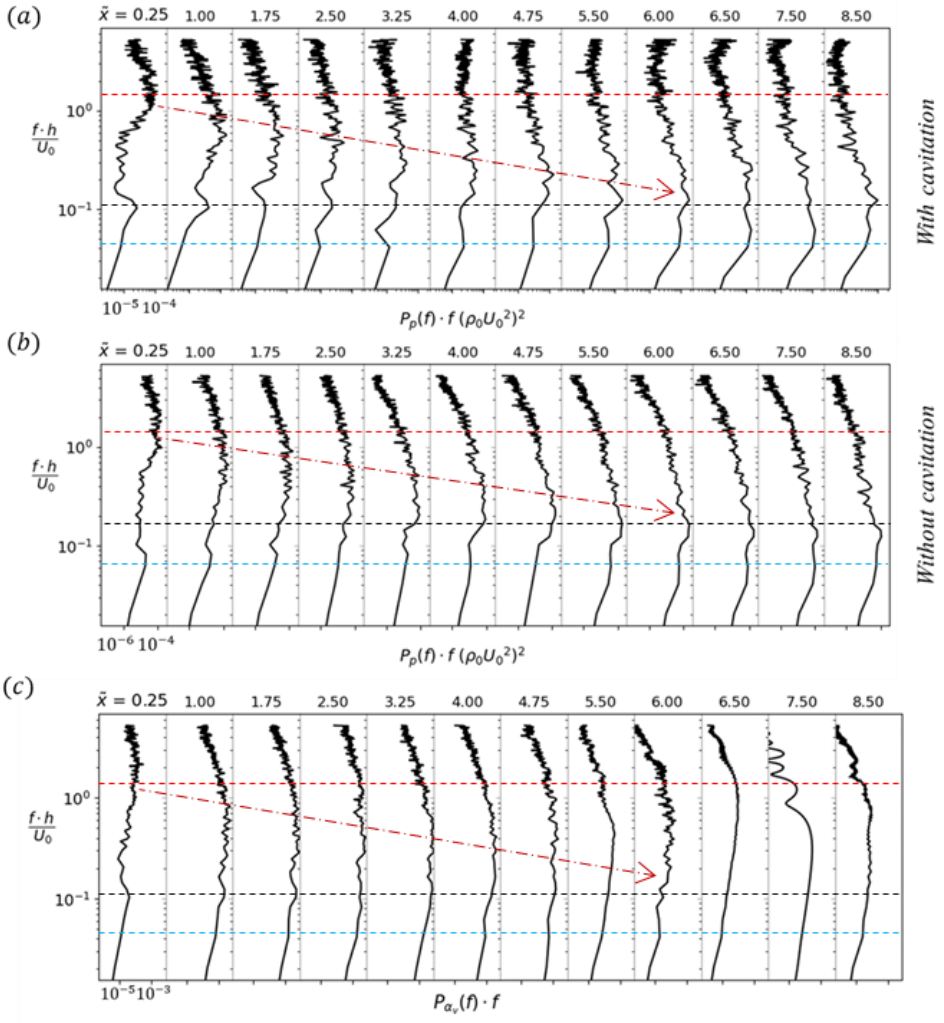

Figure 4.14 Pre-multiplied power spectral density of (a) the pressure field for case II, (b) the pressure field for case I, and (c) the void fraction for case II at several locations passing the maximum TKE [8] regions shown with markers in Figure 8(b).

The low frequency unsteadiness of TSB is linked to the "breathing" mechanism (the large-scale growth and shrinking of the separation bubble). Some studies(Fang and Tachie, 2019; Ganapathisubramani et al., 2013; Le Floc'h et al., 2020a; W. Wu et al., 2020) demonstrated that the large-scale unsteadiness of TSB can be represented by the variations in total area of the reversed flow. This estimation is particularly relevant in cases with a large portion of the reversed flow within TSB(Le Floc'h et al., 2020a), as the case in our study. The area of the reversed flow is calculated as $A_b = \iint_{\Omega_b} dxdy$, where Ω_b is the areas spanwise average of u is smaller than zero. The temporal evolution of the separation bubble size along with its PSD value are represented in Figure 4.15, where the size and time are nondimensionalized based on the step height and reference velocity.

Consistent with the results from the spectral analysis of the pressure field, the variation in reversed flow area exhibits dominant dynamics associated with two low frequencies. For both cases I and II, we observe two dominant frequencies. The smaller of these frequencies are centered around St_h values of 0.03 and 0.06 for cases I and II, respectively. On the other hand, the larger dominant frequencies manifest themselves around St_h values of 0.11 and 0.2, respectively for cases I and II. These frequencies closely match with those observed in pressure PSD, which implies that the low frequencies for both cases are related to the changes in the shape/size of the separation bubble and displacement of the reattachment point.

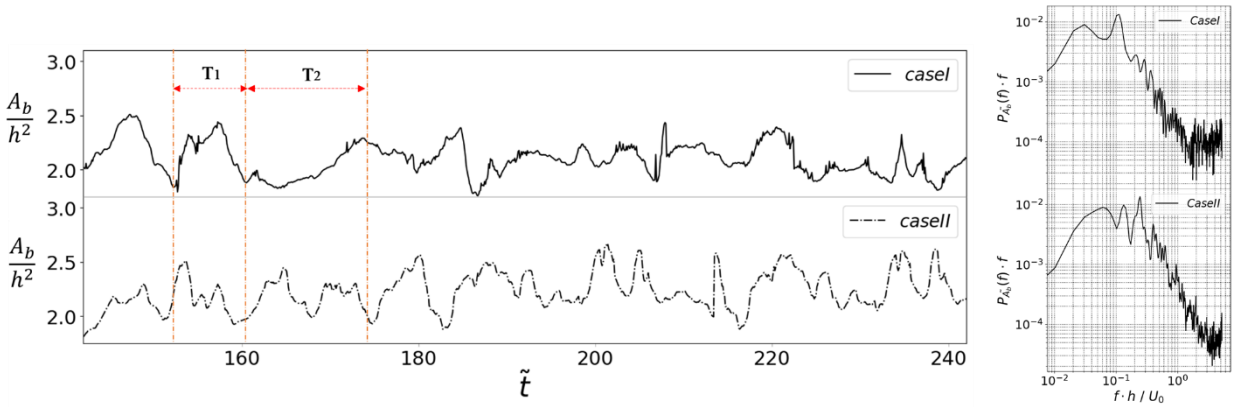

Figure 4.15 Temporal evolution and corresponding PSD values of the total reversed flow area in x-y plane.

It can be inferred that two distinct mechanisms are responsible for separation bubble contraction/expansion and reattachment displacement: one associated with LF1 and other related to the LF2 corresponding to the vortex shedding at reattachment. As reported by previous studies(Kuehn, 1980; Ra and Chang, 1990), the streamwise pressure gradient and pressure over the step strongly affect the reattachment location, and consequently, the low frequencies. The temporal evolution and PSD values for the average pressure in a cross-section over the step are presented in Figure 4.16. Still two low frequencies peaks close to LF1 and LF2 are visible in the spectral content, which suggests the existence of coupling between the pressure over the step and reattachment displacement. The coupling between these two parameters can be quantified using the spectral coherence (C_{xy}, Appendix A). The values corresponding to C_{xy} =1 show linear coupling between two signals while values close to 0 suggest that the signals are unrelated. The values between 0 and 1 can demonstrate a nonlinear relation between the signals indicating that either the

output of signal $y(t)$ is affected by $x(t)$ as well as other inputs, or there are noises in the dataset. The coherence between the average pressure over the step and reversed flow for two cases are represented in Figure 4.17. For case I, two peak values (0.4 and 0.82) in $St_h = 0.04$ and 0.11 indicate a nonlinear coupling between the reversed flow and average pressure over the step around these frequencies. For case II, the peak of the spectral coherence is visible around $St_h = 0.14$ while the coherence value is close to zero for $St_h < 0.06$, which implies that for case II, LF2 has a notable nonlinear coupling with upstream pressure, while LF1 is almost unrelated to it.

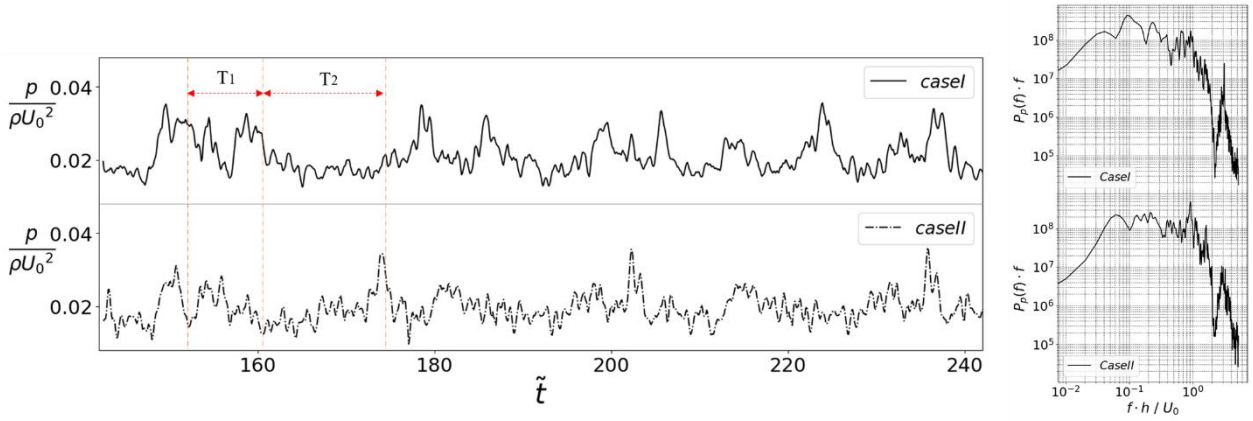

Figure 4.16 Temporal evolution and corresponding PSD value of the average pressure over the step.

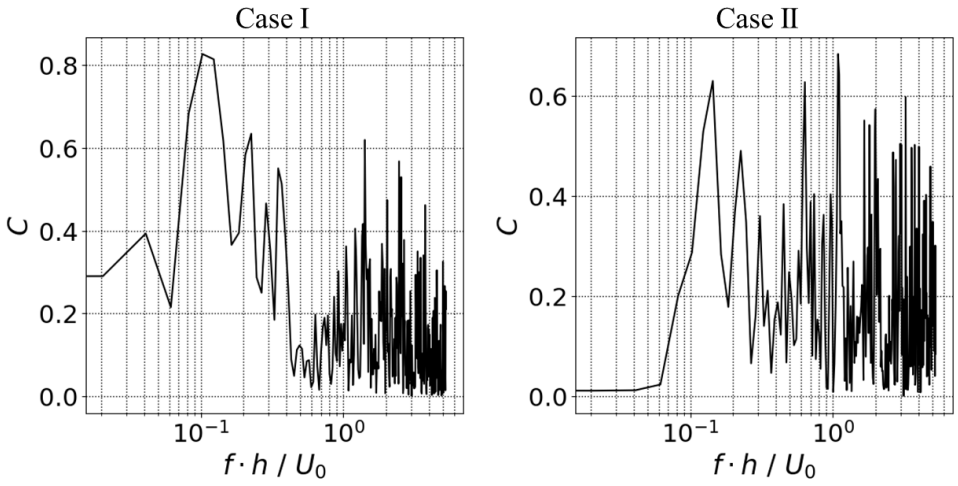

Figure 4.17 Spectral coherence between the average pressure in the cross-section area over the step and reversed flow.

To further investigate the nature of two low frequencies, the instantaneous results are provided for cases I and II in Figures 4.18, 4.19, and 4.20. For case I, two time periods related to the LF1 and LF2 are represented by T2 and T1, respectively, in Figures 4.15 and 16. The instantaneous results for one cycle of vortex shedding at reattachment is presented for case II in Figure 4.18, which consists of the pressure field shown in the left column and velocity field streamlines shown in the right column. It is noteworthy to mention that the fixed coordinate is adopted for calculations of the streamlines, and therefore transport of the coherent structures (such as those shown Figure 4.13) cannot be recognized within the velocity field. Nonetheless, considering that the vortical structures are associated with local pressure drop(Agarwal et al., 2023)**,** the local low pressure areas can be representative of the coherent structures and their transport mechanism(Dubief † and Delcayre ‡, 2000). Local low pressure elliptical regions apparent within the shear layer correspond to the spanwise structures. After separation, alternating positive and negative pressure fluctuations appear within the shear layer (above the separation bubble) corresponding to the turbulent structures resulted from the roll-up mechanism. These structures turn around the bubble and finally impinge on the wall, from which large wall-pressure fluctuations are generated in the reattached region. The primary local low pressure areas are connected to each other through quasi-streamwise low pressure zones, which is attributed to the QSV. The QSVs emerge between a pair of KH structures after development of spanwise waviness and instability in KH structures as they grow(Hayakawa and Hussain, 1989; Pierrehumbert and Widnall, 1982). As an example, one of these QSV structures is specified in the pressure field displayed in Figure 4.18 ($\tilde{t}_0 + 4\Delta\tilde{t}$). As observed, QSVs are inclined to the direction upwards from the bottom of one spanwise vorticity to the top of the next one, while they are surrounded with high pressure region in their periphery. QSVs are three dimensional structures and typically appear as counter-rotating pairs, as they are randomly distributed in the spanwise direction, some of them can be missed in the given plane (Figure 4.18). The reattachment region is characterized by a large pressure recovery, where the shear layer impinges to the bottom wall. The growth and transport of the spanwise vortical structure to the downstream of the reattachment point is traced by the white flash. We can notice that the displacement of the high pressure impingement location is associated with generation of a pressure wave along the channel upstream of the step (not shown here), which arrives to the step with a phase delay ($\tilde{t}_0 + 4\Delta\tilde{t}$). This phase delay was obtained by applying cross-correlation to the normalized values of the reversed flow and average pressure over

the step (Appendix A), showing a delay of $d\tilde{t} \approx 3.28$ for both cases. After the vortex is separated from the shear layer ($\tilde{t}_0 + 3\Delta\tilde{t}$), a new high pressure region emerges in the rear part of the shed vortex so that the shed vorticity is followed and preceded by high pressure regions. By moving the shed vorticity along the channel, its front high-pressure region is attenuated and becomes closer to the outlet pressure, while the rear high-pressure region becomes more intense. The reason for this behavior is the displacement of impingement point during the vortex shedding process, beyond which a new cycle of vortex shedding starts.

The velocity field results provide valuable information about the structure and dynamics of TSB and reverse flows during the shedding mechanism. TSB primarily forms from a group of clockwise recirculation zones, which are located in a region encompassing the backward flow and a lower region of the shear layer. The second group of TBS vortices are counterclockwise vortices, which are located near the corner behind the step and are usually combined to form a single vorticity. Upon the growth and transport of the shed vorticity behind the reattachment, the reverse flow is extended behind the adverse pressure gradient (APG) which moves downstream (Figure 4.18, black flash). Following the vortex shedding event ($\tilde{t}_0 + 4\Delta\tilde{t}$), the reattachment point abruptly re-establishes itself at its initial location, which coincides with a rapid reduction in the backward flow area (A_b). The cycle is associated with $St_h \approx 0.105$, which is close to LF2 for case II. Also, the convective velocity of the shed vortex is around $\frac{U_c}{U_0} \approx 0.316$. The variation in the backward flow (A_b in Figure 4.15) is linked to the vortex shedding at reattachment so that the initial stages before the vortex shed off ($\tilde{t}_0$ to $\tilde{t}_0 + 3\Delta\tilde{t}$) is associated with increase in A_b, while the last stage (vortex shed off at $\tilde{t}_0 + 4\Delta\tilde{t}$) is accompanied with a sudden decrease in A_b. The dynamics of TSB is affected by the coherent structures within the shear layer and vortex shedding at reattachment. For example, it is visible that upon growth of the backward flow the group of the clockwise vortices within the recirculation zone is enlarged, and new vortices are added. In addition, it is apparent that the growth and pairing of KH vortices within the initial part of the shear layer lead to an increase in the size of the clockwise vortex in this region while the size of the anticlockwise vortex diminishes in the corner behind the backward step ($\tilde{t}_0 + 3\Delta\tilde{t}$ _ $\tilde{t}_0 + 4\Delta\tilde{t}$).

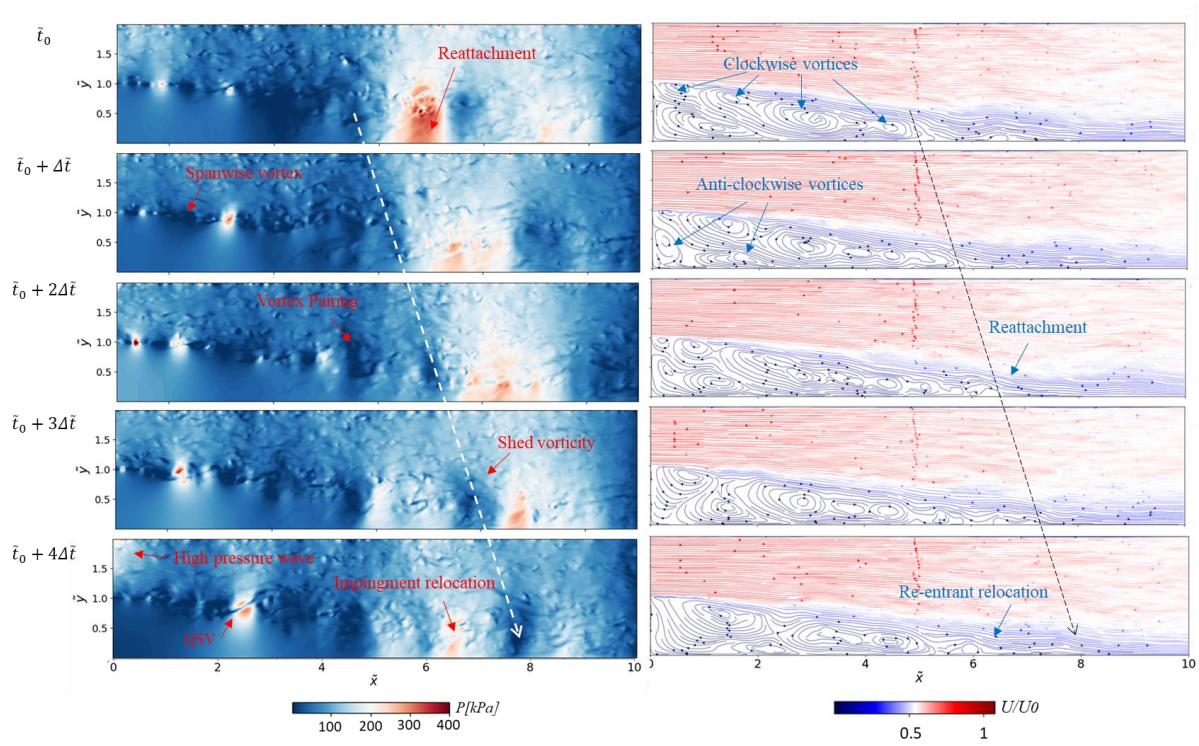

Figure 4.18 Instantaneous results for case II in the middle depth plane for the pressure field (left columns) and streamline of nondimensional velocity field (right column). Dashed flash shows the vortex shed off, $\boldsymbol{\Delta\tilde{t}}$ is expressed based on the nondimensionalized time and is equal to 2.375 (considering one cycle of shedding St_h = 0.105).

The instantaneous results for case I associated with two different frequencies are displayed in Figures 4.19 and 4.20 (related to T_1 and T_2 time periods). The low frequency mechanism in T1 period is similar to that provided for the single-phase flow (governed by vortex shedding at reattachment). Figure 4/19 (T1 period) starts with a high pressure over the step (Figure 4.16), and a small value of reverse flow area (Figure 4.15). It is noteworthy to mention that the reason for matching high pressure over the step with small value of the reverse flow area is the phase delay described in the previous section (which is also evident from comparison between Figures 4.15 and 4.16). Indeed, the downstream motion of reattachment point downstream prompts a high-pressure wave propagation along the channel, which arrives to the step ($\tilde{x} = 0$) with a phase delay of $\tilde{t} \approx 3.28$. Pressure drop within coherent structures of the shear layer triggers phase transition in these areas. The vapor packets are carried along the shear layer mainly by spanwise vortices and developed during pairing and growth of these vortices. Some portions of the

vapor packets are transported to the recirculation area, most of which collapse after the propagation of the pressure wave downstream of the step. The high-pressure generation near the wall at $\tilde{t}_0 + \Delta\tilde{t}$ and $\tilde{x} \approx 2.5$ is a footprint of such a collapse within the recirculation zone. The low-pressure zone associated with the spanwise vorticity reaches its maximum size behind the reattachment region. As the vortex growths and moves along the channel, it pushes the reattachment downstream up to $\tilde{x}$~8 at $\tilde{t}_0 + 3\Delta\tilde{t}$, where the reverse flow reaches its maximum value while still sustaining the vapor phase. After the vortex sheds off, the reattachment points return to its initial location ($\tilde{t}_0 + 4\Delta\tilde{t}$), where a cycle of shedding related to LF1 (T1) is complete. Following the shedding and relocation of the impingement point, the shed vorticity loses its ability to preserve the low-pressure core within it. The loss of the low-pressure core within the shed vorticity triggers a cascade of events, which includes vapor condensation, shock wave generation, and alterations in vorticity size and dynamics. While shedding frequency is almost the same as shown for case II ($St_h \approx 0.105$), the convective velocity and size of the shedding vortex seems to be notably increased ($\frac{U_c}{U_0} \approx 0.421$).

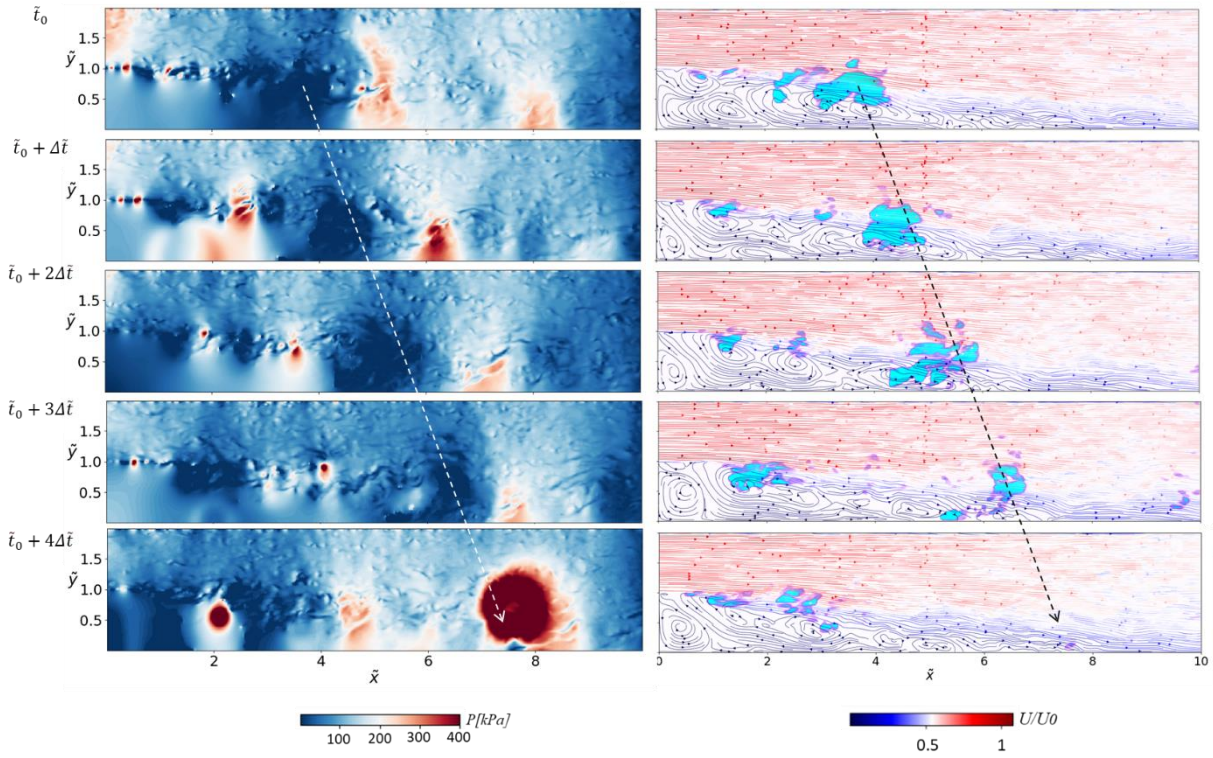

Figure 4.19 Instantaneous results for case I, T1, in the middle depth plane for the pressure field (left columns) and streamline of nondimensional velocity field (right column). Dashed flash shows the vortex that shed off, $\boldsymbol{\Delta\tilde{t}}$ is expressed based on the nondimensionalized time and is equal to 2.375 (considering one cycle of shedding St_h = 0.105).

Figure 4.20 presents instantaneous results for the time interval T2, which corresponds to LF1. In order to avoid redundancy, the time snapshot pertaining to T1-T2 interfaces and preceding times were omitted. The represented section of the cycle coincides with a decline in the reverse flow and reduced upstream pressure, as observed in Figures 4.15 and 4.16, respectively. In contrast to cycle T1, a significant amount of vapor flows into the recirculation area in this cycle, even reaching the vicinity of the bottom wall. The presence of vapor in the recirculation area can be attributed to the reduced pressure in this region, as well as over the step (as shown in Figure 4.16), which facilitates the accumulation of vapor phase without any collapse. However, only a small amount of vapor is able to traverse through the reattachment region. It is worth mentioning that the recirculation region remains relatively stable, especially during the initial three-time steps, and maintains a relatively low average pressure. As a result, the condensation of vapor packets within the recirculation region is insignificant during T2. A comparison

between Figures 4.19 and 4.20 reveals that, the shed vortices at reattachment are smaller during T2 and occur at higher frequencies ($St_h \approx 0.14$, $\frac{U_c}{U_0} \approx 0.42$) compared to T1. Additionally, the changes in the reattachment point and reverse flow during shedding in the T2 interval are minor. These observations suggest that the dynamics associated with LF1 is not influenced by vortex shedding at reattachment, but rather by the upcoming pressure wave and displacement of the reattachment point for case 1. It appears that the propagation of the upstream pressure wave over and within the separation bubble plays a critical role in the breathing mode and vapor transport. In contrast, during T1 (associated with LF2), the incoming pressure wave reinforces a favorable pressure gradient (FPG) over TSB, which results in the formation of a strong and large vorticity significantly displacing the reattachment point while maintaining low pressure within its core. In this scenario, vortex shedding has a substantial impact on the size and dynamics of TSB. Moreover, the majority of vapor phase remains confined within the shear layer and is transported within the core of the shed vorticity to distances well beyond the average reattachment point. In contrast, during T2 period (LF1), a notable pressure drop behind the step facilitates the accumulation of vapor phase within the recirculation region. Under these conditions, the shed vortices lack the strength and size to significantly displace the impingement point. Consequently, most of the vapor carried by these vortices immediately collapse upon exposure to the high-pressure impingement region, while vapor remains largely unaffected in the recirculation zone. These findings highlight the significant impact of the coupling and timing among the incoming pressure wave, phase transition, and vortex shedding on TSB dynamics.

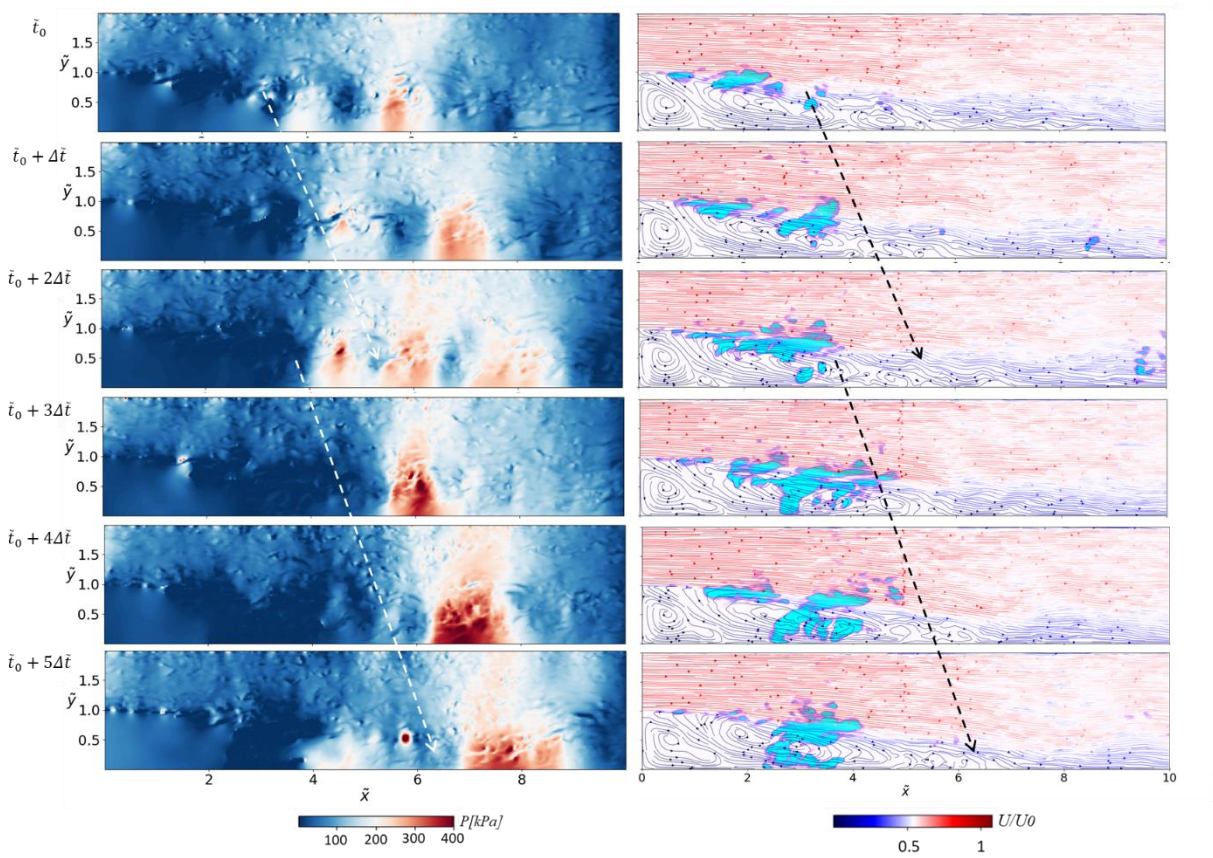

Figure 4.20 Instantaneous results for case I, T2, in the middle depth plane for the pressure field (left columns) and streamline of nondimensional velocity field (right column). Dashed flash shows the vortex shed off, $\boldsymbol{\Delta\tilde{t}}$ is expressed based on the nondimensionalized time and is equal to 2.375 (considering one cycle of shedding St_h = 0.105).

The spatio-temporal evolution of the pressure field is presented in Figure 4.21. The pressure field was averaged across the entire spanwise direction and in the depth wise direction from the bottom wall up to 0.1h above the step. The regions corresponding to T1 and T2 are indicated using white dashed lines and zoom-in counterparts are provided in the right-hand column. Several notable features can be identified from these spatiotemporal maps. Firstly, pressure waves propagating downstream are visible as red inclined stripes (the slope indicates the wave propagation speed), which originate from the step at $\tilde{x}$=0 and extend to the reattachment at $\tilde{x}$≈6. These pressure waves create necessary conditions for significant reattachment point displacement. Large reattachment point displacements are associated with strong penetration of the low-pressure zone into the channel, which is observed as black stripes that persist until the channel end. These

black stripes are generally followed by large pressure waves, which demonstrates the impact of significant displacement of reattachment on pressure wave propagation along the channel. As noted in the previous section, these structures are associated with the TSB's LF2 breathing mode.

Another intriguing observation is the presence of randomly distributed yellow spikes throughout the spatiotemporal map, which are predominantly concentrated within the latter part of the shear layer and the reattachment zone. These spikes exhibit shock wave propagation with a very steep slope, implying their high speed. Interestingly, shock waves generated by bubble collapse within the reattachment point penetrate deeper into the channel (longer spike lengths) than those occurring upstream of the reattachment point, which suggests that they are more energetic (potentially due to higher pressure recovery or a larger fraction of collapsing bubbles).

Another key observation is the presence of dark regions with large areas within the first half of the channel, particularly more pronounced for case I. These regions are associated with the LF1 mode of breathing. The spatiotemporal map reveals that they are linked to high-frequency, small-width shedding, which is represented by a jagged interface between the high and low-pressure regions around the reattachment point.

A closer examination of the zoom-in sections corresponding to the T1($\tilde{t} = 152\sim162$) and T2($\tilde{t} = 162\sim175.75$) periods provides further insights. For case I, it can be observed that T1 is associated with a thick dark stripe penetrating to the end of the channel, which is followed by a large pressure wave stripe and significant shock wave generation at the end portion. For the T2 period, high-frequency shedding with small distance between peaks and valleys at the interface is evident at the reattachment region, where the low-pressure zone is only able to slightly penetrate within the high-pressure zone.

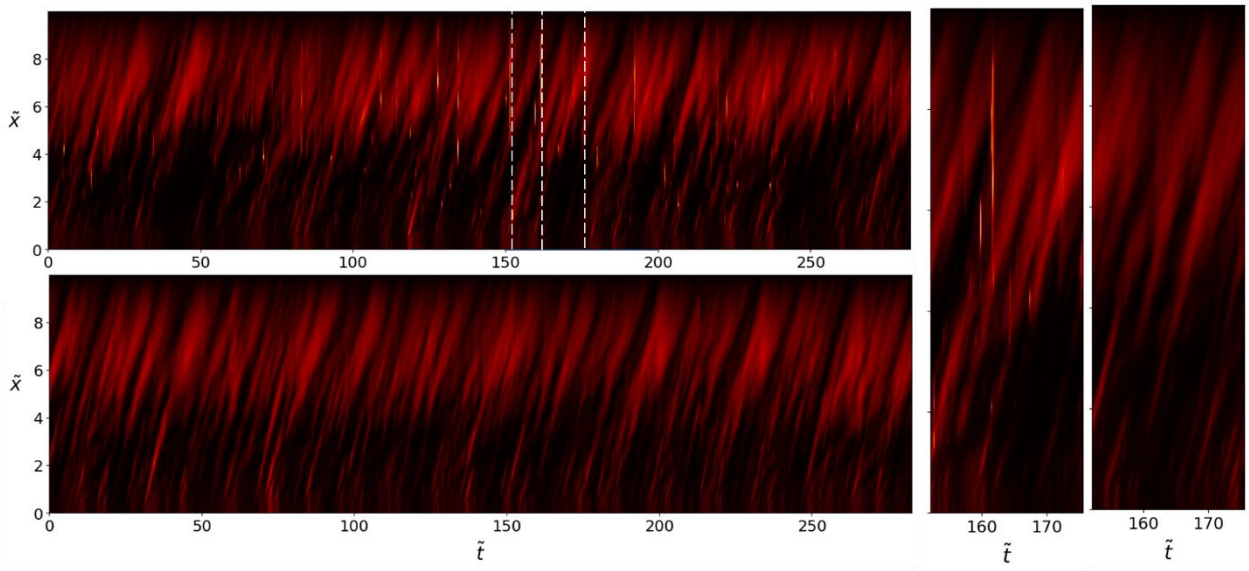

Figure 4.21 Spatio-temporal map of the pressure field for case I (top) and case II (bottom).

The results obtained from the spatio-temporal correlation ($R_{p\prime}$, Appendix A) will help in determining the frequency which is in harmony with convective velocity within the shear layer. Thus, the spatio-temporal correlation of the pressure field with reference point of $\tilde{x} = 3.5$ (point 1 in Figure 4.7(a)) are represented for both cases in Figure 4.22. The slope implies that for both cases the convective velocity within the shear layer is close to 0.51 of $U0$. As expected, convection starts with a large slope, which gradually decreases while moving towards the reattachment point. Also, the time interval of a coherent structure passing from a fixed horizontal point, $\delta\tilde{t}$, is estimated based on the maximum gradient of the correlation function with respect to the dimensionless time at the reference point. The inverse of $\delta\tilde{t}$ offers an approximation of St_h related to the transport of coherent structures within the shear layer and at the reference point, which are around 0.36 and 0.4 for cases I and II, respectively. It should be notice that these frequencies are in good agreement with dominant medium frequencies in Figure 4.14, which supports and conveys that the medium frequencies in spectral analysis are related to coherent structure transport within the shear layer. Moreover, even though both cases have more or less the same convective velocity within the shear layer, the coherent structures for case I should be larger than for case II due to larger $\delta\tilde{t}$, which is in agreement with two point auto-correlation results in Figure 4.13. Also, from the correlation plots it is evident that the structures for case II should have more coherence throughout their travel through the channel, while the

structures have maximum correlation only in a small vicinity from the reference point for case I, which implies that they should experience more variation as they travel through the channel. This is in line with the assumption that vapor generation within the shear layer reduces the coupling between Reynolds normal stress components(Belahadji et al., 1995; Iyer and Ceccio, 2002), which leads to variations in the shape of coherent structures after phase transition.

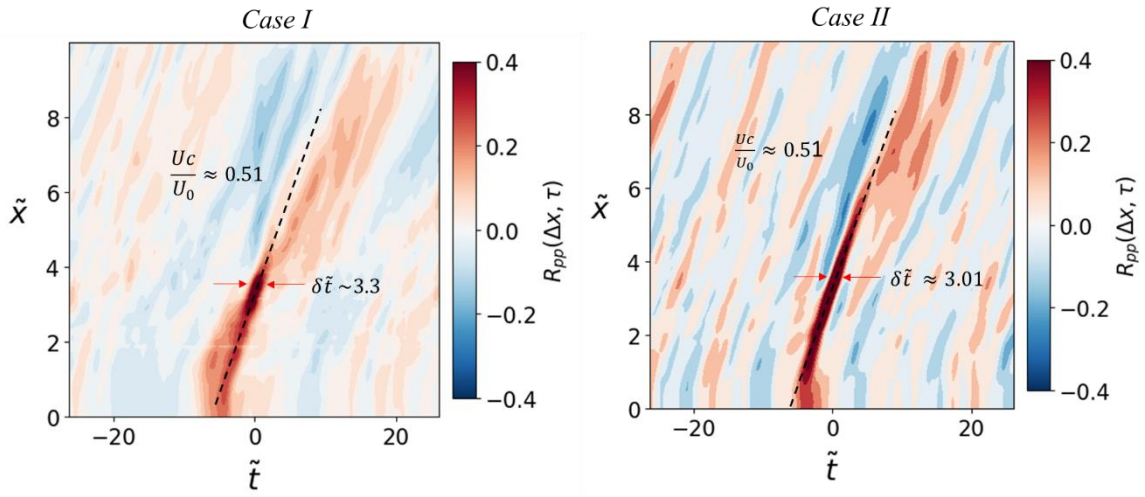

Figure 4.22 Spatio-temporal correlation of the pressure field.

4.2.5 Modal Analysis

In this section, a SPOD modal analysis proposed by Towne, Schmidt & Colonius(Towne et al., 2018) is covered to identify coherent structures associated with low and medium frequencies and to investigate spatio-temporal characteristics of energetic motions for cases I and II. SPOD is a frequency domain variant of POD specifically designed for statistically stationary flows. Details regarding SPOD calculations are provided in Appendix A.

Figure 4.23 represents the first three SPOD modes for cases I and II. The energy content of the first mode in the low frequency region ($St_h < 0.3$) encompasses a significant portion of the total energy, which emphasizes on the coherency of turbulent structures in these frequencies (low rank behavior)(Brès et al., 2018). In the previous section, two dominant low frequencies (LF1 and LF2, related to the breathing mechanism of the shear layer) and one medium frequency (MF, related to the instabilities of within the shear

layer) are covered using the spectral analysis of pressure fluctuations within the TSB. In Figure 4.23, the frequencies close to these dominant frequencies are specified for both cases. In the previous section, it is observed that LF1 and LF2 are slightly larger for case II than those for case I. In this section, SPODs of identical frequencies are explored for both cases. Since the differences between dominant frequencies of two cases are very small and a significantly large number of snapshots are required to be able to consider those differences in SPOD analysis. These dominant frequencies associated with the dynamics of TSB also manifest a high energy magnitude in the first SPOD mode, showing their significance for the dynamics of the whole flow in the studied domain. Moreover, for large frequencies modes ($St_h > 1$) case I contains on average higher energy compared to case II, which can be attributed to the high frequency fluctuations generated by bubble collapses for case I, similar to the results provided in the previous section (Figures 4.14).

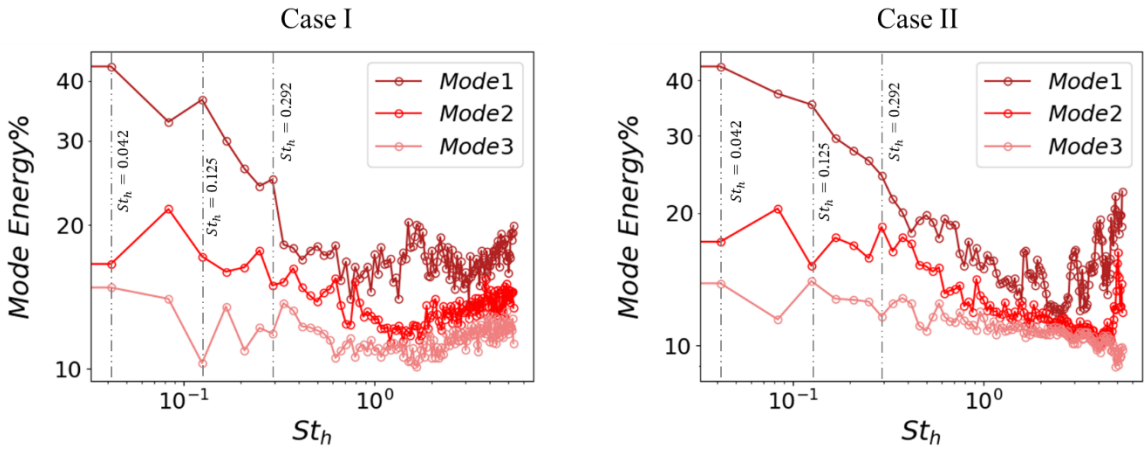

Figure 4.23 Energy spectra of the first three SPOD modes for cases I and II.

Figure 4.24 displays iso-surfaces related to the first SPOD mode associated with St_h = 0.042 for the streamwise velocity components and cases I and II. From this figure, it is apparent that this frequency is associated with large coherent structures encompassing the reverse flow and a significant portion of the shear layer close to the reattachment. The variations in these structures over one period are provided in the Supplementary Movies I and II for cases I and II, respectively. It can be seen that this mode is linked to the formation of the reverse flow and appearance and movement of large streamwise structures related to the reattachment displacement. This result confirms that LF1 in the breathing mechanism of TSB is associated with reverse flow dynamics and shedding of

an extremely large structure within the shear layer (displacement of reattachment point), which was also reported, in previous studies(Dow et al., 2022; Kiya and Sasaki, 1983). Moreover, a comparison between cases I and II suggests that the structures corresponding to $St_h = 0.042$ are more energetic, larger, and more concentrated within the shear layer and reversed flow regions for case I compared to those for case II. This result agrees with the results from the previous section where the pressure and velocity fluctuations corresponding to LF1 are more dominant and energetic for case I compared to those for case II, which implies that cavitation and phase transition reinforce low frequency motions with alterations of the dynamics of reverse flow. It is also shown that these motions are linked to the upstream perturbations and pressure wave (which is observed to be in coherence with reattachment displacement) so that it can be concluded that cavitation enhances the coupling between the upstream pressure wave and TSB dynamics (also shown in Figure 4.17).

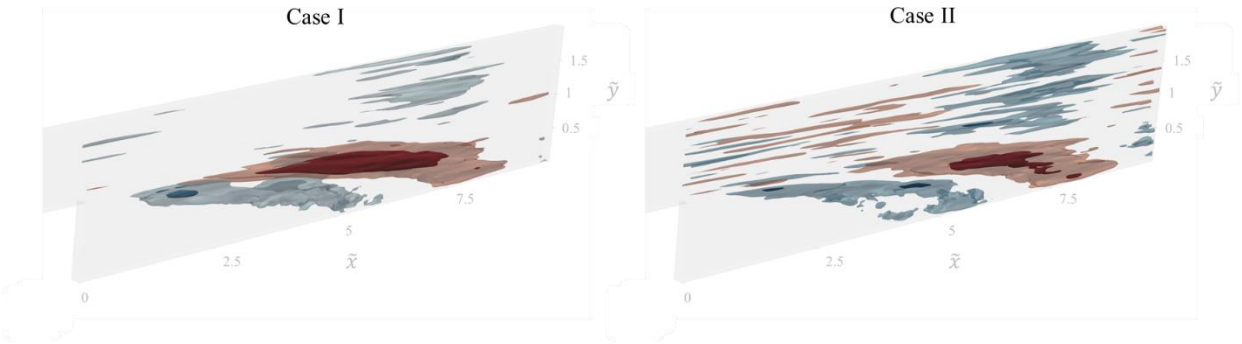

Figure 4.24 Iso-surfaces of real part of SPOD modes of the streamwise velocity associated with $\boldsymbol{St_h = 0.042}$ for Cases I and II, shown in an arbitrary phase. Red color: transparent ($\boldsymbol{0.0006 \leq \phi_{U_x} \leq 0.0025}$), opaque ($\boldsymbol{0.0013 \leq \phi_{U_x} \leq 0.0025}$). Blue color: transparent ($\boldsymbol{-0.0025 \leq \phi_{U_x} \leq -0.0006}$), opaque ($\boldsymbol{-0.0025 \leq \phi_{U_x} \leq -0.0013}$).

Figure 4.25 provides the cross-sectional view of SPOD mode of Ux in $x-y$ and $y-z$ planes, where the streamlines starting at ($\tilde{x} = 0.0, \tilde{y} = 1.0$, detachment point) and ($\tilde{x} = 0.0, \tilde{y} = 1.15$) are superimposed. For both cases, alternating positive-negative value SPOD modes appear at $y-z$ cross-sections in the spanwise direction and in the vicinity of the dividing streamline ($\psi = 0$) for $\tilde{x} = 1.8 \sim 3.4$, which is likely to be representative of counter-rotating streamwise vortices in these areas. Also, downstream of the

reattachment ($\tilde{x} \approx 6$), similar but weaker structures are visible (more evident for case II) above the second streamline.

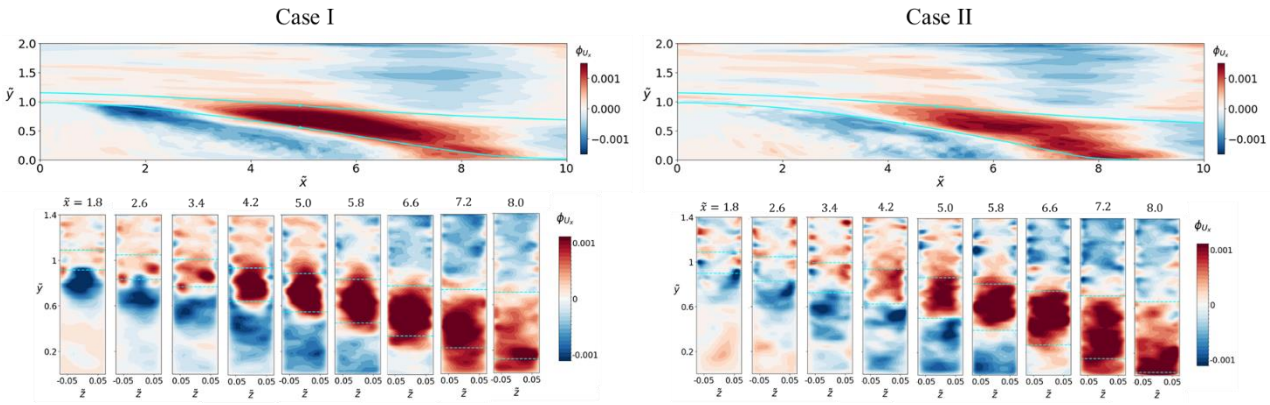

Figure 4.25 Cross-sectional view of real part of SPOD modes of streamwise velocity associated with $\boldsymbol{St_h = 0.042}$ for Cases I and II, shown in an arbitrary phase. Blue lines represent streamlines starting at ($\tilde{\boldsymbol{x}} = \boldsymbol{0.0}, \tilde{\boldsymbol{y}} = \boldsymbol{1.0}$) and ($\tilde{\boldsymbol{x}} = \boldsymbol{0.0}, \tilde{\boldsymbol{y}} = \boldsymbol{1.15}$).

Previous studies reported that the counter-rotating streamwise coherent structures developing over concave pathways within the shear layer can be related to the Görtler vortices and instability, which is coupled with low frequency dynamics of the separation bubble(Hickel et al., 2021). Görtler instability occurs due to the opposite directions in the centrifugal force generated by the curvature streamline of separated flow and the wall-normal velocity gradient(Floryan, 1991). Generally, Görtler number is used as a threshold criterion for Görtler instability, which is defined as (Floryan, 1991):

$$G_t = \frac{U_e \theta}{\nu} \sqrt{\frac{\theta}{R_c}},$$

where U_e is the free-stream velocity at the edge of the boundary layer, θ is the local momentum thickness, and R_c is the radius of the curvature of the related streamline. According to the study by Wu et al.(W. Wu et al., 2020) , the total viscosity ($\nu_{tot} = \nu + \nu_\tau$) was used in calculations of the Görtler number to account for turbulent effects. Previous studies suggested that Görtler instability appears when Görtler number exceeds 0.3(Floryan, 1991). We examined the possibility of Görtler instability by calculating the Görtler instability along the dividing streamline ($\psi = 0$) for the spanwise averaged mean flow for both cases (Figure 4.26). Even though none of the cases meet the required threshold for having Görtler instability, the variations in Görtler number along the

dividing streamline (Figure 4.26) provide some useful insights. These insights include having the highest chance of Görtler instability downstream of the reattachment, and a decline in the Görtler number in presence of cavitation, which is mainly caused by the decrease in the dividing streamline curvature in this region for the case of cavitation.

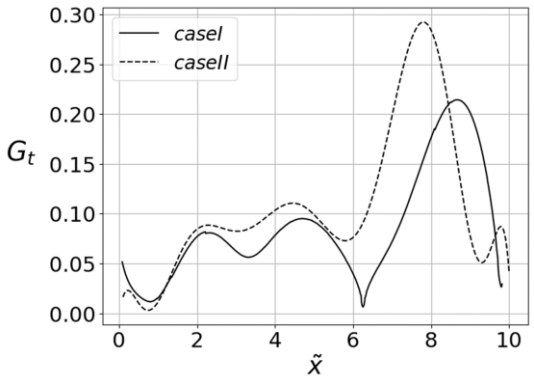

Figure 4.26 Variations in Görtler number along the dividing streamline.

The first cross-sectional view of the first SPOD mode corresponding to frequency of $St_h = 0.125$ is presented for both cases in Figure 4.27. The animation of variations in three-dimensional structures over time are provided in Supplementary Movies III and IV for cases I and II, respectively, which depicts the evolution and transport of these structures within the shear layer. This frequency is close to the LF2 frequency for both cases, which is linked to vortex shedding in the reattachment. This frequency is coupled with large alternating coherent structures initiating and developing within the shear layer and hitting the wall in reattachment region. Most of the structures related to this mode are clustered around the reattachment point, with small variations in the spanwise direction. The coherent structures are more energetic upstream of the reattachment and less energetic downstream compared for case I compared to those for case II (as an example, one can consider the difference between coherent structures of two cases around $\tilde{x} = 4$ and $\tilde{x} = 8$). Thus, it can be concluded that the mode is more in harmony with coherent structures upstream of the reattachment for case I and downstream of the reattachment for case II, which suggests that dominant fluctuations (in particular reattachment vortex shedding frequency) have smaller frequencies for case I compared to their counterparts for case II, which agrees with previous section results as well as with the results of other studies(Bhatt et al., 2021a).

Another observation is similar but much weaker structures above the shear layer moving with a phase angle with respect to the energetic ones, which are evident in $x-y$ plane. In addition, low energy alternating structures above TSB and close to forth/back walls are related to the turbulent structures generated due to the interaction of the flow with the front and back walls.

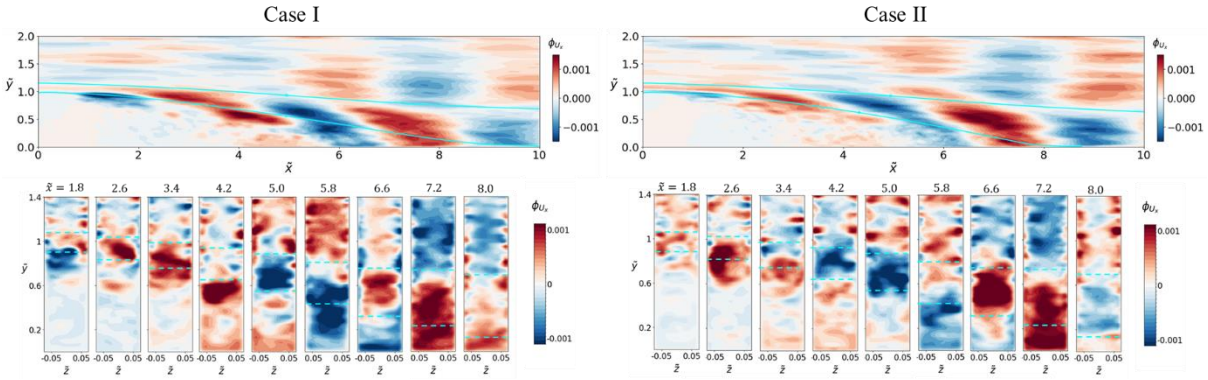

Figure 4.27 Cross-sectional view of the real part of SPOD modes of streamwise velocity associated with $\boldsymbol{St_h = 0.125}$ for Cases I and II, shown in an arbitrary phase. Blue lines represent streamlines starting at ($\tilde{\boldsymbol{x}} = \boldsymbol{0.0}, \tilde{\boldsymbol{y}} = \boldsymbol{1.0}$) and ($\tilde{\boldsymbol{x}} = \boldsymbol{0.0}, \tilde{\boldsymbol{y}} = \boldsymbol{1.15}$).

Figure 4.28 shows the first SPOD mode corresponding to $St_h = 0.292$, the frequency related to the vortex shedding within the shear layer. The alternating positive negative value coherent structures are visible within the shear layer with a shorter length compared to the previous modes. The structures with opposite signs are spread along the shear layer next to each other. The motion of these three-dimensional structures is presented in Supplementary Movies V and VI for cases I and II, respectively. The energetic structures within the shear layer are near uniform across the spanwise direction. When getting closer to the reattachment region, the structures become less energetic and more distorted. Similar to previous modes, weak turbulent structures can be observed above the shear layer.

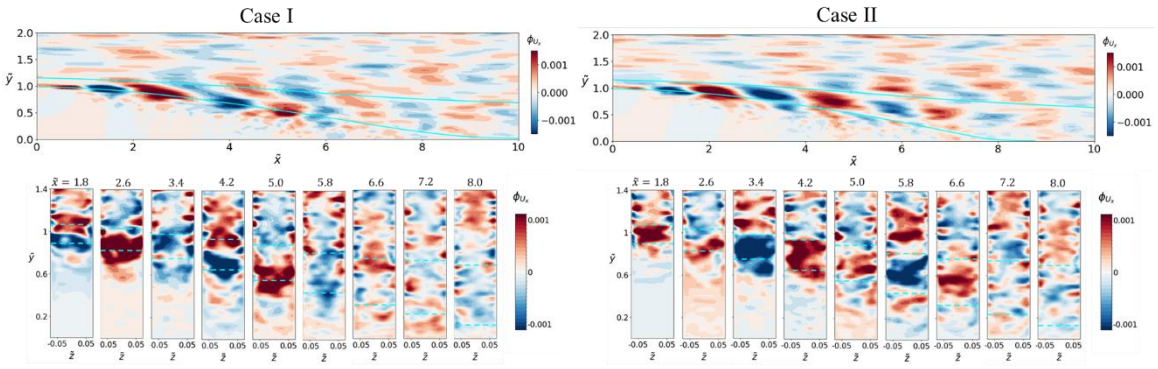

Figure 4.28 Cross-sectional view of the real part of SPOD modes of streamwise velocity associated with $\boldsymbol{St_h = 0.292}$ for Cases I and II, shown in an arbitrary phase. Blue lines represent streamlines starting at $(\tilde{\boldsymbol{x}} = \boldsymbol{0.0}, \tilde{\boldsymbol{y}} = \boldsymbol{1.0})$ and $(\tilde{\boldsymbol{x}} = \boldsymbol{0.0}, \tilde{\boldsymbol{y}} = \boldsymbol{1.15})$.

4.3 Conclusion

The effect of cavitation on mean characteristics and dynamics of TSB within a shallow microscale BFS configuration was investigated in this study. For this purpose, a numerical approach capable of capturing compressibility as well as thermodynamic non equilibrium conditions were implemented. The numerical results were validated against our experimental results and the results of the literature(Winklhofer et al., 2001). Two cases (with and without phase transition), were considered for the Reynolds number (Re_h) of 7440, and LES was used to take turbulence effects into account.

The results showed that cavitation results in a narrower shear layer and postpones the reattachment. Accumulation of the vapor phase in the shear layer significantly alters the size and shape of the coherent structures in this region. In the presence of cavitation, the spanwise vortical structures are stretched along the shear layer and become longer and thinner compared to the case in the absence of cavitation.

The analysis of the mean pressure and RMS of pressure fluctuations reveals that cavitation leads to a decline in both parameters within the shear layer (particularly the second part of the shear layer which is the most vaporous region). In contrast, both parameters increase within the reattachment region. Condensation and bubble collapse in the reattachment region provide main contributions to the increase in the mean pressure

and pressure fluctuation RMS Moreover, vapor generation triggers the conversion of Reynolds shear stress to TKE (decoupling between Reynolds stress components), while condensation and collapse lead to an increase in Reynold normal stresses (particularly streamwise Reynolds normal stress in our case).

Regarding TSB dynamics, cavitation results in a decrease in dominant frequencies. The variations in the area of reverse flow have two dominant frequencies linked to the displacement at the reattachment point for both cases (with and without cavitation). The smaller frequency, LF1, is associated with the slow growth of TSB (which is fed by the upstream turbulent boundary layer), while small vortices shed off from the end of TSB with a higher frequency. The larger frequency, LF2, is related to the cases where shed vortices are large enough so that their growth and separation significantly alter the size of TSB and relocates the impingement. In the presence of cavitation, the frequency associated with the smallest dominant frequency (LF1) is more energetic along the shear layer and reattachment, which suggests that cavitation reinforces the TSB breathing mechanism associated with LF1. Moreover, in the vicinity of the reattachment, high frequencies are more energetic for the case of cavitation, which suggests that bubble collapses in those areas lead to high frequency fluctuations.

Two different cavitation trends coupled with LF1 and LF2 can be recognized. For the case of LF1, vapor packets primarily concentrate within the second half of the shear layer and behind the impingement, while some of them are transported to the low-pressure regions within the recirculation. For this case, the pressure drop within the shed vortices is not sufficient to sustain the vapor phase across the reattachment. On the other hand, in the case of LF2, shed vortices have enough strength to sustain their low-pressure core for long distances downstream of the step. For this case, the pressure within the recirculation region is large and vapor pockets collapse upon their entry to recirculation. Therefore, they are carried deeper into the channel, and their collapses correspond to stronger pressure waves (mostly shockwaves) for LF2 compared to those for LF1.

Finally, results from the modal analysis show that for both cases large coherent structures fluctuating with LF1 frequency encompass a significant portion of the shear layer. Furthermore, the coherent structures are larger and more energetic in the presence of cavitation, which indicates that LF1 motions are more significant for this case. In addition, LF2 and MF frequencies are linked to vortex shedding within the reattachment and shear layer, respectively.

5 EFFECT OF RIBLET-MOUNTED SURFACES AND BLOCKAGE RATIO ON CAVITATING AND NON-CAVITATING SEPARATING FLOW

5.1 Introduction

This study presents a comprehensive computational investigation into the coupled effects of riblet-equipped surfaces, quantified by Blockage Ratio (BR), on turbulent flow characteristics and cavitation phenomena in a channel with a backward-facing step. Our methodology employed a customized three-dimensional Low Mach number fully compressible cavitation flow solver, as detailed in Chapter 3, which leverages a second-order, four-stage low-storage Runge-Kutta time integration technique with an adaptive Courant-Friedrichs-Lewey (CFL) criterion for temporal advancement. The flow physics were modeled using LES, specifically employing the Favre-filtered conservative equations and a mixed Subgrid-Scale (SGS) model. Our analysis of the turbulent flow, including Turbulence Kinetic Energy (TKE) budgets, Reynolds stress anisotropy, autocorrelation, spectral analysis, and Dynamic Mode Decomposition (DMD), reveals that riblets fundamentally alter the flow field. Increasing BR leads to a shift in TKE transport mechanisms from production/dissipation to enhanced turbulent diffusion and convection, particularly in the shear layer. Reynolds stress anisotropy is significantly reduced near the wall, and its distribution shifts, reflecting modified turbulent mixing. Coherent structures become larger and slower, evidenced by expanded temporal scales in spectral analysis and the formation of dominant low-frequency vortices near the ribs and crests in DMD modes. These altered flow characteristics have a profound impact on cavitation. Even at low BR, intermittent cavitation packets form within vortex cores above the ribs. With increasing BR, cavitation packets become notably larger and more intense, directly correlating with the increased strength and size of the underlying coherent structures. The recirculation zone and corner vorticity are entirely vapor-filled, and a large, cylindrically shaped vapor packet sheds from the separation bubble, whose size and intensity scale directly with BR. The channel ultimately enters a supercavitation regime in Region II, with varying void fraction distributions dependent on BR. This work

underscores the critical role of riblet-induced turbulent flow modifications, specifically changes in Reynolds stresses and coherent structures, in governing cavitation inception and evolution in complex geometries.

5.2 Test Cases and Numerical Setup

Figure 5.1 illustrates the computational domain, which comprises two main sections: a ribbed square duct (Region I) and a downstream expansion area (Region II). Region I has equal side lengths, Ly=Lz=H (where H represents the step height), and extends Lx=15H in the streamwise direction. This region includes ten rib periods (P), each measuring P=0.8H. The rectangular bars within this section have a height of H and a width of W. For our analysis, particularly when comparing with 2D plane-channel flow results, it's helpful to define the half-side length (δ=D/2). Our comparative study involved numerical modeling conducted using four different blockage ratios (Br=H/Ly): 0, 0.05, 0.1, and 0.2. A unique approach is necessary for inlet turbulent boundary conditions ecause simulating the natural development of turbulence over a very large domain would be inefficient in terms of computational resources and time.

Unlike simulations of time-evolving turbulence, Direct Numerical Simulations (DNS) or Large Eddy Simulations (LES) of flows that are spatially inhomogeneous need turbulent conditions at their inflow boundaries. We use a synthetic turbulence generation method based on a digital filter technique(Klein et al., 2003) generates the correct turbulent inflow. This method accurately replicating first- and second-order statistical moments and spectra. Crucially, it does so without adding low-frequency content that could alter the downstream low-frequency dynamics. The statistical parameters are estimated from a separate set of simulation on a separate domain under statistical stationary condition. For this purpose, we consider a domain with a periodic channel and dimensions of $10H \times H \times H$, and grid resolution of $320 \times 32 \times 32$. The simulation begins with a uniform zero-velocity initial state and continues for 50 flow-through periods. To remove any potential effects from the initial conditions or the outlet boundary, statistical calculations exclude the first flow-through time and the region downstream near the outlet. Then Reynolds stresses, turbulent length scale components, and mean velocity field of this simulation was used for synthetic

turbulence generation in the main domain inlet. Identical inlets streamwise mean velocity of $36\,m/s$ is utilized as the reference velocity (U_{ref}) for all cases, resulting in the Reynolds number of 7200. Wave transmissive condition was applied to the outlet and no-slip to the sidewalls. For timesteps, an automatic adjustable technique based on Courant and acoustic Courant numbers was utilized so that these numbers did not exceed 0.5 and 50, respectively, with maximum time steps limitation of 1e-7 s. The write time of 0.5

for the solution was utilized to capture a wide range of frequencies while avoiding storage problems. Grid generation was accomplished using block-based local refinement, close to the walls and TSB regions (Figure 5.1 (b)). Grid resolution was adjusted in such a way that the value of dimensionless wall distance ($y^+ = yu_\tau/\nu$ where u_τ is the friction velocity) close to the walls did not exceed 1 which enabled appropriate resolving of the wall shear stress.

The results for grid convergence study are presented in Figure 5.1 (c) which includes the mean streamwise velocity profile in the absence of cavitation along the channel in case of BR = 0.05. Comparisons between coarse, fine, and finer grids, with $\approx 5 \times 10^6$; 12×10^6; and 18×10^6 mesh numbers respectively, show minor differences between fine and finer grids implying a grid convergence at fine grid which was accordingly considered for this study.

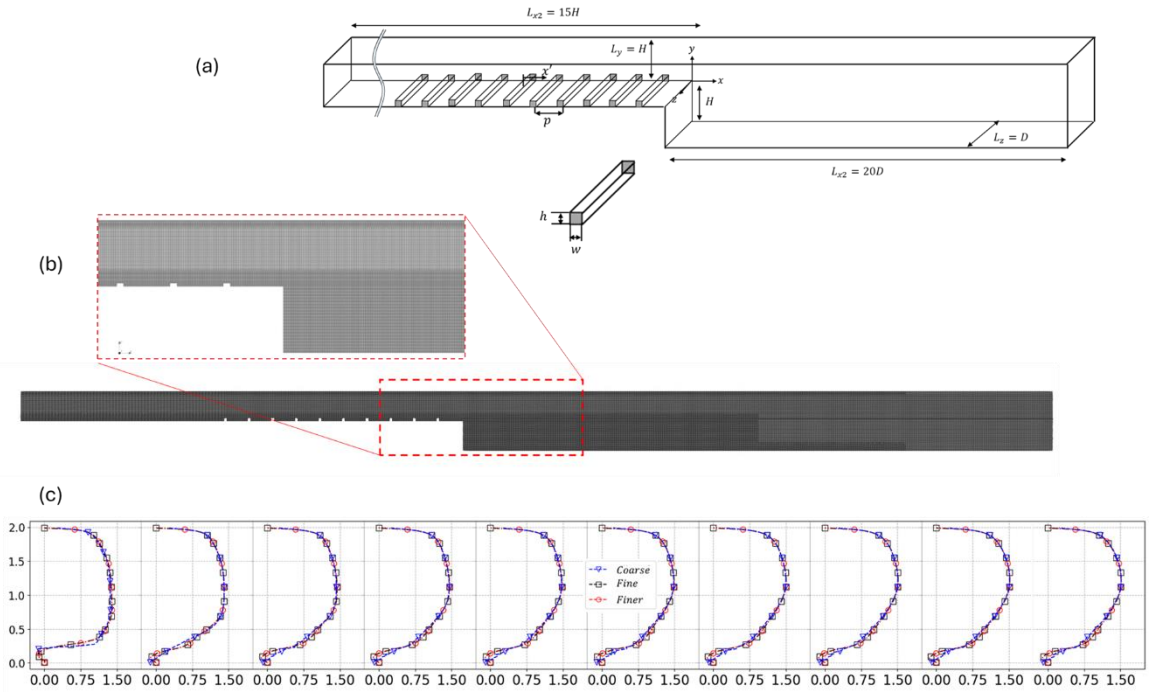

Figure 5.1 (a) The diagram illustrates a BFS equipped with transverse ribs and its associated coordinate system. The origin of this absolute coordinate system [x,y,z] can be found at the midpoint of the inlet's x–y plane. Ten rib periods are simulated. The relative streamwise coordinate (x′) is defined to facilitate the analysis of each rib period, with its origin positioned at the windward face of each rib. (b) Grid configuration inside the domain. (c) Streamlines and contours of the mean streamwise velocity along with the cross-sectional mean streamwise velocity and pressure fields at different streamwise locations for different numbers of grids.

5.3 Results and Discussions

5.3.1 Statistical Characterisation

In alignment with previous research, particularly the Direct Numerical Simulation (DNS) study of turbulent flow through a ribbed square duct(Mahmoodi-Jezeh and Wang, 2020), we focused on the region between the 5th and 6th riblets to analyze its statistical characteristics. The statistically stationary condition is generally satisfied for separating-reattaching flows with vortex shedding, provided time-averaged quantities (mean velocity, pressure, turbulence statistics) remain constant over sufficiently long-time

intervals, despite instantaneous unsteadiness. Vortex shedding introduces periodic fluctuations, but the system's long-term statistical properties stabilize with appropriate averaging(Li et al., 2024; Shi et al., 2010; B. Wu et al., 2020). Statistical characterization was performed using 3000 time steps. Convergence of the results was confirmed through a comparison with data obtained from 4000 time steps. Figure 5.2 presents the mean streamwise velocity field superimposed with streamlines for this region, specifically from the bottom wall up to a region bound to 0.3δ (δ=0.5H) above the rib crest in the mid-plane (z/ δ = 1), for Blockage Ratios (BR =0.05, 0.1, 0.2, corresponding to BFS II, III, and IV. The observed streamline patterns closely resemble those reported in the aforementioned DNS study(Mahmoodi-Jezeh and Wang, 2020), confirming that our implemented LES method possesses sufficient resolution and accuracy to replicate DNS results. A prominent feature is a large recirculation zone (A) located between the leeward face of the upstream rib and the windward face of the downstream rib. This zone forms due to initial flow separation caused by the adverse pressure gradient (APG) downstream of the expansion. Additionally, two smaller corner vortices are evident: one near the upstream rib's leeward side (B) and another close to the downstream rib's windward side (C).

For BFS II and III, the flow pattern exhibits similarities to k-type roughness elements observed on riblet surfaces. In contrast, BFS IV displays a streamline pattern akin to d-type roughness elements found on flow over planar surfaces. In BFS II and III, the flow reattaches to the bottom surface (D), followed by the development of a new boundary layer (E). The corner vortices grow in size with increasing APG strength, leading to a reduction in the distance between reattachment point D and new boundary layer development E as the blockage ratio increases. For BFS IV, this distance is significantly reduced, resulting in the merger of recirculation zone A and corner vortex C. This forms a single, large circulation region where the flow bypasses sequential ribs without reattaching to the surface. These distinct flow patterns significantly influence friction and form drag forces, as well as the turbulent structures near the bottom surface, which, in turn, remarkably alter the characteristics and dynamics of the shear layer downstream of the step. These effects will be further discussed in subsequent sections.

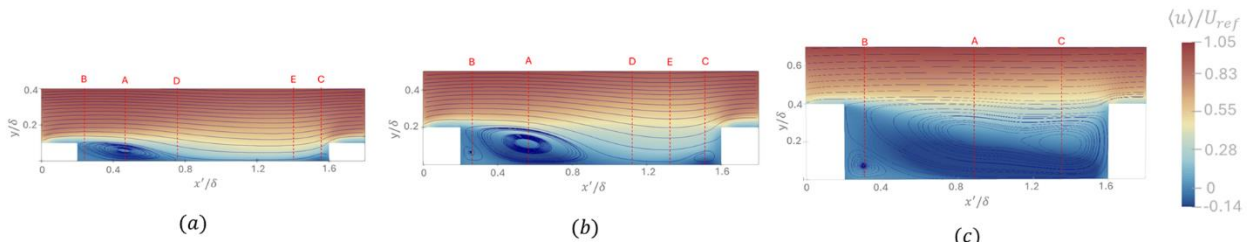

Figure 5.2 Mean streamline velocity fields superimposed with streamlines for (a) BFSII, (b) BFS III, and (c) BFS IV.

To investigate potential differences in flow patterns between sequential ribs, streamwise velocity profiles along the local distance x′ (where x′ is the distance from the windward side of the upstream rib) are presented in Figure 5.3. Beyond the initial two sequential ribs, the velocity distribution between consecutive ribs shows remarkable similarity, with the largest observed difference being less than 5% across all cases. This consistency confirms that a detailed investigation of the statistical characteristics of a single sequential rib region provides an acceptable approximation for other riblets

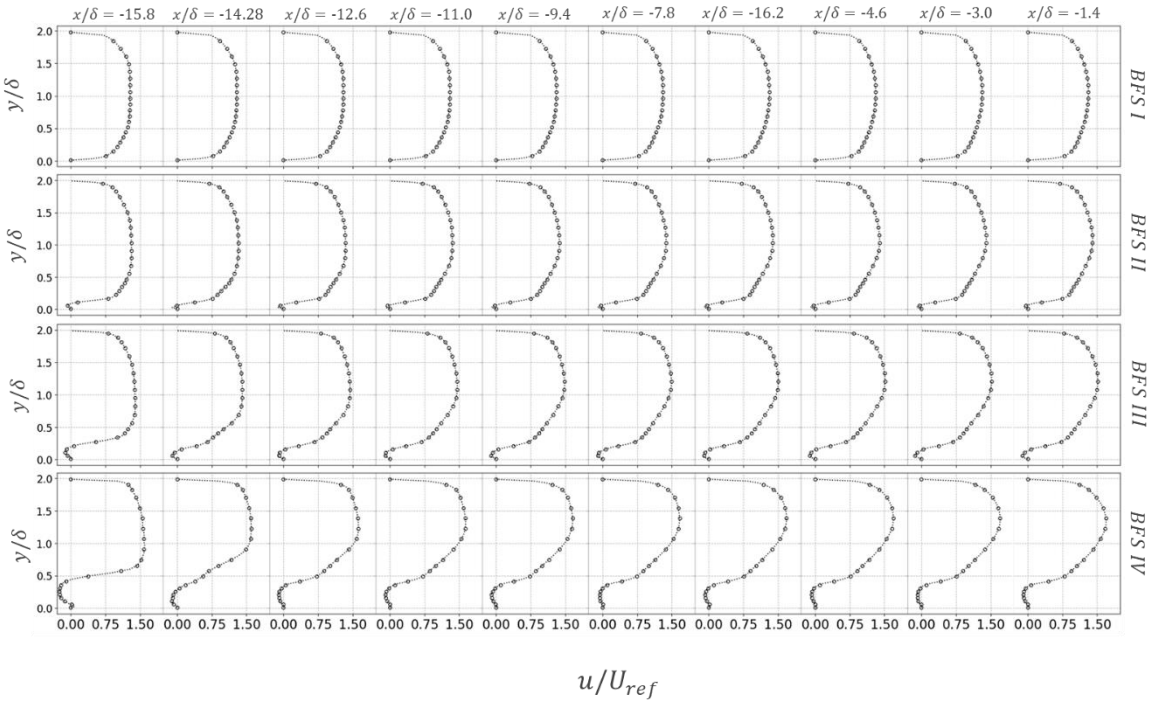

Figure 5.3 Normalized streamwise velocity profile over the local distance of x'/δ = 0.4 (local coordinate is located at beginning of the upstream rib, for each two sequential ribs) and z/δ = 0.1, for sequential ribs along the channel.

A detailed comparison of streamwise velocity and its gradient at different spatial locations along two consecutive ribs is provided in Figure 5.4. For benchmarking purposes, reference profiles from a plain channel (BR = 0) are included and depicted in blue. Leveraging the previously established negligible variations in velocity profiles across different subsequential ribs, our analysis focuses on the segment between x/H=4.0 and x/H=8.0 (corresponding to the 5th and 6th ribs). Within this specific riblet region, three representative distances from the upstream rib are chosen: x′/H=0.5, 1.0, and 1.5. In the context of BFS II and III, these locations respectively represent the large recirculation region, the zone between flow reattachment and detachment, and the area downstream of detachment. Conversely, for BFS IV, all three selected distances are situated entirely within the extensive recirculation zone.

For x′/δ=0.4, a comparison across different Blockage Ratios (BR = 0.05, 0.1, and 0.2) reveals several key trends. An increase in BR leads to a wider region of reverse flow below the crest and a more pronounced convection of the flow towards the channel center. Furthermore, the velocity gradient exhibits its largest negative value near the wall and its largest positive value above the crest for the smallest BR (0.05), indicating a stronger shear effect in these regions for lower blockage ratios. As anticipated, for the other two distances (x′/δ=1.0 and 1.5), no reverse flow is observed for BR = 0.05 and 0.1. However, the reverse flow becomes significantly stronger for BR = 0.2 at these locations. Nonetheless, unlike at x′/δ=0.4, no distinct peak in the velocity gradient is observed around the crest for any BR at these greater downstream distances. Given that x′/δ=0.4 exhibits both the highest streamwise velocity and velocity gradient near the crest, maximum turbulent production is anticipated in this specific region. Consequently, particular attention will be given to the flow characteristics at x′/δ=0.4 in the subsequent turbulence analysis section.

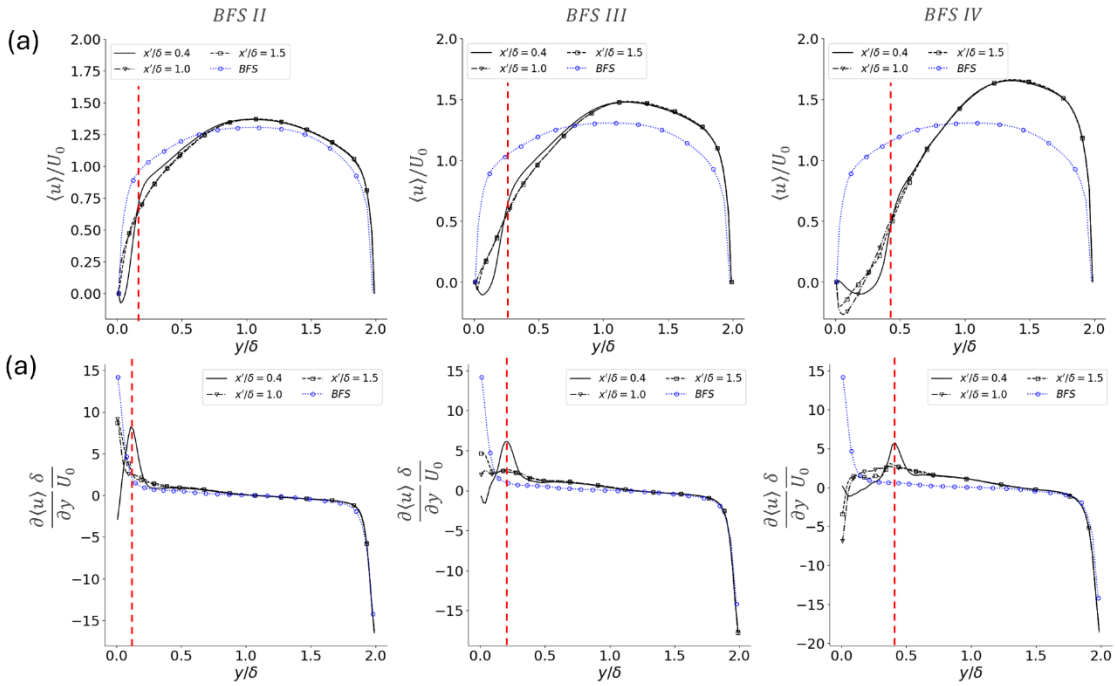

Figure 5.4 Normalized streamwise velocity and its wall normal gradient over the local distance of x'/δ = 0.4, 1, and 1.5 from beginning of the 5th rib (red line determine the rib crest region).

Downstream of the step, a substantial adverse pressure gradient (APG) induces flow separation and the formation of a separation bubble. This bubble encompasses both the recirculation zone and the developing shear layer, extending from the point of detachment to reattachment. A critical characteristic of this separation bubble is the thickness and growth rate of its associated shear layer. In reattaching shear layers, such as those observed in BFS configurations, the growth rate and thickness are influenced by various parameters, including the Reynolds number, step height ratio, and the characteristics of the incoming turbulent boundary layer.

Beyond these parameters, the morphology of the shear layer is intrinsically linked to the topology of the coherent structures within this region. These structures are the primary drivers of mass and momentum transfer from the low-momentum fluid within the separation bubble to the high-momentum fluid in the free stream. Previous studies have indicated that the growth rate of a BFS shear layer exhibits two distinct behaviors: an initial phase and a subsequent phase. In the initial part, extending from detachment up to approximately the mid-distance to reattachment, the shear layer behaves similarly to a free mixing layer, with an average shear layer thickness growth slope ranging from 0.22

to 0.47. Conversely, in the second part, which constitutes a larger portion of the reattaching shear layer, the growth slope significantly declines, and the layer grows more smoothly until it reaches the bottom surface (Figure 5.5).

Figure 5.5 illustrates the vorticity thickness, δω, along the shear layer for different Blockage Ratios (BR). The methodology for calculating this parameter is detailed in Appendix A. The slopes of the first and second parts of the shear layer, denoted as s1 and s2 respectively, were determined using linear curve fitting. It is observed that an increase in BR leads to an increase in s1 and a decrease in s2. As anticipated and consistent with findings presented in the previous section, higher BR values are associated with an increased thickness of the incoming boundary layer. (The subsequent section will demonstrate that for higher BR, turbulent production and convection extend over a larger width within the boundary layer, accompanied by greater turbulence convection to the downstream shear layer, ultimately resulting in a thicker shear layer at its initiation.) Figure 5.5(b) presents the shear layer's lower and upper bounds, superimposed on the mean streamwise velocity field within the shear region. These bounds are colored red and blue, respectively. The lower bound is estimated by the Recirculation Region Interface (RRI)(W. Wu et al., 2020), while the upper bound is determined as the summation of the lower bound and the vorticity thickness. Additionally, reattachment points are clearly indicated by yellow circles.

According to previous studies(Maleki et al., 2024; Nadge and Govardhan, 2014), for a fixed step ratio, an increase in vorticity thickness is typically associated with an earlier reattachment. However, our observations in Figure 5.5 reveal a contrasting trend: the increase in vorticity thickness with increasing BR is accompanied by a sudden decrease in the shear layer's second-part slope (s2), which, counter-intuitively, postpones reattachment. In our study, unlike in some previous investigations such as Stella (Stella, 2017), the increased vorticity thickness is not attributable to an elevated Reynolds number, which typically enhances mass/momentum entrainment and consequently promotes shear layer growth. Instead, in our specific case, the substantial thickness of the shear layer in its initial part is a direct consequence of upstream flow perturbations generated by the preceding riblets. These perturbations significantly enhance mass and momentum exchange within this nascent region. However, as the flow progresses downstream, the gradient of the velocity across the shear layer weakens, becoming insufficient to sustain further growth of local spanwise vorticities within the shear layer.

This reduction in vorticity amplification subsequently decelerates the overall growth process.

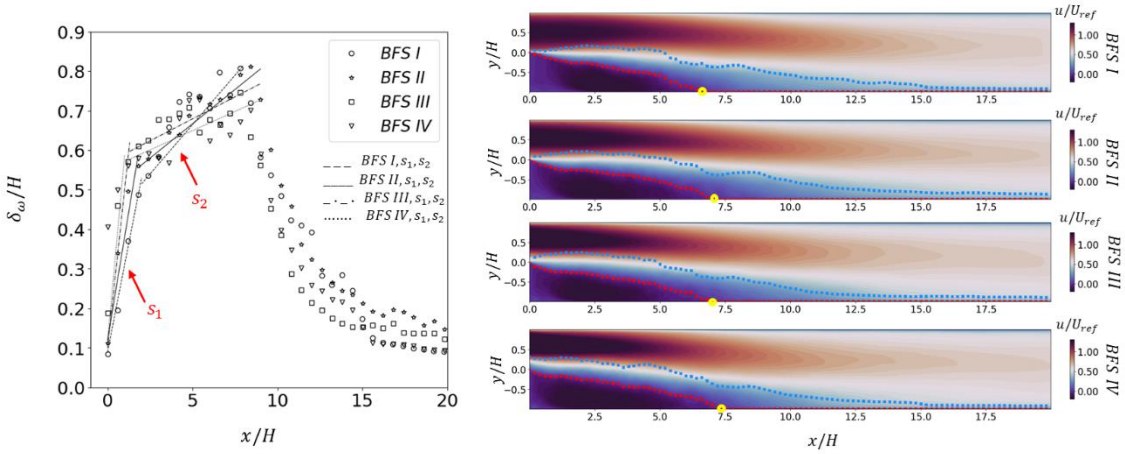

Figure 5.5 Shear layer growth. (a) vorticity thickness δω (the fitted slopes are s_1 = 0.22, 0.26, 0.4, and 0.47, s_2 = 1/20, 1/24, 1/35, and 1/40 for BR = 0, 0.05, 0.1, and 0.2, respectively.) (b) Mean separated flow superimposed on velocity field for different BR.

To further elucidate the influence of Blockage Ratio (BR) on the mean flow field downstream of the BFS, the distribution of the normalized mean streamwise velocity, $\langle u\rangle/Uref$, and its derivative, $(\partial\langle u\rangle/\partial y)\cdot(\delta/Uref)$, are presented in Figure 5.2. These profiles are shown at the center-plane (z/δ=1) for three specific streamwise distances: x/H=0.5, 5.0, and 7.5. These selected distances correspond to the initial part of the first half of the shear layer, the second half of the shear layer, and the vicinity of the reattachment point, respectively, as determined from observations in Figure 5.5.

As observed in Figure 5.6, in the initial part of the shear layer (x/H=0.5), increasing the Blockage Ratio (BR) significantly enhances the reverse flow below the step height (y/δ<0). Concurrently, above the step height, the peak velocity is augmented and shifted upwards. This upward shift of the peak velocity leads to a decreased slope and a reduced mean velocity gradient ($\partial\langle u\rangle/\partial y$) in the vicinity of the shear layer (at y/δ≈0) (Figure 5.6, x/H=0.5). Consequently, one might anticipate a decline in the mean shear layer strength, as $\partial\langle u\rangle/\partial y$ decreases with increasing BR in the first part of the shear layer. (Based on these

results, we expect and will subsequently show a decrease in turbulence production near the shear layer with increasing BR.)

In the latter half of the shear layer and close to reattachment, the differences between various BRs become less pronounced. Nonetheless, it is still evident that the reverse flow within the separation bubble is stronger for larger BR values (Figure 5.6, x/H=5), which, in turn, contributes to the postponement of reattachment (Figure 5.6, x/H=7.5).

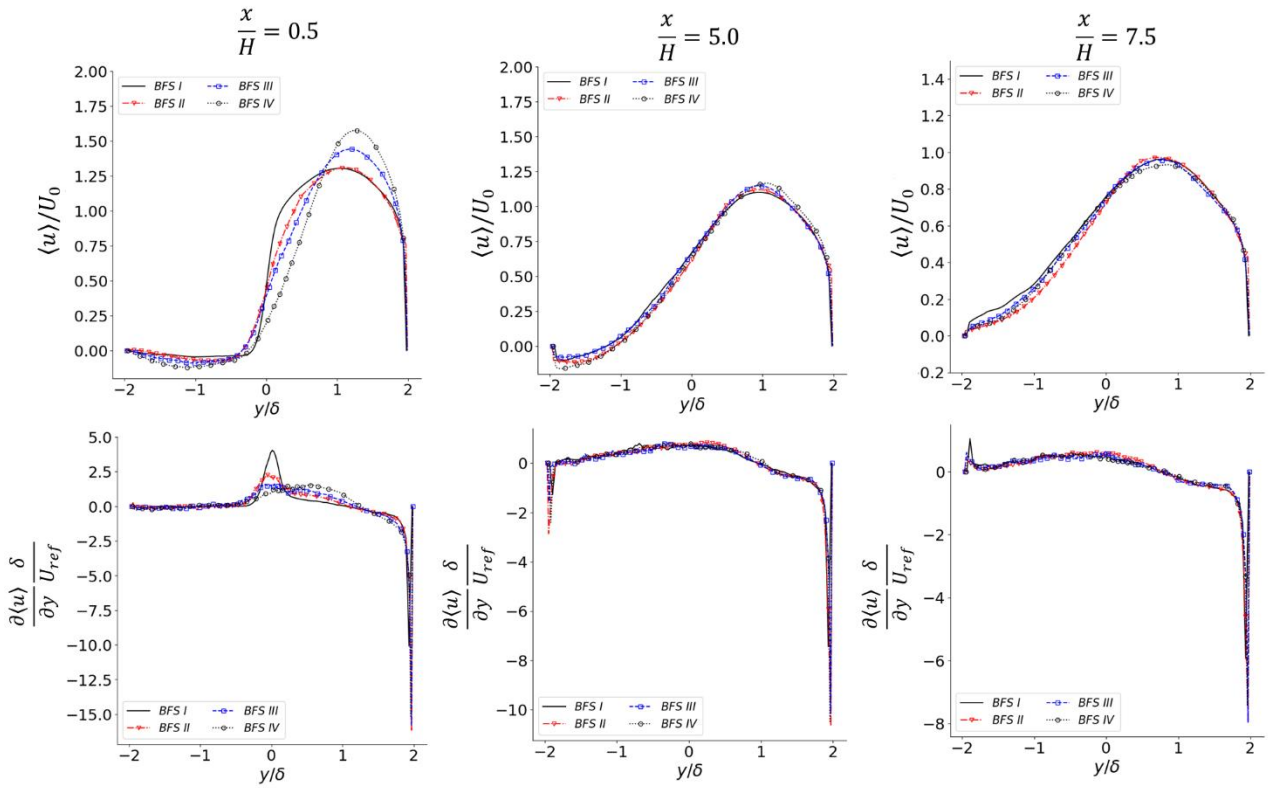

Figure 5.6 Normalized streamwise velocity and its wall normal gradient over the line at center-plane $\boldsymbol{z/\delta = 1}$, and different streamwise distances $\boldsymbol{x/\delta}$ from the BFS edge for BR = 0, 0.05, 0.1, and 0.2.

Figure 5.7(a) presents the instantaneous turbulence kinetic energy (TKE), defined as TKE=(u′2+v′2+w′2)/2, in the mid-width (z/δ=1) plane of Region I for various Blockage Ratios (BR). The results unequivocally demonstrate a remarkable increase in the TKE level within the bottom half of the channel. This intensification is most prominent directly(Ismail et al., 2018; Ma and Mahesh, 2023) above the rib crest, a region typically associated with maximum turbulence production. Furthermore, Figure 5.7(b) displays the streamwise Reynolds stress field, which quantifies the unsteadiness attributed to

streamwise velocity fluctuations. Maximum streamwise fluctuations originate within the shear layer above the rib crest, a region formed as a consequence of flow separation at the leading edge of the ribs. Within this shear layer, the shedding of both spanwise and streamwise vortices leads to significant turbulent generation, acting as a primary source of unsteadiness. (A more detailed discussion of these turbulent structures will be presented in the subsequent section.). Conversely, the recirculation zones between the ribs exhibit very small fluctuations, indicating that these regions are nearly stationary. However, the shear-induced unsteadiness penetrates into the windward region of the downstream riblets, accompanied by characteristic ejection and sweeping mechanisms occurring near the crests(Hu et al., 2023). This unsteadiness reaches its maximum intensity within the shear layer region directly above the first rib crest. The downstream transport of this unsteadiness significantly influences the formation of unsteadiness over subsequent ribs. As observed in the second row (of Figure 5.7b, presumably), the velocity fluctuations are damped because the developing shear layer above the second rib is disturbed by these upstream fluctuations. For other downstream ribs, despite some observed deviations in the intensity of this unsteadiness, the fundamental patterns largely remain consistent.

Figure 5.8 illustrates the normalized Turbulence Kinetic Energy (TKE) and the streamwise Reynolds stress field within the center plane of Region II. As anticipated, Figure 5.8(a) demonstrates that TKE is predominantly concentrated within the downstream shear layer, a direct consequence of the high turbulent production occurring in this region. A remarkable observation is that with increasing Blockage Ratio (BR), the thickness of the high-TKE flow entering the BFS downstream shear layer increases significantly. Consequently, a larger portion of Region II (particularly the area between flow detachment and reattachment) becomes occupied by this high-TKE flow. In the case of BFS I (BR = 0), the shear layer downstream of the BFS is identified as the major contributor to TKE level through production in this region(Pont-Vílchez et al., 2019; SCHÄFER et al., 2009a).

With the increasing Blockage Ratio (BR), the TKE convected from the upstream region of the BFS plays a remarkable role in shaping the TKE level and its distribution in the downstream region. Several important parameters collectively influence this TKE distribution downstream of the steps. These include the formation of long statistically stationary vortices, a smoother velocity gradient at the BFS edge attributed to a thicker,

turbulent boundary layer, the concentration of the flow towards the upper half of the channel, and an increase in the convection of high TKE with increasing BR. Each of these parameters will be detailed in the following sections.

Furthermore, it is evident that an increase in Blockage Ratio (BR) leads to the appearance and subsequent intensification of localized high-intensity TKE streaks ($TKE/U_{ref}^2 > 0.3$) within the vicinity of the shear layer. This phenomenon strongly indicates the formation or convection of exceptionally strong vortical structures in these regions.

Figure 5.8(b) displays the streamwise Reynolds stress field, which is the primary contributor to unsteadiness in Region II, at the center-plane. It is observed that increasing the BR leads to a remarkable increase in both the intensity and span of $\langle u'u' \rangle$, particularly within the first part of the shear layer (0<x/H<5). Conversely, in the second part of the shear layer, the unsteadiness patterns across all BR cases are highly similar, with the streamwise unsteadiness dissipating gradually as the flow progresses towards the reattachment point.

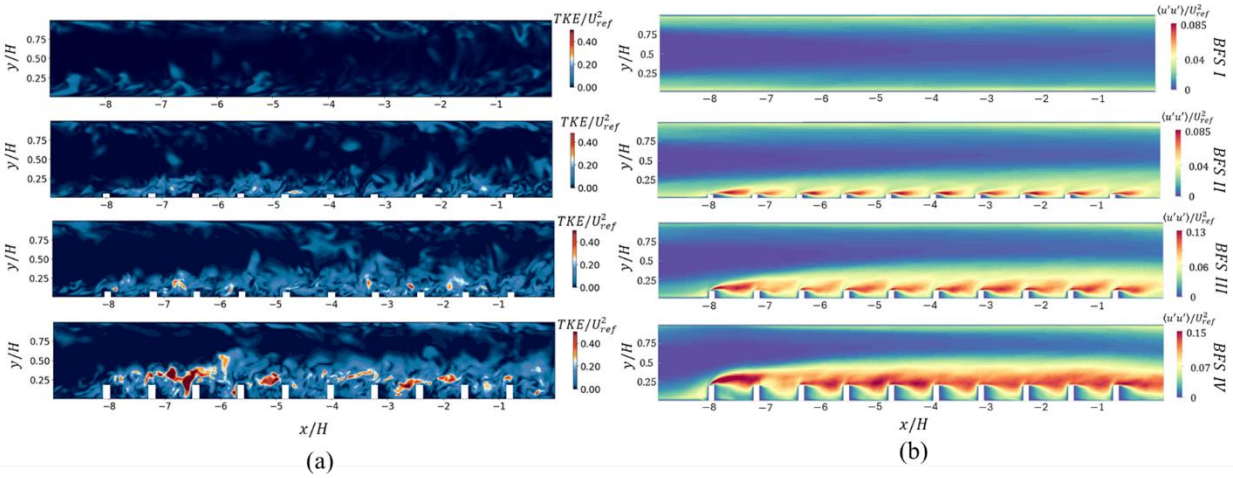

Figure 5.7 (a) Instantaneous contour of normalized turbulent kinetic energy $\boldsymbol{TKE/U_{ref}^2}$, and (b) contour of normalized streamwise Reynolds stress $\boldsymbol{\langle u'u' \rangle/U_{ref}^2}$ for different BR at $\boldsymbol{z/\delta = 1}$ in Region I.

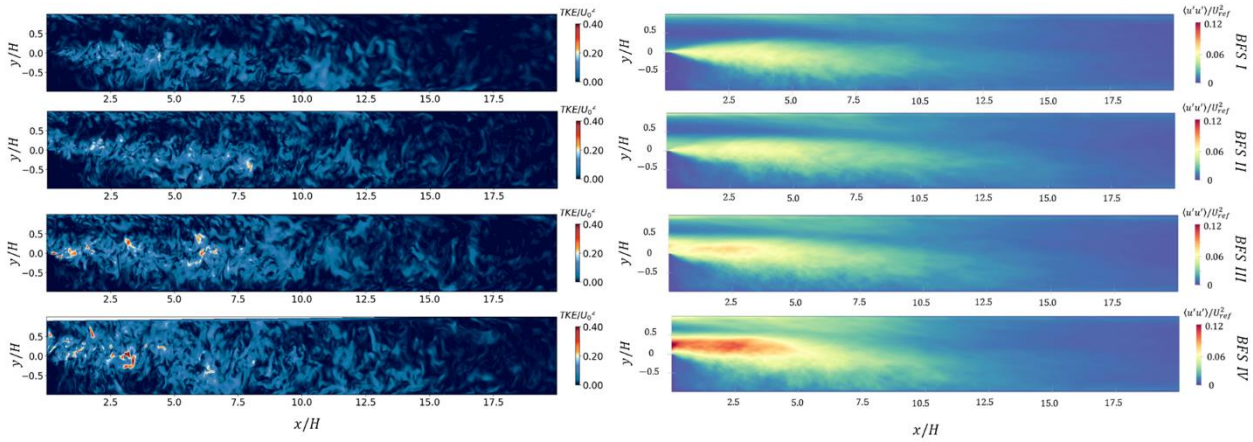

Figure 5.8 (a) Instantaneous contour of normalized turbulent kinetic energy $\boldsymbol{TKE/U_{ref}^2}$, and (b) contour of normalized streamwise Reynolds stress $\boldsymbol{\langle u'u' \rangle / U_{ref}^2}$ for different BR at $\boldsymbol{z/\delta = 1}$ in Region II.

Figure 5.9 presents the cross-sectional contours and streamlines of normalized mean streamwise velocity and vorticity for various Blockage Ratios (BR). As anticipated, in the case of BR = 0 (Figure 5.9(a)), eight distinct corner vortices are formed, comprising two counter-rotating vortices in each corner(Le Floc'h et al., 2020b). These vortices facilitate the transfer of momentum between low and high momentum regions. In the presence of a rib (e.g., for BR = 0.05, Figure 5.9(b)), a strong adverse pressure gradient (APG) drives the flow upwards towards the front face of the rib. Concurrently, a spanwise pressure gradient exists on the windward face of the step. In this region, pressure is highest in the spanwise central area and lowest in the corners. This pressure variation is attributed to the maximal momentum change occurring after stagnation in the central region compared to the corner regions. This spanwise pressure gradient effectively pushes the flow towards the upward corners. Simultaneously, this momentum transfer is compensated by a downward movement of the flow in the central region. As Blockage Ratio (BR) values increase (Figure 5.9(c) and (d)), these statistically stationary longitudinal vortices grow significantly, to the extent that they entirely suppress and eliminate the upper corner vortices.

To investigate how the flow properties in Region I, including the emergence of the pair of stationary vortices, influence the mean flow patterns downstream of the step, the mean streamwise velocity superimposed with streamlines at different distances from the step is presented in Figure 5.10. At x/H=0.5, it is observed that the streamwise vortices present prior to the step largely maintain their shape up to this point. Consequently, two large

streamwise vortices are evident in the upper half of the cross-section for BR = 0.1 and 0.2. Furthermore, the interface between the forward and reverse flow is observed to shift upwards as BR increases, which in turn leads to a larger mean velocity in the upper portion of the channel's cross-section.
Additionally, two new streamwise vortices are observed to form near the mid-height of the side walls. Detailed insights into the formation mechanisms of these stationary vortices can be found in previous studies, such as (Pirozzoli et al., 2018). Briefly, the curvature of the separation streamline within the potential flow region above the shear layer induces a pressure gradient perpendicular to this curvature (with a positive value). This resultant pressure gradient leads to a strong downward deflection of low-momentum fluid in the vicinity of the side walls.

With increasing Blockage Ratio (BR), it is observed that the strength and size of this pair of side longitudinal vortices augment, indicative of a stronger influence of centrifugal forces on the low-momentum regions. This behavior can be attributed to several contributing parameters. Firstly, an increased difference between the peak momentum at the channel center and the minimum momentum near the side walls leads to a more uneven pressure gradient effect and the generation of a stronger velocity gradient between these regions. Secondly, an increase in the mean curvature of streamlines in this region, resulting from the upward shift in the forward/reverse flow interface, may also play a significant role.

Moving downstream to x/H=5, the two longitudinal vortices initially located in the upper part of the channel deflect towards the top wall, maintaining greater strength for larger Blockage Ratios (BR). Concurrently, the side wall vortices bend towards the center of the bottom wall. The size and strength of these vortices collectively determine the mean reattachment point, which is observed to be smallest for BR = 0.

In the vicinity of the reattachment point, at x/H=7.5, the mean streamlines reveal very similar mean flow patterns across all BRs, characterized by two large streamwise vortices persisting along the sidewalls. This similarity indicates that the perturbations introduced by the ribs have largely dissipated by the time the flow reaches the reattachment point.

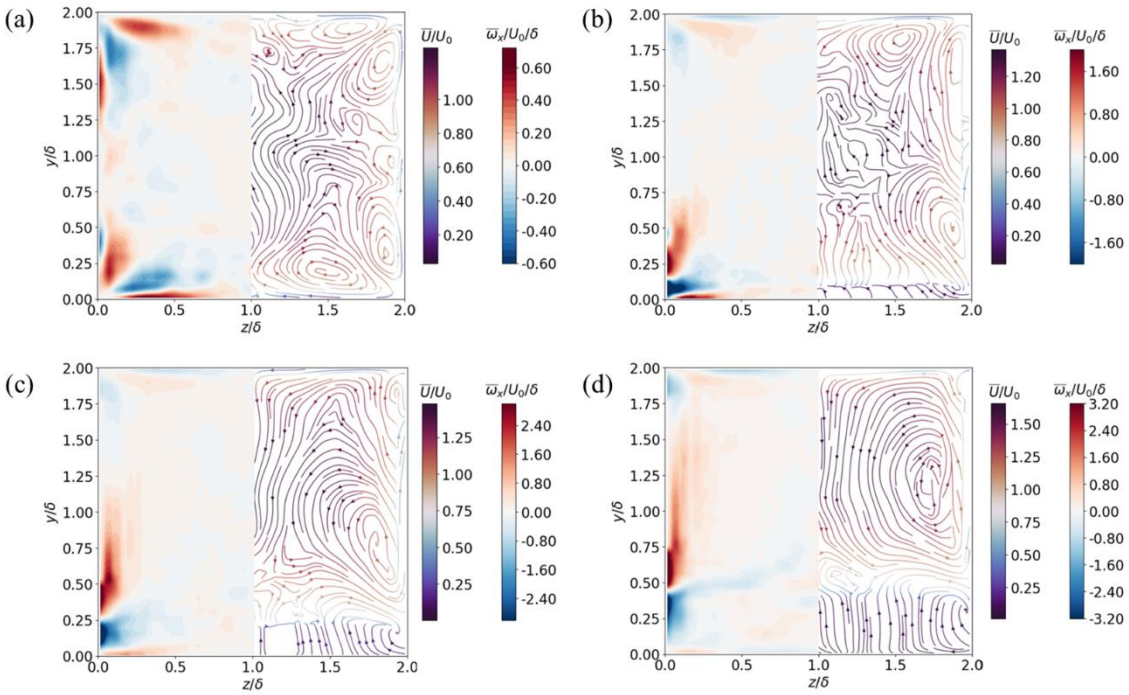

Figure 5.9 Contours of non-dimensionalized average streamwise vorticity $\overline{\boldsymbol{\omega}}_{\boldsymbol{x}}\boldsymbol{\delta}/\boldsymbol{U}_{\boldsymbol{ref}}$(left), and the streamlines of non-dimensionalized mean velocity $\overrightarrow{\boldsymbol{u}}/\boldsymbol{U}_{\boldsymbol{ref}}$ at x/δ =9.4, x'/δ=0.4 for (a) Br = 0, (b) Br = 0.05, (c) Br = 0.1 and (d) Br = 0.2.

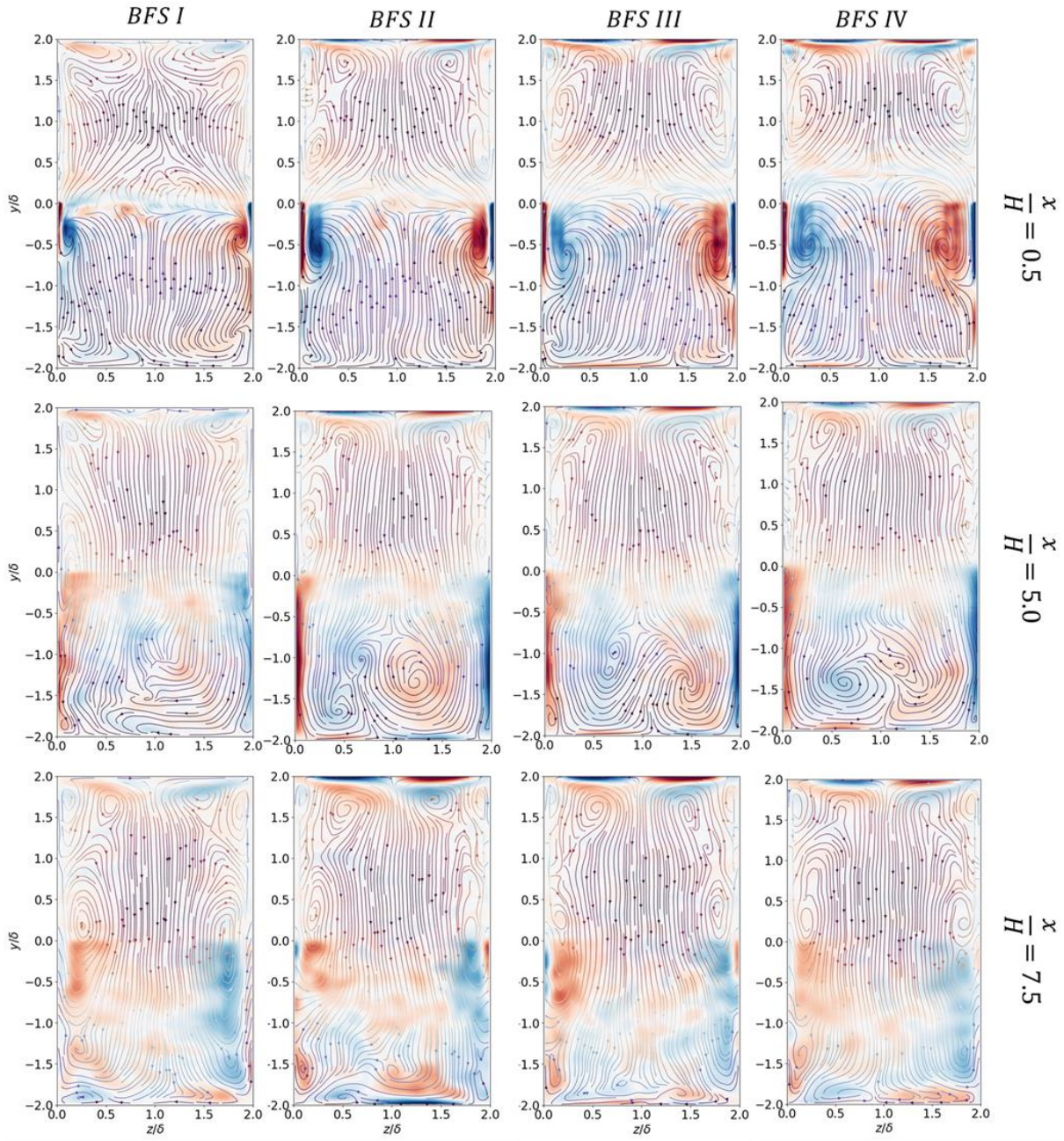

Figure 5.10 Contours of non-dimensionalized average streamwise vorticity $\overline{\boldsymbol{\omega}}_{\boldsymbol{x}}\boldsymbol{\delta}/\boldsymbol{U}_{\boldsymbol{ref}}$ superimposed with the streamlines of non-dimensionalized mean velocity $\vec{\boldsymbol{u}}/\boldsymbol{U}_{\boldsymbol{ref}}$ at x/H =0.5, x/H =5.0, and x/H =7.5 for (a) Br = 0, (b) Br = 0.05, (c) Br = 0.1 and (d) Br = 0.2.

5.3.2 Turbulent Structures

Instantaneous turbulent flow structures were obtained by applying the Q-criterion to the flow field. Figure 5.11 presents instantaneous results of Q-isosurfaces in Region I for different Blockage Ratio (BR) values. For the smooth bottom wall (BFS I, BR = 0), random streamwise fluctuations are observed throughout the channel, primarily concentrated near the walls.

In the presence of ribs, the first rib effectively acts as a forward-facing step. This configuration leads to the formation of two distinct separation bubbles: one upstream (the LS vortex, located near the windward corner) and another over the leading edge of the rib (the US vortex). Both of these separation bubbles are associated with the generation of spanwise vortices in their respective regions.

Approaching the rib, the density of vortical structures increases abruptly, a phenomenon particularly evident from the x−y plane images. Most of these structures are quasi-streamwise (QS) vortices, aligned predominantly in the streamwise-vertical direction. Downstream of the rib's leading edge, these QS vortices coalesce, forming distinct Λ-shaped or hairpin vortices (as annotated in Figure 4, BFS II case).

This observation aligns closely with the findings of(Fang et al., 2021), which highlight that counter-rotating vortices upstream of a forward-facing step (potentially representing the legs of hairpin vortices forming upstream and over the step) significantly influence the ejection and sweeping events within both the upstream and downstream separation bubbles of the step.

As detailed in (ZHOU et al., 1999), the upward and backward pumping action of counter-rotating quasi-streamwise (QS) vortices causes their inclination at the vortex head. Furthermore, the velocity gradient between the head of these QS vortices and the mainstream flow contributes to the formation of an asymmetric shear layer and the generation of a spanwise vortex in close proximity to the QS vortex heads. This process can manifest as the merging of QS vortices at their heads, leading to the formation of Λ-shaped vortices, which may subsequently develop into hairpin and Ω-shaped vortices(Santese et al., 2024a).

From Figure 5.11, it's clear that the intensity and strength (Q) of these turbulent structures increase with higher BR. Downstream of the rib's trailing edge, depending on the rib's

width-to-height ratio and the Reynolds number, one of two scenarios can occur: either a new shear layer and separation bubble form, or the existing separation bubble over the rib extends into the expansion region. Our analysis of the mean streamlines in Figure 5.2 indicates that, on average, the latter scenario is the case in this study. Under these conditions, the vortical structures generated upstream and over the leading edge are convected and evolve over the cavity region. As reattachment occurs within the cavity, these structures can break down into new, smaller structures. Meanwhile, subsequent ribs act as new turbulence generators, leading to the formation and evolution of new turbulent structures that then interact with the convected ones. The accumulation of these fluctuations along the channel intensifies and extends unsteadiness towards the center of the channel as the flow approaches the backward step edge (Figure 5.7(b)).

The formation of hairpin vortices, often evolving from quasi-streamwise vortices (QSVs) through a Λ-shaped intermediate stage to a full hairpin and eventually an Ω-shaped structure, follows a complex sequence of events. First, the QSV's inherent Q2 nature causes them to pump fluid upwards and backwards, away from the boundary region between them. This induced backflow then interacts with the mean flow, leading to the formation of a distinct shear layer visible just above the vortex structure. As these QSV pairs progress, their spanwise separation reaches a minimum near their downstream end, which is also where their strength peaks. Consequently, the shear layer exhibits its highest intensity in this downstream region of the QSVs. As the QSVs continue to curl, their vortical tongues extend further in the downstream direction, and the associated shear layer intensifies even more, particularly at the top of the QSVs. In this highly energized region, the local spanwise vorticity within the shear layer rapidly rolls up, forming a compact spanwise vortex positioned between the downstream ends of the QSVs. This newly rolled-up spanwise vortex then intensifies further and lifts the adjacent QSVs. Finally, viscous vortex connection occurs, where this newly formed spanwise vortex physically connects with the quasi-streamwise vortices, culminating in the formation of a complete hairpin-like vortex structure(ZHOU et al., 1999).

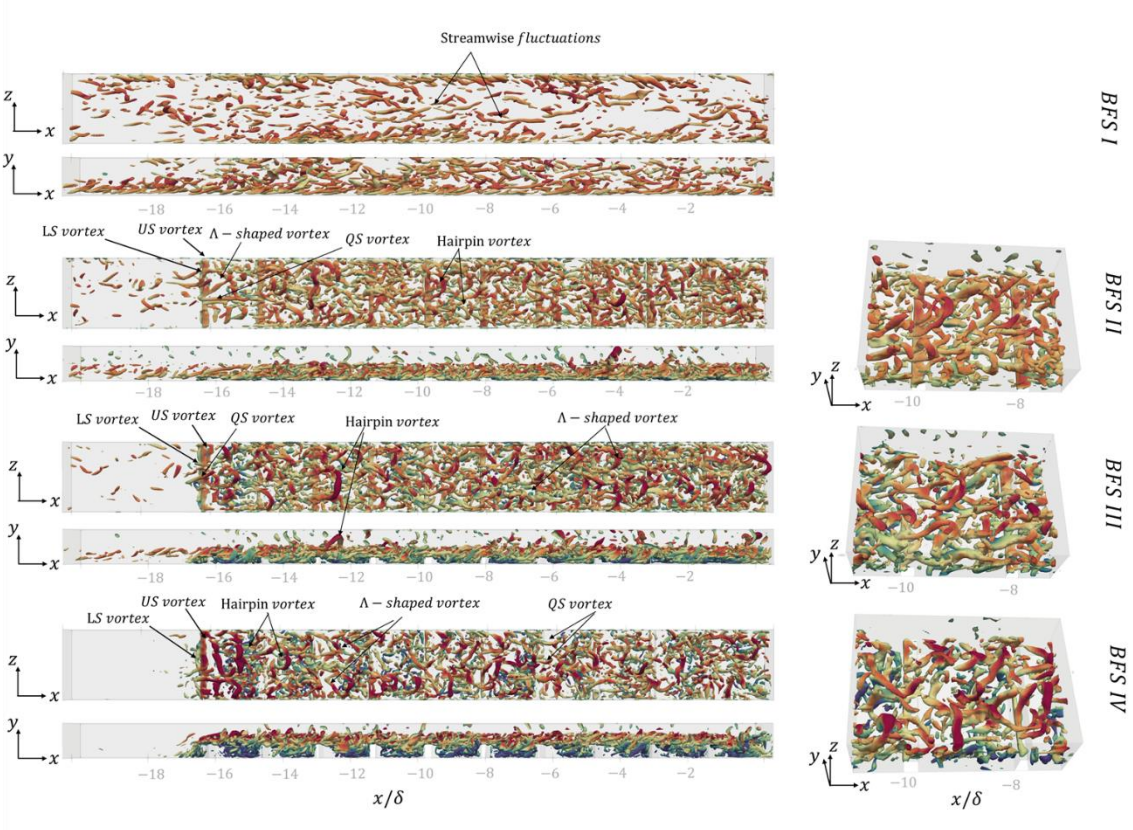

Figure 5.11 Vortical structure in region I for different BR colored by streamwise velocity. Iso surfaces show Q = 3e11, 7e11, 1e12, 2e12 for BR = 0, 0.05, 0.1, and 0.2, respectively.

The characteristic length scales and strengths of low- and high-speed streaks are clearly evident in Figure 5.12. As demonstrated by previous studies(Fang et al., 2021), the regions both upstream and downstream of a forward-facing step exhibit the formation of spanwise quasi-periodic reverse flow, which is directly associated with the presence of low-speed streaks in these areas. This quasi-periodic reverse flow can be induced by ejection events occurring between counter-rotating quasi-streamwise vortices, which may represent the legs of hairpin vortices(Fang et al., 2021). The observed increase in the length scales and strengths of both low- and high-speed streaks with increasing Blockage Ratio (BR) is consistent with the findings presented in Figure 5.11, where a notable increase in turbulence strength and intensity was observed.

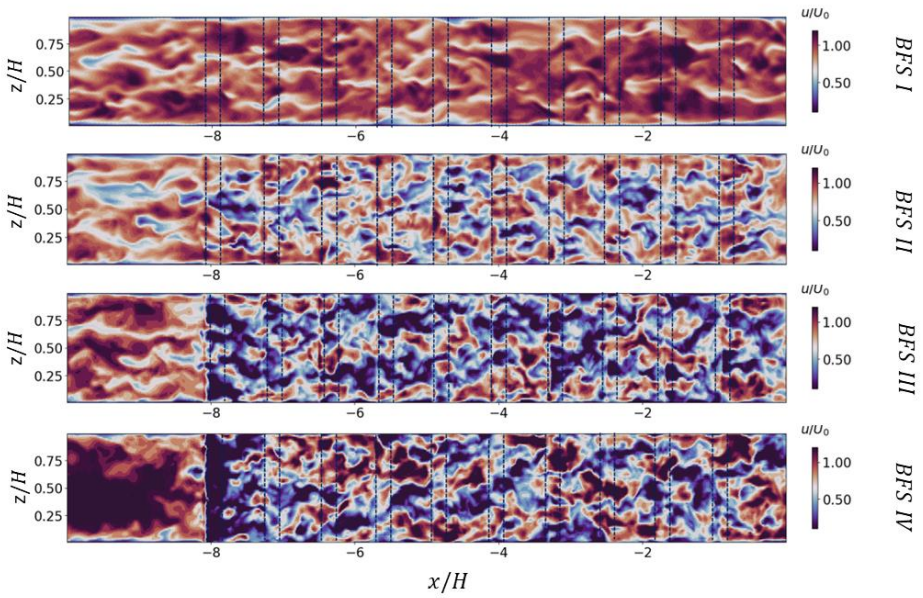

Figure 5.12 Instantaneous results of normalized streamwise velocity field on $\boldsymbol{y/\delta = 0.14, 0.14, 0.24, 0.44}$ for BR = 0, 0.05, 0.1, and 0.2, respectively.

Instantaneous representations of turbulent structures, obtained from Q-criterion in Region II, are provided in Figure 5.13 to investigate the effect of Blockage Ratio (BR) on the turbulent structures downstream of the BFS. Due to variations in turbulence intensity across different cases, distinct Q values were employed (with larger Q values used for larger BR).

For BR = 0, the observed flow structures are characteristic of those found in wall-bounded BFS flows. A brief description of the cascade of events in this flow configuration is as follows(Hickel et al., 2021; Maleki et al., 2024). Incoming turbulent structures from the TBL flow interact with the shear layer (located above the separation bubble). Within this shear layer, shear instabilities induce the formation of large, arc-shaped vortices from these smaller structures(Hickel et al., 2021). Further downstream of the BFS edge, spanwise coherent structures, driven by the cross-streamwise velocity gradient across the shear layer, transport and deform smaller turbulent structures. Although these structures are typically overwhelmed by more energetic phenomena and thus not readily visible in Figure 5.13, their footprint is discernible as a wavy interface beneath the shear layer in the x−y plane. These structures typically shed from the shear layer at the reattachment point. Furthermore, they can serve as an additional source for the generation of new Λ-shaped and hairpin vortices, particularly when exposed to spanwise perturbations

propagating through the shear layer. Increasing BR value, the strength and breadth of the incoming TBL that feed the shear layer increases remarkably (Figure 5.13), resulting in the formation of larger and stronger arc-type vortices which are more pronounced in the case of BR = 0.2.

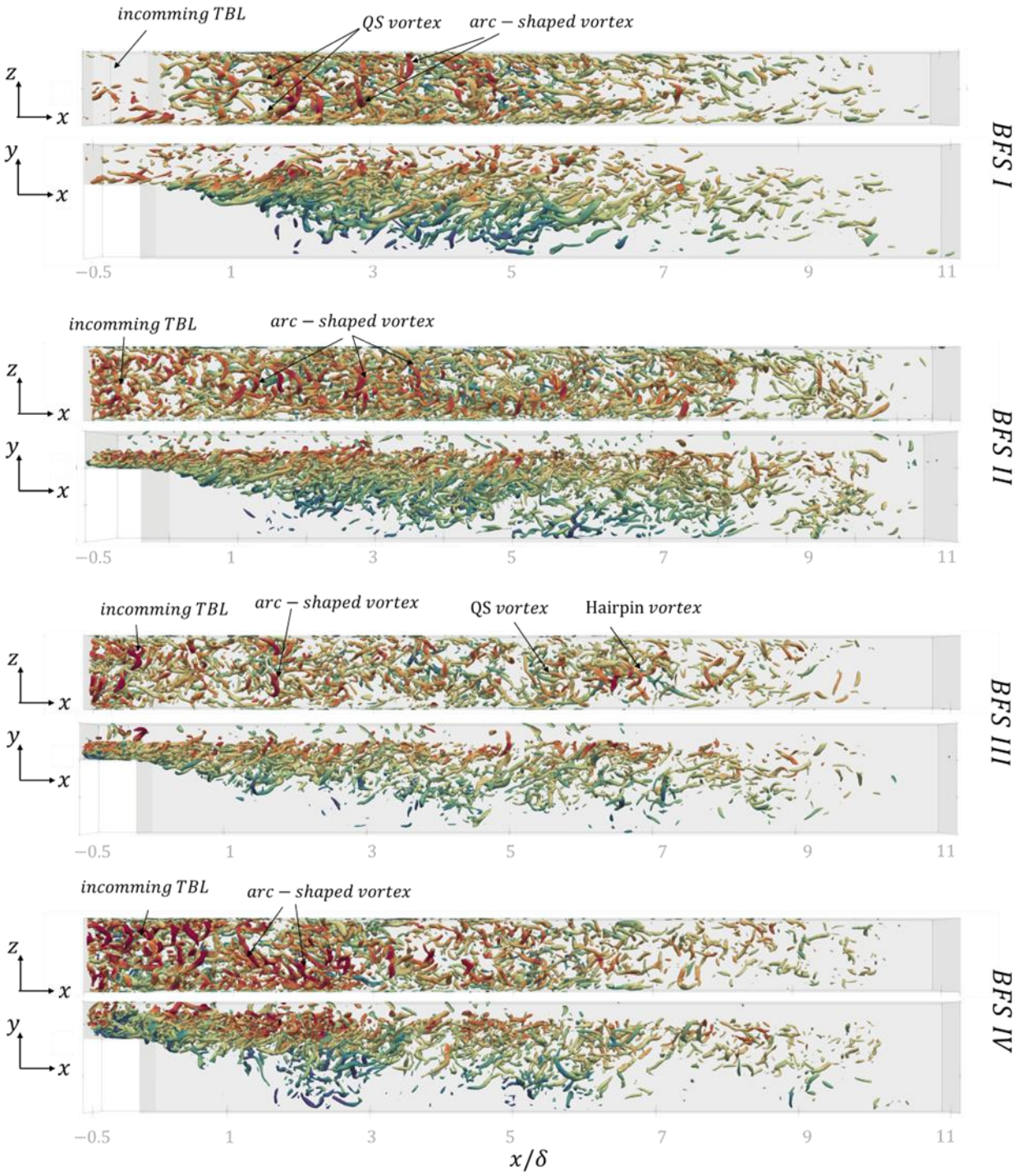

Figure 5.13 Vortical structure in region II for different BR colored by streamwise velocity. Iso surfaces show Q = 3e11, 7e11, 1e12, 2e12 for BR = 0, 0.05, 0.1, and 0.2, respectively;

5.3.3 Turbulence Analysis

To further quantify the effect of Blockage Ratio (BR) on unsteadiness in Region I, the variation of Reynolds stresses along the line at $x/\delta=-9.4$ (corresponding to $x'/\delta=0.4$, and $z/\delta=1$) is presented in Figure 5.14. The results demonstrate a clear shift of the peak unsteadiness towards the regions above the crest, coupled with a significant augmentation of unsteadiness in both shear and normal Reynolds stresses. This strongly implies the formation of robust vortices in this region, which consequently disrupt the typical symmetric/anti-symmetric stress distribution observed in a plain channel (BR = 0). For instance, Figure 5.14(b) clearly shows that the peak streamwise Reynolds stress in the BR = 0.2 case is five times greater than that in the BR = 0 case. Moreover, approximately 35% of the channel's height (within the range $0.4<y/\delta<1.1$) for BR = 0.2 exhibits a streamwise Reynolds stress exceeding the peak value observed in the BR = 0.1 case. Regarding the top wall, no significant augmentation in Reynolds stresses, apart from the streamwise component, is observed with increasing BR. This observation aligns consistently with the findings of (Fang et al., 2017; Wang et al., 2007) .

Regarding the increase in Blockage Ratio (BR), several key points emerge concerning the flow characteristics, particularly near the rib crest. An amplified strength of the shear layer at the leading edge of the ribs directly leads to higher turbulent intensity and generation, as evidenced by a larger production term. This is further supported by observations in spanwise TKE and the distribution of the mean velocity derivative, which collectively indicate an increase in normal stresses(Xun and Wang, 2016). This intensified turbulence near the crest is closely linked to enhanced fluid exchange mechanisms such as 'swap' and 'ejection' events, the influence of which diminishes rapidly with increasing distance from the crest(Nagano et al., 2004). Furthermore, analysis of the ratio of peak values reveals a reduction in anisotropy with increasing BR (e.g., 14/5 for BR = 0.2, compared to 11/3 for BR = 0.1, and 8/1 for BR = 0.05)(Mahmoodi-Jezeh and Wang, 2020). This suggests a more isotropic state of turbulence at higher BRs. Concurrently, the presence of strong secondary flows contributes to the redistribution of unsteadiness, effectively moving it into the region between the side walls and the symmetrical plane.

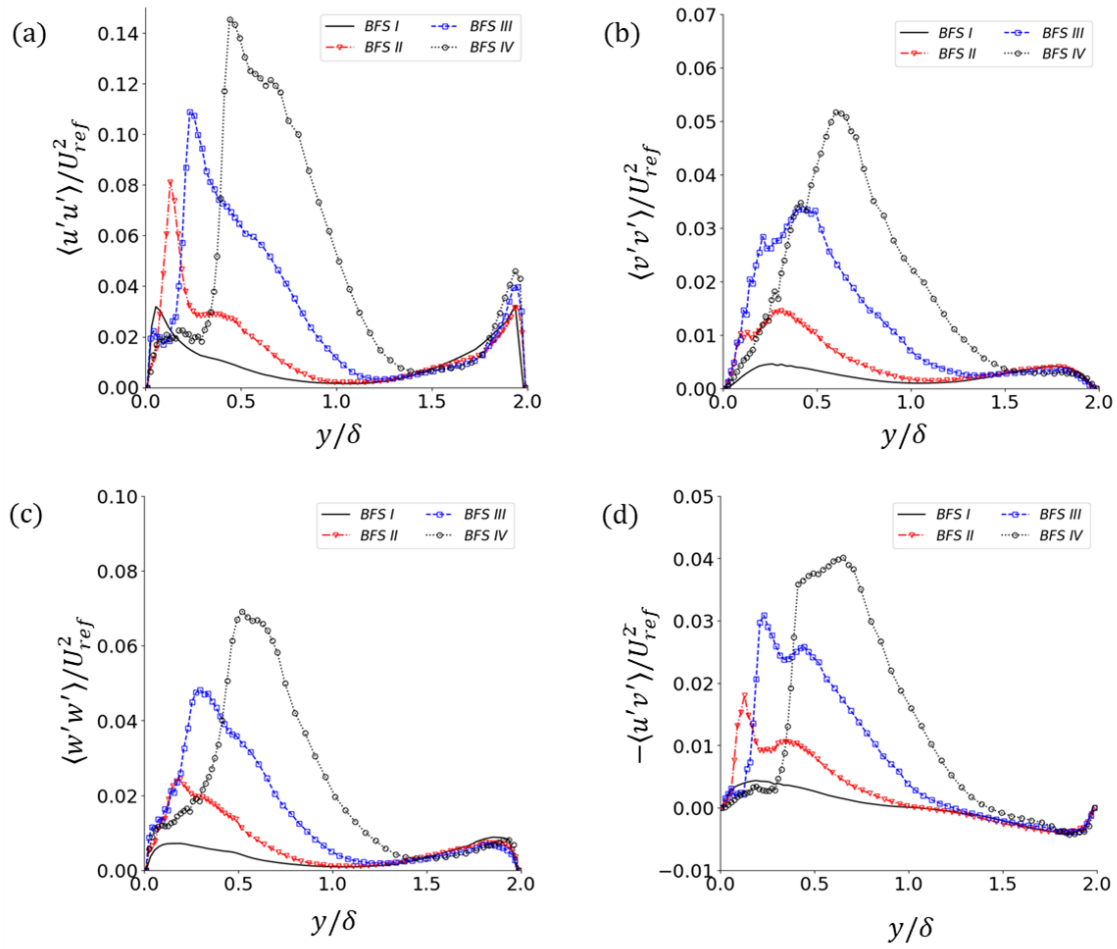

Figure 5.14 Cross-streamwise distribution of Reynolds stresses at (x/δ =9.4, x'/δ=0.4, and z/δ =0.1 for BR = 0, 0.05, 0.1, and 0.2, respectively). (a) Normalized streamwise Reynold stress, (b) Normalized cross-streamwise Reynold stress, (c) Normalized spanwise Reynold stress, and (d) Normalized shear Reynold stress.

Figure 5.15 illustrates the spanwise distribution of Reynolds stresses at a distance of y/δ (please specify the exact normalized distance, e.g., y/δ=0.4) above the rib crest for different Blockage Ratios (BR). At first glance, a significant increase in Reynolds stresses across the spanwise direction is evident, which aligns with the results discussed in the previous section. Regarding the distribution of spanwise Reynolds stress, in the smooth channel case (BR = 0), the maximum stresses are observed closer to the walls. This is likely due to the higher production of turbulent structures in the near-wall region, driven

by the substantial shear stress present there. However, as BR increases, this maximum stress shifts towards the more central regions of the channel.

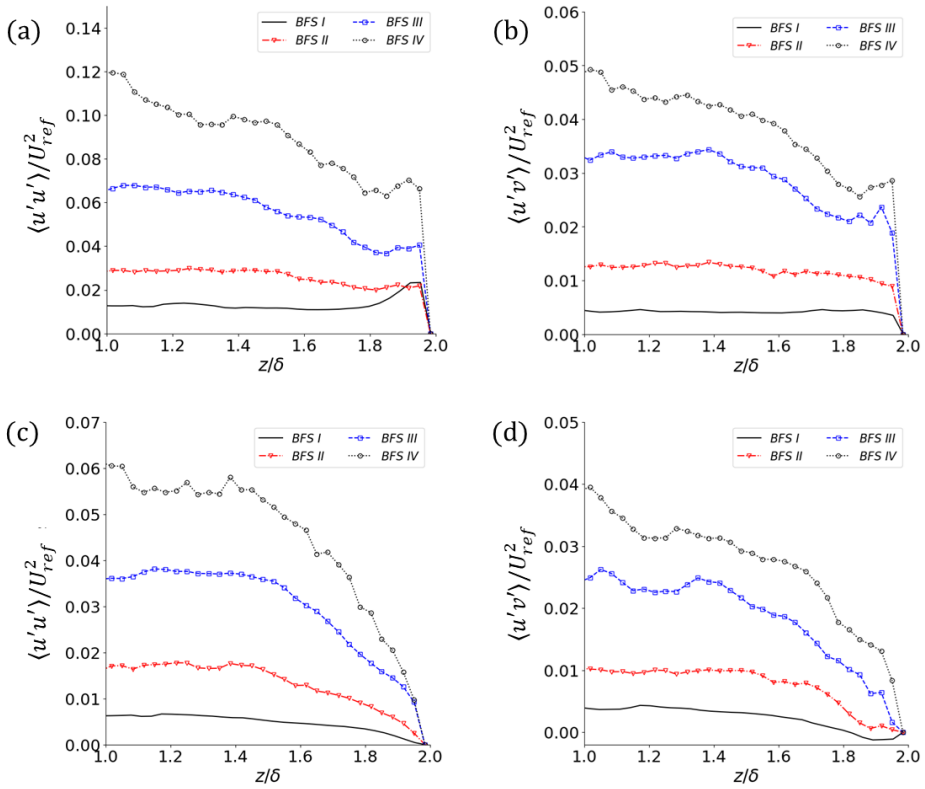

Figure 5.15 Spanwise distribution of Reynolds stresses at ($\boldsymbol{x/\delta = 9.4}$, $\boldsymbol{x'/\delta = 0.4}$, and $\boldsymbol{y/\delta = 0.3, 0.4, 0.5, 0.7}$ for BR = 0, 0.05, 0.1, and 0.2, respectively). (a) Normalized streamwise Reynold stress, (b) Normalized cross-streamwise Reynold stress, (c) Normalized spanwise Reynold stress, and (d) Normalized shear Reynold stress.

Figure 5.16 presents the distribution of normal and shear Reynolds stresses at the center-plane (z/δ=1) for various Blockage Ratio (BR) values, at streamwise distances of x/H=0.5, 5.0, and 7.5 downstream of the step. In all cases, streamwise fluctuations constitute the predominant contribution to the overall unsteadiness throughout the channel. At x/H=0.5, which corresponds to the initial part of the shear layer, Reynolds stresses are observed to be close to zero in the lower bound of the channel for all BR cases. Conversely, for the upper bound, two distinct peaks are discernible in the normal Reynolds stress profiles: one in the vicinity of the shear layer (approximately at y/δ=0) and another located close to the top wall.

Increasing the Blockage Ratio (BR) values significantly enhances unsteadiness around the shear layer in all directions and causes it to shift upwards. Concurrently, it is observed that the thickness of the velocity fluctuation region increases significantly with rising BR. As will be detailed in the turbulent budget analysis section, turbulent convection from the incoming TBL plays a remarkable role in the observed unsteadiness enhancement of the shear layer downstream of the step. Furthermore, a slight enhancement of unsteadiness close to the top wall is likely a consequence of the increased mean velocity in the upper part of the channel, as explained in the preceding section.

One notable observation is that for both the cross-streamwise ($\langle v'v' \rangle$) and spanwise ($\langle w'w' \rangle$) Reynolds stresses, their magnitudes are significantly enhanced in higher Blockage Ratio (BR) cases compared to lower BR cases. For instance, the peak value of $\langle v'v' \rangle$ for BR = 0.2 is approximately four times that for BR = 0. Additionally, increasing the BR leads to a decrease in the ratio of different normal Reynolds stress components, a trend also observed within the rib region. This, in turn, reduces the anisotropic state of turbulence in this area (further details will be provided in the turbulence anisotropy analysis section). A similar behavior is observable for the shear Reynolds stress $\langle u'v' \rangle$, with its strength showing an improvement in the strength and size of spanwise vortical structures and shear layer flapping as BR increases.

As the flow progresses downstream from the step, the magnitude of unsteadiness decreases due to the cascade of energy from large eddies to smaller eddies. For instance, the peak Reynolds stresses at x/H=5 are nearly half those observed at x/H=0.5. Concurrently, these fluctuations become more evenly redistributed across the vertical direction. Furthermore, the ratio of the peak values of the normal Reynolds stress components approaches unity. These collective changes indicate that the turbulent flow becomes more homogeneous and isotropic with increasing distance from the step. Although the peak values of unsteadiness continue to move with the shear layer towards the bottom wall of the channel, the influence of Blockage Ratio (BR) on unsteadiness enhancement significantly diminishes in these downstream regions.

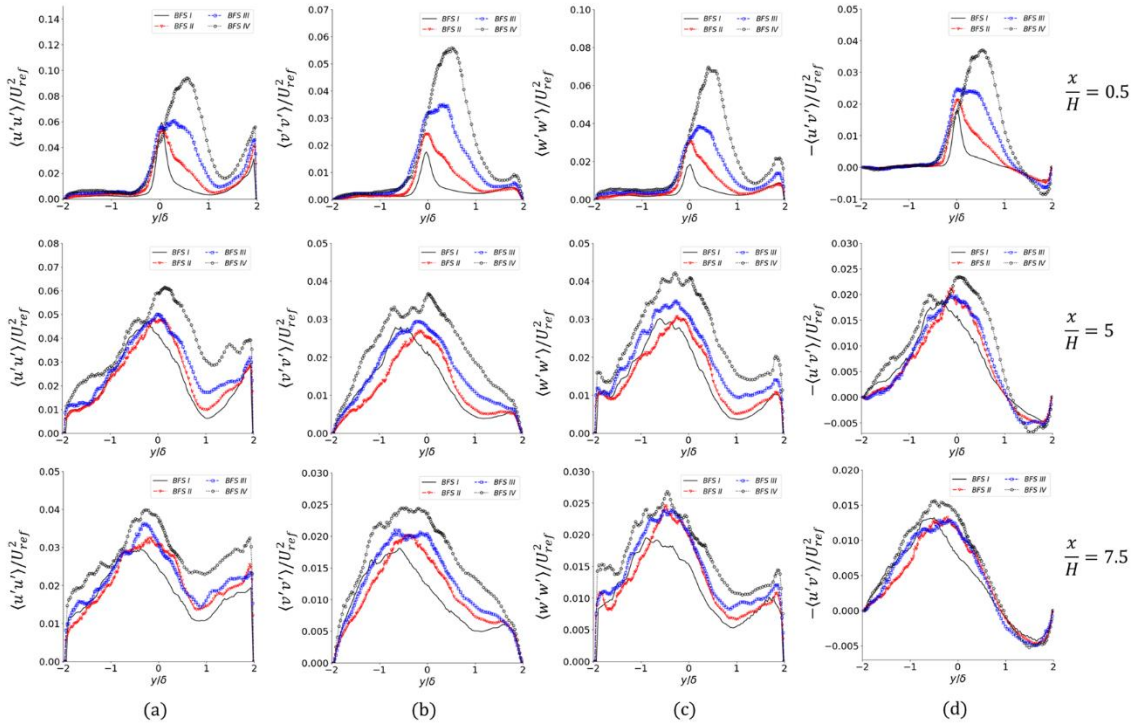

Figure 5.16 Cross-streamwise distribution of Reynolds stresses at (x/H =0.5, 5, and 7.5, and z/δ =1 for BR = 0, 0.05, 0.1, and 0.2, respectively). (a) Normalized streamwise Reynold stress, (b) Normalized cross-streamwise Reynold stress, (c) Normalized spanwise Reynold stress, and (d) Normalized shear Reynold stress.

The quality of the resolved flow field is evaluated based on the ratio of subgrid scale dissipation to the total dissipation (the relevant formulation is given in section 5.3.4), at different distances and for different BR values(Bhide and Abdallah, 2022). It is observed that this ratio is smaller than 0.1 in all cases, except for the distance of x/H = 7.5, corresponding to the reattachment region, where it is slightly larger than 0.1 in peak values. Sensitive regions (including regions with sharp mean velocity gradients) show a larger peak value, also the reason for a larger ratio at x/H = 7.5 is the mesh size is larger in this region (Figure 5.17).

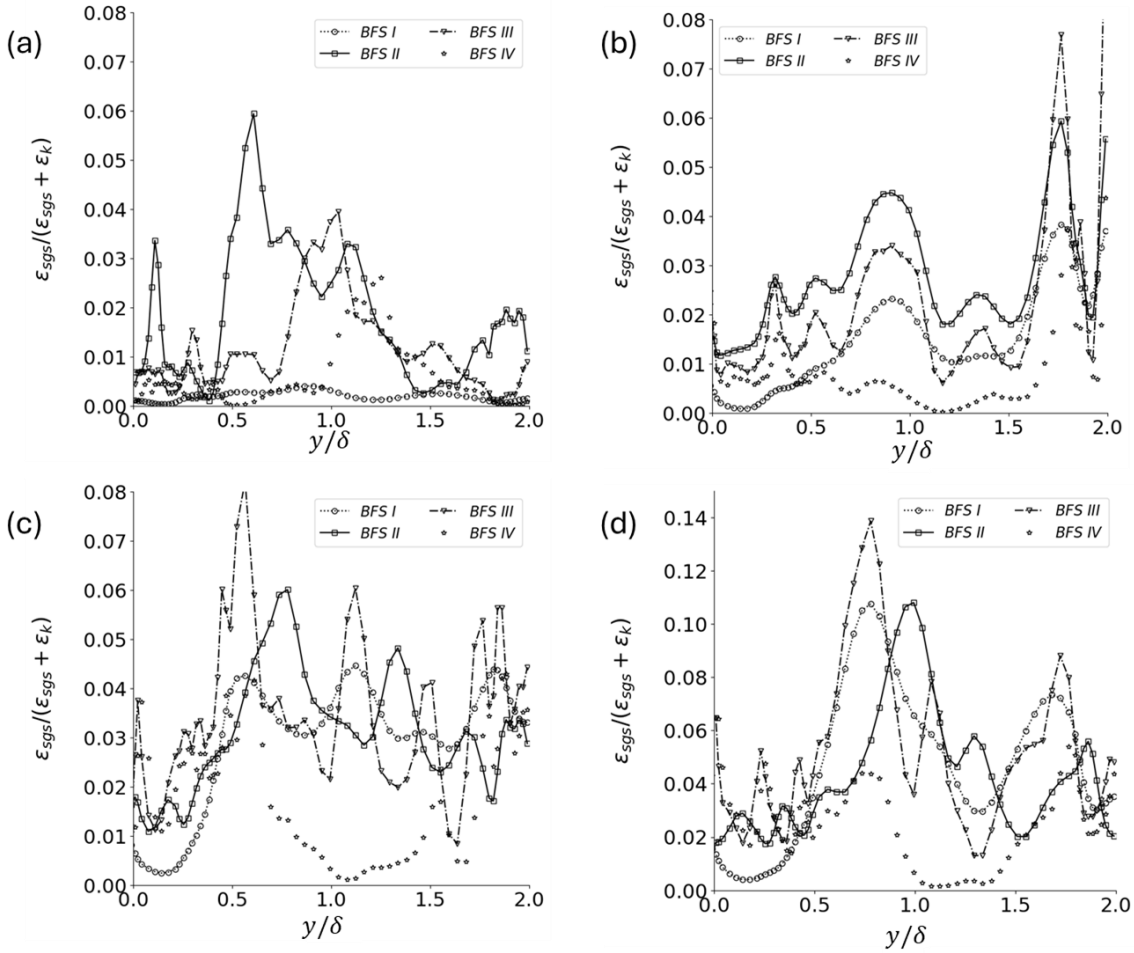

Figure 5.17 Cross-streamwise distribution of $\boldsymbol{\varepsilon_T = \varepsilon_k + \varepsilon_{sgs}}$ at (a) x/H =-4.7, (b) x/H = 0.5, (c) x/H =5, and (d) x/H =7.5, and z/δ =1 for BR = 0, 0.05, 0.1, and 0.2, respectively).

Figure 5.18(a) presents the Turbulence Kinetic Energy (TKE) production along the cross-streamwise line at x/δ=−9.4 (corresponding to x′/δ=0.4, and z/δ=1.0) for different Blockage Ratios (BR). For the plain channel (BR = 0), TKE production exhibits a symmetrical distribution with two distinct peaks located close to the walls, gradually diminishing to zero towards the channel center. These peak values coincide with the peak Reynolds stresses (particularly the streamwise Reynolds stress, which is a major contributor, as shown in Figure 5.14) (Choi et al., 1993).

The addition of ribs significantly augments the peak TKE production (the peak TKE for BR = 0.2 is nearly eight times that for BR = 0) and shifts this peak to the region above the rib crest. This location corresponds precisely to where the maximum shear effect was observed in Figure 5.4. Concurrently, TKE production close to the bottom surface (the

region below the crest) decreases due to the formation of separation bubbles within the cavities.

The peak TKE production (Pk) increases with increasing Blockage Ratio (BR), directly implying the formation of stronger shear layers. For BR > 0, the decrease of Pk to near-zero values occur in two distinct steps. Initially, there is a sharp reduction over a short distance (approximately 0.1δ) from the peak. This is followed by a smoother, more gradual decrease that continues until Pk approaches zero near the channel center. Notably, for BR = 0.2, a second, smaller peak is observed within this slowly diminishing region. The presence of non-zero Pk values in these slowly diminishing regions is attributed to the substantial unsteadiness generated by the shedding mechanism of vortical structures from the shear layer emanating from the rib edges. These dynamics can significantly influence a large portion of the channel flow.

Regarding the top wall, the behavior of TKE production is very similar to that observed for Reynolds stresses, with a small increase in the peak Pk attributed to the increased velocity gradient in that region. Turbulence dissipation ($\varepsilon_T = \varepsilon_k + \varepsilon_{sgs}$, sum of viscous and subgrid scale dissipation) exhibits a similar pattern, displaying a local peak value located close to the crest region. It then gradually broadens and decreases towards near-zero values closer to the center of the channel. The ratio of TKE production to dissipation (Figure 5.18) clearly indicates that ribs significantly enhance turbulence non-equilibrium in two distinct regions: one close to the crest, and another at higher distances from the crest where dissipation sharply decreases.

Figure 5.19 presents the spanwise profiles of TKE production (Pk), turbulence dissipation (ε_T), and their ratio (P_k/ε_T) at a distance of 0.3δ from the rib crests. The spanwise distribution of Pk exhibits a pattern similar to that of the spanwise distribution of Reynolds stresses. Specifically, one peak in Pk is observed close to the side walls, primarily driven by wall shear stress (which increases due to the enhanced mean velocity with increasing BR). Another peak is located between the sidewall and the symmetry plane, a feature controlled by the streamwise vortices, as explained in the previous section.

Conversely, spanwise dissipation (ε_T) shows only a small augmentation with increasing BR. Consequently, it is evident that both wall shear stress and secondary streamwise

vortices are the primary contributors to the non-equilibrium turbulence observed in the spanwise direction (Choi et al., 1993).

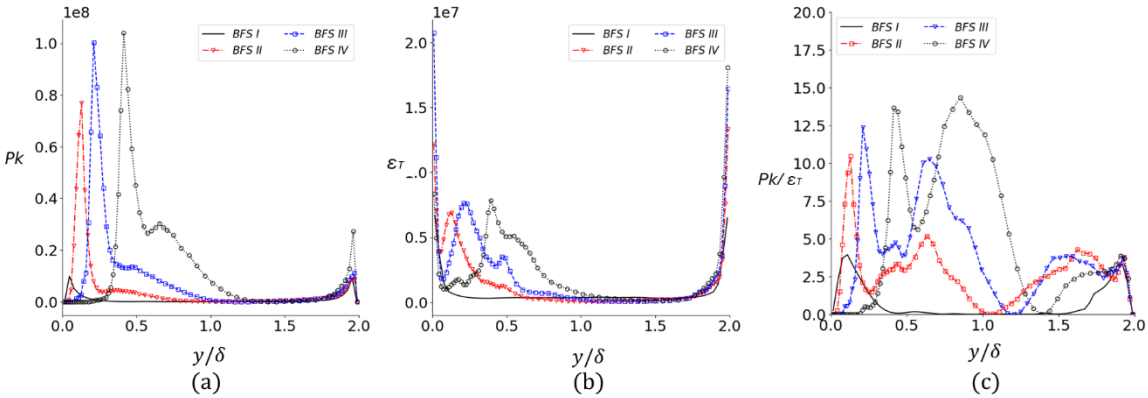

Figure 5.18 Cross-streamwise distribution of (a) TKE production $\boldsymbol{P_k}$, (b) dissipation $\boldsymbol{\varepsilon_T = \varepsilon_k + \varepsilon_{sgs}}$, and (c) their ratio ($\boldsymbol{P_k/\varepsilon_T}$) at (x/δ =9.4, x'/δ=0.4, and z/δ = 1.0 for BR = 0, 0.05, 0.1, and 0.2, respectively).

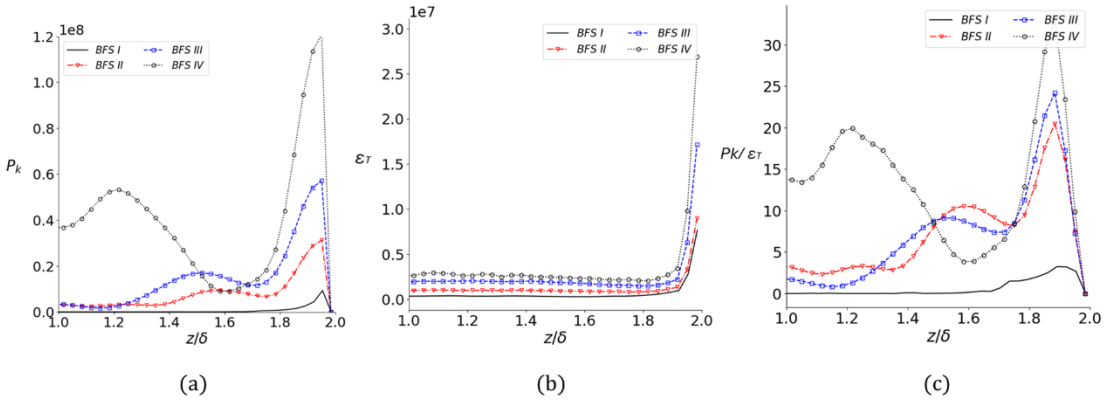

Figure 5.19 Spanwise distribution of (a) TKE production $\boldsymbol{P_k}$, (b) dissipation $\boldsymbol{\varepsilon_T = \varepsilon_k + \varepsilon_{sgs}}$, and (c) their ratio ($\boldsymbol{P_k/\varepsilon_T}$) at (x/δ =9.4, x'/δ=0.4, and y/δ =0.3,0.4,0.5,0.7 for BR = 0, 0.05, 0.1, and 0.2, respectively).

Figure 5.20 presents the distributions of TKE production (P_k), dissipation (ε_T), and the production-to-dissipation ratio (P_k/ε_T) along lines at x/H=0.5, 5.0, and 7.5, all at the center-plane (z/δ=1). These profiles aim to elucidate the influence of Blockage Ratio (BR) on turbulence equilibrium at various distances downstream of the step. At x/H=0.5, Figure 5.20(a) reveals that the peak TKE production is largest for BR = 0. As discussed

in previous sections, the thinner incoming TBL associated with lower BR leads to a sharper velocity gradient downstream of the step and a consequently stronger shear layer formation. While this sharp gradient for BR = 0 results in substantial production, this large production is spatially confined to a narrow region.

With increasing Blockage Ratio (BR), two primary parameters significantly influence the TKE production mechanism. Firstly, an increase in the thickness of the incoming TBL negatively affects the cross-streamwise velocity gradient ($\partial u/\partial y$). Secondly, the increase in streamwise mean velocity (due to the smaller cross-sectional area occupied by forward flow, as shown in Figure 5.10) can, conversely, reinforce this gradient. The intricate balance between these two competing factors governs the TKE production distribution. Therefore, as BR increases, it is observed from Figure 5.20(a) (at x/H=0.5) that TKE production decreases near the shear layer's lower bound ($-0.02<y/\delta<0.02$). This reduction is attributed to a decrease in $\partial u/\partial y$ in this specific region. However, for larger y values, TKE production is greater for higher BRs, owing to the spatial extension of significant $\partial u/\partial y$ values into these regions. Turbulent dissipation ($\epsilon\varepsilon_T$) exhibits a similar behavior, as depicted in Figure 5.20(b) (at x/H=0.5). Regarding the production-to-dissipation ratio (P_k/ε_T) presented in Figure 5.20(c) (at x/H=0.5), three distinct peaks are observed in the upper half of the channel. The first peak is located close to the step height (approximately $y/\delta\approx0$) and is largest for BR = 0. The second peak falls within the range $0.75<y/\delta<1$, and the third is positioned close to the top wall. These latter two peaks reach their maximum values for the largest BR, indicating the most significant regions of turbulent non-equilibrium.

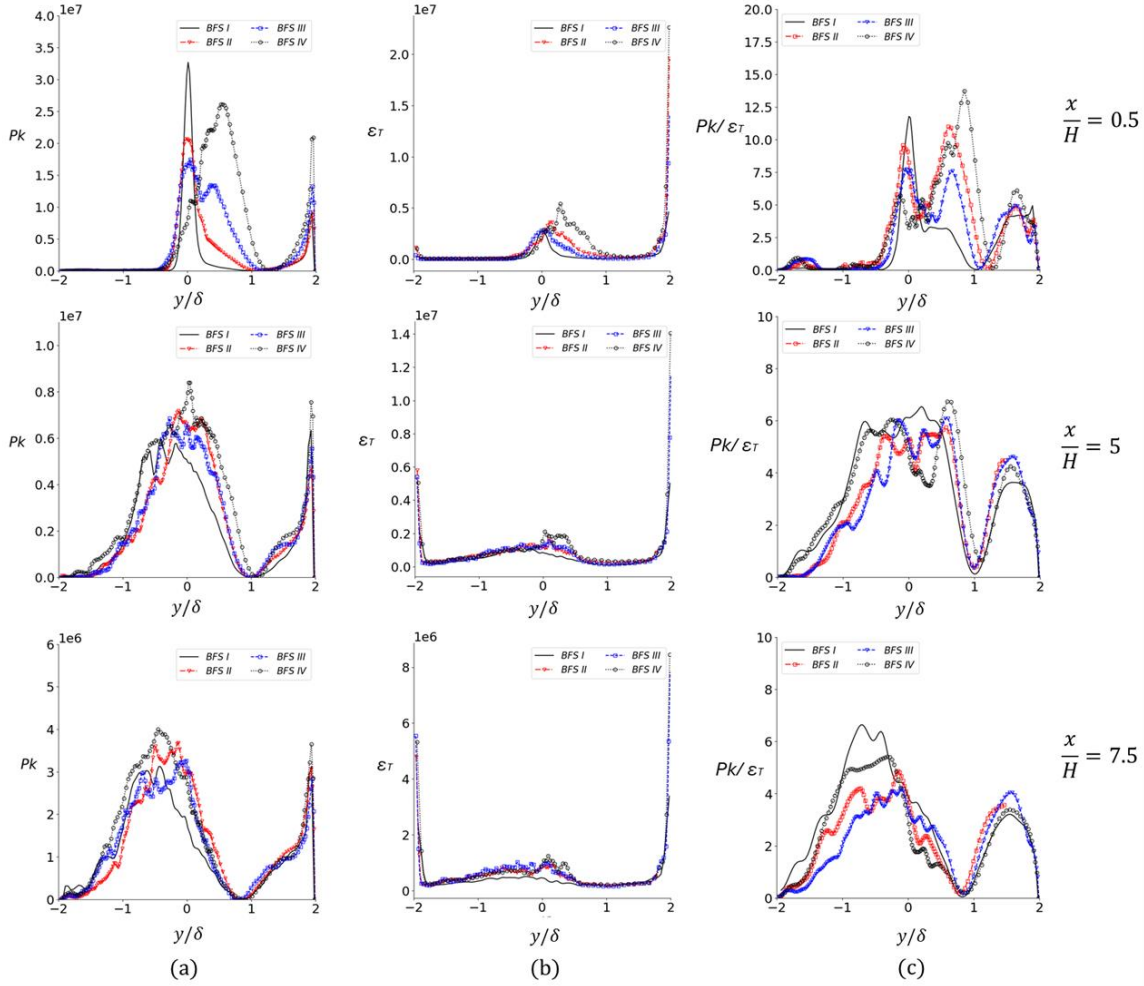

Figure 5.20 Cross-streamwise distribution of (a) TKE production $\boldsymbol{P_k}$, (b) dissipation $\boldsymbol{\varepsilon_T}$, and (c) their ratio ($\boldsymbol{P_k/\varepsilon_T}$) at x/H = 0.5, 5, and 7.5, and z/δ =1 for BR = 0, 0.05, 0.1, and 0.2, respectively).

5.3.4 TKE Budget

The transport equation for turbulent kinetic energy is given as(Bhide and Abdallah, 2022; Plasseraud et al., 2023):

$$\underbrace{\langle u_j \rangle \frac{\partial k}{\partial x_j}}_{C_k} = \underbrace{-\frac{1}{\rho}\frac{\partial \langle p' u''j \rangle}{\partial x_j}}_{\Pi_k} \underbrace{-\frac{1}{2}\frac{\partial \langle u_i'' u_i'' u_j'' \rangle}{\partial x_j}}_{T_k} + \underbrace{\frac{\partial}{\partial x_j}\langle \tau_{ij}'' u_i'' \rangle}_{D_k} + \underbrace{\frac{\partial}{\partial x_j}\left\langle \tau_{ij}^{\text{sgs}} u_i'' \right\rangle}_{D_k^{sgs}}$$

$$\underbrace{-\langle u_i' u'_j \rangle \frac{\partial \langle u_i \rangle}{\partial x_j}}_{P_k} \underbrace{-\langle \tau_{ij}'' \frac{\partial u_i''}{\partial x_j} \rangle}_{\varepsilon_k} \underbrace{-\langle \tau_{ij}^{\text{sgs}} \frac{\partial u_i''}{\partial x_j} \rangle}_{\varepsilon_k^{sgs}}$$

Where $C_k, \Pi_k, T_k, D_k, P_k,$ and ε_k , respectively, show convection, pressure transport, turbulent diffusion, viscous diffusion, production and pseudo dissipation of the TKE. D_k^{sgs} and ε_k^{sgs} are SGS diffusion and dissipation. Figure 5.21 exhibits the distribution of Turbulence Kinetic Energy (TKE) budget terms along the line at x/δ=−9.4 (corresponding to x′/δ=0.4, and z/δ=1.0) for different Blockage Ratio (BR) values. The distributions of the production and dissipation terms have been previously detailed in Figure 5.19 and Figure 5.20, respectively. The production term, which quantifies the energy transfer from the mean flow to turbulent fluctuations, is the dominant TKE transport term across all BR values and is primarily balanced by the dissipation term(Teng and Piomelli, 2022).

In the plain channel case (BR = 0), production and dissipation are the sole dominant TKE budget terms. However, with increasing BR, turbulent diffusion and convection terms begin to contribute remarkably to the TKE budget. For instance, in the BR = 0.05 case (Figure 5.21(b)), it is observed that the turbulent diffusion term has a positive effect in the vicinity of the wall, reaching its maximum value below the crest at approximately y/δ≈0.032. This positive contribution then decreases but remains positive up to a point above the crest, at about y/δ≈0.075. Beyond this point, the turbulent diffusion term makes a negative contribution in the region between y/δ≈0.075 and y/δ≈0.194, which is then followed by another positive contribution. It is noteworthy that the negative peak in the turbulent diffusion term is balanced by a peak in production, implying that turbulence diffuses from the region of highest TKE production to its surroundings (both below the crest and above the shear layer). In this specific scenario (BR = 0.05), turbulent diffusion is the primary mechanism for TKE transfer, whereas with further increases in the BR value, convection emerges as an additional significant mechanism.

With further increases in the Blockage Ratio (BR), as shown in Figure 5.21(c) and (d), the effect of turbulent diffusion is significantly enhanced. Notably, the positive contribution of turbulent diffusion extends considerably over a substantial portion of the channel height. Furthermore, for these higher BR ratios, the convection of TKE towards the crest vicinity makes a notable contribution to the overall TKE transport

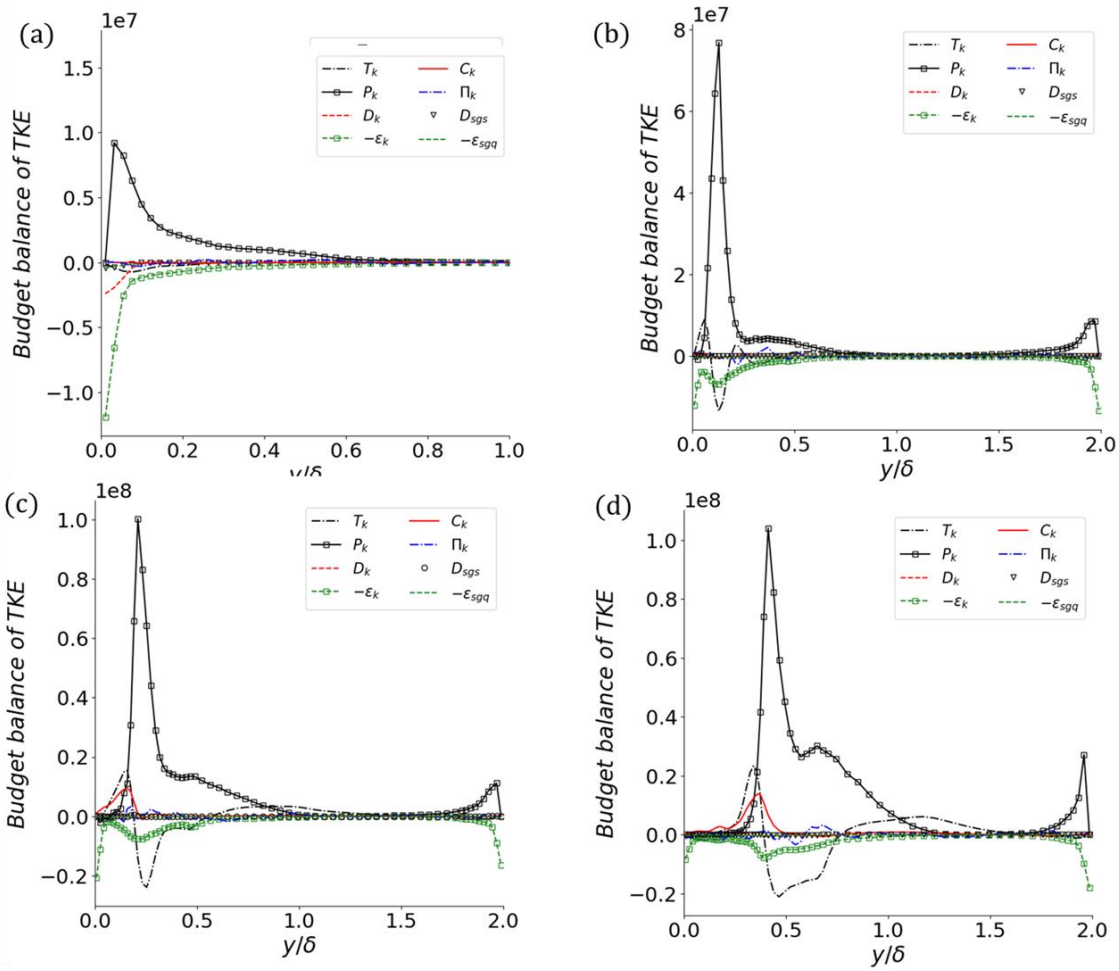

Figure 5.21 Cross-streamwise distribution of turbulent budget terms of TKE transport equation for (a) BR = 0, (b)BR = 0.05, (c) BR = 0.1, and (d) BR =0.2 at x/δ =-9.4, x'/δ=0.4, and z/δ = 1.0.

Figures 5.22, 5.23, and 5.24 illustrate the distribution of turbulent budget terms downstream of the step at x/H=0.5, 5.0, and 7.5, respectively, all at the center-plane (z/δ=1). These figures aim to investigate the influence of Blockage Ratio (BR) on TKE transport terms downstream of the step. Similar to Region I, in Region II, TKE production, dissipation, turbulent diffusion, and turbulent convection are the most significant turbulent transport terms. However, it is notable that the overall magnitude of these terms is remarkably smaller for BR > 0 in Region II compared to their peak values in Region I, while for BR = 0, they are larger in Region II, as observed in Figure 5.21.

According to Figure 5.22 (at x/H=0.5), TKE diffusion primarily balances its production around the shear layer center. This occurs at y/δ≈0,0.05,0.1, and 0.2 for BR = 0, 0.05, 0.1, and 0.2, respectively, which are also the locations of maximum production. Additionally,

two positive local peaks of TKE diffusion and convection are observed around the "knees" of the TKE production distribution. Even though the peak value of production decreases for non-zero BR values, the contribution and zone of influence of positive TKE convection and diffusion are significantly enhanced. This highlights the crucial role of TKE transfer by convection and diffusion in shaping the TKE distribution around the shear layer for large BR values. For example, as shown in Figure 5.22(d), the positive TKE convection and diffusion cover a region of $-0.56 < y/\delta < 0.25$ and $0.5 < y/\delta < 1.68$, with peaks representing between 16% and 20% of the TKE production peak for BR = 0.2. In contrast, for BR = 0, these terms cover a region of $-0.37 < y/\delta < 0.31$, and their peaks range between 4.3% and 8.6% of the TKE production peak.

Moving downstream to $x/H \approx 5.0$, this trend reverses, and the peak production becomes larger for non-zero BR values, although the overall production still decreases significantly. As observed in previous results (Figures 5.4 and 5.6) for $x/H = 5$ and 7.5, the mean streamwise velocity and velocity gradient profiles for different BR values become very similar. However, Reynolds stresses still demonstrate a notable enhancement for larger BR values. Considering these results, along with those from the Q-criterion analyses, it can be concluded that at a distance of $x/H = 5$, the strong vortical structures convected streamwise from the incoming TBL experience smaller dissipation/diffusion rates compared to the vortical structures generated within the downstream shear layer. These convected structures, therefore, continue to act as a significant source of TKE production in these regions.

Further downstream ($\frac{x}{H} = 7.5$), most of the TKE is transferred from large energetic structures to small less energetic structures, which has smaller production rate but distribute more uniformly across the channel (Figure 5.24), leading to a smoother production distribution across the vertical axis. Under this condition, difference between distribution and magnitude of TKE budget terms for different BR become very small. At this point, TKE convection is most effective in regions with larger mean velocity, while TKE diffusion effect covers a significant portion of the channel.

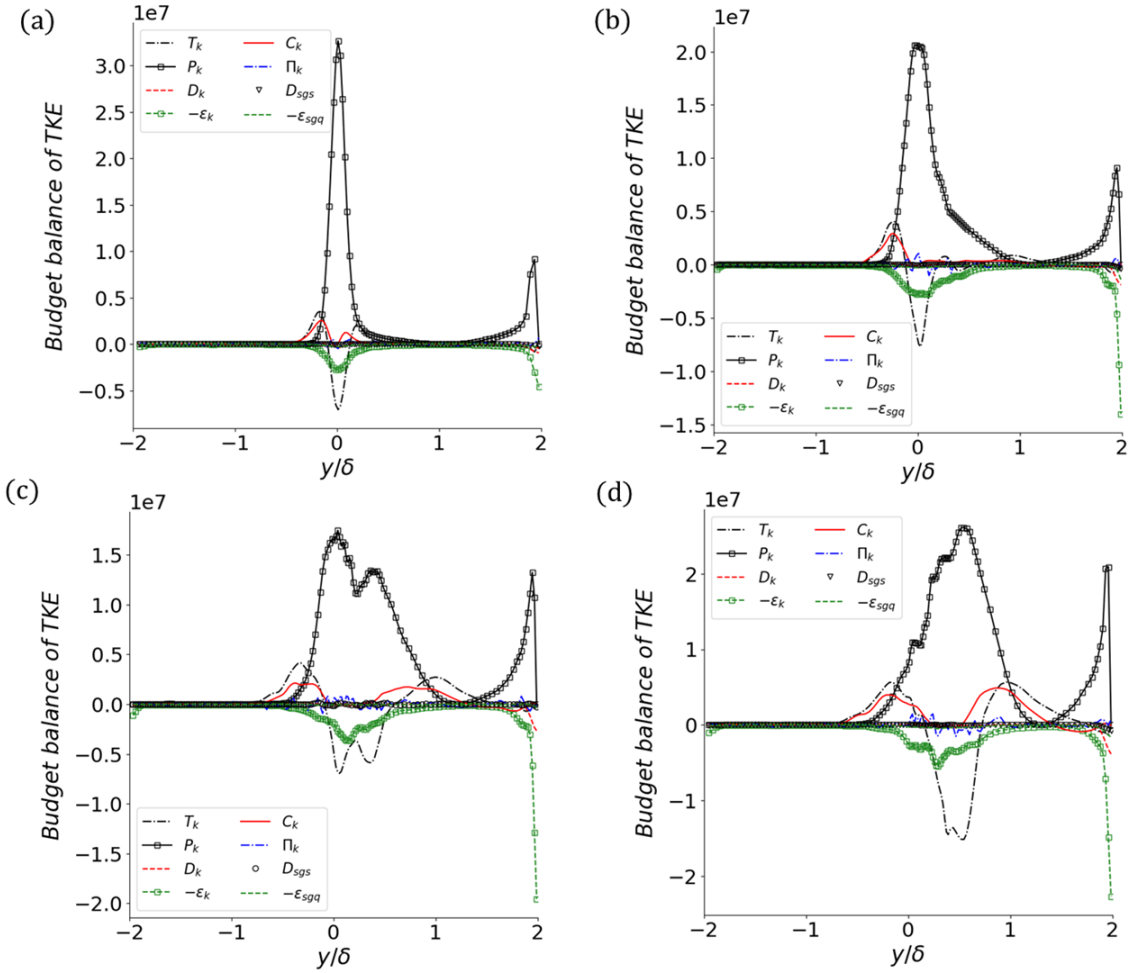

Figure 5.22 Cross-streamwise distribution of turbulent budget terms of TKE transport equation for (a) BR = 0, (b)BR = 0.05, (c) BR = 0.1, and (d) BR =0.2 at x/δ =0.5, and z/δ = 1.0.

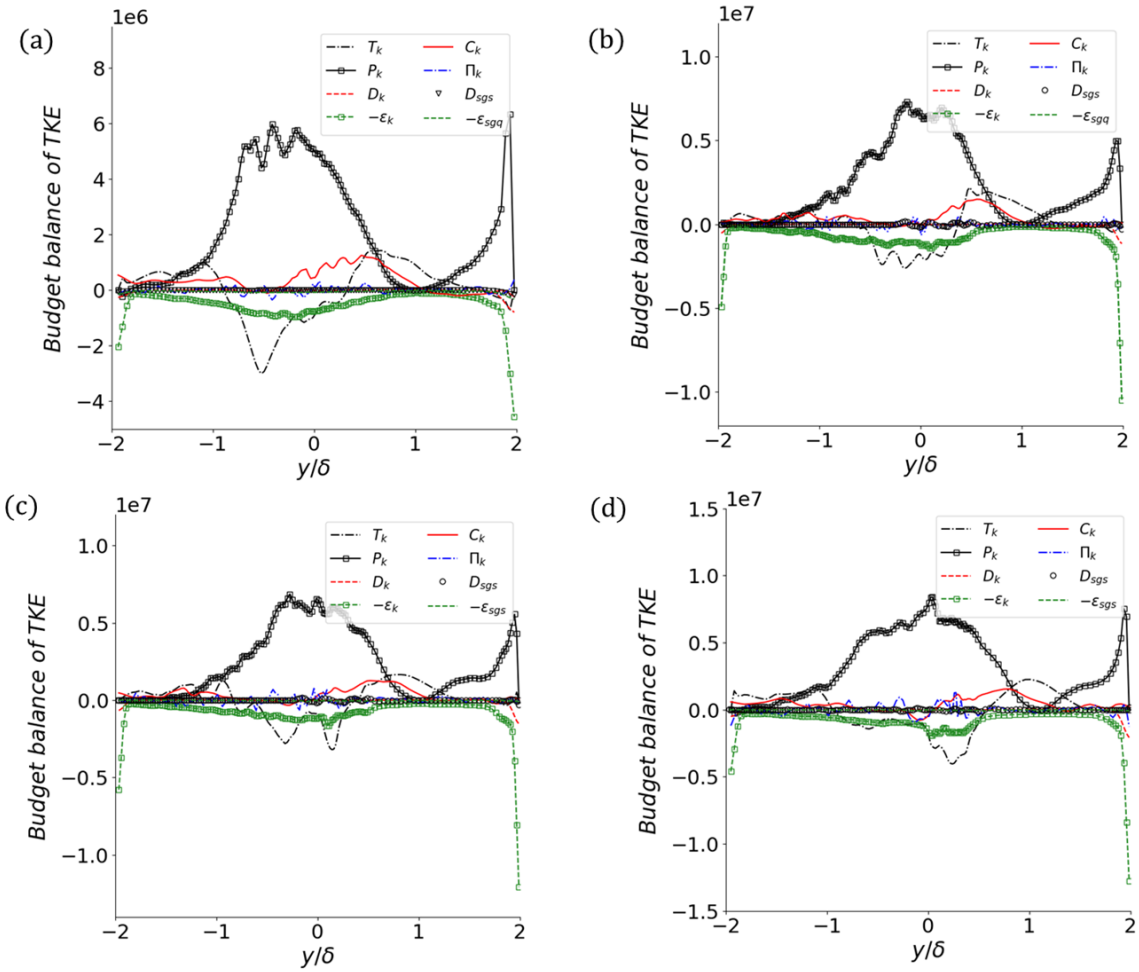

Figure 5.23 Cross-streamwise distribution of turbulent budget terms of TKE transport equation for (a) BR = 0, (b)BR = 0.05, (c) BR = 0.1, and (d) BR =0.2 at x/δ =5.0, and z/δ = 1.0.

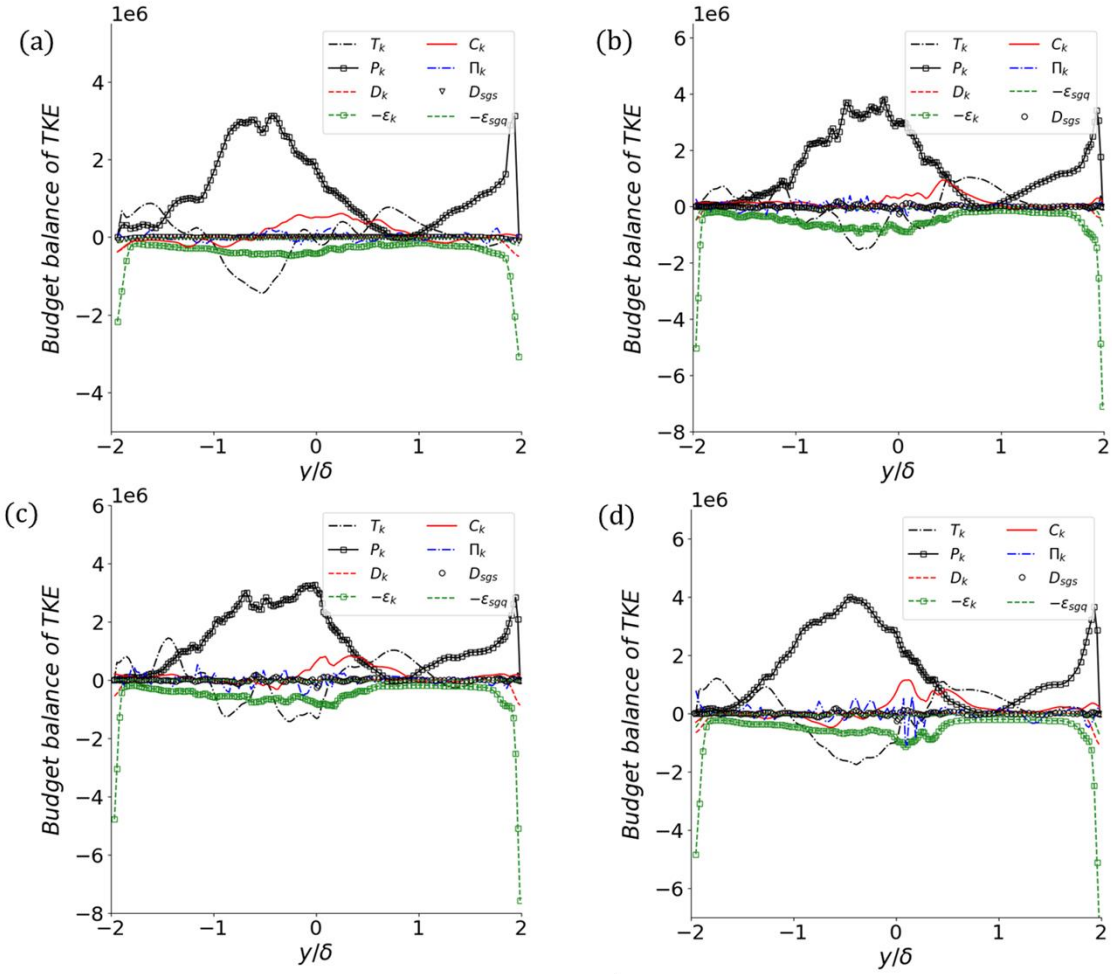

Figure 5.24 Cross-streamwise distribution of turbulent budget terms of TKE transport equation for (a) BR = 0, (b)BR = 0.05, (c) BR = 0.1, and (d) BR =0.2 at x/δ =7.5, and z/δ = 1.0.

5.3.5 Quadrant Analysis and Third Order Moment of Fluctuating Velocity

Third order moment of fluctuating velocity typically is used for elucidating turbulent transport mechanism(Krogstadt and Antonia, 1999) or identification of ejection sweeping process in turbulent flows, which are particularly visible around hairpin structures.

In the case of hairpin vortical structures the quasi-streamwise counter rotating legs and the hairpin head, are the major contributor to the flow ejection from low momentum region (typically close to walls) to the high momentum regions. The compensation of the ejection flows occurs through directing the high momentum flows form above the hairpin

structures downwards to the outer region of hairpin structures(Adrian and Liu, 2002). As observed (from the Figure corresponding to the Q2), hairpin structures are majorly formed above and close to the rib crests, where the shear layer develops, convect and evolve downstream. Henceforth, these structures can have a remarkable effect of unsteadiness and turbulence characteristics of flow in this region and also downstream shear layer. ejection accompanies with $u'' > 0$ and $v'' < 0$, and sweep event is associated with $u'' < 0$ and $v'' < 0$ ($''$ shows resolved fluctuations). As previous studies have shown, in the third moment fluctuations in diagrams, ejection and sweeping happen when $\langle u''u''u'' \rangle$ and $\langle v''v''v'' \rangle$ switch their signs from positive to negative and vice versa.

Figure 5.25 demonstrates the distributions of the third-moment fluctuating velocities along the line at x/δ=−9.4 (corresponding to x′/δ=0.4, and z/δ=1.0). For the analysis of velocity fluctuation diffusion terms, only the two vertical diffusion terms, $\langle u''v''v'' \rangle$ and $\langle u''u''v'' \rangle$, are considered, as previous studies have identified them as the most effective diffusion terms. From Figures 5.25(a) and (b), it is evident that the vicinity of the rib crest is associated with large positive $\langle u''u''u'' \rangle$ values and large negative $\langle v''v''v'' \rangle$ values. This combination is indicative of the flapping motion of the shear layer, which leads to an enhancement of both ejection and sweeping events(Mahmoodi-Jezeh and Wang, 2020). An increase in Blockage Ratio (BR) positively influences the magnitude of these large positive $\langle u''u''u'' \rangle$ and large negative $\langle v''v''v'' \rangle$ values in this region, signifying reinforced flapping motions (which will be investigated in more detail in the spectral and modal analysis sections).

The negative values of $\langle u''u''v'' \rangle$ observed below the crest imply the vertical diffusion of streamwise fluctuations ($\langle u''u'' \rangle$) towards the low-momentum bottom wall, which is associated with sweeping events in these areas. This phenomenon coincides with positive values of $\langle u''u''u'' \rangle$, thereby demonstrating a streamwise acceleration of this diffusion within the region. Conversely, on top of the crest, $\langle u''u''v'' \rangle$ exhibits a positive sign, indicating the vertical diffusion of streamwise fluctuations towards the high-momentum flow away from the crest region (via ejection). Simultaneously, $\langle u''u''u'' \rangle$ is negative, suggesting a streamwise deceleration during the ejection event as the flow moves away from the crest. This implies that $\langle u''u'' \rangle$ diffuses outwards from the rib vicinity (in the

vertical direction) with contrasting signatures on either side, suggesting that the source driving these fluctuations is located around the rib.

Furthermore, the opposite sign of the vertical diffusion of the shear Reynolds stress $\langle u''v''v''\rangle$ indicates the diffusion of shear stresses towards the rib region. This behavior is consistent with the shear layer generation of hairpin structures, as explained in(Mahmoodi-Jezeh and Wang, 2020).

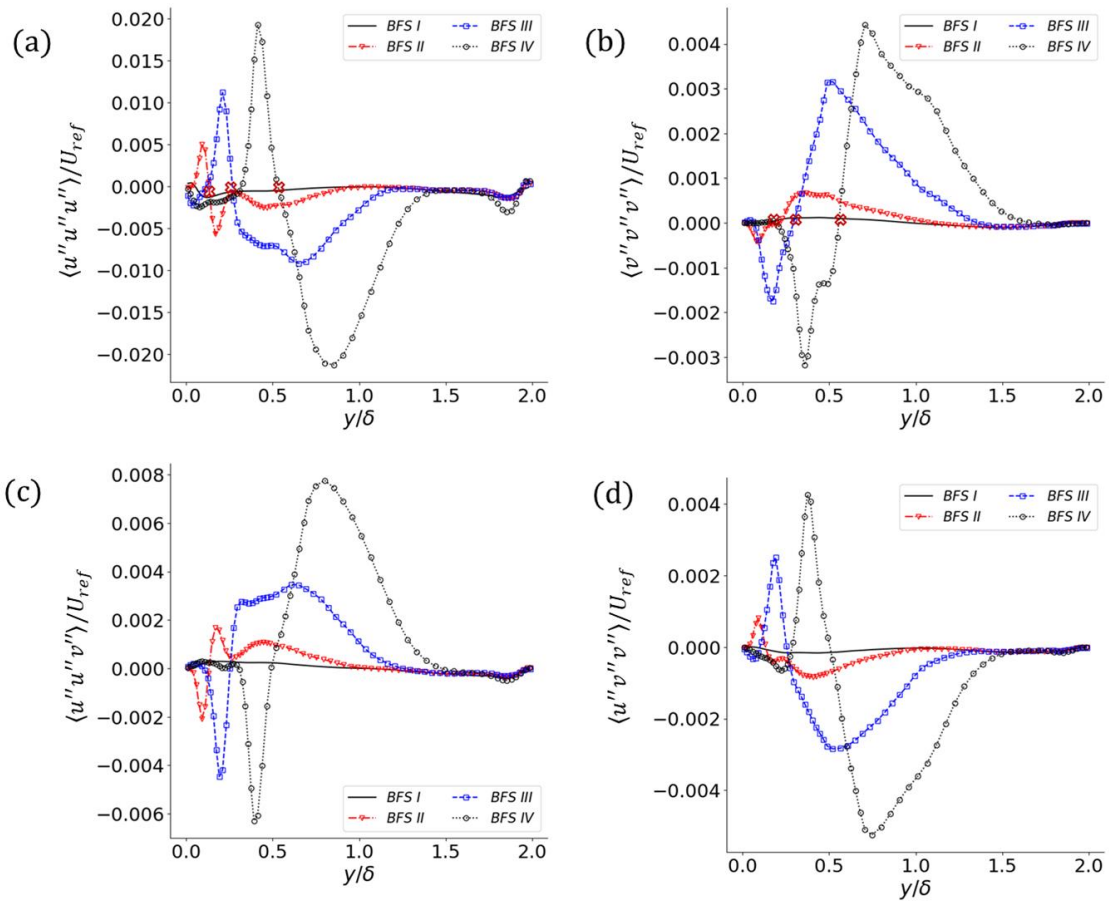

Figure 5.25 Third-order moment of fluctuating velocity at (x/δ =-9.4, x'/δ=0.4, and z/δ = 1.0 for BR = 0, 0.05, 0.1, and 0.2, respectively).

Moving downstream of the step (x/H=0.5), the trend of the third-order moments of fluctuating velocity remains very similar to that observed in the rib region (Figure 5.25). A clear inflection point is still evident in both $\langle u''u''u''\rangle$ and $\langle v''v''v''\rangle$, this time located closer to the shear layer. This inflection point shifts upwards from y/δ=0 to y/δ=0.57 as the Blockage Ratio (BR) increases from 0 to 0.2 (assuming '2' was a typo for '0.2' based on previous context, Figure 5.26(a) and (b)). Consequently, one can infer that the ejection

and sweeping events shift towards larger y values and become more intense in this region with increasing BR. Similar conclusions regarding the vertical diffusion of $\langle u''u'' \rangle$ and $\langle u''v'' \rangle$ can also be drawn from Figure 5.26(c) and (d), mirroring the behavior discussed for the rib region.

As the flow progresses even further downstream, this general trend is maintained, although the inflection point shifts downwards for all BRs, consistently remaining close to the shear layer. Concurrently, the magnitudes of the moments decrease and become more similar across all BR values (Figures 5.27 and 5.28). This indicates that the ejection and sweeping events become weaker and more uniform across different BRs as the flow moves away from the step.

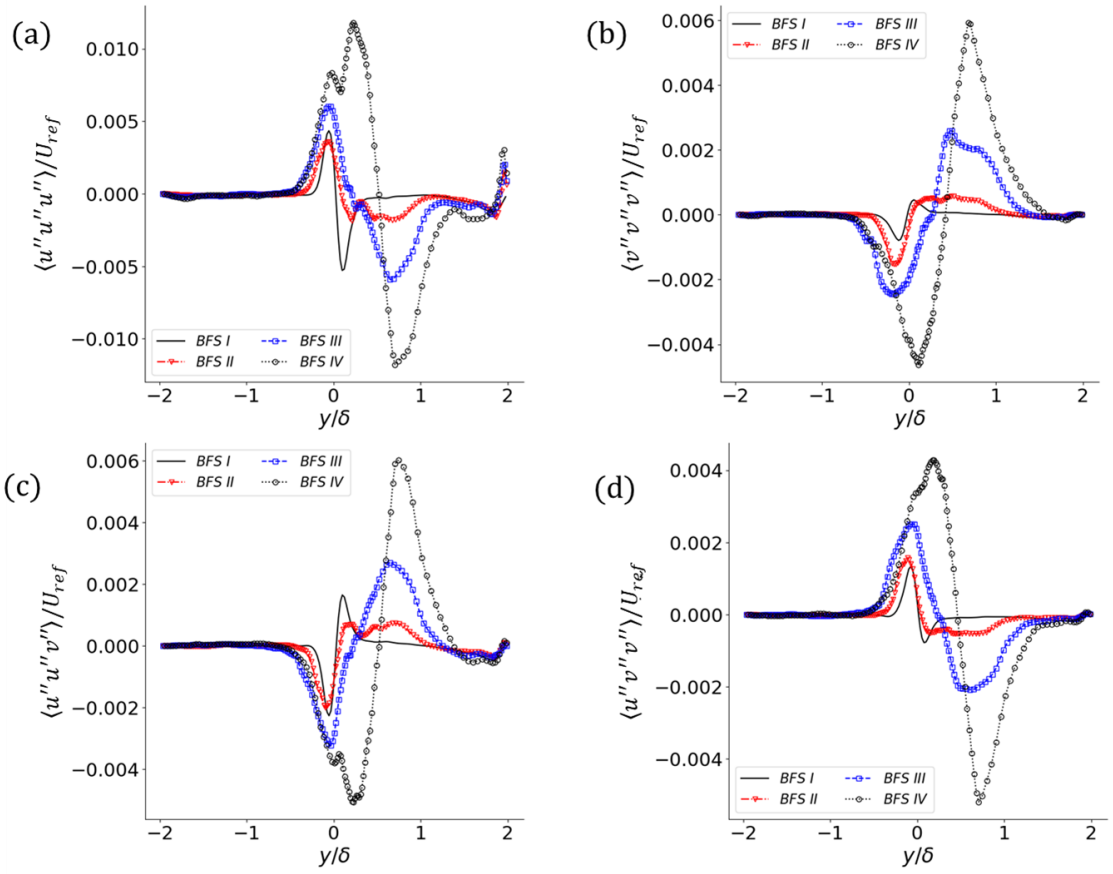

Figure 5.26 Third-order moment of fluctuating velocity at (x/H =0.5, and z/δ = 1.0 for BR = 0, 0.05, 0.1, and 0.2, respectively).

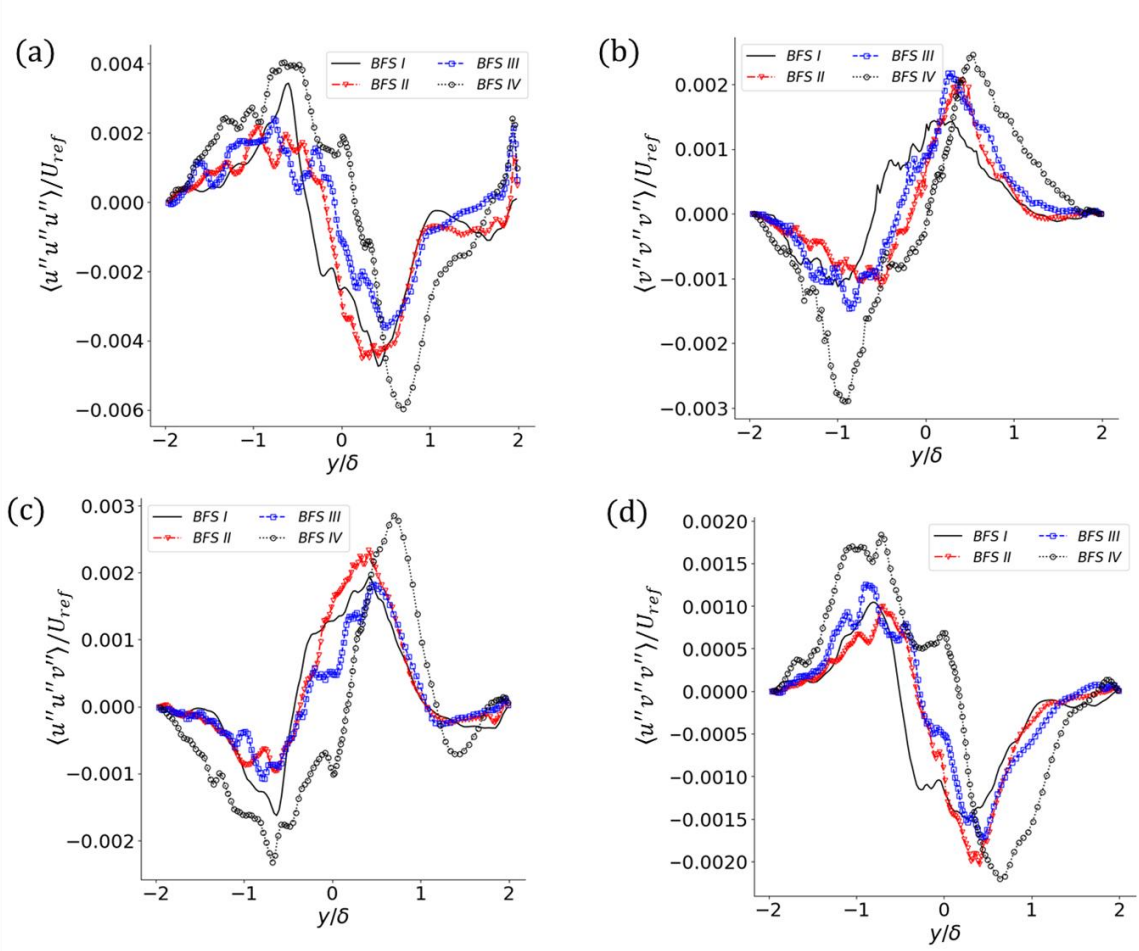

Figure 5.27 Third-order moment of fluctuating velocity at (x/H = 5.0, and z/δ = 1.0 for BR = 0, 0.05, 0.1, and 0.2, respectively).

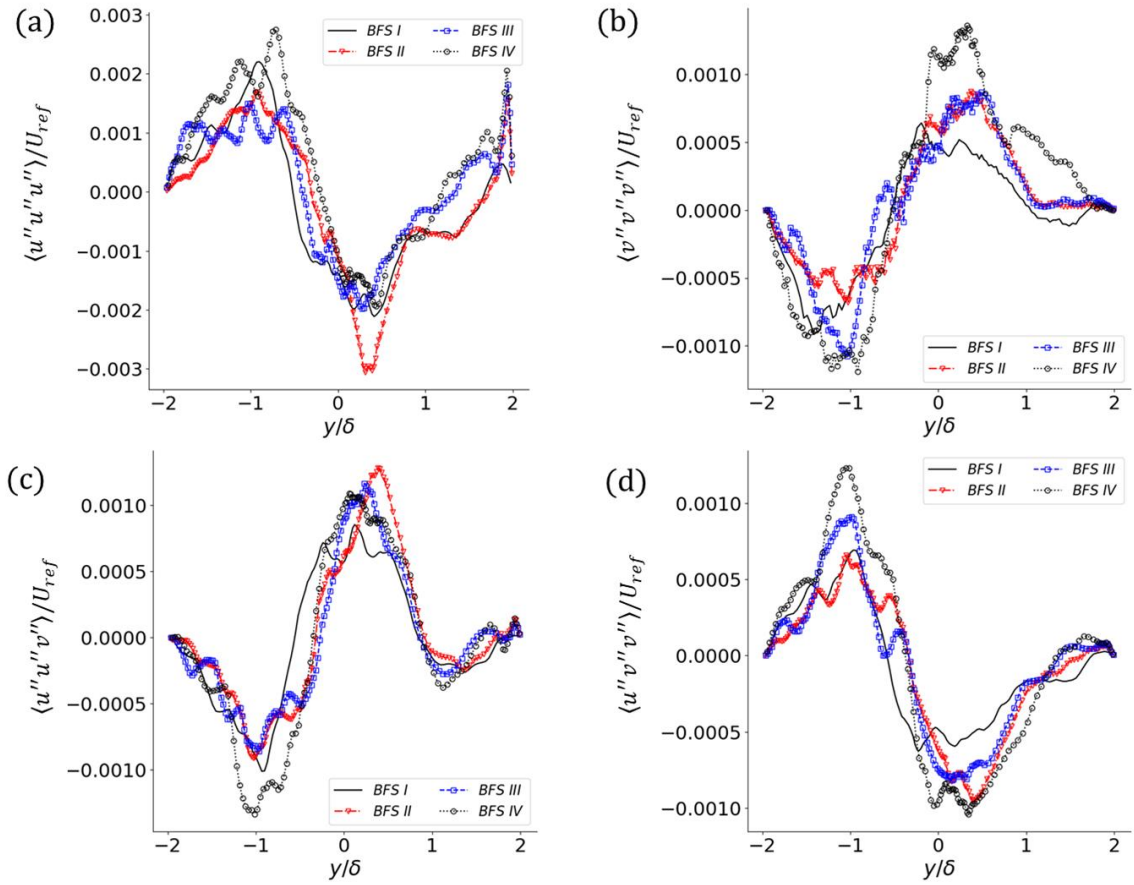

Figure 5.28 Third-order moment of fluctuating velocity at (x/H =7.5, and z/δ = 1.0 for BR = 0, 0.05, 0.1, and 0.2, respectively).

Quadrant analysis is employed to investigate the intensity of ejection and sweeping events at different distances from the crest. In this study, we utilize the joint probability distribution function (JPDF) of $\langle u'' \rangle$ and $\langle v'' \rangle$ at three distinct elevations (Figure 5.29: close to the crest and at higher distances) to perform the quadrant analysis. Each distribution is thus decomposed into four regions corresponding to: (1) $u'' > 0$ and $v'' > 0$, (2) $u'' < 0$ and $v'' > 0$, (3) $u'' < 0$ and $v'' < 0$, and (4) $u'' > 0$ and $v'' < 0$. According to previous studies(KROGSTAD et al., 2005; Lelouvetel et al., 2009), the second $(u'' < 0, v'' > 0)$ and fourth $(u'' > 0, v'' < 0)$ quadrants are associated with ejection and sweeping events, respectively.

The JPDF results demonstrate that for a smooth surface (Figures 5.29(a), (b), and (c)), in the vicinity of the boundary layer, the JPDF predominantly fills the second and fourth quadrants, forming an angle of approximately 135∘ with respect to the horizontal axis.

These results indicate that at distances closer to the wall, ejection events are dominant (Figure 5.29(a)) due to higher JPDF values in this region. As one moves away from the wall (Figures 5.29(b) and (c)), sweeping events become dominant.

With increasing Blockage Ratio (BR), it is observed that at elevations around the crest (Figures 5.29(d), (g), and (j)), the distribution across all quadrants becomes nearly identical, suggesting the presence of random, uncorrelated ejection and sweeping events in these regions. Moving away from the crest, a correlated JPDF distribution with a 135∘ angle re-emerges in all cases. Specifically, at the given distances, the JPDF exhibits larger values in the ejection quadrant ($u'' < 0, v'' > 0$) for BR = 0.05 (Figures 5.29(e) and (f)). In contrast, for BR = 0.1 and 0.2, sweeping-dominant patterns appear (Figures 5.29(h) and (k)), which subsequently transition into ejection-dominant patterns as one moves further away from the crest (Figures 5.29(i) and (l)).

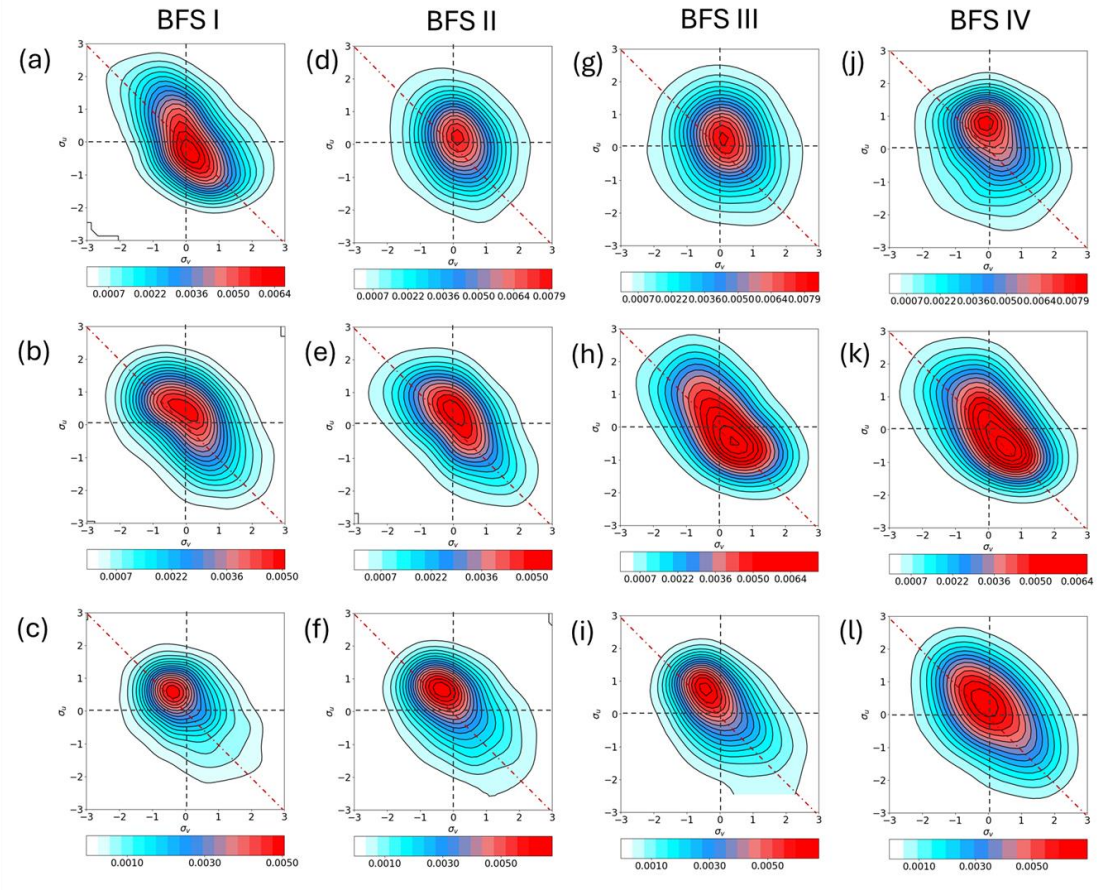

Figure 5.29 Joint probability distribution function JPDF of ($\boldsymbol{\sigma_u = u''/U_{ref}}$ and $\boldsymbol{\sigma_v = v''/U_{ref}}$) at different distances from the rib crest at x/δ =9.4, x'/δ=0.4, and z/δ = 1.0 and

(a) y/δ = 0.05, (b) y/δ = 0.1, (c) y/δ = 0.2 for BFS I; (d) y/δ =0.05, (e) y/δ = 0.14, and (f) y/δ = 0.6 for BFS II; (g) y/δ =0.1, (h) y/δ = 0.24, and (i) y/δ = 0.6 for BFS III; (j) y/δ =0.2, (k) y/δ = 0.44, and (l) y/δ = 0.6 for BFS IV;

5.3.6 Turbulence Anisotropy

The Reynolds stress anisotropy tensor, which quantifies the departure of a turbulent flow from an isotropic (spherical) state, is typically given by the following formula(Pope, 2000; Shahab et al., 2011):

$$b_{ij} = \frac{\langle u_i' u_j' \rangle}{\langle u_k' u_k' \rangle} - \frac{1}{3}\delta_{ij}$$

Previous studies have utilized the Reynolds stress anisotropy tensor to investigate the influence of wall roughness on the anisotropic state of turbulence near walls in both two-dimensional planes(KROGSTAD et al., 2005) and three-dimensional channels(Stiperski et al., 2021). As the ratio of these stress tensor components approaches unity, the turbulent flow becomes more isotropic.

Figure 5.30 illustrates the distribution of the Reynolds stress anisotropy tensor for its b11 , b22, b33, and b12 components. These results demonstrate a significant reduction in the magnitude of the b11, b22, and b33 components close to the wall and near the crest region. Furthermore, it's observed that the peaks and valleys of these components shift towards the right across the entire channel with increasing BR, indicating a change in the flow's anisotropic state as BR values rise. Lumley & Newman (1976) and(KROGSTAD et al., 2005) proposed using an invariant function as an estimation for the overall anisotropy of the Reynolds stress tensor within the flow.

This function is expressed as $F = 1 + 9II + 27III$, where $II = \frac{1}{2} b_{ij} b_{ji} = b_{11}^2 - b_{22} b_{33} + b_{12}^2$ and $III = \frac{1}{3} b_{ij}\, b_{jk} b_{ki} = b_{33}(b_{11} b_{22} - b_{12}^2)$. Figure 5.30(e) shows the distribution of the invariant function along the line at x/δ=−9.4 (corresponding to x′/δ=0.4, and z/δ=1.0). A notable observation is a significant reduction in the invariant function below the crest region for larger BR values. This reduction is followed by local peaks and valleys that shift to the upper region of the channel. This pattern clearly reveals that ribs decrease the overall turbulence anisotropy below the crest. However, the anisotropic state above the

crest merely shifts horizontally with increasing BR, showing negligible variations in its magnitude. This includes the local anisotropic peaks above the crest, which are formed from shear stresses.

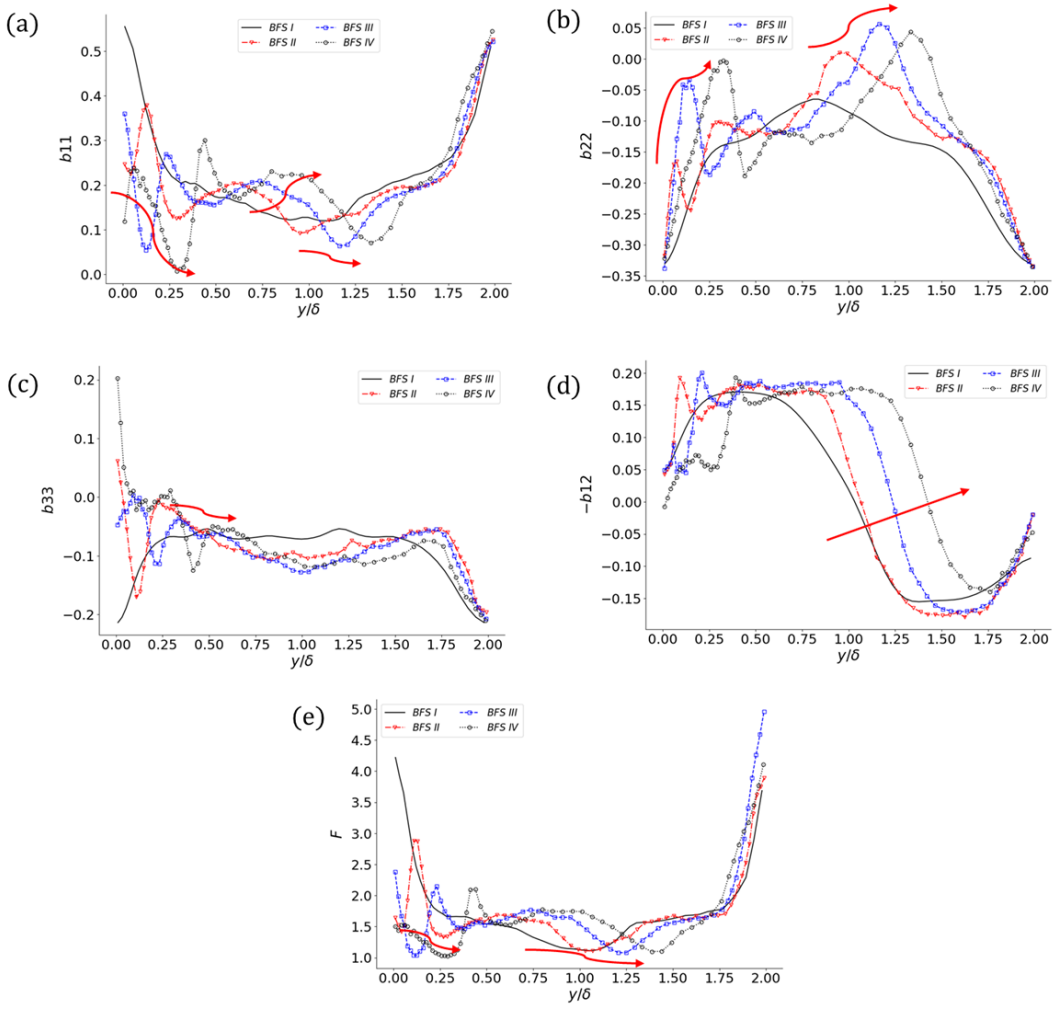

Figure 5.30 Cross-streamwise distribution of anisotropy Reynolds stress tensor distribution at (x/δ =-9.4, x'/δ=0.4, and z/δ = 1.0 for BR = 0, 0.05, 0.1, and 0.2, respectively) for (a) b_{11}, (b) b_{22}, (c) b_{33}, (d) b_{12} components, and (e) Invariant function F =1+9II+27III (red flash shows the direction of increasing BR for BR>0).

To investigate the effect of Blockage Ratio (BR) on the turbulent anisotropic state downstream of the step, the distribution of Reynolds stress anisotropy tensor components at the center-plane (z/δ=1) and at different streamwise distances from the step (x/H=0.5,5.0, and 7.5) are presented in Figures 5.31, 5.32, and 5.33, respectively.

Figures 5.31(a), (b), and (c) demonstrate that at x/H=0.5, the shear layer remarkably enhances the magnitude of the b11, b22, and b33 components of the anisotropy Reynolds stress tensor for BR = 0 in the vicinity of y/δ≈0. However, this enhancement is significantly attenuated with increasing BR. Figure 5.31(e) exhibits the same trend for the overall turbulence anisotropic state of the flow, characterized by a local peak close to y/δ≈0. The location of this local peak coincides with the significant mean velocity gradient present in this region, which is particularly pronounced for small BR values. According to previous studies(Stiperski et al., 2021), velocity gradients and shear effects can enhance turbulence anisotropy through several mechanisms, including but not limited to the injection of energy into preferential velocity components, the exertion of linear strain on turbulent eddies resulting in the alignment of these structures in a particular direction, and the suppression of cross-gradient motions.

Moving downstream, as the mean velocity gradient across the shear layer attenuates, its effect on the anisotropic state of the flow becomes mitigated (Figures 5.32 and 5.33). Despite this, a local peak in the invariant function (F) is still observed, centered around y/δ=0.5 and y/δ=0.4 in Figures 5.32 and 5.33, respectively.

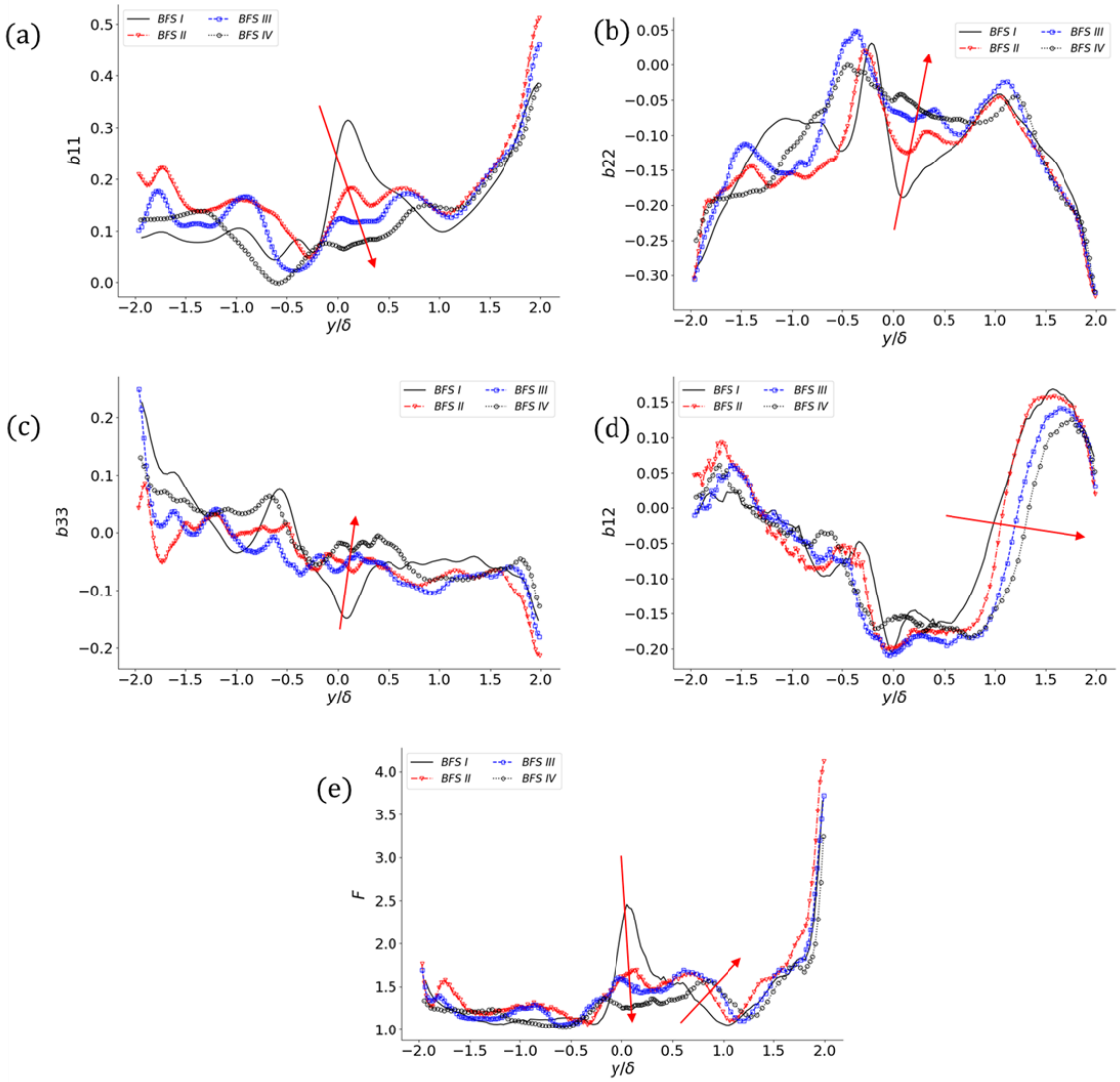

Figure 5.31 Cross-streamwise distribution of anisotropy Reynolds stress tensor distribution at (x/δ =0.5, and z/δ = 1.0 for BR = 0, 0.05, 0.1, and 0.2, respectively) for (a) b11, (b) b22, (c) b33, (d) b12 components, and (e) Invariant function F =1+9II+27III (red flash shows the direction of increasing BR for BR>0)

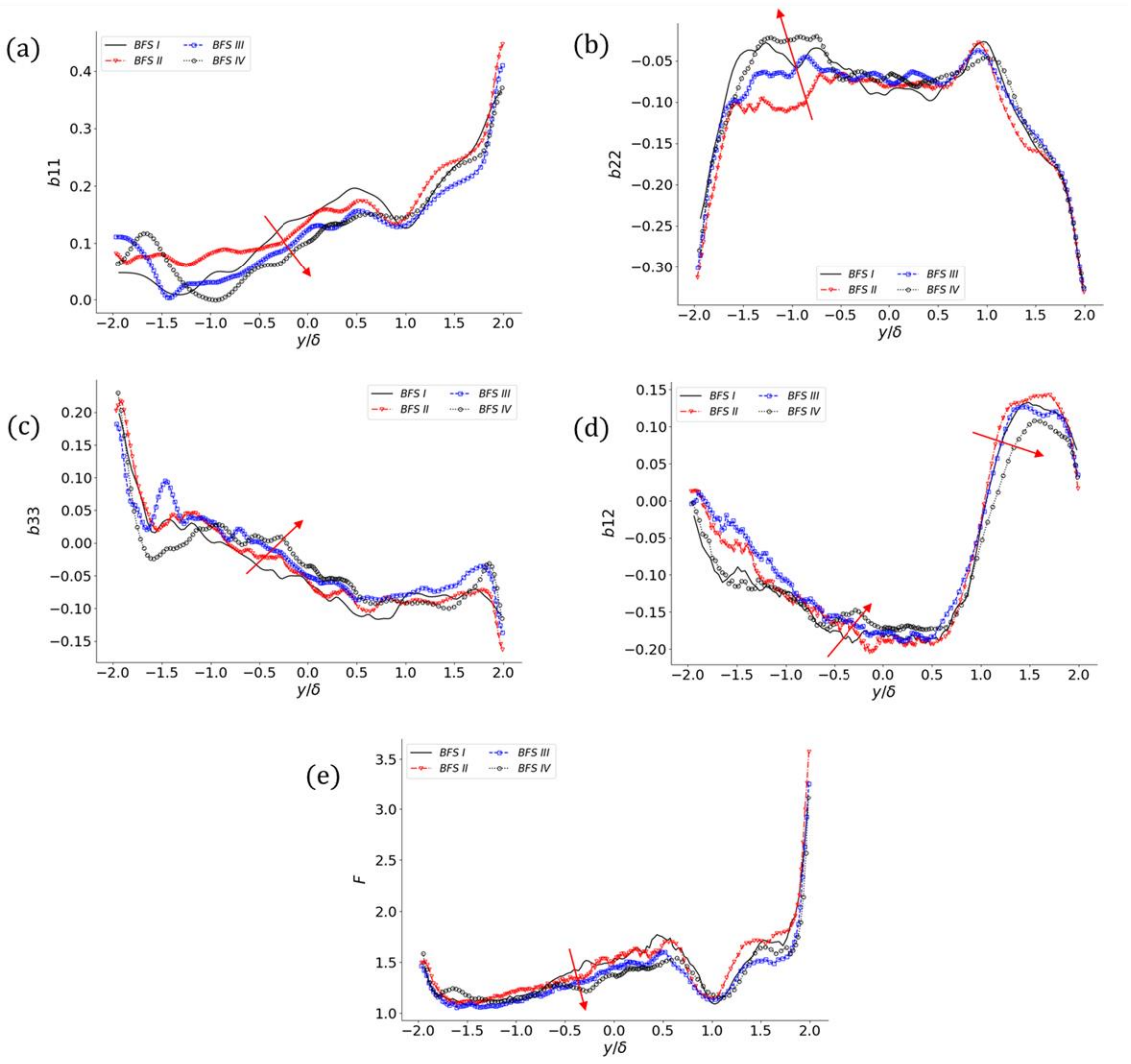

Figure 5.32 Cross-streamwise distribution of anisotropy Reynolds stress tensor distribution at (x/δ =5.0, and z/δ = 1.0 for BR = 0, 0.05, 0.1, and 0.2, respectively) for (a) b11, (b) b22, (c) b33, (d) b12 components, and (e) Invariant function F =1+9II+27III (red flash shows the direction of increasing BR for BR>0)

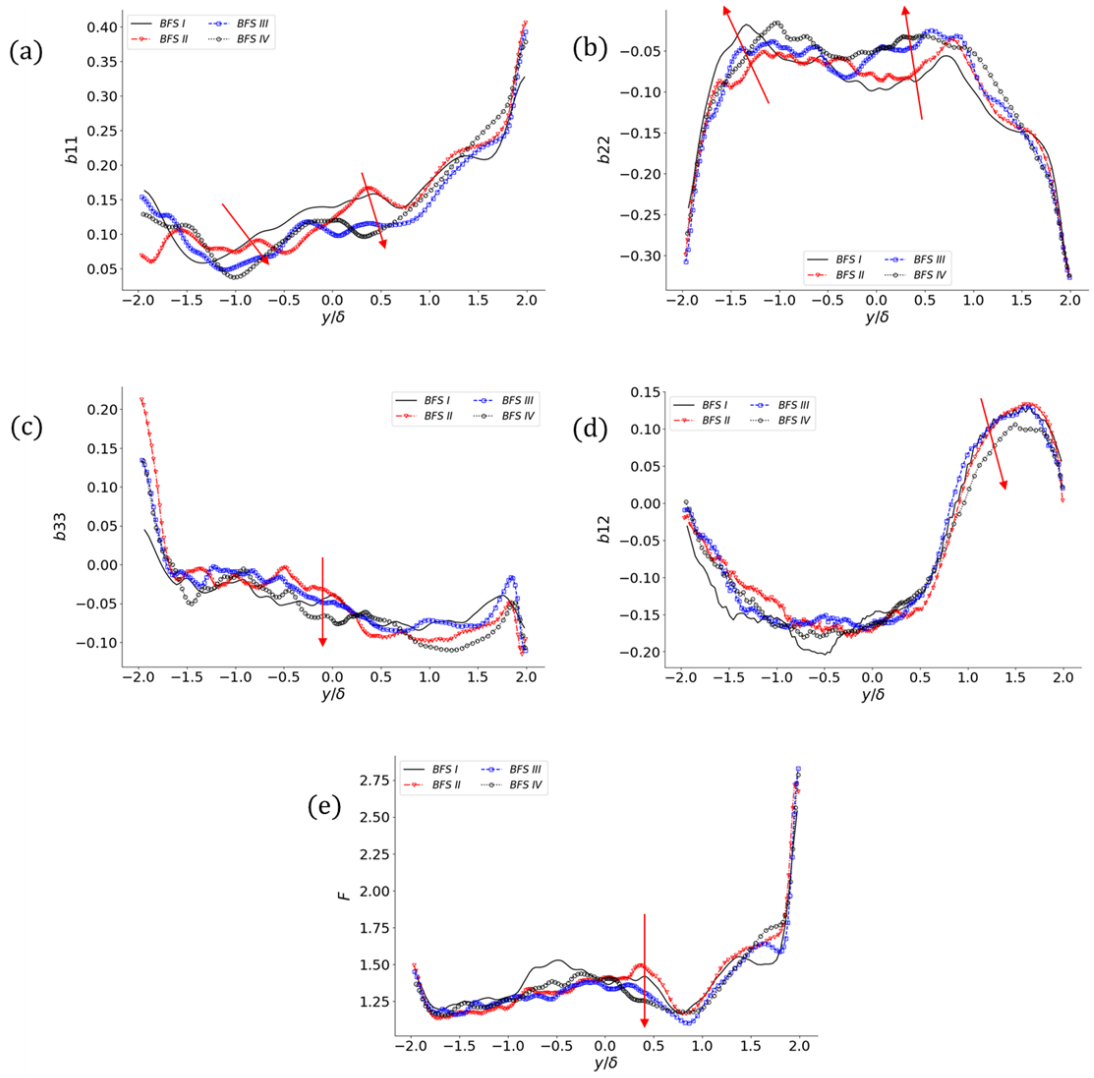

Figure 5.33 Cross-streamwise distribution of anisotropy Reynolds stress tensor distribution at (x/δ =7.5, and z/δ = 1.0 for BR = 0, 0.05, 0.1, and 0.2, respectively) for (a) b11, (b) b22, (c) b33, (d) b12 components, and (e) Invariant function F =1+9II+27III (red flash shows the direction of increasing BR for BR>0)

Figure 5.34 presents the autocorrelation of the three components of velocity fluctuations at specific distances from the rib crest. These selected heights correspond to regions of maximum fluctuations, as depicted in Figure 5.14. Various studies(ADRIAN et al., 2000; VOLINO et al., 2009) have employed velocity fluctuation autocorrelation to identify hairpin structures and determine their characteristic lengths and inclination angles in diverse flow fields, including 2D planes and 3D channel flows. This technique can also be valuable for identifying other coherent structures, such as spanwise and quasi-streamwise vortices.

According to(VOLINO et al., 2009), the inclination angle of a hairpin structure is highly dependent on its location within the flow. Furthermore,(ADRIAN et al., 2000) suggests that three distinct signatures in a 2D plane can reveal hairpin structures. Considering the JPDF results in Figure 5.29, where we observed that Q2 and Q4 dominant regions are located with a small distance at approximately the same heights used here, coupled with the turbulent structures identified by the Q-criterion, the selected regions are indeed strong candidates for hairpin structure identification across different Blockage Ratios (BR).

The first observation from the streamwise fluctuation autocorrelation is a monotonic increase in the width of the isopleth, accompanied by a decrease in the inclination angle. According to (Israel et al., 2024), a stagnation point develops in front of a hairpin structure where Q2 and Q4 dominant regions converge, which directly specifies the corresponding inclination angle. Therefore, the observed decrease in this angle indicates that sweeping is more dominant for larger BR values at the specified distance from the crest. This finding is consistent with the results presented in Figure 5.29. On the other hand, the isopleths of spanwise fluctuations become shorter with increasing BR, suggesting that the hairpin legs are smaller in these cases.

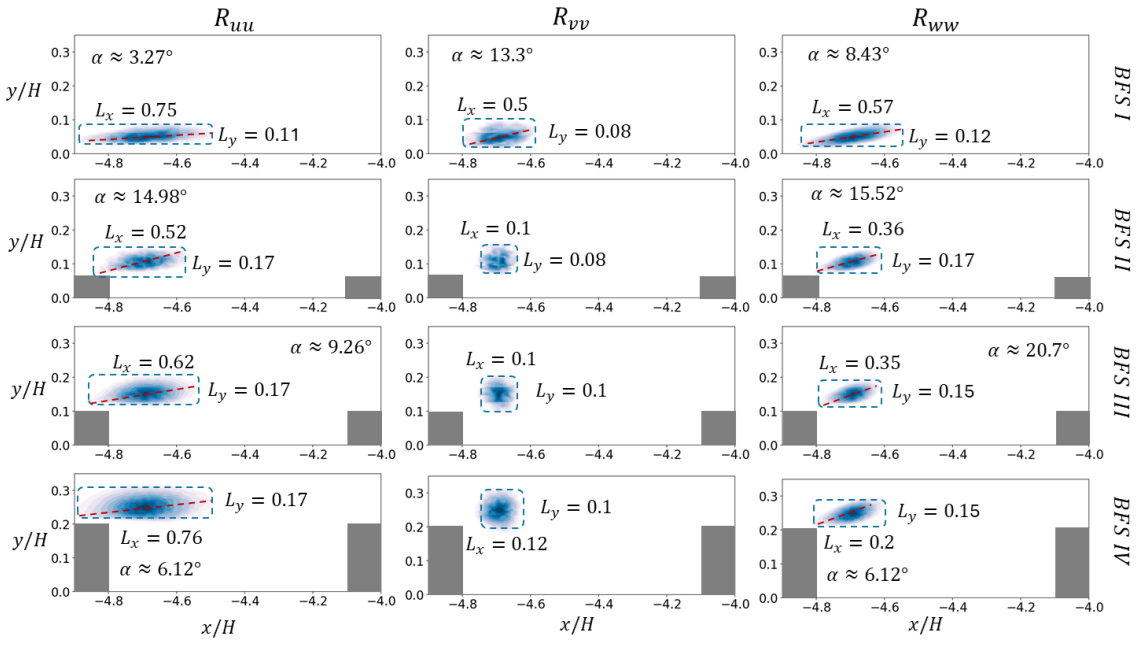

Figure 5.34 Isopleth of auto-correlation of velocity fluctuation components (u, v, and w) at x/δ =-9.4, x'/δ=0.4, and z/δ = 1.0, and elevations of y/δ= 0.05, 0.14, 0.24, and 0.44

for BR = 0, 0.05, 0.1, and 0.2, respectively). Where $\boldsymbol{L_x}$ and $\boldsymbol{L_y}$ represent horizontal and vertical lengths of the isopleth normalized by $\boldsymbol{\delta}$.

Figure 5.35 provides contours of isopleths for the autocorrelation of streamwise velocity fluctuation, located close to the mean separation streamline downstream of the step. Additionally, the horizontal (Lx) and vertical (Ly) lengths of selected isopleths (denoted as b1, b2, and b3, representing isopleths at x/H=0.5, 7.0, and 10.0, respectively) are detailed in Table 5.1.

It can be observed that these isopleths form an elliptical shape, predominantly oriented in the streamwise direction. These isopleths are interpreted as representing spanwise coherent structures that possess high spatial integrity in the streamwise direction(Israel et al., 2024). For all BR values, the isopleths are seen to spatially evolve along the shear layer, a phenomenon likely resulting from the pairing process of smaller spanwise vortices.

A comparison between identical isopleths for different BR values reveals that increasing BR leads to an increase in the size of b1 and b3, while the size of b2 decreases. This observation aligns consistently with the results for vorticity thickness (Figure 5.5), which demonstrated that increasing BR causes the shear layer thickness to increase in its initial part, decrease in the second part, and then increase again downstream of the reattachment point. These findings collectively indicate that the properties of the incoming TBL, which vary with BR values, significantly influence the integrity of coherent structures downstream of the step.

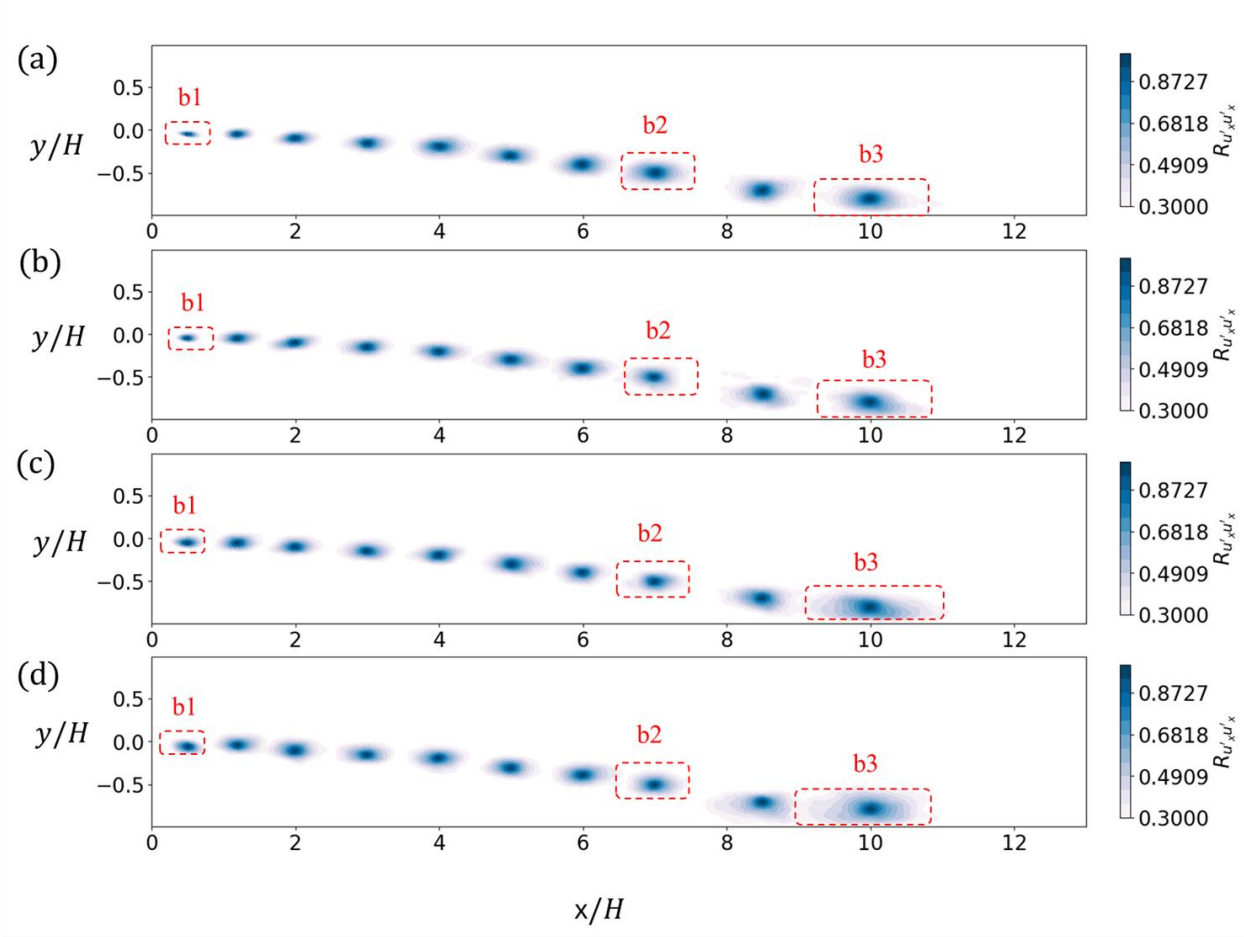

Figure 5.35 Isopleth of auto-correlation of streamwise velocity fluctuation components (u) at x/δ =0.5, 5.0, and 7.5, along the shear layer and reattachment for (a) BR = 0, (b) BR = 0.05, (c) BR = 0.1, and (d) BR = 0.2.

Table 5.1 Normalized sizes corresponding to isopleths in Figure 5.34, where $\boldsymbol{L_x}$ and $\boldsymbol{L_y}$ represent horizontal and vertical lengths of the isopleth normalized by H.

		b1	*b2*	*b3*
BFS I	Lx/H	0.36	1.15	1.55
	Ly/H	0.12	0.42	0.35
BFS II	Lx/H	0.39	1.0	1.65
	Ly/H	0.15	0.4	0.35
BFS III	Lx/H	0.55	1.0	2.1
	Ly/H	0.22	0.4	0.45
BFS IV	Lx/H	0.56	0.9	2.1
	Ly/H	0.2	0.37	0.49

5.3.7 Spectral Analysis (Shear Layer and Rib Wake)

Spectral analysis was conducted to explore the frequency characteristics of unsteadiness and turbulent structures in both Region I (corresponding to the incoming turbulent boundary layer, TBL) and Region II (downstream of the step). For this purpose, the pre-multiplied power spectral density (PSD) of streamwise velocity frequency was calculated for points at different streamwise distances.

Figure 5.36 represents variations of the pre-multiplied PSD versus a dimensionless temporal scale (the inverse of which indicates the Strouhal number). The region between the two red dotted vertical lines denotes the range of temporal scales where the pre-multiplied PSD exceeds 70% of its peak value, thereby representing the zone of highly energetic motions. As the PSDs were calculated at the same points as the isopleths presented in Figure 5.36, it can be inferred that these temporal scales are indicative of ejection/sweeping events (or the shedding of hairpin vortices) in this region.

Two dominant trends are observed with increasing Blockage Ratio (BR). First, the range of highly energetic motion temporal scales expands, indicating that a broader spectrum of fluctuation frequencies falls within the high-energy zone. Second, the center of this high-energetic zone shifts towards larger temporal scales, signifying that the characteristic frequency of the dominant motions becomes slower.

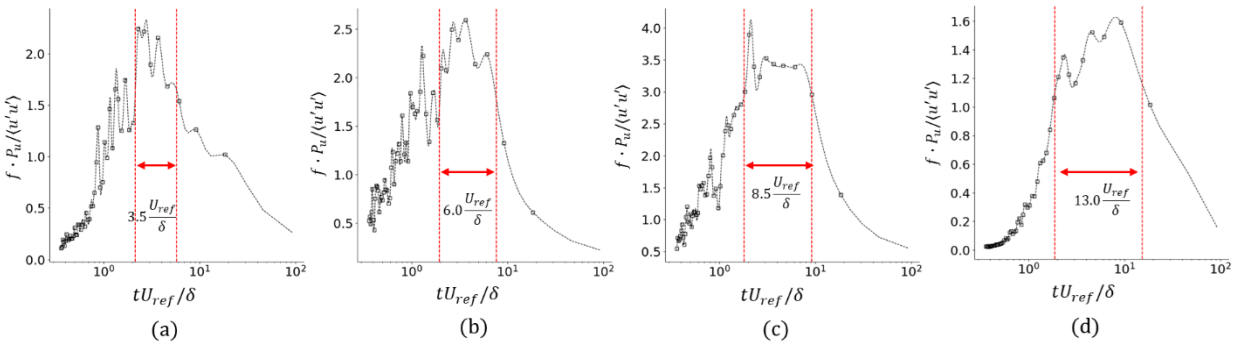

Figure 5.36 Comparison of the Premultiplied PSD, $\boldsymbol{f \cdot P_u/\langle u'u' \rangle}$, of streamwise velocity fluctuations for different blockage ratios at the elevation above the rib crest (at x/δ =-9.4, x'/δ=0.4, and z/δ = 1.0, and elevations of y/δ= 0.05, 0.14, 0.24, and 0.44). (a) Br = 0.05, (b) Br = 0.1 and (c) Br = 0.2.

Figure 5.37 provides the pre-multiplied power spectral density (PSD) of streamwise velocity at various points along the shear layer downstream of the step for different

Blockage Ratios (BR). Dominant timescales, characterized by local peaks in the pre-multiplied PSD, are represented by ti, where the subscript i ranges from 1 to 3, denoting the smallest to the largest dominant timescale, respectively.

Previous studies have shown that the smallest dominant timescale, t1 (corresponding to the highest frequency), is typically associated with fluctuations of small spanwise coherent structures in the initial part of the shear layer(Hudy et al., 2007; W. Wu et al., 2020). As the flow progresses along the shear layer, vortices grow, and subsequent pairs of vortices merge, forming larger spanwise vortices that shed within the shear layer at a larger timescale (t2, which is nearly double t1) and a correspondingly lower frequency(Hudy et al., 2007). Further downstream along the shear layer, the influence of the small timescale shedding is mitigated, as evidenced by a decrease in the PSD level corresponding to t1. Simultaneously, new PSD peaks emerge and grow at a larger timescale (t3), eventually reaching their maximum near the reattachment region. This indicates that t3 is associated with the slow displacement of the reattachment point and the shedding of vortices in this region.

Previous research has linked this low-frequency dynamics to the breathing mechanism of separation bubble dynamics. This includes phenomena such as the feedback of disturbances from the impingement point to the separation point(Hasan, 1992), the cutting of the recirculation zone by large structures moving upstream and heating the wall, and the low-frequency forcing of the separation bubble by large streamwise Görtler-like vortices expanding from separation to downstream of reattachment, accompanied by the low-frequency release (shedding) of groups of vortices from the separation bubble (at the reattachment point)(W. Wu et al., 2020). In the next section, modal analysis will be implemented to further investigate this effect and the influence of BR values on these dynamics.

The pre-multiplied Power Spectral Density (PSD) of streamwise velocity fluctuations (Figure 5.37) at x/H=0.5 reveals that the ratio of the local peak PSD level corresponding to the t2 timescale to that of the t1 timescale varies between 1.5 and 2 for cases with BR > 0. In contrast, for the smooth case (BR = 0), this ratio is approximately 1. This

observation indicates that the addition of riblets significantly increases the contribution of motions with the t2 timescale in this initial part of the shear layer.

As previously observed in earlier sections (including analyses of vorticity growth, two-point autocorrelation, and Reynolds stresses in relevant figures), an increase in BR leads to the thickening of the incoming TBL and the initial part of the shear layer. Consequently, one can infer the formation of larger coherent structures in this part of the shear layer as BR increases, which subsequently shed at a lower frequency within the shear layer compared to the smaller structures in the smooth case. This inference is also consistent with the results presented in Figure 5.36, which show a shift of the dominant timescale towards slower motions. This further suggests the formation of larger and slower coherent structures within the TBL, which, in turn, influences the dynamics of the downstream separation bubble.

Moving downstream to x/H=5.0, low-frequency motions (t3) become dominant in cases with BR > 0, whereas for BR = 0, no clear signature of these motions is yet recognized. This implies that in BR > 0 cases, low-frequency motions exhibit a broader signature across the separation bubble compared to BR = 0.

At x/H=7.5, close to the reattachment point (and post-reattachment for BR < 0.2), the signature of low-frequency motions (t3) becomes completely recognizable across all BR

values. Concurrently, the PSD level of high-frequency motions (t1) reaches its minimum value.

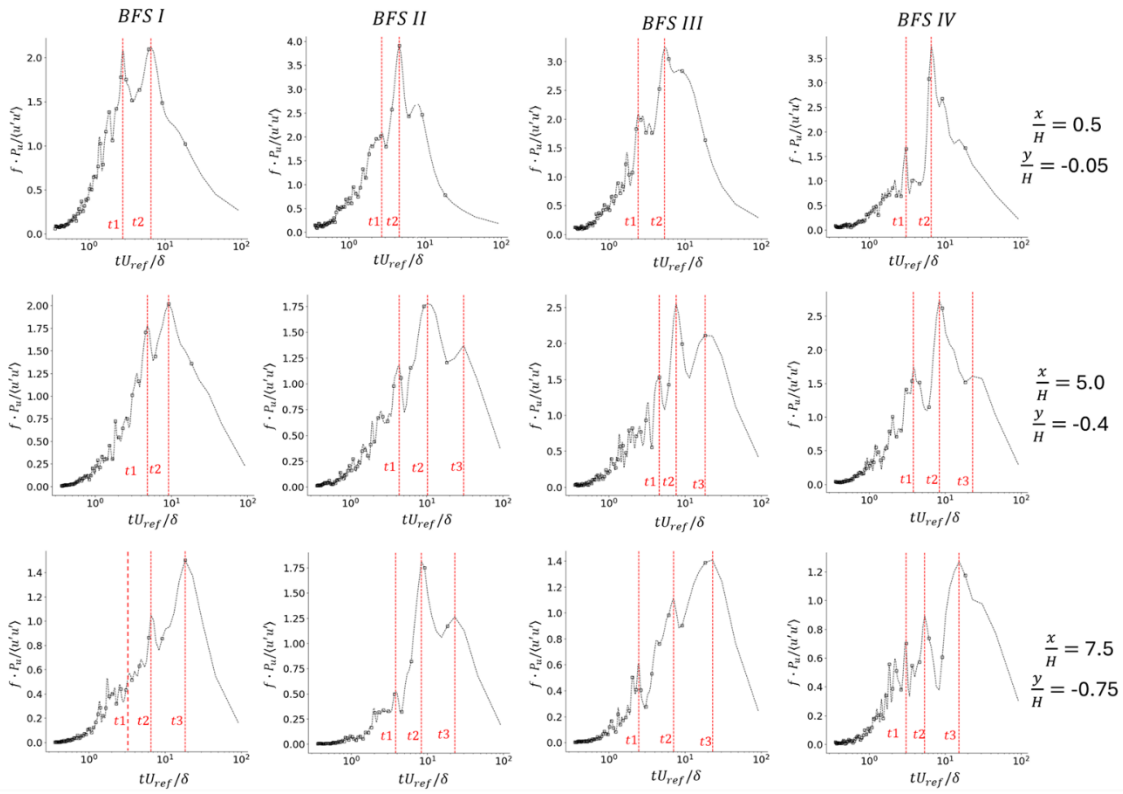

Figure 5.37 Comparison of the Premultiplied PSD, $\boldsymbol{f \cdot P_u/\langle u'u' \rangle}$, of streamwise velocity fluctuations for different blockage ratios along the separation streamline (at x/H =0.5, 5, and 7.5, z/δ = 1.0, and elevations of y/H= -0.05, -0.4, and -0.75) for BR = 0, 0.05, 0.1, and 0.2.

5.3.8 Modal Analysis

Dynamic Mode Decomposition (DMD) modal analysis was applied to identify three-dimensional, frequency-orthogonal modes. This technique helps to gain a better understanding of the effect of riblet obstacles on the evolution and dynamics of coherent structures, both upstream of the step (within the incoming turbulent boundary layer) and downstream of the step (primarily within the shear layer).

DMD was first introduced by Schmid(Schmid, 2010) as a method to identify the most significant modes and extract dynamic information from a flow system. In this technique, each mode is uniquely associated with a single frequency, thereby characterizing the

dynamics of that corresponding mode. The combination of these individual modes can then be used to reconstruct the complex behavior of the entire flow field. One of the main applications of DMD, implemented in various studies(Hickel et al., 2021; Wang et al., 2020), is the identification of coherent structures.

For first N mode, the dynamic mode system is represented as follows:

$$Q^N = \underbrace{[\phi_1, \phi_2, \dots, \phi_N]}_{\phi} \underbrace{\begin{bmatrix} \alpha_1 & & \\ & \alpha_2 & \\ & & \ddots \\ & & & \alpha_N \end{bmatrix}}_{D(\alpha)=diag(\alpha)} \underbrace{\begin{bmatrix} 1 & \mu_1 & \cdots & \mu_1^N \\ 1 & \mu_2 & \cdots & \mu_2^N \\ \vdots & \vdots & & \vdots \\ 1 & \mu_N & \cdots & \mu_N^N \end{bmatrix}}_{V_\mu}$$

where ϕ_k represent the ith mode, α_k shows the amplitude of the ith mode, and μ_k shows the corresponding eigenvalue within the Vandermonde matrix, which represents the temporal evolution of the system. According to(Hickel et al., 2021) μ_k is converted to the complex stability plane through a logarithmic mapping ($\lambda_k = \ln(\mu_k)/\Delta t$). Two new parameters β_i and ω_i are extracted from the mapped eigenvalues which are respectively stand for growth rate and angular frequency(Leroux et al., 2005):

$$\beta_i = \Re(\lambda_k) = \ln|\mu_k|/\Delta t$$

$$\omega_k = \Im(\lambda_k) = \arctan(\mu_k)/\Delta t$$

The information regarding each mode and its corresponding frequency and amplitude then are used to reconstruct evolution of the associated coherent structures within the flow field, which can be superimposed to the mean flow field using the following formulation:

$$q(x,t) = q_{ave} + \Re\left(\alpha_k \phi_k e^{i\theta_k}\right), \quad \theta_k = \omega_k t$$

The computational domain was strategically divided into two distinct subdomains for Dynamic Mode Decomposition (DMD) analysis. Region I encompassed the step upstream area, spanning x/H=−10 to x/H=−0.5. Region II covered the step downstream area, extending from x/H=0.5 to x/H=20.

To optimize computational efficiency while maintaining data integrity, a systematic sparse sampling strategy was implemented. Temporally, the dataset was reduced from 3000 to 1500 snapshots through uniform decimation; we preserved the total time interval by removing every alternate snapshot. Spatially, a structured downsampling approach was

applied by keeping every second element throughout the domain. This balanced data reduction while maintaining sufficient resolution for meaningful analysis.

Eigenvalues spectrum of one of the cases (BFS Region I) is provided in the Figure 5.38(a). Most of the eigen values are on the unit circle ($|\mu_k| \approx 1$), and some of them are in the decaying region. For the reconstruction the decaying modes ($|\mu_k| < 0.95$) where not considered. Figure 5.39(b) provides the normalized amplitude ($\psi_k = \alpha_k/\alpha_{max}$) for the selected positive frequency versus the Strouhal number. The intensity of each color bar is proportional with the growth rate parameter (β_k), so the darker the bar the higher the growth rate. For each subdomain three different modes (ϕ_1, ϕ_2, ϕ_3) were selected based on the frequency range (in three regions of $Sth < 0.1$, $0.1 < Sth < 0.5$, and $0.5 < Sth$) and normalized amplitude ($0.2 < \psi_k$ for $Sth < 0.5$ and $0.05 < \psi_k$ for $0.5 < Sth$).

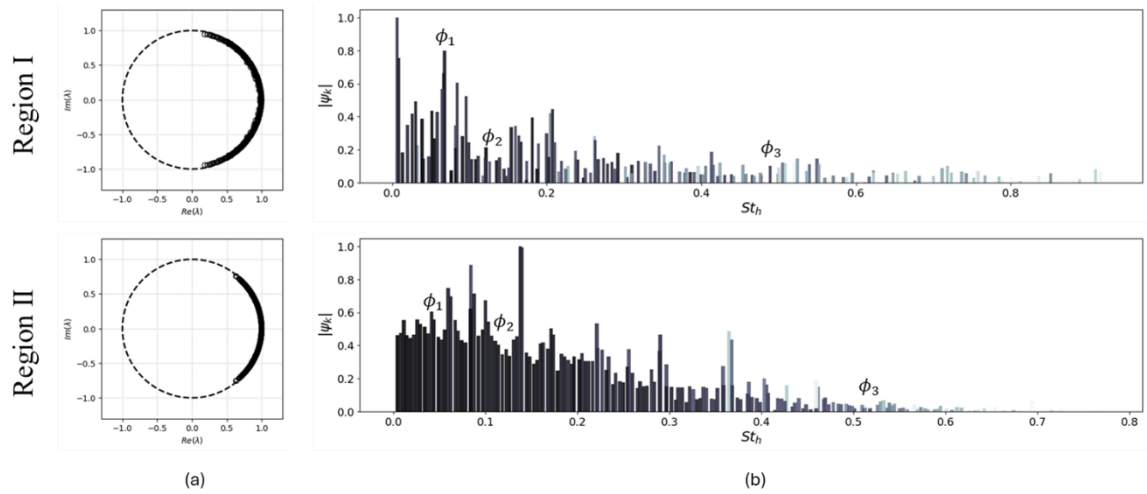

Figure 5.38 (a) Eigenvalue spectrum of BFS, (b) Normalized amplitude versus Strouhal number and selected modes.

Dynamic Mode Decomposition (DMD) analysis was performed specifically for the streamwise velocity component to identify coherent vortices within the dominant modes and across various frequencies. Information regarding the normalized mode amplitude, Strouhal number, and growth rate for each flow domain (Region I and Region II) is presented in Table 5.2.

Table 5.2 Information regarding normalized amplitude, Strouhal number and growth rate for the selected modes.

		BFSI RI	*BFSI RII*	*BFSII RI*	*BFSII RII*	*BFSIII RI*	*BFSIII RII*	*BFSIV RI*	*BFSIV RII*
$\boldsymbol{\phi_1}$	$\lvert\psi\rvert$	0.66	0.451	0.399	0.342	0.218	0.509	0.879	0.879
	St_h	0.067	0.048	0.096	0.082	0.054	0.084	0.054	0.05
	β	-0.004	-0.0001	-0.014	-0.0005	-0.024	-0.0003	-0.023	-0.0237
$\boldsymbol{\phi_2}$	$\lvert\psi\rvert$	0.212	0.336	0.349	0.260	0.384	0.284	0.546	0.546
	St_h	0.121	0.125	0.269	0.219	0.1329	0.204	0.236	0.236
	β	-0.005	-0.0006	-0.018	-0.012	-0.0226	-0.0004	-0.029	-0.029
$\boldsymbol{\phi_3}$	$\lvert\psi\rvert$	0.145	0.054	0.108	0.108	0.20	0.055	0.271	0.271
	St_h	0.55	0.538	0.540	0.624	0.609	0.626	0.559	0.55
	β	-0.012	-0.0075	-0.027	-0.013	-0.039	-0.008	-0.049	-0.049

Figure 5.39 presents the streamwise velocity fluctuations corresponding to the DMD mode $\phi 1$ (low frequency) in Region I for different Blockage Ratio (BR) domains. For each computational domain, two cases with a phase difference of $\pi/2$ are displayed. In all analyzed cases, strong streamwise coherent structures are observable, exhibiting remarkable differences between varying BR values.

In the absence of riblets (BFS I), alternating low-frequency coherent structures are uniformly distributed along the channel, maintaining an almost constant size and shape throughout Region I. The addition of riblets, however, completely perturbs this pattern. In BFS II, upstream of the riblets, the low-frequency coherent structures closely resemble those found in BFS I. Upon encountering the riblets, these structures are broken down into smaller structures, exhibiting a non-uniform size distribution in the spanwise direction, with the largest structures located in the middle of the spanwise extent. Smaller structures are primarily situated between the riblets on the bottom surface, while larger ones extend up to the rib crests.

In contrast to BFS II, a remarkable growth in the low-frequency coherent structures is observed near the bottom wall *after* the riblets in BFS III, reaching their maximum size at the end of the riblet region. These streamwise vortices form immediately after the first rib and persist up to the step. In BFS IV, a pair of strong and large streamwise structures emerges near the fourth riblet. Prior to these structures, in the initial part of the riblet region, small, alternating coherent structures are formed on the bottom surface between sequential ribs. This indicates that vortices between riblets possess shedding frequencies close to the low-frequency range (details on sweep and ejection events in d-type and k-type ribs are provided in the statistical analysis section). These initial structures subsequently grow to the crest region and transform into the large pairwise streamwise

vortices. These low-frequency structures are presumed to correspond to the streamwise vortices represented in the cross-sectional streamlines in Figure 5.10. This evidence suggests that d-type riblets in a closed channel can facilitate the formation of strong, pairwise, low-frequency vortices near the rib crest, which significantly influence the dynamics and structure of the downstream shear layer.

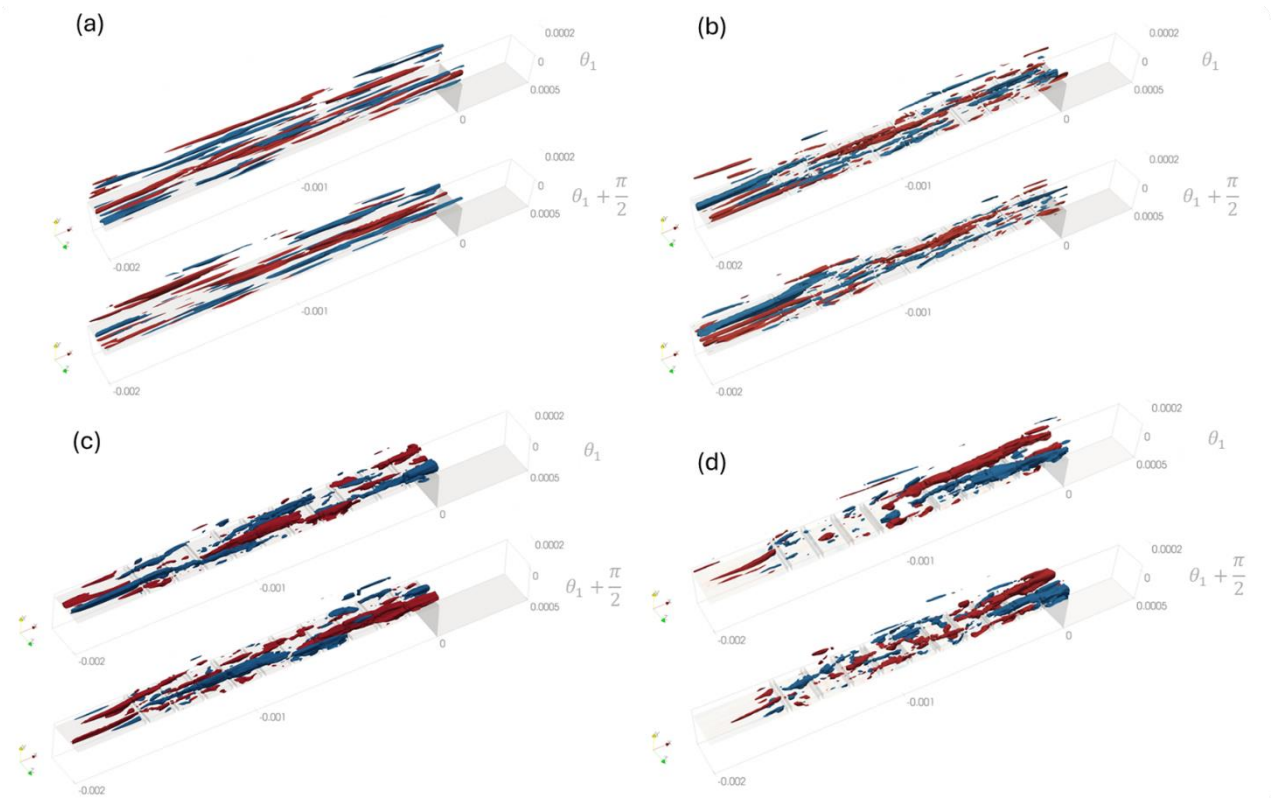

Figure 5.39 Isosurfaces of the streamwise velocity fluctuations (DMD mode $\boldsymbol{\phi_1}$) in Region I. Blue isosurfaces show $\boldsymbol{u/U_{ref} = -0.6}$ and red isosurfaces show $\boldsymbol{u/U_{ref} = 0.6}$. (a) BFS I, (b) BFS II, (c) BFS III, and (d) BFS IV.

Figure 5.40 displays the streamwise velocity fluctuations corresponding to the DMD mode ϕ2, which represents the mid-range frequency. In the plain channel (BFS I), structures similar to those observed for the ϕ1 mode (low frequency) are present, but with smaller characteristic sizes. In cases featuring riblets (BFS II, BFS III, and BFS IV), strong, growing vortices are formed over the bottom surfaces and rib crests, reaching their maximum sizes upstream of the step. Compared to the lower frequency mode, ϕ1, these

mid-range frequency fluctuations exhibit a greater tendency to extend towards the central region of the duct.

Regarding the DMD mode ϕ3 (high-frequency mode, Figure 5.41), the fluctuations demonstrate a more uniform size distribution across Region I, maintaining a remarkable distance from the bottom surface. From these combined results, it can be concluded that riblets facilitate the formation of strong low-frequency vortices predominantly close to the bottom surface, while higher-frequency vortices are more prominent above the rib crest. Furthermore, for the high-frequency mode (ϕ3), it is observed that increasing the riblet size leads to an increase in the characteristic size of the high-frequency coherent structures.

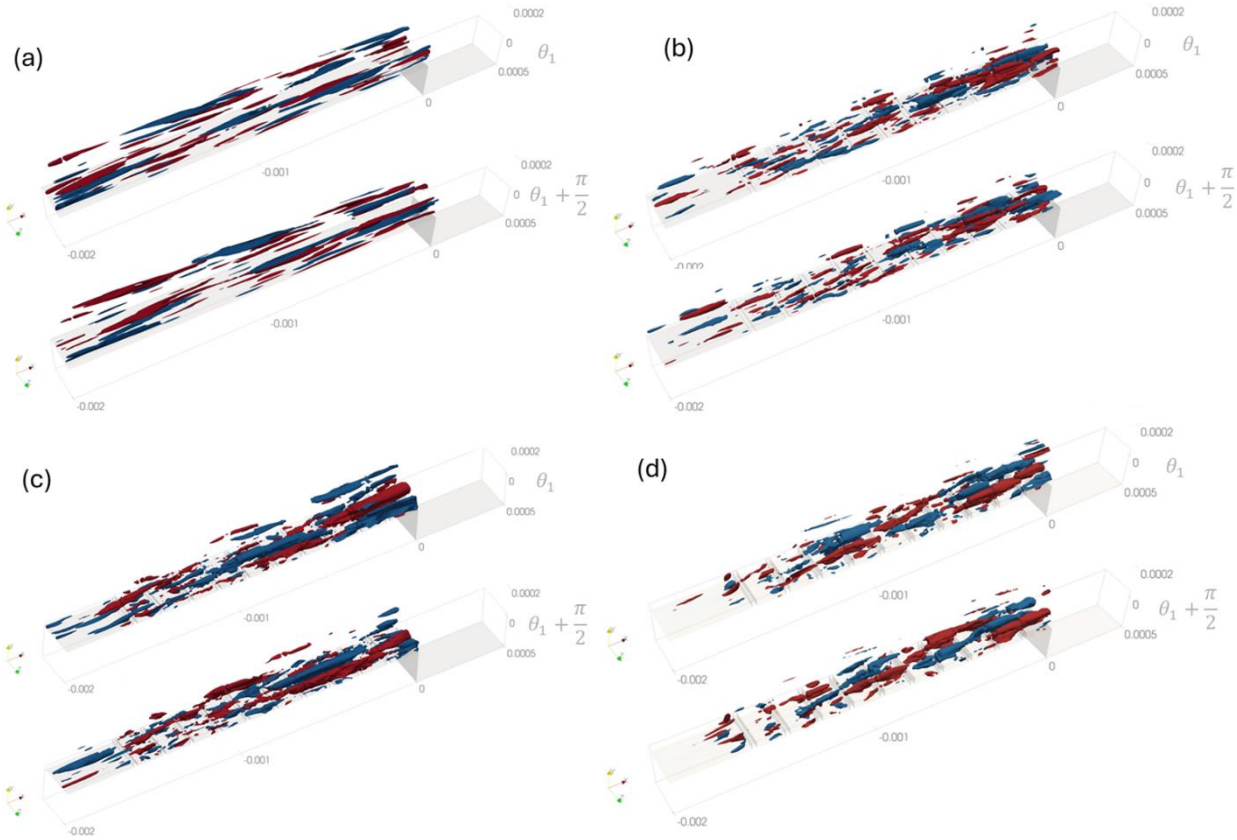

Figure 5.40 Isosurfaces of the streamwise velocity fluctuations (DMD mode $\boldsymbol{\phi_2}$) in Region I. Blue isosurfaces show $\boldsymbol{u/U_{ref} = -0.5}$ and red isosurfaces show $\boldsymbol{u/U_{ref} = 0.5}$. (a) BFS I, (b) BFS II, (c) BFS III, and (d) BFS IV.

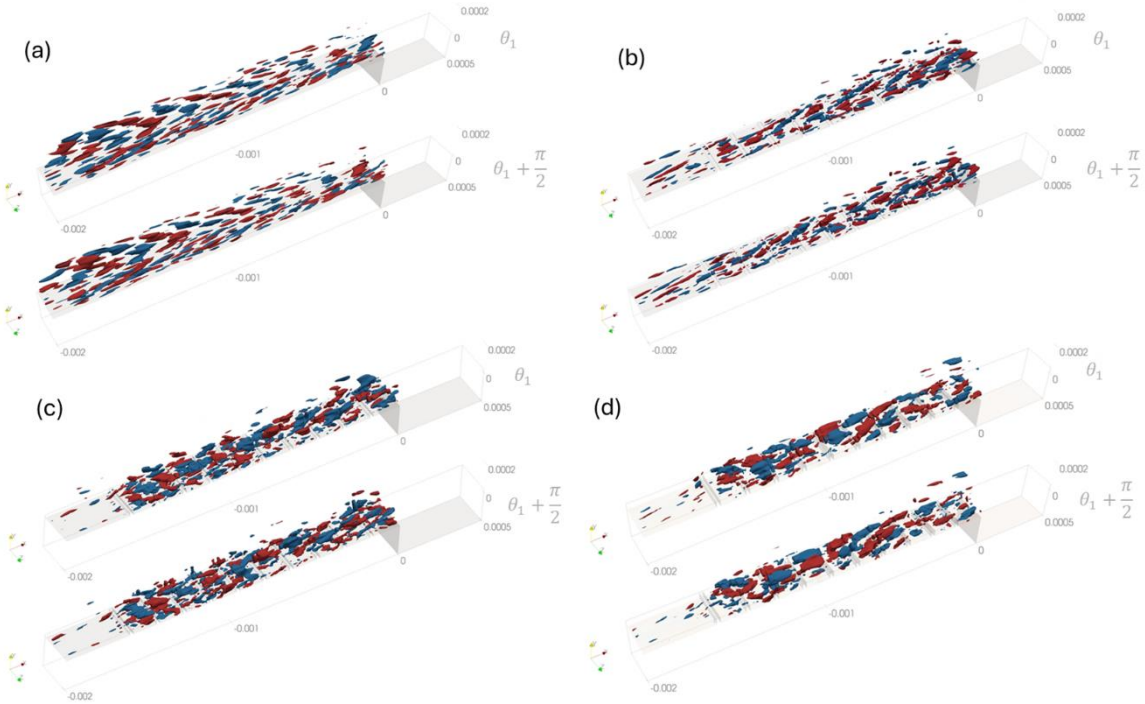

Figure 5.41 Isosurfaces of the streamwise velocity fluctuations (DMD mode $\boldsymbol{\phi_3}$) in Region I. Blue isosurfaces show $\boldsymbol{u/U_{ref} = -0.4}$ and red isosurfaces show $\boldsymbol{u/U_{ref} = 0.4}$. (a) BFS I, (b) BFS II, (c) BFS III, and (d) BFS IV.

A similar modal analysis was conducted for the shear layer regions, focusing on three different dominant modes. Figures 5.42, 5.43, and 5.44 represent the isosurfaces of streamwise velocity fluctuations in Region II for DMD mode ϕ1 (low-frequency mode), ϕ2, and ϕ3, respectively. In all cases, large structures associated with low frequency encompass both the shear layer and the reverse flow region(Santese et al., 2024b).

Ribs facilitate the formation of pairwise low-frequency structures within the shear region, a phenomenon more clearly observable for BFS III and BFS IV. These structures are likely the downstream extension of the large pair vortices previously observed in Region I, highlighting the significant impact of the ribs on the morphology of coherent structures forming within the shear region.

Another important observation is that the length of these structures reduces with increasing riblet height. As detailed in the characterization of the shear layer section, previous studies(Mahmoodi-Jezeh and Wang, 2020; Maleki et al., 2024) have shown that increasing the incoming turbulent boundary layer thickness leads to an increased shear layer growth rate/thickness and shifts its reattachment point upstream.

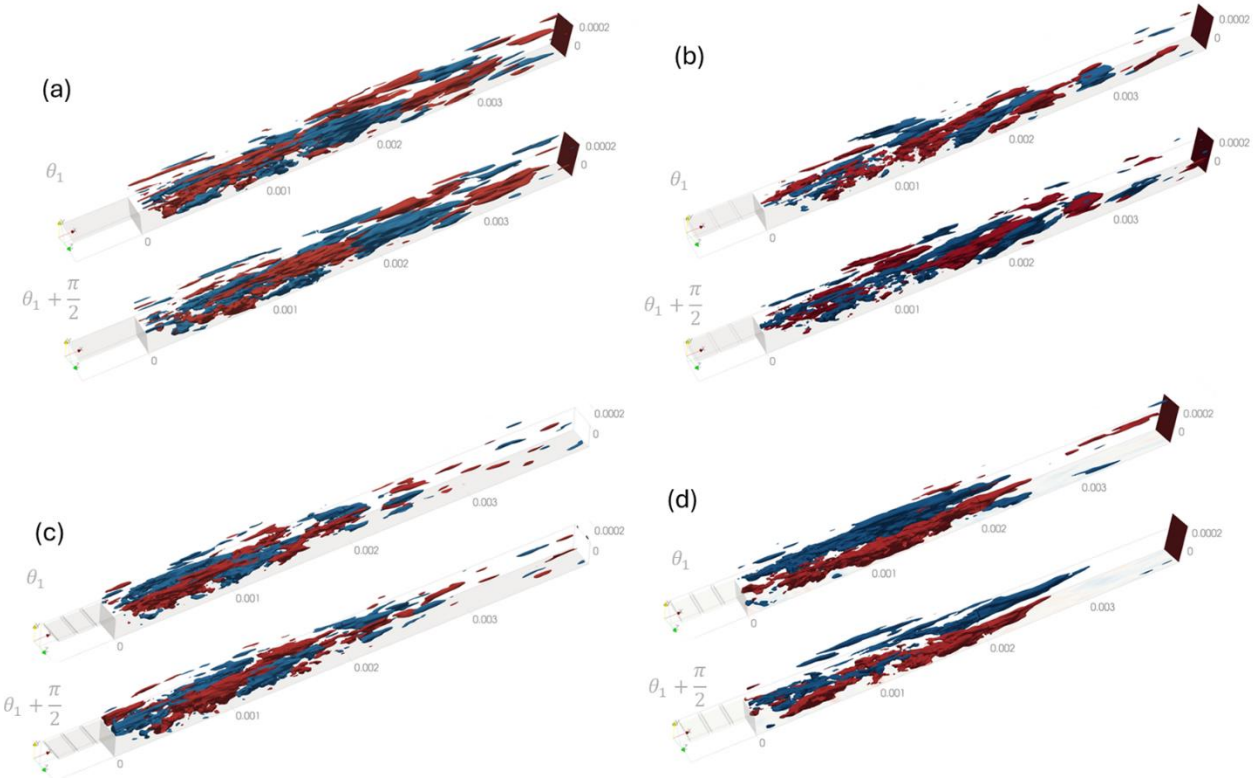

Figure 5.42 Isosurfaces of the streamwise velocity fluctuations (DMD mode $\boldsymbol{\phi_1}$) in Region II. Blue isosurfaces show $\boldsymbol{u/U_{ref} = -0.6}$ and red isosurfaces show $\boldsymbol{u/U_{ref} = 0.6}$. (a) BFS I, (b) BFS II, (c) BFS III, and (d) BFS IV.

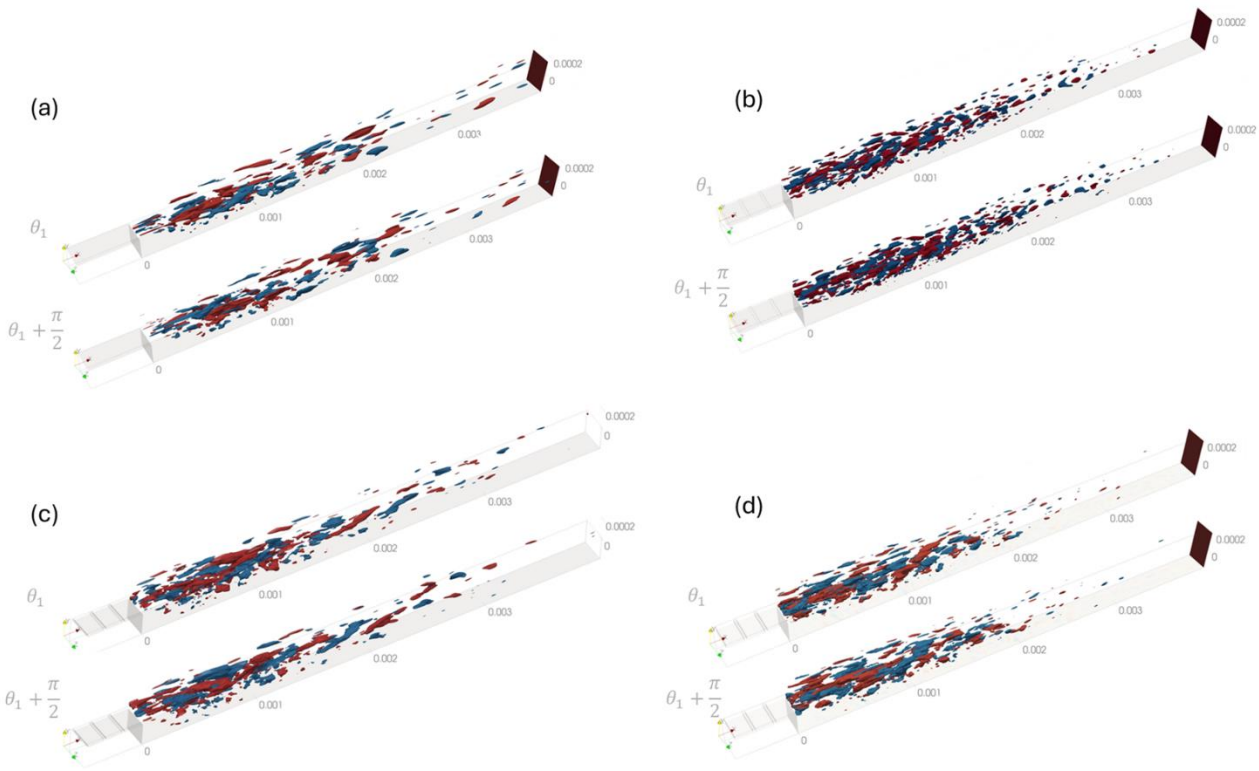

Figure 5.43 Isosurfaces of the streamwise velocity fluctuations (DMD mode $\boldsymbol{\phi_2}$) in Region II. Blue isosurfaces show $\boldsymbol{u/U_{ref} = -0.5}$ and red isosurfaces show $\boldsymbol{u/U_{ref} = 0.5}$. (a) BFS I, (b) BFS II, (c) BFS III, and (d) BFS IV.

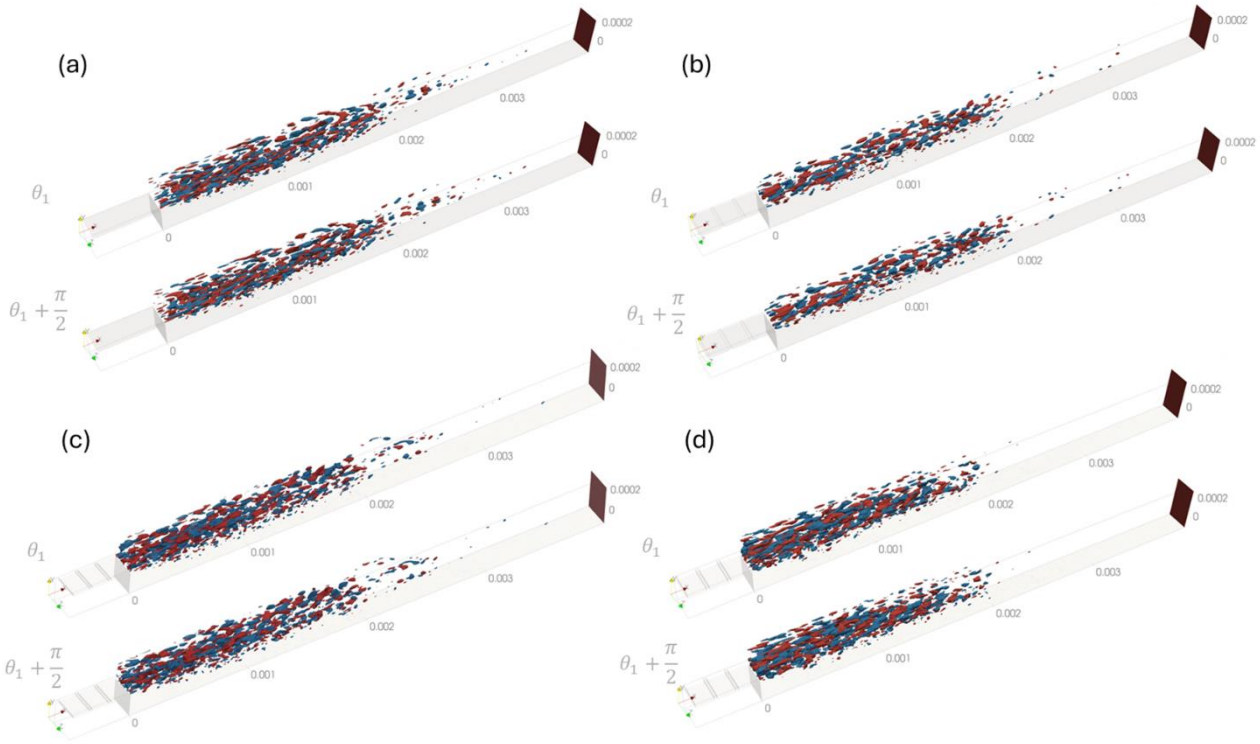

Figure 5.44 Isosurfaces of the streamwise velocity fluctuations (DMD mode $\boldsymbol{\phi_3}$) in Region II. Blue isosurfaces show $\boldsymbol{u/U_{ref} = -0.4}$ and red isosurfaces show $\boldsymbol{u/U_{ref} = 0.4}$. (a) BFS I, (b) BFS II, (c) BFS III, and (d) BFS IV.

5.4 Effect of Riblet Blockage Ratio on Cavitation Patterns

This section explores how Blockage Ratio (BR) values at the inlet impact cavitation patterns in Region I (upstream of the step) and Region II (downstream of the step). We used the compressible cavitation flow solver described in Chapter 3 for this analysis.

To ensure consistency, we kept the boundary conditions the same as those in our single-phase study, and we adopted the fluid properties from Chapter 4. As a result, the Reynolds number, based on the inlet hydraulic diameter, stays constant at 7200 across all scenarios. However, the cavitation number changes for each case, as detailed in Table 5.3. This happens because we apply atmospheric pressure at the channel outlet, while the upstream pressures fluctuate due to the different hydraulic resistances linked to each BR value.

Table 5.3 Nondimensional numbers for different BR values.

BR	0	0.05	0.1	0.2
Re	7200	7200	7200	7200
σ_v	0.74	0.887	1.08	1.311

Figure 5.45 presents instantaneous results of cavitating flow evolution across three sequential time steps for a Blockage Ratio (BR) of 0.05. The visualization includes void fraction using two different iso-surfaces (a transparent one at αv=0.1 and an opaque one at αv=0.5), pressure contours on a side plane, and velocity field distribution on various planes.

As discussed in the previous section, in the current flow regime, separation occurs above the ribs, even at small BR values like 0.05. This separation is accompanied by the formation of velocity gradients and shear layers above each rib. Vortices that form within the cores of these shear layers above each rib induce a significant pressure drop. If the surrounding liquid pressure is sufficiently low, this vortex-induced pressure drop leads to the formation and evolution of cavitation packets.

Figure 5.45(a) reveals the presence of intermittent cavitation packets even over the most upstream rib, despite its location in the region of highest surrounding pressure. This intermittent cavitation is formed within the core of rolled-up vortices above the rib region,

a phenomenon similar to the intermittent vortices observed in restriction regions(CECCIO and LABERTEAUX, 2001; Ganesh et al., 2016).

Moving downstream along the channel, a significant portion of the riblet becomes covered with a sheet of vapor (Figure 5.45(b)). This occurs due to a decrease in the surrounding pressure, while the strength of vortices over the ribs remains almost constant. Downstream of the ribs, the vapor evolves within the streamwise structures, which most likely correspond to the legs of hairpin-like structures formed in this region. If a hairpin vortex possesses sufficient strength, a considerable portion of it will be filled with vapor, allowing its shape to be recognizable through the void fraction (Figure 5.45(c)). Structures similar to these have also been observed in previous studies (CECCIO and LABERTEAUX, 2001).

From the velocity field contours, high- and low-speed streaks are discernible on the bottom surface, appearing most significantly between the two outermost ribs. These streaks are associated with the ejection and sweeping mechanisms discussed in the previous section. In the case of cavitating flow, however, reverse flow can also be induced and intensified in the presence of an APG generated by cavitation closure(Bhatt and Mahesh, 2020).Prior to the last rib, cavitation packets exhibit intermittent shedding (Figure 5.46(c)), primarily governed by the advection of vortical structures along the channel. The convected bubbles collapse as soon as they are exposed to a high-pressure region, resulting in the generation of strong pressure waves and the subsequent breakup of surrounding vapor structures (Figure 5.46(b)).

Downstream of the last rib, the surrounding pressure drop is substantial enough that cavitation covers a remarkable portion of the bottom wall. This cavitation then extends downstream of the step. In the current flow regime, we observed that most of Region II will be occupied by vapor, leading to the occurrence of supercavitation in this region. Nonetheless, as will be discussed, the distribution and intensity of the void fraction in the extension region differ significantly for various BR values.

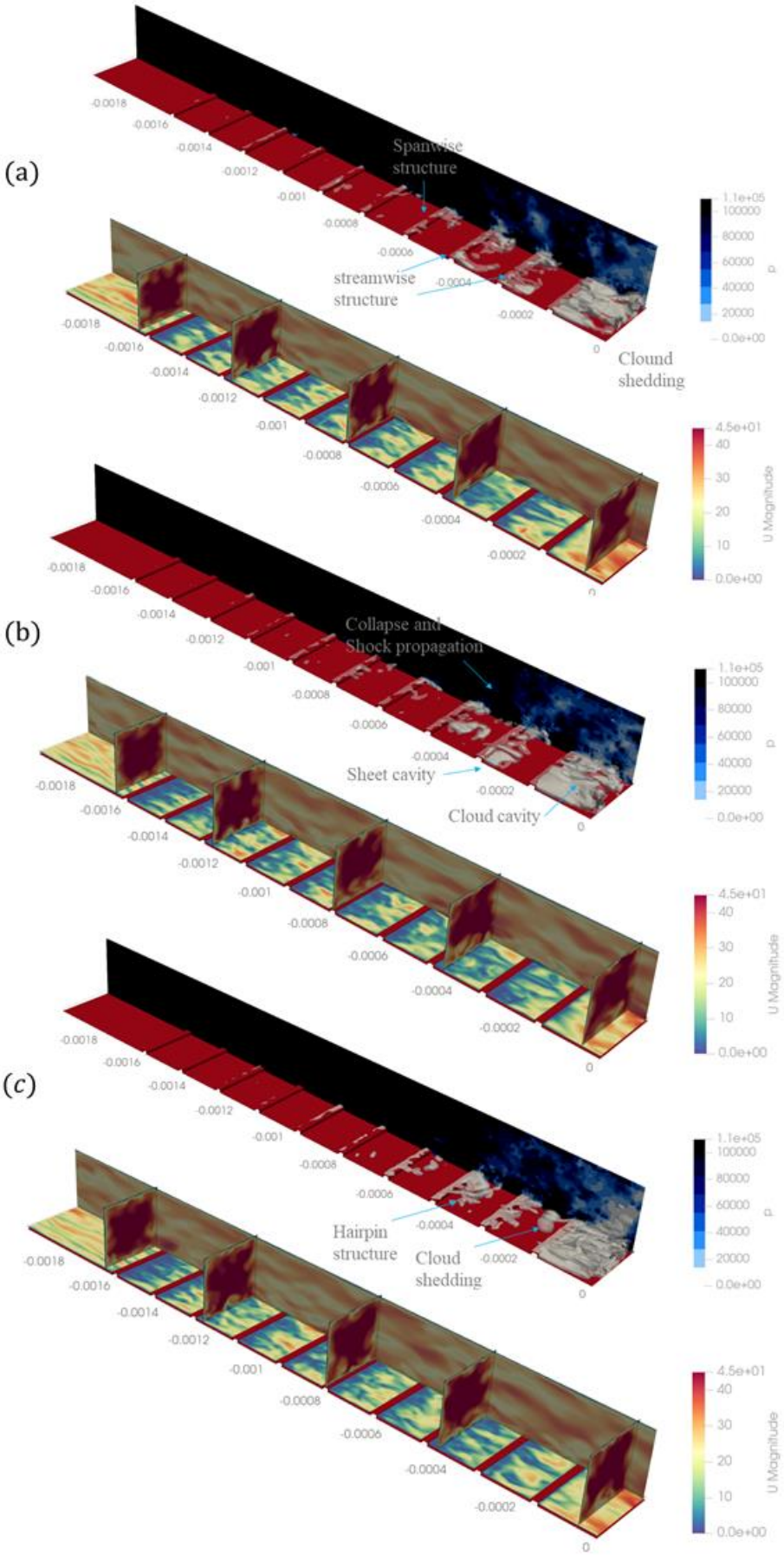
(a)
Spanwise structure
streamwise structure
Clound shedding
(b)
Collapse and Shock propagation
Sheet cavity
Cloud cavity
(c)
Hairpin structure
Cloud shedding
U Magnitude

Figure 5.45 3D representation of the vapor void fraction, pressure field, and velocity field distribution in cavitating flow in Region I of the BFS II configuration. Transparent iso-contour corresponds to $\alpha_v=0.1$ and opaque iso-contour corresponds to $\alpha_v=0.5$, at (a) t_{ref}, (b) $t_{ref}+\delta t$, and (c) $t_{ref}+2\delta t$ (δt=5e-6s).

Figures 6.46 and 6.47 illustrate the cavitating flow patterns for Blockage Ratios (BR) of 0.1 and 0.2, respectively. In general, these cavitation patterns bear a resemblance to those previously described for BR = 0.05. However, two major differences are consistently observable. Firstly, the size of cavitation packets formed within the vortical structures is notably larger for higher BR values. For instance, a comparison of the cavitation within the hairpin structures clearly demonstrates this increase in size, which further corroborates the formation of stronger and larger coherent structures with increasing BR values (as also supported by Figure 5.34). Secondly, these cavitation patterns are present across a larger portion of the channel height.

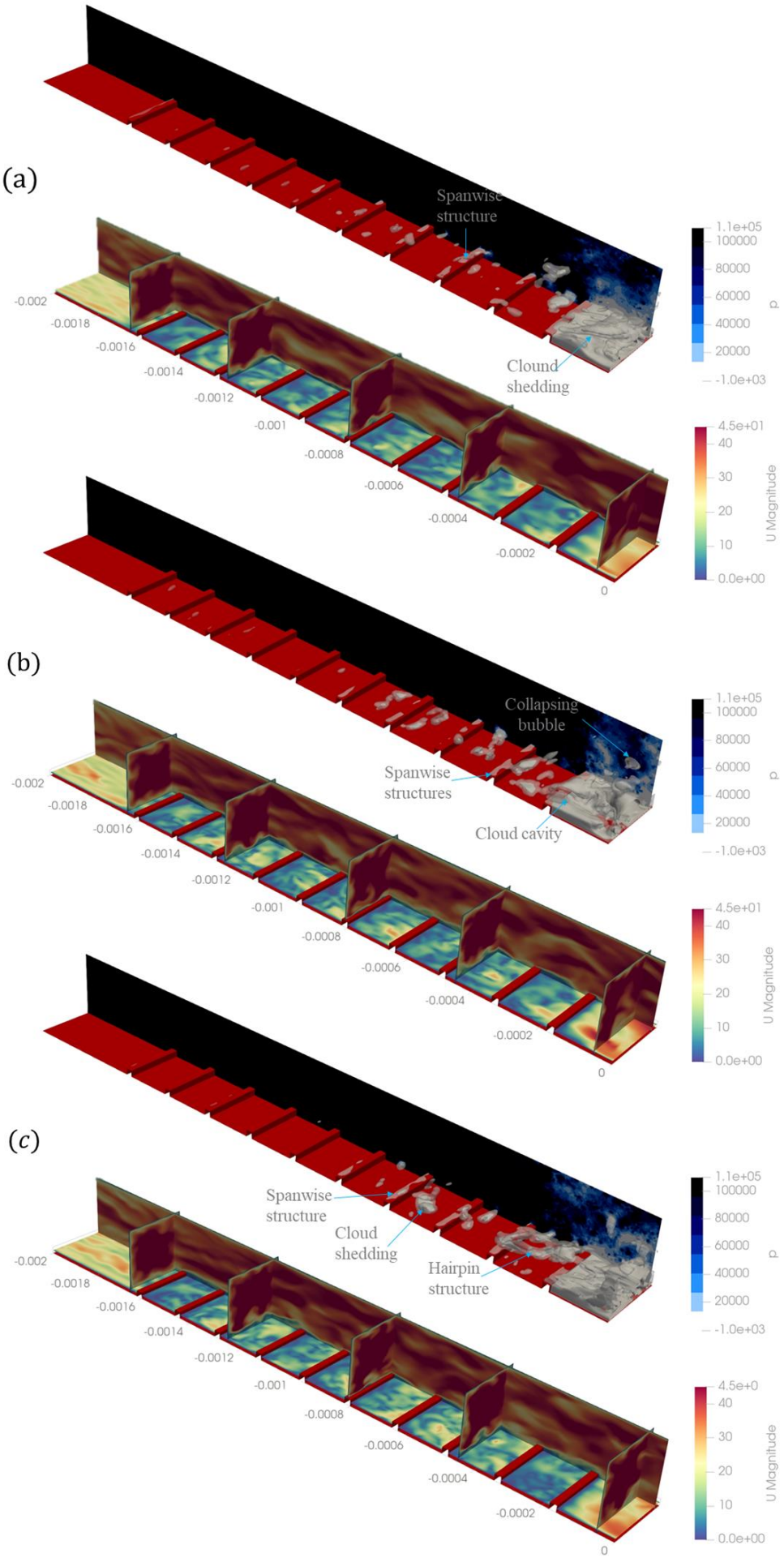
(a)
Spanwise structure
Clound shedding
-0.002
-0.0018
-0.0016
-0.0014
-0.0012
-0.001
-0.0008
-0.0006
-0.0004
-0.0002
0
1.1e+05
100000
80000
60000
40000
20000
-1.0e+03
p
4.5e+01
40
30
20
10
0.0e+00
U Magnitude
(b)
Collapsing bubble
Spanwise structures
Cloud cavity
(c)
Spanwise structure
Cloud shedding
Hairpin structure

Figure 5.46 3D representation of the vapor void fraction, pressure field, and velocity field distribution in cavitating flow in Region I of the BFS III configuration. Transparent iso-contour corresponds to $\boldsymbol{\alpha_v = 0.1}$ and opaque iso-contour corresponds to $\boldsymbol{\alpha_v = 0.5}$, at (a) $\boldsymbol{t_{ref}}$, (b) $\boldsymbol{t_{ref} + \delta t}$, and (c) $\boldsymbol{t_{ref} + 2\delta t}$ ($\boldsymbol{\delta t = 5e-6s}$).

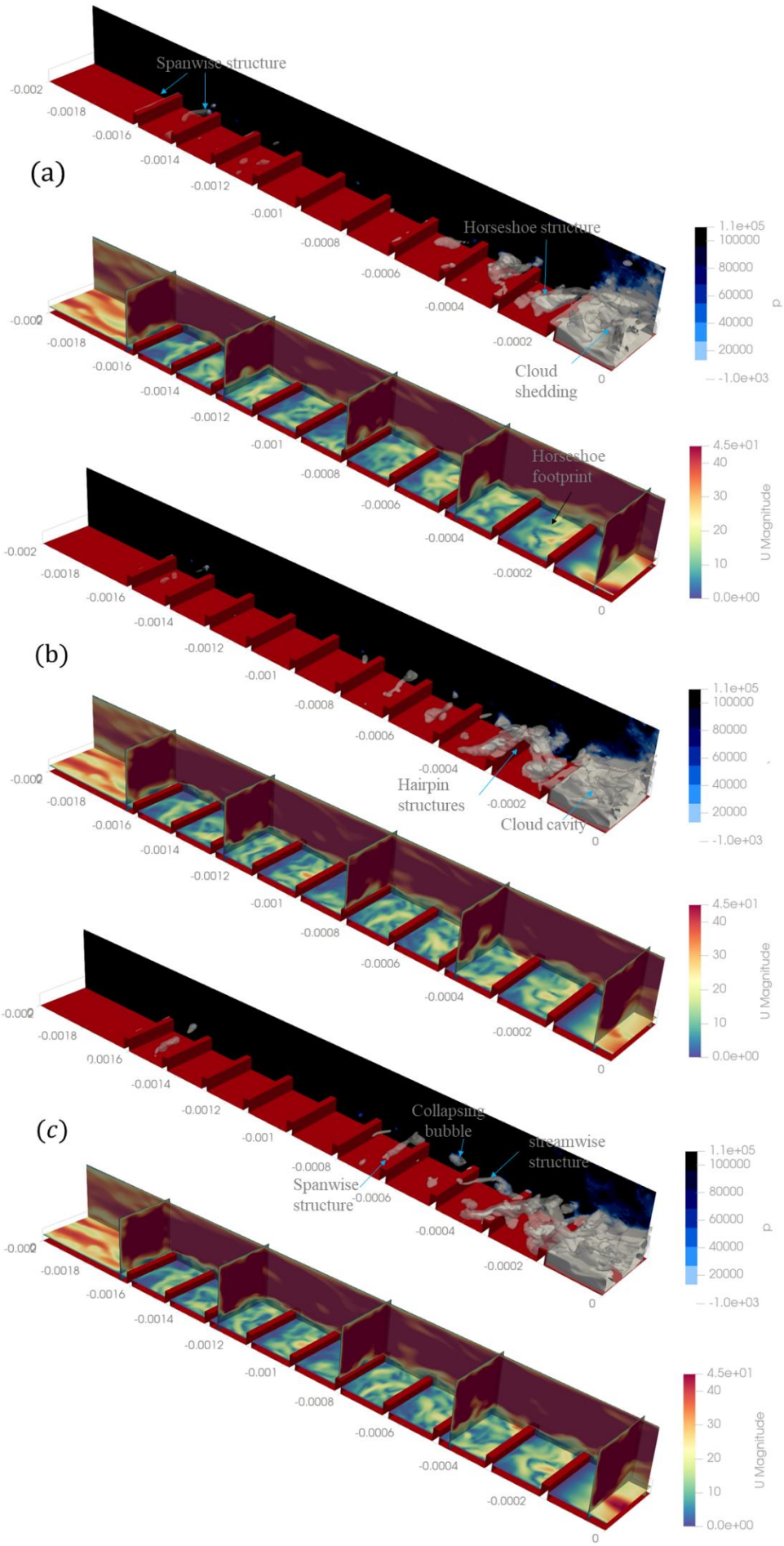
(a)
Spanwise structure
Horseshoe structure
Cloud shedding
Horseshoe footprint
(b)
Hairpin structures
Cloud cavity
(c)
Collapsing bubble
streamwise structure
Spanwise structure
p
U Magnitude

Figure 5.47 3D representation of the vapor void fraction, pressure field, and velocity field distribution in cavitating flow in Region I of the BFS IV configuration. Transparent iso-contour corresponds to $\boldsymbol{\alpha_v = 0.1}$ and opaque iso-contour corresponds to $\boldsymbol{\alpha_v = 0.5}$, at (a) $\boldsymbol{t_{ref}}$, (b) $\boldsymbol{t_{ref} + \delta t}$, and (c) $\boldsymbol{t_{ref} + 2\delta t}$ ($\boldsymbol{\delta t = 5e-6s}$).

Figure 5.48 illustrates the isosurfaces of void fraction (αv=0.1 for the transparent surface and αv=0.5 for the opaque surface), along with the side and bottom plane pressure fields, for different Blockage Ratio (BR) values in the extension region (Region II). To provide further insight, the corresponding velocity fields are presented in Figure 5.49. At first glance, it's evident that in all cases, the recirculation zone and corner vorticity are completely filled with dense vapor. Downstream of the recirculation zone, a large, cylindrically shaped vapor packet sheds from the end of the separation bubble (labeled as "shed cavity from the separation bubble (SB)"). The size and intensity of this shed cavity significantly increase with BR values, indicating a corresponding increase in the size and strength of this vortical structure as BR rises.

Above the step, cavitation packets enter the extension region from Region I. As most of these cavitation packets originate within high-frequency (HF) coherent structures in the riblet region, they are depicted as "convected" or "HF cavitation" in Figure 5.48. Since the majority of the channel is filled with cavitation and a low-pressure region, it can be classified as a supercavitation region. The large pressure regions, identifiable by dark blue contours, likely correspond to transient local pressure fluctuations and condensation within the channel. The velocity field distribution (Figure 5.49) further demonstrates that the magnitude of velocity remarkably increases with increasing BR. This suggests more intense cavitation at larger BR values, leading to a greater increase in fluid volume and velocity across the channel.

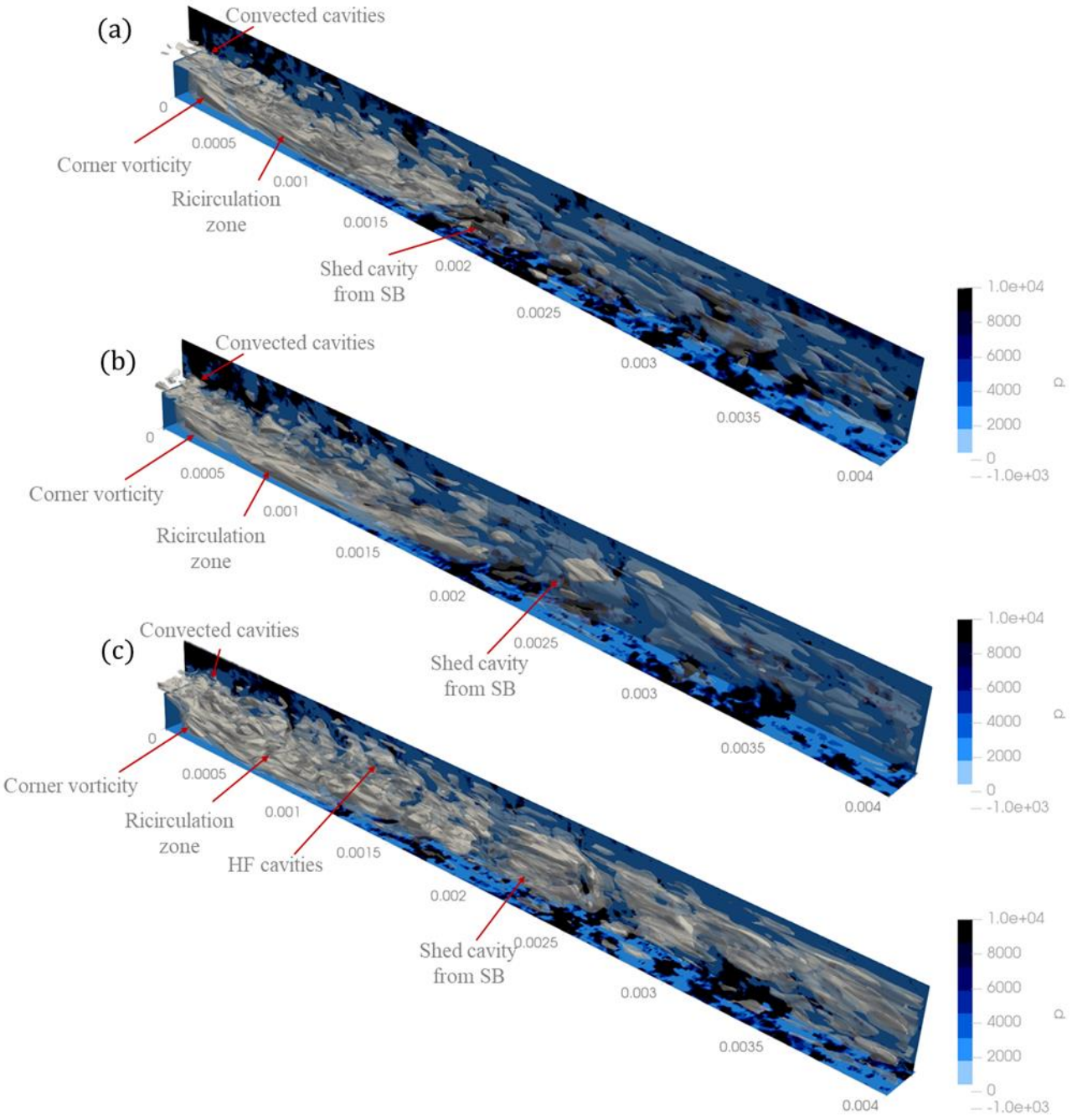

Figure 5.48 Instantaneous 3D representation of the vapor void fraction, pressure field distribution in cavitating flow in Region II of (a) BFS II, (b) BFS III, and (c) BFS IV. Transparent iso-contour corresponds to $\boldsymbol{\alpha_v = 0.5}$ and opaque iso-contour corresponds to $\boldsymbol{\alpha_v = 0.99}$

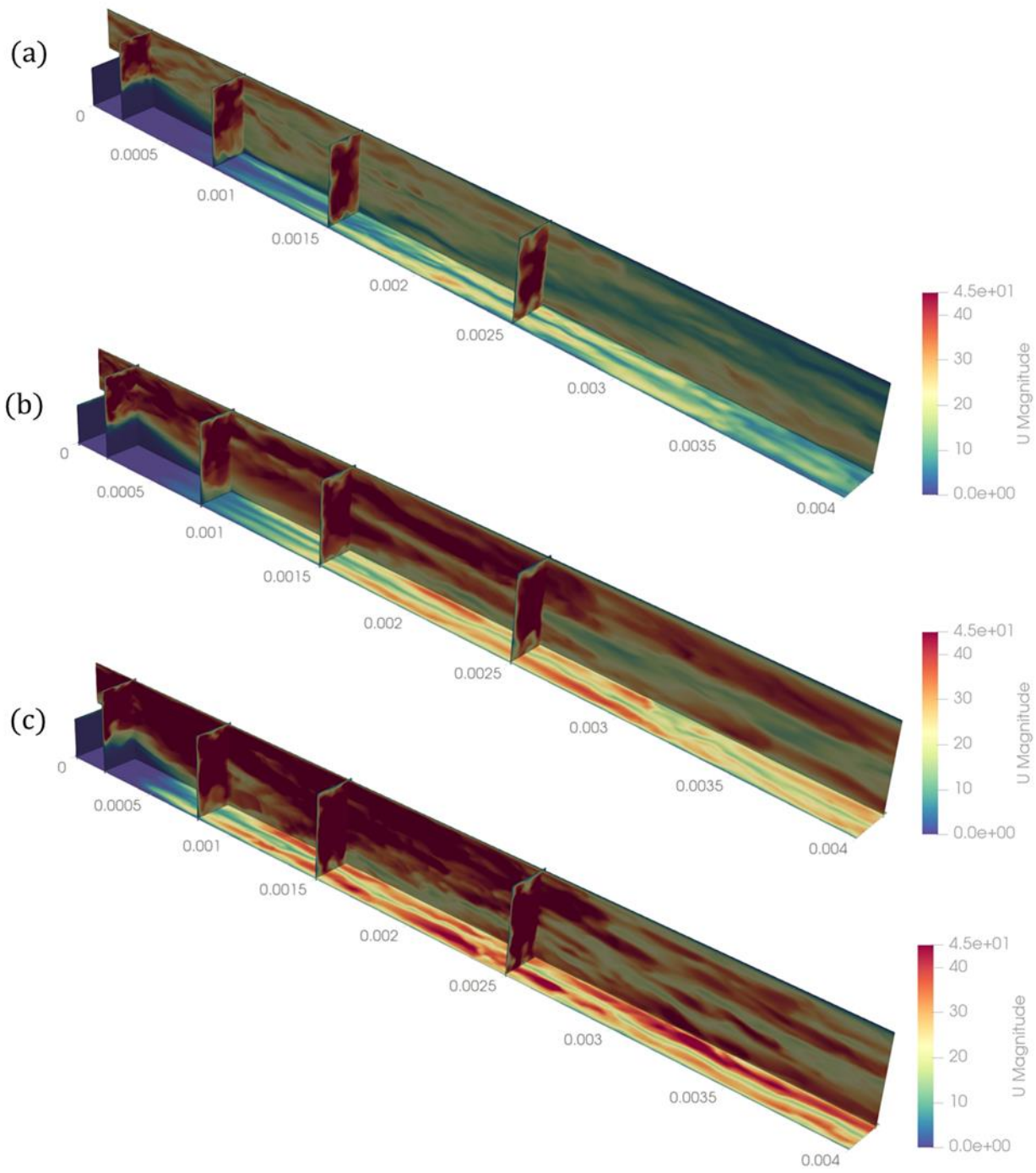

Figure 5.49 Instantaneous 3D representation of the velocity field distribution in cavitating flow in Region II of (a) BFS II, (b) BFS III, and (c) BFS IV.

5.5 Conclusion

This comprehensive analysis has elucidated the profound and multi-faceted impact of riblet-equipped surfaces, quantified by the BR, on the turbulent flow characteristics and subsequent cavitation patterns within a channel featuring a step. Our findings underscore a strong interrelationship where changes in the fundamental turbulent flow structures, driven by the presence and geometry of riblets, directly dictate the inception, evolution, and intensity of cavitation phenomena.

1. Altered TKE Dynamics: The presence of riblets fundamentally shifts the TKE budget. While production and dissipation are dominant in smooth channels (BR=0), increasing BR introduces and amplifies the roles of turbulent diffusion and convection. For lower BR (e.g., BR=0.05), turbulent diffusion becomes a key mechanism for TKE transfer, primarily redistributing energy from regions of high production. As BR increases further, convection emerges as a significant TKE transport mechanism. Downstream of the step (Region II), although overall TKE magnitudes are generally lower for BR>0 cases, the positive contributions of TKE convection and diffusion are notably enhanced, especially within the shear layer. This highlights their crucial role in TKE distribution and is directly linked to the thickening of the incoming TBL due to increasing BR, which promotes the formation of larger coherent structures in the initial shear layer.

2. Modification of Reynolds Stresses and Flow Anisotropy: The introduction of riblets significantly impacts the Reynolds stresses, which represent the additional stresses arising from turbulent velocity fluctuations and are key indicators of turbulent mixing and momentum transfer. Specifically, the magnitude of the normal anisotropy components (b11, b22, b33) is substantially reduced near the wall and rib crest. Furthermore, the characteristic peaks and valleys of these components, along with the overall anisotropy invariant function, undergo horizontal shifts with increasing BR, indicating a fundamental alteration in the flow's anisotropic state. Downstream of the step, the enhancement of anisotropy within the shear layer—a prominent feature in smooth channels—is attenuated with increasing BR. Nevertheless, local peaks in the anisotropy invariant function persist, consistently aligning with regions of significant mean velocity gradients, signifying

ongoing turbulent activity. These changes in Reynolds stresses reflect the modified momentum transport and turbulent mixing across the flow field due to the riblets.

3. Morphological Transformation of Coherent Structures: Autocorrelation analysis provided direct evidence of how riblets alter the morphology of coherent structures. An increase in BR leads to a monotonic increase in the width of streamwise velocity fluctuation isopleths and a decrease in their inclination angle, which is indicative of a more dominant sweeping motion near the wall. Conversely, the spanwise velocity fluctuation isopleths shorten with increasing BR, suggesting the formation of smaller hairpin legs. These observations are highly consistent with the previously noted TBL thickening and the subsequent formation of larger, slower coherent structures. The altered Reynolds stress profiles are directly linked to these modified coherent structures, as they are the primary carriers of turbulent momentum flux.

4. Dominance of Low-Frequency Dynamics and Larger Structures: Spectral analysis of streamwise velocity fluctuations demonstrated two critical trends with increasing BR: an expanded range of energetic motion temporal scales and a distinct shift of the high-energy zone towards larger temporal scales (lower characteristic frequencies). This strongly indicates the formation of larger and slower coherent structures within the TBL, which, in turn, exerts a significant influence on the dynamics of the downstream separation bubble. Downstream of the step, low-frequency motions (associated with t3) become dominant for BR>0 cases earlier in the channel compared to BR=0, exhibiting a broader spatial signature across the separation bubble. Near reattachment, these low-frequency motions are universally recognizable across all BR values, while the high-frequency motions (associated with t1) reach their minimum PSD levels.

5. DMD-Identified Coherent Vortices and Riblet-Induced Structures: The Dynamic Mode Decomposition (DMD) analysis quantitatively confirmed these structural and dynamic changes. In Region I, riblets profoundly disrupt the uniform distribution of low-frequency coherent structures observed in smooth channels, leading to their breakdown into non-uniform, smaller structures. Higher BR values (BFS III, IV) specifically promote the growth of strong low-frequency vortices near the bottom wall and the formation of large pairwise low-frequency vortices near the rib crest. These are identified as the downstream extension of the large pair vortices observed in cross-sectional streamlines, underscoring the significant impact of ribs on the morphology of coherent structures. Mid-range

frequency modes ($\phi 2$) show strong, growing vortices extending towards the duct central region, while high-frequency modes ($\phi 3$) exhibit a more uniform size distribution and are located farther from the bottom surface. An increase in riblet size directly correlates with an increase in the size of high-frequency coherent structures. These coherent structures, identified by DMD, are directly responsible for generating the Reynolds stresses observed, as they represent the organized, time-averaged contributions of the fluctuating velocities to momentum transfer.

6. Direct Influence on Cavitation Patterns: The altered flow characteristics and the modified coherent structures, particularly the low-frequency, larger vortices, directly dictate the cavitation patterns. Even at small BR, intermittent cavitation packets nucleate within the cores of vortices formed above the ribs due to localized pressure drops. As the flow progresses downstream, these cavitation patterns persist, with vapor evolving prominently within hairpin-like structures. Crucially, increasing BR leads to the formation of larger and more intense cavitation packets, serving as direct evidence of the stronger and larger coherent structures facilitated by the riblets. In Region II, the recirculation zone and corner vorticity are completely filled with dense vapor. A large, cylindrically shaped vapor packet sheds from the end of the separation bubble, and its size and intensity significantly increase with BR values, directly reflecting the increased size and strength of the underlying shedding vortical structures. The channel ultimately transitions into a supercavitation regime in Region II for all BRs, with the specific distribution and intensity of the void fraction varying significantly with BR, reflecting the distinct flow characteristics induced by each riblet geometry. The pressure fluctuations induced by these cavitating structures, in turn, influence the overall flow field, creating an intricate feedback loop.

In conclusion, this study unequivocally demonstrates that riblets are not merely passive surface modifications but actively reshape the turbulent flow field. They promote the formation of larger, slower, and more organized coherent structures, particularly at low frequencies and near the solid boundaries. This fundamental shift in flow characteristics, explicitly evident in the TKE budget, Reynolds stress anisotropy, autocorrelation, and DMD modes, directly dictates the inception, evolution, and intensity of cavitation. The ability of riblets to foster strong, low-frequency vortical structures directly translates into more pronounced and extensive cavitation phenomena, particularly in the reattachment

and extension regions. This comprehensive understanding of the interplay between riblet geometry, turbulent flow characteristics, Reynolds stresses, coherent structures, and cavitation dynamics is critical for the design and optimization of flow systems operating under cavitating conditions.

6 INSIGHTS ON CAVITATING FLOWS OVER A MICROSCALE BFS-EXPERIMENTAL STUDY

6.1 Introduction

This study introduces the first experimental analysis of shear cavitation in a microscale BFS configuration. It explores shear layer cavitation under various flow conditions in a microfluidic device with a depth of 60 μm and a step height of 400 μm. The BFS configuration, with its unique characteristics of upstream turbulence and post-reattachment pressure recovery, provides a controlled environment for studying shear-induced cavitation without the complexities of other microfluidic geometries. Experiments were conducted across four flow patterns: inception, developing, shedding, and intense shedding, by varying upstream pressure and Reynolds number. The study highlights key differences between microscale and macroscale shear cavitation, such as the dominant role of surface forces on nuclei distribution, vapor formation, and distinct timescales for phenomena like shedding and shockwave propagation. It is hypothesized that vortex strength in the shear layer plays a significant role in cavity shedding during upstream shockwave propagation. Results indicate that increased pressure notably elevates the mean thickness, length, and intensity within the shear layer. Instantaneous data analysis identified two vortex modes (shedding and wake modes) at the reattachment zone, which significantly affect cavitation shedding frequency and downstream penetration. The wake mode, characterized by stronger and lower-frequency vortices, transports cavities deeper into the channel compared to the shedding mode. Additionally, vortex strength, proportional to the Reynolds number, affects condensation caused by shockwaves. The study confirms that nuclei concentration peaks in the latter half of the shear layer during cavitation inception, aligning with the peak void fraction region.

6.1.1 Experimental Overview

6.1.1.1 Device Fabrication and Configuration

Experiments were conducted on a microfluidic HC-on-a-chip device (reactor) with a BFS configuration, whose dimensions and geometry are shown in Figure 6.1. The reactor consisted of two primary sections which were the microchannel and the extension channel. The inlet port, with a diameter of 1000 μm, was connected to the microchannel, which had dimensions of 400 μm in height, 4000 μm in length, and 60 μm in depth. Following the microchannel, there was an extension channel where cavitating flow patterns were observed. The dimensions of the extension channel were 800 μm in height, 4000 μm in length, and 60 μm in depth. The outlet port, with a diameter of 1000 μm, was located at the end of the extension channel. The reactor was fabricated using a process flow derived from semiconductor microfabrication techniques. The major fabrication steps included a silicon (Si) wafer grinding, silicon dioxide (SiO_2) coating, photolithography, SiO_2 and Si etching, protective layer deposition, wet etching, and piranha cleaning as illustrated in Figure 6.2. In the final step, the Si-based substrate was cleaned and anodically bonded to a Borofloat 33 glass to form a high-pressure-resistant semi-transparent closed channel structure for visualization. The detailed fabrication process flow can be found in the previous study(Rokhsar Talabazar et al., 2021).

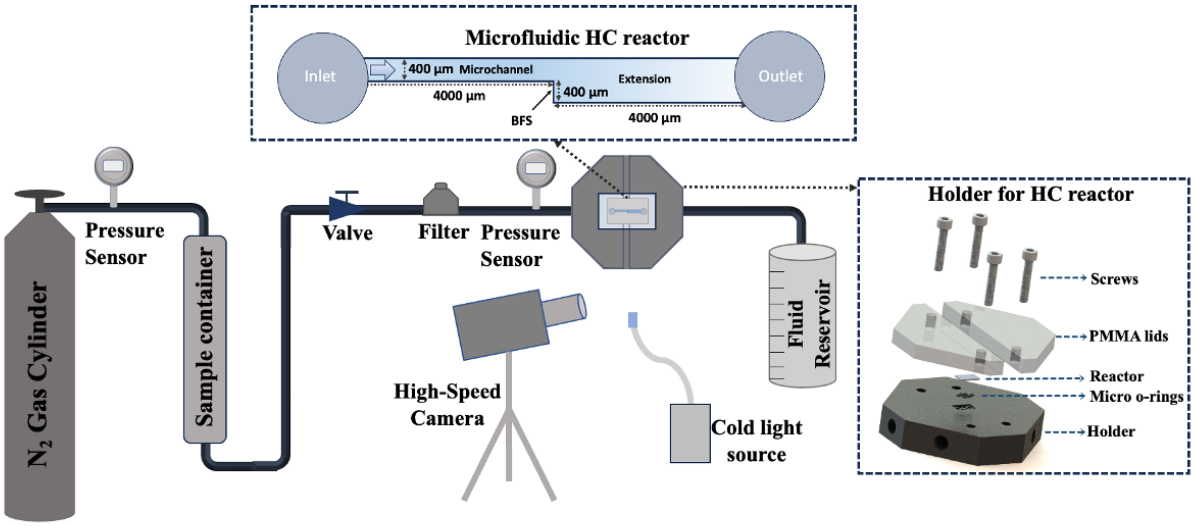

Figure 6.1 Schematic of the experimental setup, microfluidic HC reactor, and holder for HC reactor.

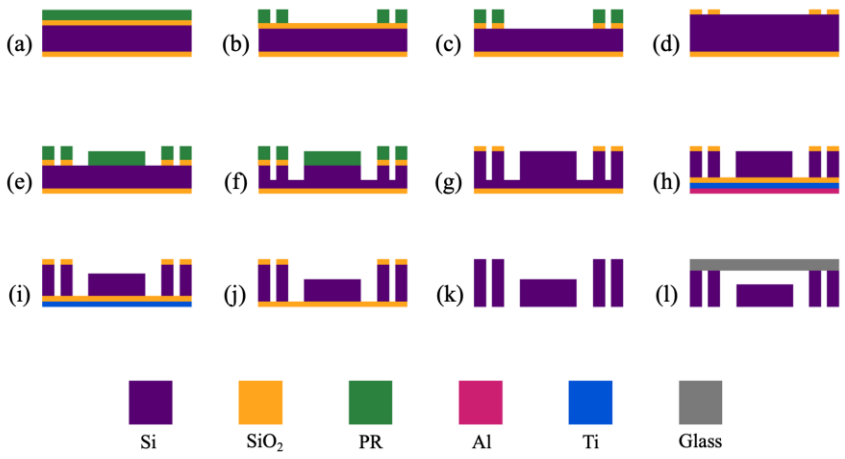

Figure 6.2 Microfluidic HC Reactor Fabrication Steps: a) A 4-micrometer layer of photoresist is cast onto a silicon (Si) wafer, which is pre-coated with 500nm of silicon dioxide (SiO2). b) A maskless lithography process is then used to pattern features designed with Layout Editor Software. c) The SiO2 layer is subsequently etched using an ICP-based high-density plasma source (SPTS APS). d) Stripping of the photoresist. e) Lithography for the fabrication of the ports. f) Deep Reactive Ion Etching (DRIE) for the etching of Si. g) Photoresist stripping. h) 10 nm of Titanium (Ti) and 2 µm of Aluminum (Al) sputtering on the backside of the Si wafer to increase its durability. Wet

etching and second DRIE to form the inlet and outlet. i) Wet etching for the removal of Al. i) Wet etching of Ti. k) Wet etching of SiO2 layer. l) Anodic bonding of the glass following etching of SiO2 layer.

6.1.1.2 Experimental Setup and Procedure

The experimental setup, as depicted in Figure 6.1, comprised a pressurized pure N_2 gas cylinder (BOC, UK), a sample container (Swagelok, Erbusco, Italy), pressure sensors (Omega, Manchester, UK, with an accuracy value of ±0.25% and a range of up to 3000 psi), stainless steel tubing (Swagelok, Erbusco, Italy), and an aluminum holder. The aluminum holder featured a grove with a depth similar to that of the reactor. The reactor was further equipped with convenient inlet/outlet connections sealed via micro-O-rings. To ensure optimal sealing and safety, the reactor was then tightly sandwiched with transparent Poly(methacrylic acid methyl ester) (PMMA) lids. The experiments were initiated by feeding the sample container with the working fluid (in this study: de-ionized water). Pressurized N_2 gas was then released in a controlled manner using a pressure regulator to compress and convey the fluid into the system. The fluid was filtered by a 15 μm nominal pore size micro-T-type filter (Swagelok) to remove undesirable particles before entering the package. The upstream pressure was monitored by a pressure sensor located just before the holder. Different flow patterns were generated by increasing the inlet pressure, while the outlet pressure was kept constant as atmospheric pressure. The fluid was collected in a reservoir with 20 mL volume after passing through the reactor to calculate the volumetric flow rate. The experiments were performed at four different inlet pressures corresponding to four different flow patterns which were characterized by four cases in this study, namely Case I, Case II, Case III and Case IV. The details of experimental parameters regarding flow condition, flow parameters, and nondimensional numbers, including Re numbers ($Re_D = UD_h/\nu$), where Re_D is the Re number based on the

hydraulic diameter (D_h), U is the mean velocity within the microchannel calculated based on the volumetric flow rate, and ν is kinematic viscosity) and cavitation numbers ($\sigma = (p_{in} - p_{sat})/(\frac{1}{2}\rho_w U^2)$, where p_{in} is inlet pressure, p_{sat} is vapor saturation pressure of

water and ρ_w shows water density) are provided in Tables 6.1 and 6.2 (ρ_v and μ_v represent vapor density and dynamic viscosity, respectively).

Multiple runs of the experiments were performed under strict control over experimental conditions to evaluate the consistency of our results. Specifically, the experiments were performed at least three times to ensure the consistency and reliability. The sensors used in this study were calibrated regularly before the experiments to minimize any potential measurement deviations. A detailed uncertainty analysis is also included in Table 6.3, which implies the potential errors arising from microfabrication and measurements. The variability of the results was quantified by calculating the percentage uncertainty. The uncertainty propagation method was used for this(Kline, 1953), and error values of sensors are received from the manufacturer's datasheet.

Table 6.1 Fluid properties and flow conditions of the current study.

$\rho_w \left[\frac{kg}{m^3}\right]$	$\rho_v \left[\frac{kg}{m^3}\right]$	$p_{sat}[MPa]$	$\mu_w \left[\frac{Ns}{m^2}\right]$	$\mu_v \left[\frac{Ns}{m^2}\right]$	$\gamma \left[\frac{N}{m}\right]$	$T_{ambient}[K]$	$p_{outlet}[MPa]$
998.2	0.554	2.34e-3	0.9e-3	0.74e-6	0.07	293.16	0.1

Table 6.2 Inlet pressure and flow regimes in the current study.

	Case I	*Case II*	*Case III*	*Case IV*
$p_{in}[MPa]$	2.38	2.90	3.79	4.83
σ	3.183	3.074	2.896	2.155
Re_D	3,820	4,291	5,054	6,633

Table 6.3 Uncertainties in experimental parameters

Uncertainty	*Error*

Flow rate	±1.3%
Cavitation number	±6.5%
Reynolds number	±5.6%
Hydraulic diameter	±3.4%
Pressure drop	±0.3%

6.1.1.3 Visualization and Quantification of Void Fraction

High-speed visualizations were performed in-situ using a high-speed camera (Fastcam SA-Z 2100 K (Photron, UK)) equipped with a Navitar 12 × zoom lens (0.5 × 0.009–0.051NA 1–50012) with resolution as low as 6.66 μm and depth of field ranging from 0.19 – 6.17 mm. The cavitation zone inside the reactor was illuminated by a high-power cold light source (Karl Storz Power LED 175, Germany) from the front. The cavitation phenomena were recorded at a rate of up to 10^5 frame per second (fps). In order to maintain desirable spatial resolutions, the images were acquired at a frequency of 80000 Hz at 0.23 megapixels in this study. The image resolution was 752×312 with an optical magnification of 0.27 mm px^{-1}, and the image depth was 8 bit. For all the series of images obtained with the high-speed camera, camera settings for brightness and contrast were kept constant and equal. The details regarding the data analysis are included in Appendix A.

6.2 Results and Discussions

6.2.1 Flow Regimes, Inception, and Nuclei Content

In this study, four distinct flow regimes were identified by varying the inlet pressure and maintaining atmospheric pressure at the outlet. These regimes are shown as instantaneous snapshots in Figure 6.3 and are also summarized by casting their

corresponding flow conditions. Inlet pressures were systematically selected based on preliminary tests to encompass the full range of cavitation regimes, from inception to intense shedding. This approach allowed for a comprehensive analysis of shear cavitation dynamics within the microscale backward-facing step geometry. In turbulent shear cavitation, cavitation inception (case I) is associated with the first appearance of cavitation or the first occurrence within quasi-streamwise vortices (QSV) as they are stretched between spanwise vortices of the shear layer(Agarwal et al., 2023). As the inlet pressure increases, the mean kinetic energy of the flow also rises, which leads to a decrease in the cavitation number. Consequently, more intense cavitation becomes visible with increasing inlet pressure. The primary factor contributing to this observation is the strengthening of vortices and associated increase in the local velocity within the shear layer. These strengthened vortices induce a significant drop in local static pressure, creating conditions favorable for cavitation inception. In Case II, cavitation preferentially develops near the middle of the shear layer and around the reattachment point, aligning with the location of spanwise vortices (the vortices developed due to the Kelvin-Helmholtz instability and velocity gradient within the shear layer). In Case III, a thicker and more intense cavitation region forms closer to the step. Finally, Case IV exhibits intense shedding cavitation encompassing the entire shear layer, with numerous bubbles present within the separation bubble (the volume enclosed by the region of the separated flow) that are shed from the main cavitation region.

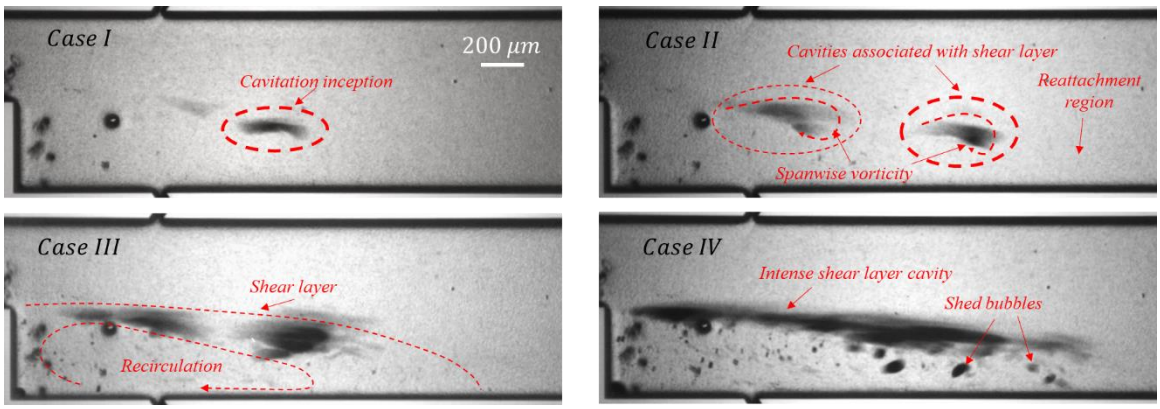

Figure 6.3 High speed camera snapshots of different cavitating flow regimes in BFS configuration. Case I: inception, Case II: developing, Case III: shedding, Case IV: intense shedding.

Figure 6.4 depicts the development of vapor packets (cavitation) behind the BFS at various time intervals and positions. These observations were made at the upstream pressure of 2.38 MPa, which corresponds to the critical pressure for the first observation of cavitation on the reactor. The complex flow patterns within the reactor, featuring different types of vortices and high shear stress zones within the shear layer, act as nucleation sites for cavitation bubbles. These vortices and high shear stress regions accelerate the rapid growth and collapse of cavitation nuclei, triggering cavitation events. Several studies (Agarwal et al., 2023, 2018; Bhatt et al., 2021a; Katz and O'Hern, 1986; Maurice et al., 2021) reported cavitation inception within QSV structures. The high-speed camera visualization shows that cavitation inception occurs after nuclei become trapped within the shear layer. These bubbles likely originate from the upstream location of the step or are remnants of previous cavitation collapses near the reattachment zone. As can be seen in Figure 6.4, cavitation incepts within the shear layer formed behind the BFS. The inception process involves the repeated formation and collapse of vapor bubbles, likely due to nuclei trapped in the shear layer or fluctuating local pressure. [11,12,20–22] In some cases, these bubbles progress to larger spanwise vortices within the shear layer. These bubbles have significant shape and size changes before collapsing in high-pressure regions. Trapped nuclei first expand in low-pressure areas within the shear layer, then rapidly contract and collapse upon entering high-pressure zones. Furthermore, local variations in the shear layer, such as changes in the velocity gradients and pressure

fluctuations, influence the formation and collapse of these bubbles (Iyer and Ceccio, 2002).

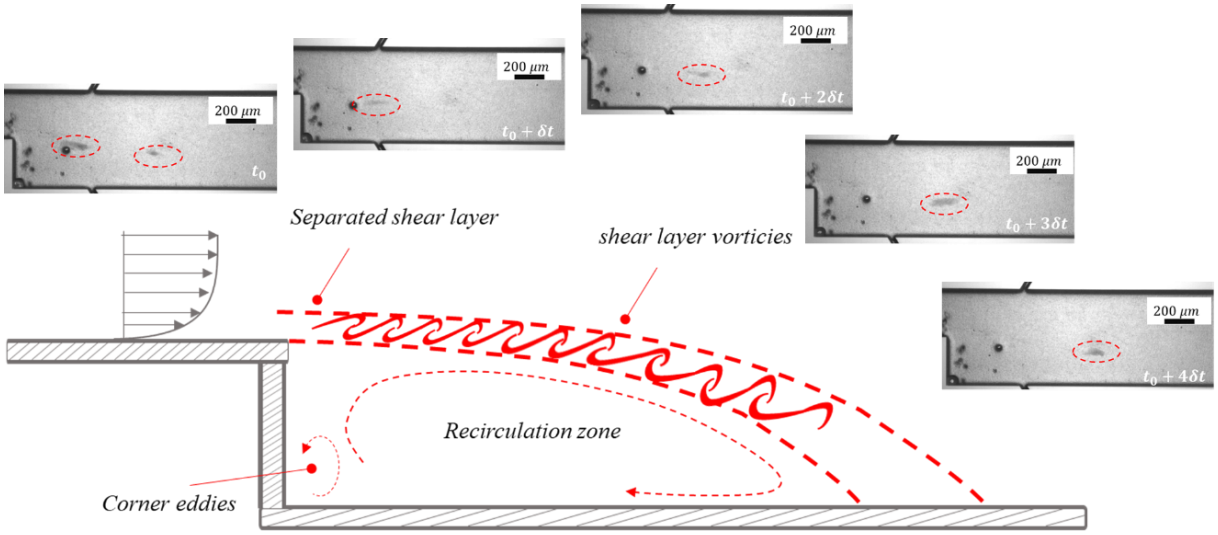

Figure 6.4 Sequence of images extracted from high-speed videos showing the evolution of a discrete incipient cavity.

The number and distribution of nuclei in the wake of the BFS significantly affects cavitation. When these nuclei coincide with local low-pressure zones, cavitation intensifies in susceptible regions. As shown in previous studies(Allan et al., 2023), a higher concentration of nuclei leads to more intense cavitation within the shear layer. Based on the observations, it can be deduced that bubble collapses near the reattachment zone significantly contribute to the nuclei population within the separation bubble. These shed bubbles are primarily trapped within the separation bubble before re-entering the shear layer and intensifying cavitation. Therefore, the focus is on quantifying the spatial distribution of these bubbles within the separation zone to identify areas with the highest nuclei concentration. Additionally, it is aimed to investigate the impact of the cavitation regime on the distribution and fluctuations of these nuclei.

Figure 6.5 presents the time-averaged distribution of normalized nuclei concentration within the separation bubble for various cavitation regimes. Nondimensional coordinates normalized by step height are shown by $\tilde{x}$ and $\tilde{y}$. In the inception regime, most nuclei are concentrated in the region defined by $\tilde{x}\sim 2-4$ and $\tilde{y}\sim 0.5$. As the pressure increases downstream of this region, vapor bubbles primarily collapse here, generating new nuclei. These nuclei become trapped within the recirculation zone and are then transported back

to the center of the shear layer, triggering new cavitation events. At a higher pressure of 2.9 MPa, the nuclei level within the separation bubble increases. Additionally, a high concentration of bubbles is observed not only in the second half of the shear layer but also in the corner vortex and first half of the shear layer, which contributes to cavitation within the first half of the layer at this pressure. At even higher upstream pressures, the nuclei concentration further increases, particularly within the first half of the separation bubble.

Figure 6.6 depicts the RMS bubble concentration, which reflects the temporal variations of bubble nuclei across the spatial domain. High RMS values correspond to regions with a high average bubble concentration (as shown in Figure 6.5), indicating significant fluctuations in bubble presence within these areas. The RMS values are remarkable across a large portion of the separation bubble and downstream of the reattachment zone, suggesting a scattered distribution of bubbles throughout these regions.

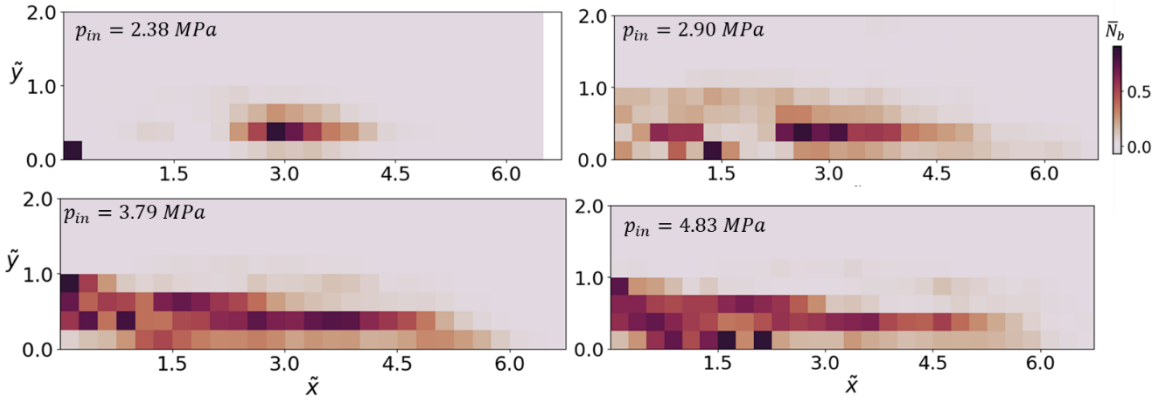

Figure 6.5 Time averaged of spatial distribution of nuclei bubbles in the BFS separation bubble at four different upstream pressures. The concentration in each discrete square region was obtained by summing the number of discrete bubbles in the corresponding region over all time steps and dividing with the number of time steps.

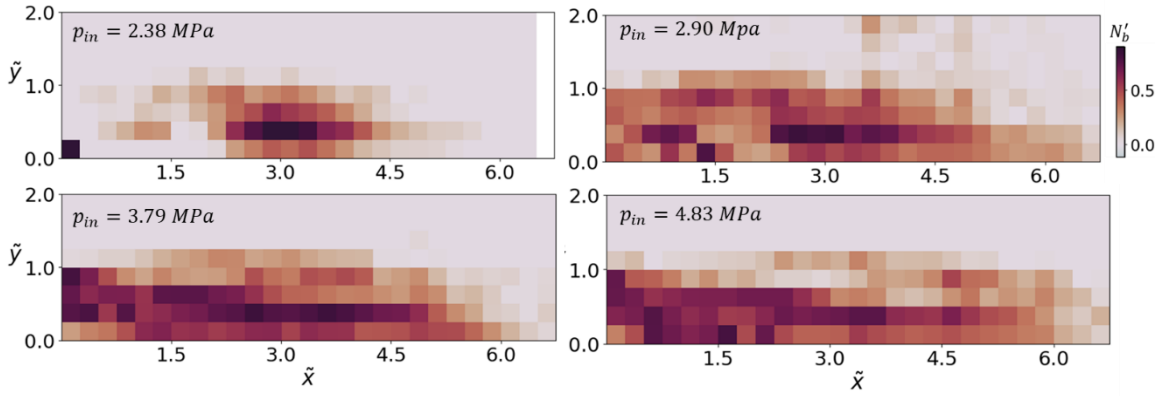

Figure 6.6 RMS of spatial distribution of nuclei bubbles in the BFS separation bubble at four different upstream pressures. The concentration in each discrete square region was obtained by summing the number of discrete bubbles in the corresponding region over all time steps and dividing with the number of time steps.

6.2.2 Mean Characteristics of Void Fraction

The mean and standard deviation of void fractions are presented in Figure 6.7 for all cases. It can be seen that for all cases the maximum mean void fraction lies within the shear layer, and its intensity and length increase for smaller cavitation number.

The RMS values of void fraction fluctuations generally exhibit a similar pattern to the mean void fractions, with one notable exception observed for Case III. Here, the peak in the mean void fraction (occurring near the step) does not coincide with the peak in void fraction fluctuations, which is located within the middle region of the shear layer. This discrepancy suggests that for Case III, while the average vapor content is highest near the step, the most significant fluctuations (rapid changes in vapor content) occur within the shear layer. Furthermore, Cases III and IV have noticeably higher void fraction fluctuations within the recirculation zone. This observation aligns with the expectation that the number of shed bubbles from cavitation packets increases as the cavitation number decreases (indicating more intense cavitation). These bubbles likely contribute to the increased fluctuations observed within the recirculation zone.

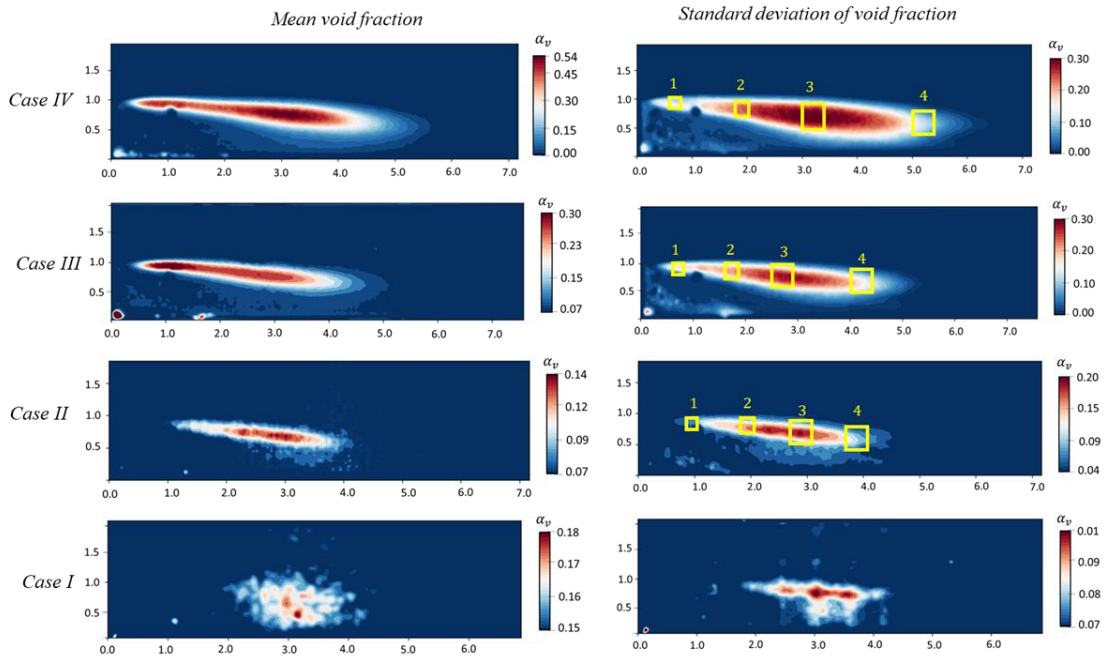

Figure 6.7 Contours of mean (left column) and standard deviation (right column) of void fractions for Cases I to IV. Red squares indicate the probes used for spectral analysis, numbered for easy reference. To enhance clarity, separate color bars with distinct value ranges are employed for void fraction data.

Figure 6.8(a) presents the maximum values of the mean void fraction ($\bar{\alpha}_{max}$) along the streamwise direction. These values offer valuable insights into the evolution of vapor content within the shear layer. As they are independent of transverse coordinate (y), they can be used to evaluate mean global behavior in each flow regime. As demonstrated by Maurice et al. (Maurice et al., 2021), the cavitation region can be segmented into three distinct zones: cavitation generation which is characterized by the increase in void fraction, eddy transport region where the void fraction is almost constant and cavities are transported with shear layer vortices, and condensation associated with decrease in void fraction. Four cases of cavitation regimes are evaluated based on these cavitation zones. The region of cavitation generation is typically associated with a rise in the maximum mean void fraction along the streamwise direction (indicated by $\bar{\alpha}_{max}$ in Figure 6.8a). The observations for Case IV reveal that this peak corresponds to the cavitation generation zone which lies in $(0 < \tilde{x} < 0.8)$. Interestingly, the width of this generation region expands with increasing cavitation number, which implies that as the cavitation number increases (indicating less intense cavitation conditions), cavitation occurs further

downstream from the step. In Cases I and II, it is observed that the area of peak void fraction aligns with the peak nuclei concentration observed in Figure 6.7, indicating that the second half of the shear layer is the most susceptible one to cavitation and also the location with the highest nuclei concentration during inception.

The region with relatively flat variations in the maximum mean void fraction ($\bar{\alpha}_{max}$) corresponds to the zone with eddy transport for the cavitation bubbles. For Case IV, the plateau region ($0.8 < \tilde{x} < 3.5$) aligns with this transport zone. The width of this transport region exhibits a decrease with increasing cavitation number (with moving of peak in generation downstream). This observation can be explained by the fact that cavitation inception occurs further downstream within the shear layer as the cavitation number increases. Moreover, it can be observed that the condensation starts almost at the same location ($\tilde{x} = 3.5$) for all cases, while the slope of $\bar{\alpha}_{max}$ in generation and condensation significantly decrease with an increase in the cavitation number.

To further investigate differences in characteristics of shear cavitation for different regimes, the mean shear cavitation thickness within the shear layer was used as the characteristic length scale using the following equation (Maurice et al., 2014):

$$L_{\bar{\alpha}}(\Delta x, \tau) = \int_{-h/2}^{h/2} R_{\alpha\alpha}(x, \Delta y)\, d\Delta y \tag{6.1}$$

where the spatial correlation ($R_{\alpha\alpha}(x, \Delta y)$) is defined as:

$$R_{\alpha\alpha}(x, \Delta y) = \frac{\langle \bar{\alpha}(x_{ref}, y_{ref}) \bar{\alpha}(x_{ref}, y_{ref} + \Delta y) \rangle}{\alpha'_{rms}(x_{ref}, y_{ref}) \alpha'_{rms}(x_{ref}, y_{ref})} \tag{6.2}$$

In this equation, $\langle\ \rangle$ represents the ensemble average, $\bar{\alpha}$ is the temporal mean of the void fraction, and α'_{rms} is RMS of the void fraction fluctuations. Figure 6.8(b) depicts the evolution of the estimated characteristic length scale, which is directly proportional to the thickness of the vapor phase within the shear layer. For all cases, it is evident that the maximum thickness occurs approximately at the midpoint of the shear layer ($\tilde{x} \approx 3.3$), which indicates that the maximum cavitation thickness is attained before reaching the condensation region, where subsequent condensation leads to a reduction in this thickness. Moreover, the thickness decreases notably with an increase in the cavitation number (and simultaneously decreasing the *Re* number), indicating a decrease in both the size and strength of spanwise vortices within the shear layer.

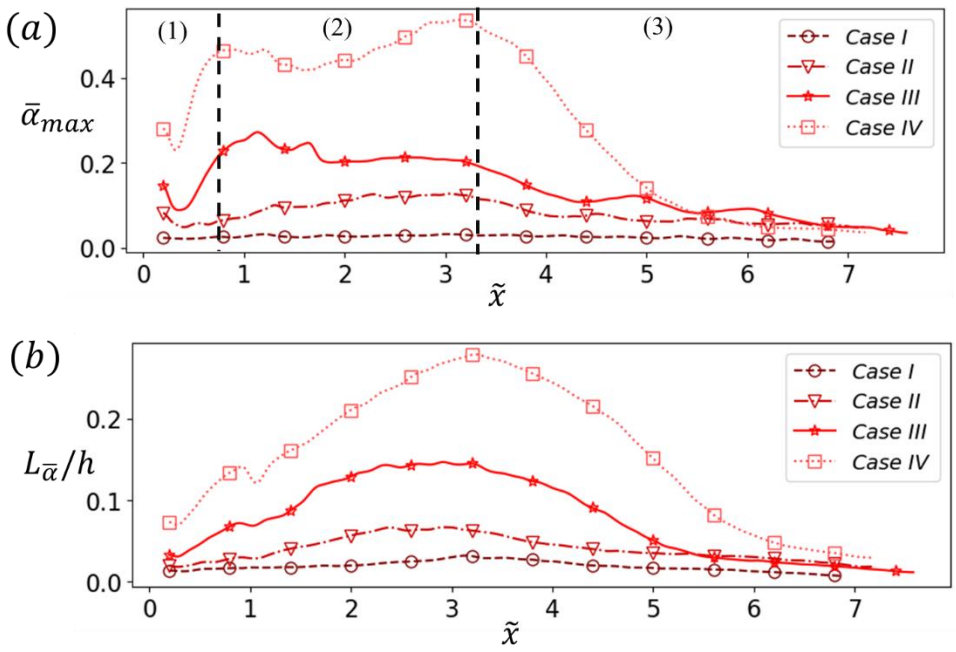

Figure 6.8 (a) Evolution of the maximum of the mean void fraction field (1, 2, and 3 show regions of the vapor generation, transport and condensation, respectively), and (b) Characteristic void fraction length-scale evolution along the longitudinal direction

Spatio-temporal correlation for the fluctuating void fraction field was calculated as (Weiss et al., 2015):

$$R_{\alpha\alpha}(\Delta x, \tau) = \frac{\langle \alpha'(x_{ref}, t_{ref}) \alpha'(x_{ref}+\Delta x, t_{ref}+\tau) \rangle}{\alpha'_{rms}(x_{ref}) \alpha'_{rms}(x_{ref}+\Delta x)} \tag{6.3}$$

Figure 6.9 presents the spatio-temporal correlations for Cases III and IV. Spatio-temporal correlations are not considered for Cases I and II due to limitations in the data. Case II has a limited number of snapshots, hindering accurate estimation of these correlations. Additionally, the sparse and transient presence of void fractions, especially in Case I, makes tracking void movement impractical, further complicating the reliable estimation of spatio-temporal correlations. Spatio-temporal correlation quantifies the statistical relationship between fluctuations in void fraction at different spatial locations and across time within the cavitating shear layer, which helps to understand how variations in the vapor content are interconnected. The normalized convective velocities were approximated by fitting a linear function to the local maxima observed in the correlation functions. The results reveal that the mean convective velocities in both cases are

approximately half of the mean bulk velocity of the flow (particularly in transport zone). This aligns with previous observations of convective velocities for coherent structures within free shear layers (Dimotakis, 1986), which decreases along the shear layer. This result confirms that the vapor is mainly transported within these spanwise vortical structures.

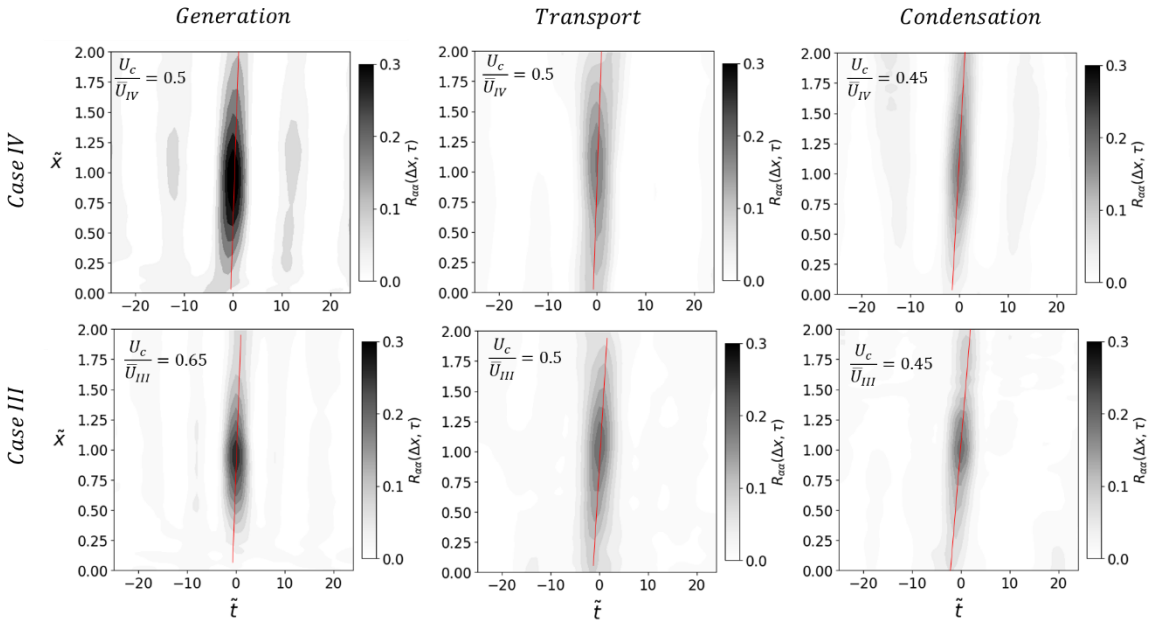

Figure 6.9 Spatio-temporal correlation of void fraction for Cases IV and III in three different regions which were obtained based on Figure 8 (Generation: $\mathbf{0.0 < \tilde{x} < 2}$, Transport: $\mathbf{2 < \tilde{x} < 4}$, Condenstaion: $\mathbf{4 < \tilde{x} < 6}$). The red line was obtained using linear fitting of the correlation maxima. The slope of the line represents the mean convective velocity ($\boldsymbol{U_c}$) of the void fraction in each region. The normalized value of convective velocity (normalized by reference velocity in the corresponding case) is provided in each plot.

6.2.3 Spatio-temporal Dynamics of Void Fraction

The images from the high-speed camera are presented in Figure 6.10 for the upstream pressure of 4.83 MPa (Case IV) along with the spatio-temporal map of void fraction in this regime. Only time series of Cases IV and III are studied here because the sparse and

short-lived presence of void fractions, especially in Case I, makes it difficult to follow their movement in the given temporal resolution. The time interval between sequential images is $12.5\ \mu s$. As already discussed in the previous section, pressure drops within spanwise vortices of the shear layer provide suitable conditions for cavitation development. In the snapshot related to the time instance of t_0, separate vapor packets along the shear layer are visible (indicated by 1, 2, 3 markers). In this case, the vapor phase fills the spanwise vortical structures, which are connected to each other through QSVs. Furthermore, many small bubbles (with sizes between $5\mu m$ to $20\ \mu m$) which are shed from the large vapor packets within the shear layer are observed within the recirculation zone. These small bubbles help in visualization of vorticity distributions and their variations within the recirculation region. They also feed and reinforce cavitation at different locations within the shear layer. As indicated in time instance $t_0 + \delta t$, recirculation region encompasses multiple clockwise and anti-clockwise vortices, which have shape variation, merge and split as the reattachment is displaced along the wall. In this time instance, vapor packet 1 develops which corresponds to the development and growth of spanwise vortices associated with the packet. Meanwhile, a link of vapor forms between the 1st and 2nd packets, demonstrating development of vapor towards streamwise structures which connect two sequential spanwise structures. Once the separation bubble reaches its maximum size, a vortex associated with vapor packet 3 detaches from the downstream end of the separation bubble. Prior studies(Durst and Tropea, 1983; Nadge and Govardhan, 2014; SCHÄFER et al., 2009b) demonstrated that the length of the separation bubble, particularly in turbulent flows, is primarily controlled via the balance between forces exerted by the pressure field and Reynolds normal and shear stresses along the recirculation zone or bubble boundary. The high Reynolds shear stress near the reattachment point promotes a longer reattachment length. In contrast, both of the forces due to Reynolds normal stress and pressure field act along the upstream direction. At lower *Re* numbers, viscous shear and normal stresses dominate, while Reynolds stresses become negligible. Furthermore, Nadge and Govardhan (Nadge and Govardhan, 2014) reported that both Reynolds shear and normal stresses depend on the geometry and *Re* number, while the pressure force component remains independent of step size. Any imbalance in these forces, such as differences in the entrainment to the shear layer from the recirculation zone and re-entrainment (Durst and Tropea, 1983), can trigger a shedding mechanism at the reattachment point. This event is coupled with the displacement of the reattachment, change in the size and shape of the vortices within the

recirculation and merging of spanwise vortices within the shear layer which corresponds to the 1st and 2nd vapor packets within the shear layer. In the light of the image sequence, the velocity of the shed vapor at the reattachment (packet 3) can be approximated as $\approx 32.6\, m/s$. After reestablishment of the reattachment in the time instance of $t_0 + 3\delta t$, cavitation is developed within the shear layer so that the shear layer is filled with vapor. Then, the reattachment gradually moves downstream. At the same time, vapor packets move along the wall at the front of the reattachment. The time slot between $t_0 + 4\delta t$ and $t_0 + 7\delta t$ demonstrates that vapors cannot pass through the reattachment within the shed vortices, which suggests that the shed vortices are not strong enough to sustain the required low pressure in their cores for carrying vapor packets deep into the channel. Consequently, the vapor condenses immediately in front of the reattachment zone, forming small bubbles that are dispersed and carried to the upstream location by the reentrant jet. To elucidate the mechanism by which vapor collapse at the end of the shear layer leads to bubble shedding and their subsequent transport and distribution within the separation bubble, movies visualizing the bubble tracking process are provided. Movie 1 (Multimedia view) tracks the generated bubbles within the separation bubble. Most of these bubbles rejoin the shear layer at various locations, primarily in the middle region (interface between the clockwise and counterclockwise vortices within the recirculation zone). Furthermore, the images reveal minimal displacement of the reattachment point and variation in the size and shape of the separation bubble during this time period (compared t_0 to $t_0 + 3\delta t$). This suggests the presence of smaller shed vortices during this time, which is further displayed in the spatio-temporal map of void fraction in Figure 6.10(a).

As the time progresses to $t_0 + 8\delta t$, the vortices within the recirculation zone and spanwise vortices within the shear layer continue to develop and convect. Consequently, a relatively large vapor packet located within a shear layer vortex begins to break apart and detach from the separation bubble. The collapse of the large vapor packet and resulting pressure wave significantly reduce the vapor intensity and shear layer thickness between time slot $t_0 + 9\delta t$ and $t_0 + 11\delta t$. In the instance of $t_0 + 12\delta t$, the recirculation zone undergoes a dramatic change. A large recirculation vortex, along with vapor trapped within the shear layer, begins to detach from the separation bubble (TSB). This detachment carries a significant portion of vapor with the vortex, initiating a new cycle.

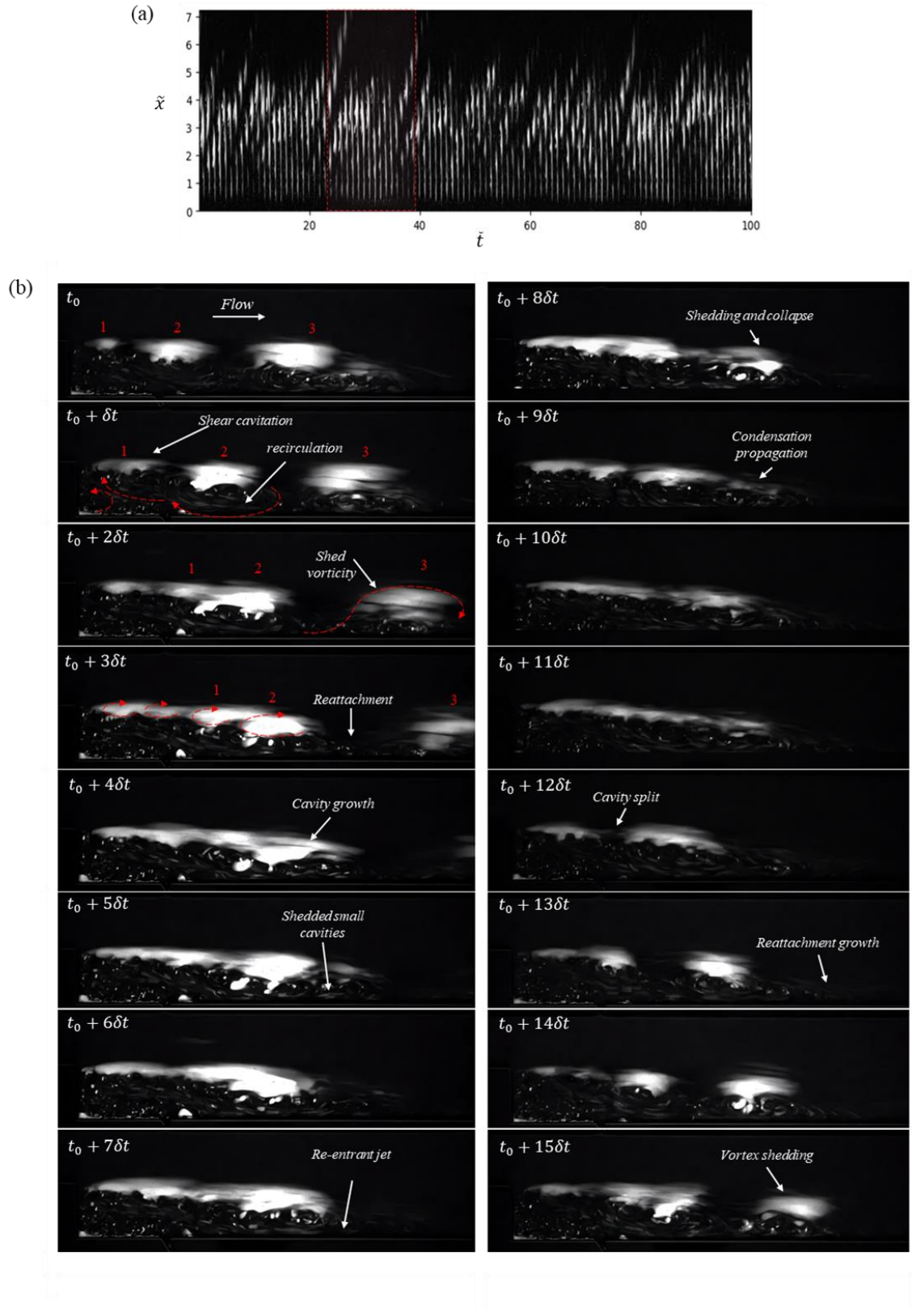

Figure 6.10 Time sequence of cavitation development and dynamics for the upstream pressure of 4.83MPa ($\boldsymbol{\delta t = 1.25\mu s}$). The initial stages (frames 1-4) utilize markers (1, 2, and 3) to track the movement of distinct vapor packets, each associated with a

separate shear layer spanwise vorticity. For better clarity, some vorticities within the shear layer, recirculation zone, and region after reattachment (shed vorticity) are highlighted with dashed red lines. The corresponding time interval within the spatio-temporal map is highlighted by a red overlay.

Figure 6. 11 demonstrates that the shedding mechanisms during the time slot between (t_0 to $t_0 + 3\delta t$) and ($t_0 + 12\delta t$ to $t_0 + 15\delta t$) differ significantly from the mechanism observed during the time slot between $t_0 + 4\delta t$ and $t_0 + 11\delta t$. These two distinct shedding behaviors closely resemble the two modes of wake and shear shedding identified by Hudy et al. (Hudy et al., 2007) and observed by Maurice et al. (Maurice et al., 2021). Hudy et al. (Hudy et al., 2007) identified two distinct shedding modes in the flow behind a step. In the wake mode, large, and strong vortical structures detach and convect downstream, accompanied by more energetic pressure fluctuations along the wall (characterized by large peaks and valleys). Conversely, the shear mode is characterized by the continuous growth and merging of spanwise vortices within the shear layer. Here, vortices shed from the shear layer once their size reaches a size comparable to the step size. As shown by Hudy et al. (Hudy et al., 2007), this mode is associated with less dramatic pressure fluctuations, characterized by smaller peaks and valleys which suggests weaker vortex shedding. The vapor distribution observed in Figure 6.11 aligns perfectly with these distinct shedding modes. Figure 6.11 provides two specific time instances, each relevant to a particular mode. In the wake mode (Figure 6.11, left), separate packets of vapor reside within the large vortical structures. This coincides with the high-pressure peaks observed between the vapor packets and low-pressure valleys within them. In contrast, in the shear mode (Figure 6.11, right), less intense vapor fills the entire shear layer (including the vortices). Additionally, the recirculation region in this mode consists of small and randomly oriented vortices. Comparable shedding mechanisms were identified in our recent numerical investigation(Maleki et al., 2024) of cavitating flow within a BFS microchannel. Two shedding modes (coexisting with slow breathing motions) were observed: a high-frequency mode characterized by small vortex shedding at the end of the separation bubble, and a low-frequency mode associated with larger reattachment region excursions.

Our findings suggest that the wake mode is most likely initiated by the pressure wave generated during the collapse of the large vapor packet at the downstream end of the shear

layer ($t_0 + 8\delta t$). This observation agrees with the results of a previous study by Maurice et al. (Maurice et al., 2021). They reported a similar wake mode triggered by vapor collapse downstream of the reattachment point, followed by pressure wave generation and propagation upstream towards the step. As previously discussed, the pressure wave generated by the collapse at $t_0 + 8\delta t$ is insufficient to fully condense the vapor within the strong spanwise vortices of the shear layer. It can, however, cause a marginal condensation effect. Despite this limitation, the pressure wave possesses enough strength to disturb the shear layer and recirculation zone, triggering a breakdown of the recirculation from its midsection ($t_0 + 12\delta t$). This stands in contrast to the shear mode, where the shed vortices at the reattachment point are the same vortices that develop within the shear layer. Consequently, they show the frequency of the same order as the spanwise vortices of the shear layer. The spatio-temporal map in Figure 6.10(a) further illustrates the distinct vortex shedding behavior observed in the wake and shear modes. In the shear mode, vortex shedding at the reattachment point has a relatively high frequency with a smaller amount of vapor penetration into the channel. Conversely, the wake mode is characterized by significantly lower shedding frequency and a more random shedding pattern (frequency of around ~60 kHz versus ~300 kHz in the case shear mode). This behavior, combined with the stronger shed vortices associated with the wake mode, leads to a larger penetration of vapor within the channel.

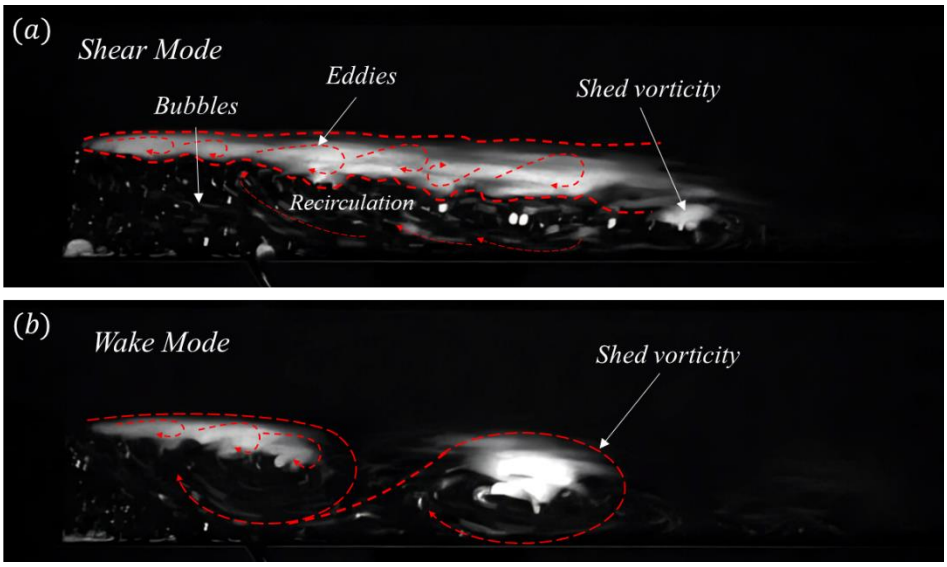

Figure 6.11 Instantaneous results showing the (a) wake mode and (b) shear mode of vortex shedding in BFS cavitating flow.

Figure 6.12(b) presents time instances of cavitation development for an upstream pressure of 3.79 MPa (corresponding cavitation and *Re* number given in Table. 6.2). Similar to the case of 4.83 MPa, both wake and shear shedding modes are observed at this pressure. However, some notable differences exist between the two upstream pressure conditions. As illustrated in previous studies (Ji and Wang, 2012), a reduction in *Re* number generally leads to a decrease in the mean reattachment length compared to the case with a higher *Re* number. This trend is also evident in the spatio-temporal map provided in Figure 6.12(a). The vapor content within the channel and shear layer is significantly lower at 3.79 MPa compared to the case with a higher *Re* number (Figure 6.12). This decrease is primarily attributed to the weakened strength of the vortices within the shear layer at a lower *Re* number. Consequently, even during the shear mode, the vapor is unable to fully occupy the shear layer (t_0). The collapse of the vapor packet within the shear layer near the reattachment point ($t_0 + \delta t$) is accompanied by a propagating condensation wave and a significant reduction in vapor content within the shear layer ($t_0 + \delta t$ to $t_0 + 4\delta t$). Notably, condensation in this case appears to be much more pronounced compared to the higher *Re* number case. This increased sensitivity to pressure waves can be attributed to the weaker strength of the spanwise vortices within the shear layer at lower *Re* number. This weakness is caused by a smaller velocity gradient across the width of the shear layer. Consequently, the vortices are unable to generate strong local pressure drops within the shear layer, making vapor more susceptible to condensation when a pressure wave propagates through the medium. As discussed earlier, the presence of shed bubbles within the recirculation zone plays a crucial role in facilitating the development of new cavities within susceptible regions of the shear layer. Bubbles primarily originate from the shear mode regime, where small vapor collapses occur near the reattachment point. In contrast, during the wake mode, the vapor is transported further downstream and predominantly condenses far away from the recirculation zone (see $t_0 + 11\delta t$). This large distance of condensation from the recirculation prevents the generated bubbles from rejoining the shear layer via the reversed flow, thereby effectively removing them from the region where they could contribute to the new cavity formation (the velocity of the represented wake vorticity is approximately 17.3 m/s). Movie 2 (Multimedia view) reveals that most of the shed bubbles successfully return to the shear layer, facilitating the regeneration of cavitation within the layer after condensation ($t_0 + 5\delta t$). This observation aligns with the

behavior observed in the higher *Re* number case. Similar to the previous case, the shear mode is followed by the wake mode. As discussed earlier, the pressure wave generated during the final stage of the shear mode triggers the wake mode ($t_0 + 7\delta t$). However, in this case, the vapor within the wake vortices condenses before reaching the end of the channel, which suggests that the wake vortices in this case are weaker compared to those observed at higher *Re* number (first case). This difference in the strength is linked to the lower mean pressure within the channel at 3.79MPa compared to the first case. Furthermore, the spatio-temporal map of void fraction in Figure 6.12(a) does not exhibit a clear distinction between the shear and wake modes at 3.79 MPa, which is likely due to the weaker wake vortices and their limited impact on vapor transport compared to the Case IV.

Figure 6.12 Time sequence of cavitation development and dynamics for upstream pressure of 3.79 MPa (δt=1.25μs). For better clarity, some vorticities within the shear layer, recirculation zone, and region after reattachment (shed vorticity) are highlighted

with dashed red lines. The corresponding time interval within the spatio-temporal map is highlighted by a red overlay.

The spatio-temporal map of the void fraction is provided in Figure 6.12(a). As can be seen, incidents with deep penetration of vapor packets within the channel are apparent, while a long period of almost uniform small penetrations can be observed. These results suggest that phase transition within the shear layer changes the strength and dynamics of the shed vortices at the end of the shear layer.

Figure 6.13 illustrates a schematic of shear and wake mode in shear cavitating flow, which includes more details about cavitation dynamics in these modes. The shear mode (Figure 6.13(1)) includes a developed separation bubble. As mentioned, this mode is associated with small vortex shedding and small collapses which do not release enough energy to have a remarkable influence on the vapor within the shear layer. This shedding continues for a while (depending on the flow condition) until development and movements of eddies within the shear layer leads to a collapse of a large amount of vapor at the end of the shear layer (Figure 6.13(2)). The speed of a shock wave is governed by the pressure ratio across the wave and the thermophysical properties of the medium. While analytical relations exist for ideal gases, predicting shock wave speed in complex two-phase media becomes more challenging. For such cases, numerical simulations or experimental data are often required to determine the shock wave speed. The Mach number (Ma), which represents the ratio of the relative velocity of the shock wave to the local speed of sound in the undisturbed medium, can be calculated using the relative shock wave speed and local speed of sound. In experimental results the shock wave speed can be approximated as the speed of condensation front. Estimating the speed of sound in a two-phase blend is possible through the homogeneous equilibrium model (accounting for immediate inter-phase heat transfer) or the homogeneous frozen model (neglecting heat transfer between phases). The general formulation that can be used by both models for estimation of local speed of sound can be expressed as follows(Bhatt et al., 2021a; Brennen, 2013):

$$\frac{1}{\rho_m c_i} = \frac{\alpha_i}{p_i}[(1-\epsilon_v)f_v + \epsilon_v g_v] + \frac{1-\alpha_i}{p_i^{1+\eta}}\epsilon_l g^* p_c^{\eta} \tag{6.4}$$

where ρ_m shows the local mixture density, α_i and p_i are local void fraction and pressure, $p_c$is critical pressure, $f_v, g_v, \eta,$ and g^* are material dependent parameters. $\epsilon_l = \epsilon_v = 0$

corresponds to the homogeneous frozen model and $\epsilon_l = \epsilon_v = 1$ corresponds to the homogeneous equilibrium model. From speed of condensation within the two-phase mixture in Figure 6.12 ($t_0 + \delta t$ to $t_0 + 5\delta t$) (Mach number, $Ma > 1$) it can be inferred that the collapse leads to a shockwave generation. After the propagation of the shockwave through the shear layer condensation occurs. According to our results, (Figures 6.13 and 6.12), the amount of condensation highly depends on the strength of vortices within the shear layer, which is proportional to the velocity gradient across the shear layer width and *Re* number. The condensation of the vapor within the shear layer triggers the wake mode and breaking of the separation bubble (Figure 6.13(4)). Figures 6.13(5) and 6.13(6) show wake mode shedding and subsequent development of the separation bubble, as was discussed earlier. Since Cases III and IV exhibit comparable shedding mechanisms, a unified schematic will be presented to illustrate the critical parameters governing this phenomenon in shear cavitating flow. The upstream propagation of pressure waves triggered by the collapse of large vapor packets during reattachment initiates the breakup of the separation bubble and transition to wake mode, which is a notable finding, also supported by previous study of Maurice et al. (Maurice et al., 2021). This suggests that the pressure wave propagation exacerbates the imbalance between effective forces involved in turbulent separation bubble formation, specifically the Reynolds stress and pressure forces, as previously discussed. Consequently, more frequent and intense collapses in the reattachment area are likely to enhance the wake mode. The collapse intensity and frequency are influenced by several parameters, including the bubble size, distribution, and compression rate, which are dependent on *Re* and cavitation numbers.

Despite previous studies demonstrating the occurrence of the wake mode across various *Re* numbers in single-phase flows, there remains a gap in understanding of how the Reynolds number affects the shedding mode behavior. Given that the pressure and velocity fluctuations due to cavitation and bubble collapses significantly impact the equilibrium between Reynolds stress and pressure forces, drawing definitive conclusions about the effect of Reynolds number on the shedding behavior independently is challenging.

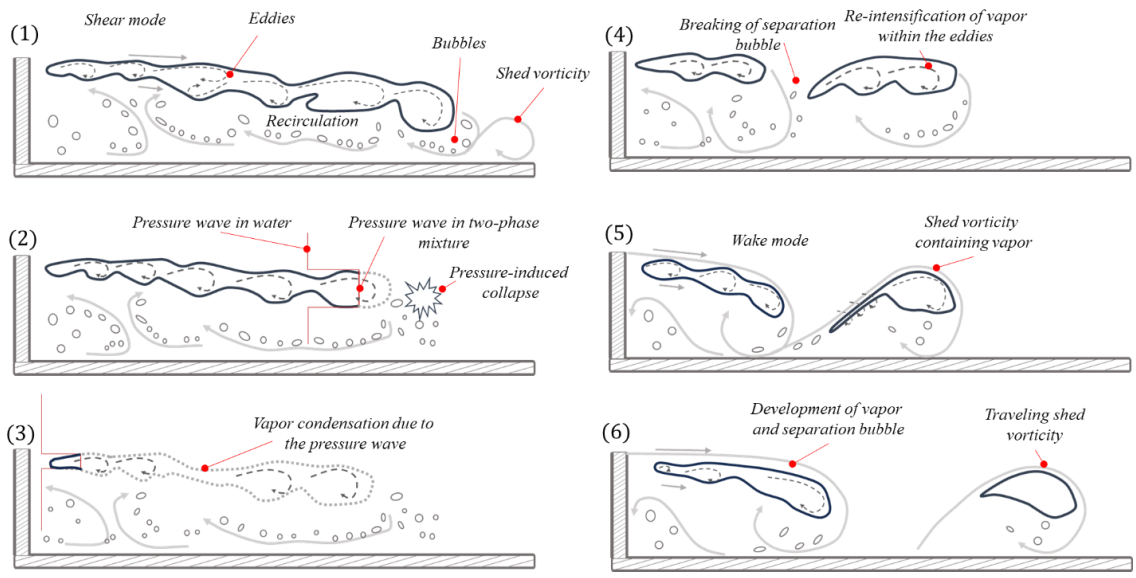

Figure 6.13 Schematic illustration shear and wake mode shedding mechanism in shear cavitating flow (numbering is in accordance with the sequence of events). (1) shear mode shedding, (2) pressure-induced collapse of vapor packet at reattachment, (3) vapor condensation within the shear layer, (4) breaking if separation bubble, (5) wake mode shedding, and (6) development of vapor and separation bubble.

The frequency characteristics of Cases III and IV are examined using the pre-multiplied power spectral density (PSD) at particular streamwise positions along the path of maximum fluctuation in void fraction (α'_{rms}). The positions of the probes are indicated by red square zones in Figure 6.7 (right column). For Case III, the peak PSD values correspond to Strouhal numbers (St_h) of approximately 0.005, 0.06, and 0.14, representing the slow, medium, and high-frequency void fraction fluctuations within the shear layer (Figure 6.14(a)). These Strouhal numbers can be interpreted as dimensionless frequencies that characterize the shedding or oscillation patterns within the TSB. The dominant frequency observed at Probe 1 (plot specific to each probe is determined by the probe number) for Case III falls within the medium frequency range of the PSD plot. By considering the spatio-temporal map and instantaneous images in Figure 6.13, it can be inferred that this frequency likely corresponds to the shedding of vapor packets in the wake mode of the TSB. In the wake mode, almost the entire vapor content within the shear layer condenses. Therefore, the observed frequency likely reflects the shedding frequency of shear cavitation in the wake mode. Probes 2 and 3 exhibit a broader range of dominant frequencies, encompassing low, medium, and high frequencies. The high

frequencies stem from KH instabilities within the shear layer, which influences the fluctuations of vapor content in this region. In the case of the micro step, the flow separation and the presence of the shear layer can create velocity differences that trigger the KH instability. The Kelvin-Helmholtz instability is characterized by the development of spanwise vortices within the shear layer. These vortices can form due to the shearing motion between the fluid layers with different velocities. As the vortices grow and interact with the surrounding flow, they cause mixing and deformation of the shear layer. Probe 3, situated in the region of the maximum void fraction, also shows a significant presence of low-frequency components in the PSD. The characteristic time scale associated with this dominant low frequency is considerably larger (almost 12 times) compared to the typical frequencies of wake mode shedding. This suggests that this low-frequency component is linked to external factors such as pressure pump fluctuations. Finally, the dominant frequencies at Probe 4 lie in the medium and high ranges, which correspond to the wake mode and shedding mode near the reattachment zone.

Case IV exhibits a similar pattern of dominant frequencies compared to Case III, but with two key differences (Figure 6.14(b)). Firstly, two distinct medium frequencies are observed, particularly prominent in Probes 2 and 3. These frequencies appear to be harmonics of each other, suggesting a relationship between their periodicities. Secondly, the overall range of dominant frequencies in Case IV is lower compared to Case III. This difference might be attributed to the influence of the vapor phase on the dynamics of coherent structures within the shear layer. Similar observations have been reported in other studies(Bhatt et al., 2021a; Maurice et al., 2021) .

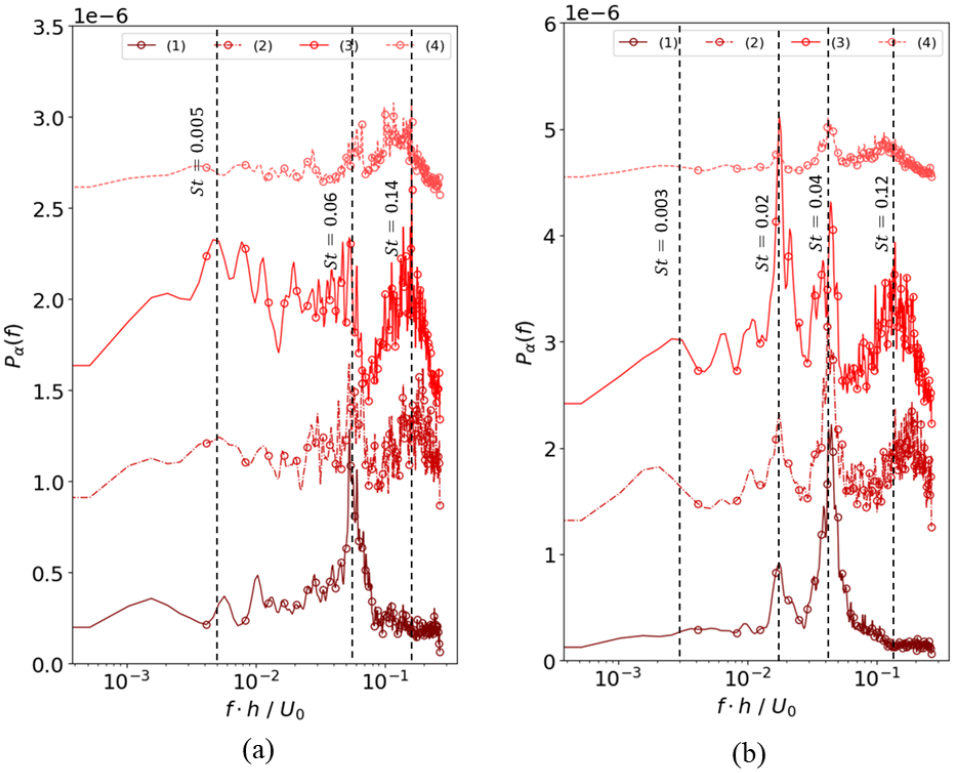

Figure 6.14 Premultiplied power spectral density of void fraction for (a) Case III, and (b) Case IV for four probes (probes (1)-(4)) determined by red squares in Figure 8 right column (Each subplot is determined with the corresponding probe numbers 1 to 4.).

6.3 Conclusion

This study presents the first comprehensive experimental investigation of shear cavitation within a microscale BFS configuration. By examining four distinct cavitation regimes and analyzing void fraction distribution, we identified three primary cavitation zones: generation, transport, and condensation. The influence of Reynolds number and cavitation number on these zones was elucidated.

For cases III and IV, two distinct vortex shedding mechanisms were identified near the reattachment zone: wake mode and shear mode. Similar shedding regimes were documented in the study by Maurice et al.(Maurice et al., 2021) investigating cavitating flow within a macro-scale backward-facing configuration. In our case, the wake mode was initiated by a disruption of the separation bubble. This disruption resulted from the pressure wave generated by the collapse of large vapor packets, which subsequently disturbed the shear layer and recirculation zone, allowing for deeper vapor penetration within the channel. These findings suggest that the disturbances introduced by cavitation and collapse events substantially alter the equilibrium of forces within the separation bubble, ultimately triggering wake mode shedding. Conversely, the shear mode exhibits higher shedding frequency with less vapor penetration. The influence of these shedding modes depends on flow regimes. At higher upstream pressure (4.83 MPa), both modes are observed, with the wake mode leading to deeper vapor penetration due to its stronger vortices. At lower pressure (3.79 MPa), weaker vortices limit vapor transport within the shear layer even during the shedding mode. Additionally, the weaker vortices at lower *Re* number are more susceptible to pressure wave condensation, which results in a more reduction in vapor content compared to the higher *Re* number case.

The results indicate that nuclei predominantly accumulate in the second half of the shear layer during cavitation inception, coinciding with the region of maximum void fraction. This area is also where vapor bubbles collapse, generating new nuclei that become entrained within the recirculation zone and contribute to subsequent cavitation. As pressure rises, nuclei distribution extends throughout the separation bubble, including the first half of the shear layer and the corner vortex. While the free stream is the primary source of nuclei in the inception regime, a reduction in cavitation number leads to a predominance of nuclei originating from collapsing vapor packets. This finding aligns

with Allan *et al.* study[17] that incipient cavity collapse sites serve as preferential locations for new bubble formation.

Additionally, RMS of bubble concentration indicates substantial fluctuations in bubble population within these regions, emphasizing the dynamic nature of the nuclei distribution. Other findings, such as the association of cavitation inception with coherent structures in the shear layer and the impact of cavitation on shedding dynamics, align with previous studies of cavitating flow in a macroscale backward-facing step device. These results contribute significantly to understanding the influence of nuclei distribution and dynamics on cavitation inception and development within microscale BFS flows.

The results of this study offer valuable insights that may inform future research on shear cavitation at the microscale. Exploring the effects of fluid properties and geometric variations on shear cavitation could be a promising direction for future studies.

7 CONCLUSION AND RECOMMENDATIONS

7.1 Summary and Conclusions

This doctoral thesis presents a comprehensive investigation on intricate dynamics of turbulent separated flows and cavitation within microscale BFS configurations. Through a synergistic combination of advanced numerical simulations and novel experimental analyses, this thesis advanced our understanding of the fundamental mechanisms governing cavitation inception, development, and its interaction with complex turbulent structures, particularly in the presence of surface modifications. This thesis will present the following contribution to the literature:

Methodological Advancements: The foundation of this research lies in a robust and sophisticated methodological framework. A custom-developed three-dimensional fully compressible cavitation flow solver, built upon OpenFOAM's rhoCentralFoam and enhanced with Helmholtz-Zentrum Dresden-Rossendorf (HZDR)'s Subgrid-Scale (SGS) model, proved instrumental. This solver's capability to handle low Mach number compressible flow physics and thermodynamic non-equilibrium through a dedicated vapor volume fraction transport equation was critical for accurately capturing intricate phenomena such as shock waves and baroclinic vortex dynamics inherent in cavitating flows. The use of a second-order, four-stage low-storage Runge-Kutta time integration scheme with adaptive Courant-Friedrichs-Lewey (CFL) control ensured both accuracy and computational efficiency for the Large Eddy Simulations (LES). Complementing these numerical capabilities, the thesis introduced the first comprehensive experimental analysis of shear cavitation in a microscale BFS configuration, providing invaluable

validation and opening new avenues for understanding microscale cavitation complexities.

Cavitation's Impact on Turbulent Separated Flows: The initial phase of this research meticulously investigated the intrinsic influence of cavitation on the mean characteristics and unsteady behavior of the TSB. Numerical results, rigorously validated against experimental data and established literature, demonstrated that cavitation significantly alters the shear layer, leading to its narrowing and a postponement of reattachment. The accumulation of vapor within the shear layer profoundly reshaped coherent structures, making spanwise vortical structures longer and thinner. Analysis of mean pressure and RMS pressure fluctuations revealed a decline within the shear layer but a marked increase in the reattachment region, directly attributable to the intense condensation and bubble collapse events. Crucially, vapor generation was shown to trigger a decoupling between Reynolds stress components, converting Reynolds shear stress to TKE, while condensation and collapse intensified Reynolds normal stresses, particularly in the streamwise direction. Regarding TSB dynamics, cavitation consistently led to a decrease in dominant frequencies. Two prominent low-frequency modes, LF1 and LF2, were identified as being linked to reattachment point displacement. Cavitation was found to reinforce the TSB breathing mechanism associated with LF1, leading to more energetic low-frequency fluctuations along the shear layer and reattachment. Conversely, high-frequency fluctuations became more energetic in the reattachment region under cavitating conditions, indicative of frequent bubble collapses. Modal analysis, including SPOD, highlighted that large coherent structures fluctuating at LF1 were more significant and energetic in the presence of cavitation, underscoring the deep coupling between phase change and dominant flow structures.

Geometric Control (the Role of Riblets): Building upon the fundamental understanding of cavitation-turbulence interaction, the thesis then delved into the transformative role of riblet-equipped surfaces. This work unequivocally established the Blockage Ratio (BR) as a pivotal parameter governing the fluid dynamics. Riblets fundamentally reshaped the Turbulence Kinetic Energy (TKE) budget, shifting TKE transport from local production/dissipation to significantly enhanced turbulent diffusion and convection, particularly within the shear layers above the ribs. The Reynolds stress tensor underwent substantial modifications, with anisotropy components near the wall notably reduced and their spatial distribution altered, signifying a profound change in turbulent mixing and

momentum transfer. Morphological and spectral analyses of coherent structures revealed that riblets promote larger and slower structures, evidenced by expanded temporal scales and a shift of the high-energy zone towards lower frequencies. Dynamic Mode Decomposition (DMD) provided compelling visualizations, showing that riblets disrupt uniform coherent structures, fostering distinct, often pairwise, low-frequency vortices near the ribs and crests that were demonstrably stronger and larger with increasing BR. Crucially, these riblet-modified flow characteristics directly dictated the observed cavitation patterns. Even at low BR, intermittent cavitation initiated within vortex cores above the ribs. As BR increased, the enhanced strength and size of these coherent structures translated into significantly larger and more intense cavitation packets. The complete vapor-filling of the recirculation zone and corner vorticity, alongside the shedding of large, cylindrical vapor packets from the separation bubble whose size and intensity directly scaled with BR, provided irrefutable evidence of this direct linkage. The channel ultimately transitioned into a supercavitation regime in Region II for all BRs, with varying void fraction distributions dependent on the specific riblet geometry.

Microscale Peculiarities (Experimental Insights): The experimental component of the thesis provided unprecedented insights into shear cavitation unique to microscale environments. This first-ever experimental analysis in a microscale BFS configuration systematically explored four distinct cavitation regimes. It highlighted critical differences from macroscale phenomena, emphasizing the dominant role of surface forces on nuclei distribution and vapor formation at the microscale. Distinct timescales were identified for phenomena like shedding and shockwave propagation. The study revealed that vortex strength in the shear layer plays a critical role in cavity shedding during upstream shockwave propagation. Increased pressure was shown to notably elevate the mean thickness, length, and intensity of cavitation within the shear layer. The identification of two distinct vortex modes (shedding and wake) at the reattachment zone, analogous to macroscale findings but with unique microscale characteristics, elucidated their impact on cavitation shedding frequency and downstream penetration. The stronger, lower-frequency wake mode was found to transport cavities deeper into the channel. Furthermore, nuclei predominantly accumulated in the second half of the shear layer during cavitation inception, coinciding with the region of maximum void fraction and subsequent bubble collapse, which generates new nuclei entrained into the recirculation zone.

Overall Contribution: In conclusion, this Ph.D. thesis stands as a significant contribution to the fields of turbulent flows and cavitation, particularly within microscale systems. By seamlessly integrating sophisticated numerical modeling, capable of handling compressible flow physics across relevant Mach number regimes and complex thermodynamic interactions, with pioneering experimental observations, it has elucidated the profound and multi-faceted interplay between fluid mechanics, phase change, and geometric design. The findings demonstrate that engineering surface features like riblets are not passive elements but actively reshape turbulence (affecting TKE transport, Reynolds stresses, and coherent structures), which, in turn, directly governs the inception, evolution, and intensity of cavitation. This holistic understanding is paramount for the advanced design, optimization, and control of microfluidic devices, energy conversion systems, and other applications where both turbulent flow characteristics and cavitation are critical considerations, offering novel pathways for targeted flow control strategies.

The outputs of this thesis have led to the following research articles:

- **Maleki, M.**, Imanzadeh, M., Kosar, A., Ghorbani, M. Effect of Riblet-Mounted Surfaces and Blockage Ratio on Separating Flow. To be submitted.

- **Maleki, M.**, Priyadarshi, A. Tzanakis, I., Kosar, A., Ghorbani, M. New insights into the cavitation instabilities in micro-venturi channel revealed using in-situ high-speed imaging. To be submitted.

- **Maleki, M.,** Rokhsar Talabazar, F., Heyat Davoudian, S., Dular, M., Koşar, A., Petkovšek, M., Šmid, A., Zupanc, M., & Ghorbani, M. The formation of hydroxyl radicals during hydrodynamic cavitation in microfluidic reactors using salicylic acid dosimetry. Chemical Engineering Journal, 511, (2025).

- **Maleki, M.**, Rokhsar Talabazar, F., Toyran, E., Priyadarshi, A., Aghdam, A.S., Villanueva, L.G., Grishenkov, D., Tzanakis, I., Kosar, A., Ghorbani, M. New Insights on Cavitating Flows Over a Microscale Backward-Facing Step, Physics of Fluids 36, no. 9 (2024).

- **Maleki, M.**, Rokhsar Talabazar, F., Koşar, A., & Ghorbani, M. On the spatio-temporal dynamics of cavitating turbulent shear flow over a microscale backward-facing step: a numerical study, International Journal of Multiphase Flow 177 (2024).

- **Maleki, M.**, Rokhsar Talabazar, F., Seyedmirzaei Sarraf, S., Sheibani Aghdam, A., Bayraktar, S., Tuzcuoğlu, E., Koşar, A. and Ghorbani, M, Detergent dissolution intensification via energy-efficient hydrodynamic cavitation reactors. ACS Omega 8, no. 32 (2023): 29595-29607.

- Rokhsar Talabazar, F, **Maleki M**, Aghdam AS, Grishenkov D, Ghorbani M, Kosar A. Cavitation inception and evolution in cavitation on a chip devices at low upstream pressures. Physics of fluids. 2023;35(1).

- Seyedmirzaei Sarraf S, Rokhsar Talabazar F, Namlı İ, **Maleki M**, Sheibani Aghdam A, Gharib G, Grishenkov D, Ghorbani M, Koşar A. Fundamentals, biomedical applications and future potential of micro-scale cavitation-a review. Lab on a Chip. 2022 Jun 14;22(12):2237-58.

7.2 Recommendations for Future Research

Building upon the foundational understanding established in this thesis, several promising avenues for future research emerge. A crucial next step involves a comprehensive investigation into the broader influence of surface roughness on TSB and cavitation dynamics in separating flows, utilizing both experimental and advanced numerical studies. Methodologically, there is a clear need for developing novel numerical models that more accurately account for surface nucleation phenomena and rigorously integrate the subgrid-scale (SGS) effects of individual bubbles within multiphase flow simulations. This could be achieved either by combining the Eulerian framework with a Lagrangian framework accounting for individual SGS bubbles, or through developing an appropriate SGS model considering SGS surface tension effects. Furthermore, conducting controlled studies specifically targeting the cavitation inception mechanism in devices featuring various types of roughness would provide invaluable insights. Ultimately, extending the findings of this research to more complex geometries prevalent in industrial applications will be vital for translating fundamental knowledge into practical engineering solutions for cavitating flow systems.

BIBLIOGRAPHY

Abe, H., 2017. Reynolds-number dependence of wall-pressure fluctuations in a pressure-induced turbulent separation bubble. J Fluid Mech 833, 563–598. https://doi.org/DOI: 10.1017/jfm.2017.694

Abe, K., 2013. An improved anisotropy-resolving subgrid-scale model with the aid of a scale-similarity modeling concept. Int J Heat Fluid Flow 39, 42–52.

Abu-Al-Saud, M.O., Popinet, S., Tchelepi, H.A., 2018. A conservative and well-balanced surface tension model. J Comput Phys 371, 896–913. https://doi.org/https://doi.org/10.1016/j.jcp.2018.02.022

Adams, E.W., Johnston, J.P., 1988. Effects of the separating shear layer on the reattachment flow structure part 2: Reattachment length and wall shear stress. Exp Fluids 6, 493–499. https://doi.org/10.1007/BF00196511

Adrian, R.J., Liu, Z.C., 2002. Observation of vortex packets in direct numerical simulation of fully turbulent channel flow. J Vis (Tokyo) 5, 9–19. https://doi.org/10.1007/BF03182598

ADRIAN, R.J., MEINHART, C.D., TOMKINS, C.D., 2000. Vortex organization in the outer region of the turbulent boundary layer. J Fluid Mech 422, 1–54. https://doi.org/DOI: 10.1017/S0022112000001580

Aeschlimann, V., Barre, S., Djeridi, H., 2011a. Velocity field analysis in an experimental cavitating mixing layer. Physics of Fluids 23, 055105. https://doi.org/10.1063/1.3592327

Aeschlimann, V., Barre, S., Legoupil, S., 2011b. X-ray attenuation measurements in a cavitating mixing layer for instantaneous two-dimensional void ratio determination. Physics of Fluids 23, 055101. https://doi.org/10.1063/1.3586801

Agarwal, K., Ram, O., Katz, J., 2018. Cavitating Structures at Inception in Turbulent Shear Flow, in: Katz, J. (Ed.), Proceedings of the 10th International Symposium on Cavitation (CAV2018). ASME Press, p. 0. https://doi.org/10.1115/1.861851_ch33

Agarwal, K., Ram, O., Lu, Y., Katz, J., 2023. On the pressure field, nuclei dynamics and their relation to cavitation inception in a turbulent shear layer. J Fluid Mech 966, A31. https://doi.org/DOI: 10.1017/jfm.2023.368

Aitken, F., Foulc, J.-N., 2019. From Deep Sea to Laboratory 3: From Tait's Work on the Compressibility of Seawater to Equations-of-State for Liquids. WILEY, pp. 245–283.

Akhilesh, P., Jagadeesh, G., Srinath, L., Sriram, R., 2022. Shock-induced leading-edge separation in hypersonic flows. J Fluid Mech 947, A14. https://doi.org/DOI: 10.1017/jfm.2022.619

Allan, E.S.C., Barbaca, L., Venning, J.A., Russell, P.S., Pearce, B.W., Brandner, P.A., 2023. Nucleation and cavitation inception in high Reynolds number shear layers. Physics of Fluids 35, 013317. https://doi.org/10.1063/5.0132054

Anderson, B.W., Domaradzki, J.A., 2012. A subgrid-scale model for large-eddy simulation based on the physics of interscale energy transfer in turbulence. Physics of Fluids 24.

Arndt, R.E.A., 2002. CAVITATION IN VORTICAL FLOWS. Annu Rev Fluid Mech 34, 143–175. https://doi.org/10.1146/annurev.fluid.34.082301.114957

Arndt, R.E.A., George, W.K., 1979. Pressure Fields and Cavitation in Turbulent Shear Flows, in: National Academy of Sciences. National Academy of Sciences.

Arun, S., Girimaji, S.S., Sameen, A., Srinivasan, B., 2019. Topology-based characterization of compressibility effects in mixing layers. J Fluid Mech 874, 38–75. https://doi.org/DOI: 10.1017/jfm.2019.434

Barbaca, L., Brandner, P.A., Ceccio, S.L., Ganesh, H., Pearce, B.W., 2019. On the unsteady behaviour of cavity flow over a two-dimensional wall-mounted fence. J Fluid Mech 874, 483–525. https://doi.org/DOI: 10.1017/jfm.2019.455

Barbosa-Saldaña, J.G., Anand, N.K., 2007. Flow Over a Three-Dimensional Horizontal Forward-Facing Step. Numeri Heat Transf A Appl 53, 1–17. https://doi.org/10.1080/10407780701446473

BARDINA, J., FERZIGER, J., REYNOLDS, W., 1980. Improved subgrid-scale models for large-eddy simulation, in: 13th Fluid and PlasmaDynamics Conference, Fluid Dynamics and Co-Located Conferences. American Institute of Aeronautics and Astronautics. https://doi.org/doi:10.2514/6.1980-1357

Bechlars, P., Sandberg, R.D., 2017. Variation of enstrophy production and strain rotation relation in a turbulent boundary layer. J Fluid Mech 812, 321–348. https://doi.org/DOI: 10.1017/jfm.2016.794

Belahadji, B., Franc, J.P., Michel, J.M., 1995. Cavitation in the rotational structures of a turbulent wake. J Fluid Mech 287, 383–403. https://doi.org/DOI: 10.1017/S0022112095000991

Bensow, R.E., Bark, G., 2010. Implicit LES Predictions of the Cavitating Flow on a Propeller. J Fluids Eng 132. https://doi.org/10.1115/1.4001342

Berk, T., Medjnoun, T., Ganapathisubramani, B., 2017. Entrainment effects in periodic forcing of the flow over a backward-facing step. Phys Rev Fluids 2, 74605. https://doi.org/10.1103/PhysRevFluids.2.074605

Bhatt, A., Ganesh, H., Ceccio, S.L., 2021a. Cavitating flow behind a backward facing step. International Journal of Multiphase Flow 139, 103584. https://doi.org/https://doi.org/10.1016/j.ijmultiphaseflow.2021.103584

Bhatt, A., Ganesh, H., Ceccio, S.L., 2021b. Cavitating flow behind a backward facing step. International Journal of Multiphase Flow 139, 103584. https://doi.org/https://doi.org/10.1016/j.ijmultiphaseflow.2021.103584

Bhatt, M., Mahesh, K., 2021. A numerical approach to address the acoustic stiffness in cavitating flows. International Journal of Multiphase Flow 103568.

Bhatt, M., Mahesh, K., 2020. Numerical investigation of partial cavitation regimes over a wedge using large eddy simulation. International Journal of Multiphase Flow 122, 103155. https://doi.org/https://doi.org/10.1016/j.ijmultiphaseflow.2019.103155

Bhide, K., Abdallah, S., 2022. Anisotropic Turbulent Kinetic Energy Budgets in Compressible Rectangular Jets. Aerospace 9. https://doi.org/10.3390/aerospace9090484

Bilu, I., Bombek, G., irok, B., Hoevar, M., Cencîc, T., Petkovek, M., 2014. The experimental analysis of cavitating structure fluctuations and pressure pulsations in the cavitation station. Strojniski Vestnik-journal of Mechanical Engineering 60, 147–157.

Bottaro, A., Cherubini, S., De Palma, P., Robinet, J.-C., 2011. The minimal seed of turbulent transition in the boundary layer. J Fluid Mech 689, 221–253. https://doi.org/DOI: 10.1017/jfm.2011.412

Bouriga, M., Taher, R., Morency, F., Weiss, J., 2015. Numerical investigation of secondary flows in a constant-width wind-tunnel contraction. The Aeronautical Journal 119, 613–630. https://doi.org/DOI: 10.1017/S000192400001071X

Bradshaw, P., 1987. Turbulent Secondary Flows. Annu Rev Fluid Mech 19, 53–74. https://doi.org/10.1146/annurev.fl.19.010187.000413

Brandao, F.L., Mahesh, K., 2022. Large-eddy simulation of cavitation inception in a shear flow. International Journal of Multiphase Flow 146, 103865. https://doi.org/https://doi.org/10.1016/j.ijmultiphaseflow.2021.103865

Brennen, C.E., 2013. Cavitation and Bubble Dynamics. Cambridge University Press, Cambridge. https://doi.org/DOI: 10.1017/CBO9781107338760

Brès, G.A., Colonius, T., Rigas, G., Schmidt, O.T., Towne, A., 2018. Spectral analysis of jet turbulence. J Fluid Mech 855, 953–982. https://doi.org/DOI: 10.1017/jfm.2018.675

Browand, F.K., Troutt, T.R., 1985. The turbulent mixing layer: geometry of large vortices. J Fluid Mech 158, 489–509. https://doi.org/DOI: 10.1017/S0022112085002737

CECCIO, S.L., LABERTEAUX, K.R., 2001. Partial cavity flows. Part 1. Cavities forming on models without spanwise variation. J Fluid Mech 431, 1–41. https://doi.org/DOI: 10.1017/S0022112000002925

Chen, L.-C., Zhu, Y., Papandreou, G., Schroff, F., Adam, H., 2018. Encoder-Decoder with Atrous Separable Convolution for Semantic Image Segmentation, in: Ferrari, V., Hebert, M., Sminchisescu, C., Weiss, Y. (Eds.), Computer Vision – ECCV 2018. Springer International Publishing, Cham, pp. 833–851.

Cherry, N.J., Hillier, R., Latour, M.E.M.P., 1984. Unsteady measurements in a separated and reattaching flow. J Fluid Mech 144, 13–46. https://doi.org/DOI: 10.1017/S002211208400149X

Choi, H., Moin, P., Kim, J., 1993. Direct numerical simulation of turbulent flow over riblets. J Fluid Mech 255, 503–539. https://doi.org/DOI: 10.1017/S0022112093002575

Chong, M.S., Perry, A.E., Cantwell, B.J., 1990. A general classification of three-dimensional flow fields. Physics of Fluids A: Fluid Dynamics 2, 765–777. https://doi.org/10.1063/1.857730

CHOU, J.H., HU, C.C., MIAU, J.J., WU, S.J., 2005. On low-frequency modulations and three-dimensionality in vortex shedding behind a normal plate. J Fluid Mech 526, 117–146. https://doi.org/DOI: 10.1017/S0022112004002721

Clark, R.A., Ferziger, J.H., Reynolds, W.C., 1979. Evaluation of subgrid-scale models using an accurately simulated turbulent flow. J Fluid Mech 91, 1 – 16. https://doi.org/10.1017/S002211207900001X

Cooper, G.J., Verner, J.H., 1972. Some Explicit Runge”Kutta Methods of High Order. SIAM J Numer Anal 9, 389–405. https://doi.org/10.1137/0709037

Demirdžić, I., Lilek, Ž., Perić, M., 1993. A collocated finite volume method for predicting flows at all speeds. Int J Numer Methods Fluids 16, 1029–1050. https://doi.org/https://doi.org/10.1002/fld.1650161202

Deng, X., 2023a. A unified framework for non-linear reconstruction schemes in a compact stencil. Part 1: Beyond second order. J Comput Phys 481, 112052. https://doi.org/https://doi.org/10.1016/j.jcp.2023.112052

Deng, X., 2023b. A new open-source library based on novel high-resolution structure-preserving convection schemes. J Comput Sci 74, 102150. https://doi.org/https://doi.org/10.1016/j.jocs.2023.102150

Dimotakis, P.E., 1986. Two-dimensional shear-layer entrainment. AIAA Journal 24, 1791–1796. https://doi.org/10.2514/3.9525

DIWAN, S.S., RAMESH, O.N., 2009. On the origin of the inflectional instability of a laminar separation bubble. J Fluid Mech 629, 263–298. https://doi.org/DOI: 10.1017/S002211200900634X

Djilali, N., Gartshore, I.S., Salcudean, M., 1991. Turbulent Flow Around a Bluff Rectangular Plate. Part II: Numerical Predictions. J Fluids Eng 113, 60–67. https://doi.org/10.1115/1.2926498

Dow, K., Fang, X., Tachie, M.F., 2022. Turbulent separations beneath semi-submerged bluff bodies with smooth and rough undersurfaces. J Fluid Mech 947, A19. https://doi.org/DOI: 10.1017/jfm.2022.661

Dubief †, Y., Delcayre ‡, F., 2000. On coherent-vortex identification in turbulence. Journal of Turbulence 1, N11. https://doi.org/10.1088/1468-5248/1/1/011

Durst, F., Tropea, C., 1983. Flows over Two-Dimensional Backward — Facing Steps, in: Dumas, R., Fulachier, L. (Eds.), Structure of Complex Turbulent Shear Flow. Springer Berlin Heidelberg, Berlin, Heidelberg, pp. 41–52.

Eaton, J.K., Johnston, J.P., 1981. A Review of Research on Subsonic Turbulent Flow Reattachment. AIAA Journal 19, 1093–1100. https://doi.org/10.2514/3.60048

Egerer, C.P., Schmidt, S.J., Hickel, S., Adams, N.A., 2016. Efficient implicit LES method for the simulation of turbulent cavitating flows. J Comput Phys 316, 453–469. https://doi.org/https://doi.org/10.1016/j.jcp.2016.04.021

Eppink, J.L., 2020. Mechanisms of stationary cross-flow instability growth and breakdown induced by forward-facing steps. J Fluid Mech 897, A15. https://doi.org/DOI: 10.1017/jfm.2020.367

Fang, X., Tachie, M.F., 2019. On the unsteady characteristics of turbulent separations over a forward–backward-facing step. J Fluid Mech 863, 994–1030. https://doi.org/DOI: 10.1017/jfm.2018.962

Fang, X., Tachie, M.F., Bergstrom, D.J., Yang, Z., Wang, B.-C., 2021. Three-dimensional structural characteristics of flow separation induced by a forward-facing step in a turbulent channel flow. J Fluid Mech 919, A24. https://doi.org/DOI: 10.1017/jfm.2021.395

Fang, X., Yang, Z., Wang, B.-C., Tachie, M.F., Bergstrom, D.J., 2017. Large-eddy simulation of turbulent flow and structures in a square duct roughened with perpendicular and V-shaped ribs. Physics of Fluids 29, 065110. https://doi.org/10.1063/1.4985715

Fleischmann, N., Adami, S., Adams, N.A., 2020. A shock-stable modification of the HLLC Riemann solver with reduced numerical dissipation. J Comput Phys 423, 109762. https://doi.org/https://doi.org/10.1016/j.jcp.2020.109762

Floryan, J.M., 1991. On the görtler instability of boundary layers. Progress in Aerospace Sciences 28, 235–271. https://doi.org/https://doi.org/10.1016/0376-0421(91)90006-P

Ganapathisubramani, B., Goulart, P.J., Pearson, D.S., 2013. Turbulent separation upstream of a forward-facing step. J Fluid Mech 724, 284–304. https://doi.org/DOI: 10.1017/jfm.2013.113

Ganesh, H., Mäkiharju, S.A., Ceccio, S.L., 2016. Bubbly shock propagation as a mechanism for sheet-to-cloud transition of partial cavities. J Fluid Mech 802, 37–78. https://doi.org/DOI: 10.1017/jfm.2016.425

Garnier, E., Adams, N., Sagaut, P., n.d. Large Eddy Simulation for Compressible Flows, 1st ed. Springer, Dordrecht. https://doi.org/https://doi.org/10.1007/978-90-481-2819-8

Giussani, F., Piscaglia, F., Saez-Mischlich, G., Hèlie, J., 2020a. A three-phase VOF solver for the simulation of in-nozzle cavitation effects on liquid atomization. J Comput Phys 406, 109068. https://doi.org/https://doi.org/10.1016/j.jcp.2019.109068

Giussani, F., Piscaglia, F., Saez-Mischlich, G., Hèlie, J., 2020b. A three-phase VOF solver for the simulation of in-nozzle cavitation effects on liquid atomization. J Comput Phys 406, 109068. https://doi.org/https://doi.org/10.1016/j.jcp.2019.109068

Harten, A., Lax, P.D., Leer, B. van, 1983. On upstream differencing and Godunov-type schemes for hyperbolic conservation laws. SIAM review 25, 35–61.

Hasan, M.A.Z., 1992. The flow over a backward-facing step under controlled perturbation: laminar separation. J Fluid Mech 238, 73–96. https://doi.org/DOI: 10.1017/S0022112092001642

Hayakawa, M., Hussain, F., 1989. Three-dimensionality of organized structures in a plane turbulent wake. J Fluid Mech 206, 375–404. https://doi.org/DOI: 10.1017/S0022112089002338

He, X.(何潇), Fang, Z.(方舟), Rigas, G., Vahdati, M., 2021. Spectral proper orthogonal decomposition of compressor tip leakage flow. Physics of Fluids 33, 105105. https://doi.org/10.1063/5.0065929

Hertz, D., Azaria, M., 1985. Time delay estimation between two phase shifted signals via generalized cross-correlation methods. Signal Processing 8, 235–257. https://doi.org/https://doi.org/10.1016/0165-1684(85)90076-3

HG Weller, 2008. A new approach to VOF-based interface capturing methods for incompressible and compressible flow. https://doi.org/OpenCFD Ltd., Report TR/HGW

Hickel, S., Hu, W., van Oudheusden, B.W., 2021. Low-frequency unsteadiness mechanisms in shock wave/turbulent boundary layer interactions over a backward-facing step. J Fluid Mech 915, A107. https://doi.org/DOI: 10.1017/jfm.2021.95

Hirt, C.W., Nichols, B.D., 1981. Volume of fluid (VOF) method for the dynamics of free boundaries. J Comput Phys 39, 201–225. https://doi.org/https://doi.org/10.1016/0021-9991(81)90145-5

https://www.hzdr.de/db/Cms?pNid=0 [WWW Document], 2024.

Hu, W., Hickel, S., van Oudheusden, B., 2019. Dynamics of a supersonic transitional flow over a backward-facing step. Phys Rev Fluids 4, 103904. https://doi.org/10.1103/PhysRevFluids.4.103904

Hu, X., Hayat, I., Park, G.I., 2023. Wall-modelled large-eddy simulation of three-dimensional turbulent boundary layer in a bent square duct. J Fluid Mech 960, A29. https://doi.org/DOI: 10.1017/jfm.2023.143

Hudy, L.M., Naguib, A., Humphreys, W.M., 2007. Stochastic estimation of a separated-flow field using wall-pressure-array measurements. Physics of Fluids 19, 024103. https://doi.org/10.1063/1.2472507

Inagaki, M., 2011. A new wall-damping function for large eddy simulation employing Kolmogorov velocity scale. Int J Heat Fluid Flow 32, 26–40. https://doi.org/https://doi.org/10.1016/j.ijheatfluidflow.2010.07.001

Ismail, U., Zaki, T.A., Durbin, P.A., 2018. Simulations of rib-roughened rough-to-smooth turbulent channel flows. J Fluid Mech 843, 419–449. https://doi.org/DOI: 10.1017/jfm.2018.119

Israel, M.K., Karen, D., Shawn P., C., and Tachie, M.F., 2024. PIV investigation of the effects of simulated ice blocks on the turbulent flow dynamics around a partially submerged horizontal circular cylinder. Journal of Hydraulic Research 62, 395–411. https://doi.org/10.1080/00221686.2024.2399836

Issa, R.I., 1986. Solution of the implicitly discretised fluid flow equations by operator-splitting. J Comput Phys 62, 40–65. https://doi.org/https://doi.org/10.1016/0021-9991(86)90099-9

Iyer, C.O., Ceccio, S.L., 2002. The influence of developed cavitation on the flow of a turbulent shear layer. Physics of Fluids 14, 3414–3431. https://doi.org/10.1063/1.1501541

Jasak, H., 1996. Error analysis and estimation for the finite volume method with applications to fluid flows.

Ji, M., Wang, M., 2012. Surface pressure fluctuations on steps immersed in turbulent boundary layers. J Fluid Mech 712, 471–504. https://doi.org/DOI: 10.1017/jfm.2012.433

Jimenez, J., 1983. A spanwise structure in the plane shear layer. J Fluid Mech 132, 319–336. https://doi.org/DOI: 10.1017/S0022112083001639

Katz, J., Liu, X., 2013. Vortex-corner interactions in a cavity shear layer elucidated by time-resolved measurements of the pressure field. J Fluid Mech 728, 417–457. https://doi.org/DOI: 10.1017/jfm.2013.275

Katz, J., O'Hern, T.J., 1986. Cavitation in Large Scale Shear Flows. J Fluids Eng 108, 373–376. https://doi.org/10.1115/1.3242589

Kiya, M., Sasaki, K., 1983. Structure of a turbulent separation bubble. J Fluid Mech 137, 83–113. https://doi.org/DOI: 10.1017/S002211208300230X

Klein, M., Ketterl, S., Engelmann, L., Kempf, A., Kobayashi, H., 2020. Regularized, parameter free scale similarity type models for Large Eddy Simulation. Int J Heat Fluid Flow 81, 108496. https://doi.org/https://doi.org/10.1016/j.ijheatfluidflow.2019.108496

Klein, M., Sadiki, A., Janicka, J., 2003. A digital filter based generation of inflow data for spatially developing direct numerical or large eddy simulations. J Comput Phys 186, 652–665. https://doi.org/https://doi.org/10.1016/S0021-9991(03)00090-1

Kline, S.J., 1953. Describing Uncertainties in Single-Sample Experiments. Mechanical Engineering 75, 3–8.

Kobayashi, H., 2018. Improvement of the SGS model by using a scale-similarity model based on the analysis of SGS force and SGS energy transfer. Int J Heat Fluid Flow 72, 329–336. https://doi.org/https://doi.org/10.1016/j.ijheatfluidflow.2018.06.012

Koch, M., Lechner, C., Reuter, F., Köhler, K., Mettin, R., Lauterborn, W., 2016. Numerical modeling of laser generated cavitation bubbles with the finite volume and volume of fluid method, using OpenFOAM. Comput Fluids 126, 71–90. https://doi.org/https://doi.org/10.1016/j.compfluid.2015.11.008

Koop, A.H., 2008. Numerical simulation of unsteady three-dimensional sheet cavitation. University of Twente.

Kourta, A., Thacker, A., Joussot, R., 2015. Analysis and characterization of ramp flow separation. Exp Fluids 56, 1–14.

KROGSTAD, P.-Å., ANDERSSON, H.I., BAKKEN, O.M., ASHRAFIAN, A., 2005. An experimental and numerical study of channel flow with rough walls. J Fluid Mech 530, 327–352. https://doi.org/DOI: 10.1017/S0022112005003824

Krogstadt, P.-Å., Antonia, R.A., 1999. Surface roughness effects in turbulent boundary layers. Exp Fluids 27, 450–460. https://doi.org/10.1007/s003480050370

Kuehn, D.M., 1980. Effects of Adverse Pressure Gradient on the Incompressible Reattaching Flow over a Rearward-Facing Step. AIAA Journal 18, 343–344. https://doi.org/10.2514/3.50765

Le Floc'h, A., Weiss, J., Mohammed-Taifour, A., Dufresne, L., 2020a. Measurements of pressure and velocity fluctuations in a family of turbulent separation bubbles. J Fluid Mech 902, A13. https://doi.org/DOI: 10.1017/jfm.2020.530

Le Floc'h, A., Weiss, J., Mohammed-Taifour, A., Dufresne, L., 2020b. Measurements of pressure and velocity fluctuations in a family of turbulent separation bubbles. J Fluid Mech 902, A13. https://doi.org/DOI: 10.1017/jfm.2020.530

LE, H., MOIN, P., KIM, J., 1997. Direct numerical simulation of turbulent flow over a backward-facing step. J Fluid Mech 330, 349–374. https://doi.org/DOI: 10.1017/S0022112096003941

Le, Q., Franc, J.P., Michel, J.M., 1993. Partial Cavities: Global Behavior and Mean Pressure Distribution. J Fluids Eng 115, 243–248. https://doi.org/10.1115/1.2910131

Lelouvetel, J., Bigillon, F., Doppler, D., Vinkovic, I., Champagne, J.-Y., 2009. Experimental investigation of ejections and sweeps involved in particle suspension. Water Resour Res 45. https://doi.org/https://doi.org/10.1029/2007WR006520

Leroux, J.-B., Coutier-Delgosha, O., Astolfi, J.A., 2005. A joint experimental and numerical study of mechanisms associated to instability of partial cavitation on two-dimensional hydrofoil. Physics of Fluids 17, 052101. https://doi.org/10.1063/1.1865692

Li, J.-H., Wang, B.-F., Qiu, X., Zhou, Q., Fu, S.-X., Liu, Y.-L., 2024. Vortex dynamics and boundary layer transition in flow around a rectangular cylinder with different aspect ratios at medium Reynolds number. J Fluid Mech 982, A5. https://doi.org/DOI: 10.1017/jfm.2024.87

Li, J.(李佳佳), Carrica, P.M., 2023. Numerical study of the cavitating flow over backward facing step with a polydisperse two-phase flow model. Physics of Fluids 35, 063313. https://doi.org/10.1063/5.0147595

Liou, M.-S., 1996. A Sequel to AUSM: AUSM+. J Comput Phys 129, 364–382. https://doi.org/https://doi.org/10.1006/jcph.1996.0256

Liou, M.-S., Steffen, C.J., 1993. A New Flux Splitting Scheme. J Comput Phys 107, 23–39. https://doi.org/https://doi.org/10.1006/jcph.1993.1122

Loshchilov, I., Hutter, F., 2019. Decoupled Weight Decay Regularization, in: ICLR.

Ma, R., Mahesh, K., 2023. Boundary layer transition due to distributed roughness: effect of roughness spacing. J Fluid Mech 977, A27. https://doi.org/DOI: 10.1017/jfm.2023.937

Mahmoodi-Jezeh, S. V, Wang, B.-C., 2020. Direct numerical simulation of turbulent flow through a ribbed square duct. J Fluid Mech 900, A18. https://doi.org/DOI: 10.1017/jfm.2020.452

Maleki, M., Rokhsar Talabazar, F., Koşar, A., Ghorbani, M., 2024. On the spatio-temporal dynamics of cavitating turbulent shear flow over a microscale backward-facing step: A numerical study. International Journal of Multiphase Flow 177, 104875. https://doi.org/https://doi.org/10.1016/j.ijmultiphaseflow.2024.104875

Markatos, N.C., 1986. Modelling of two-phase transient flow and combustion of granular propellants. International Journal of Multiphase Flow 12, 913–933. https://doi.org/https://doi.org/10.1016/0301-9322(86)90035-2

Maurice, G., Djeridi, H., Barre, S., 2014. Experimental investigation of a cavitating backward-facing step flow. IOP Conf Ser Earth Environ Sci 22, 052008. https://doi.org/10.1088/1755-1315/22/5/052008

Maurice, G., Machicoane, N., Barre, S., Djeridi, H., 2021. Coupled x-ray high-speed imaging and pressure measurements in a cavitating backward facing step flow. Phys Rev Fluids 6, 44311. https://doi.org/10.1103/PhysRevFluids.6.044311

Mestayer, P., 1982. Local isotropy and anisotropy in a high-Reynolds-number turbulent boundary layer. J Fluid Mech 125, 475–503. https://doi.org/DOI: 10.1017/S0022112082003450

Mihatsch, M., 2017. Numerical Prediction of Erosion and Degassing Effects in Cavitating Flows.

Minoshima, T., Miyoshi, T., 2021. A low-dissipation HLLD approximate Riemann solver for a very wide range of Mach numbers. J Comput Phys 446, 110639. https://doi.org/https://doi.org/10.1016/j.jcp.2021.110639

Mohammed-Taifour, A., Weiss, J., 2016. Unsteadiness in a large turbulent separation bubble. J Fluid Mech 799, 383–412. https://doi.org/DOI: 10.1017/jfm.2016.377

MOIN, P., NA, Y., 1998. The structure of wall-pressure fluctuations in turbulent boundary layers with adverse pressure gradient and separation. J Fluid Mech 377, 347–373. https://doi.org/DOI: 10.1017/S0022112098003218

Moser, R.D., Zandonade, P., 2004. Development of High Reynolds Number Optimal Les Models, in: Smits, A.J. (Ed.), IUTAM Symposium on Reynolds Number Scaling in Turbulent Flow. Springer Netherlands, Dordrecht, pp. 169–174.

NA, Y., MOIN, P., 1998. Direct numerical simulation of a separated turbulent boundary layer. J Fluid Mech 374, 379–405. https://doi.org/DOI: 10.1017/S002211209800189X

Nadge, P.M., Govardhan, R.N., 2014. High Reynolds number flow over a backward-facing step: structure of the mean separation bubble. Exp Fluids 55, 1657. https://doi.org/10.1007/s00348-013-1657-5

Nagano, Y., Hattori, H., Houra, T., 2004. DNS of velocity and thermal fields in turbulent channel flow with transverse-rib roughness. Int J Heat Fluid Flow 25, 393–403. https://doi.org/https://doi.org/10.1016/j.ijheatfluidflow.2004.02.011

Nicoud, F., Ducros, F., 1999. Subgrid-Scale Stress Modelling Based on the Square of the Velocity Gradient Tensor. Flow Turbul Combust 62, 183–200. https://doi.org/10.1023/A:1009995426001

OHTA, T., SAKAI, H., OKABAYASHI, K., KAJISHIMA, T., 2011. Investigation of Interaction between Vortices and Cavitation in a Turbulent Shear Layer. Journal of Fluid Science and Technology 6, 1021–1035. https://doi.org/10.1299/jfst.6.1021

O'NEIL, J., MENEVEAU, C., 1997. Subgrid-scale stresses and their modelling in a turbulent plane wake. J Fluid Mech 349, 253–293. https://doi.org/DOI: 10.1017/S0022112097006885

OpenFoam. The Open Source CFD Toolbox openfoam foundation [WWW Document], 2023. URL https://www.openfoam.com/ (accessed 3.9.23).

Patankar, S. V, Spalding, D.B., 1972. A calculation procedure for heat, mass and momentum transfer in three-dimensional parabolic flows. Int J Heat Mass Transf 15, 1787–1806. https://doi.org/https://doi.org/10.1016/0017-9310(72)90054-3

Pierrehumbert, R.T., Widnall, S.E., 1982. The two- and three-dimensional instabilities of a spatially periodic shear layer. J Fluid Mech 114, 59–82. https://doi.org/DOI: 10.1017/S0022112082000044

Pires Araujo, P., Tenório Rezende, A.L., 2017. Comparison of Turbulence Models in the Flow over a Backward Facing Step. International Journal of Engineering Research and Science 3, 88–93. https://doi.org/10.25125/engineering-journal-ijoer-nov-2017-19

Pirozzoli, S., Modesti, D., Orlandi, P., Grasso, F., 2018. Turbulence and secondary motions in square duct flow. J Fluid Mech 840, 631–655. https://doi.org/DOI: 10.1017/jfm.2018.66

Plasseraud, M., Kumar, P., Mahesh, K., 2023. Large-eddy simulation of tripping effects on the flow over a 6 : 1 prolate spheroid at angle of attack. J Fluid Mech 960, A3. https://doi.org/DOI: 10.1017/jfm.2023.175

Poinsot, T.J., Lelef, S.K., 1992. Boundary conditions for direct simulations of compressible viscous flows. J Comput Phys 101, 104–129. https://doi.org/https://doi.org/10.1016/0021-9991(92)90046-2

Pont-Vílchez, A., Trias, F.X., Gorobets, A., Oliva, A., 2019. Direct numerical simulation of backward-facing step flow at $Re_{\unicode[STIX]{x1D70F}}=395$ and expansion ratio 2. J Fluid Mech 863, 341–363. https://doi.org/DOI: 10.1017/jfm.2018.1000

Pope, S.B., 2000. Turbulent Flows. Cambridge University Press, Cambridge. https://doi.org/DOI: 10.1017/CBO9780511840531

Ra, S.H., Chang, P.K., 1990. Effects of pressure gradient on reattaching flow downstream of a rearward-facing step. J Aircr 27, 93–95. https://doi.org/10.2514/3.45901

Rokhsar Talabazar, F., Jafarpour, M., Zuvin, M., Chen, H., Gevari, M.T., Villanueva, L.G., Grishenkov, D., Koşar, A., Ghorbani, M., 2021. Design and fabrication of a vigorous "cavitation-on-a-chip" device with a multiple microchannel configuration. Microsyst Nanoeng 7, 44. https://doi.org/10.1038/s41378-021-00270-1

Santese, T., Martinez-Sanchis, D., Sternin, A., Manfletti, C., 2024a. Investigation of Sidewall and Reynolds Number Effects in a Ribbed Square Duct. Flow Turbul Combust 113, 391–417. https://doi.org/10.1007/s10494-024-00554-2

Santese, T., Martinez-Sanchis, D., Sternin, A., Manfletti, C., 2024b. Investigation of Sidewall and Reynolds Number Effects in a Ribbed Square Duct. Flow Turbul Combust 113, 391–417. https://doi.org/10.1007/s10494-024-00554-2

Saul, A., Wagner, W., 1987. International Equations for the Saturation Properties of Ordinary Water Substance. J Phys Chem Ref Data 16, 893–901. https://doi.org/10.1063/1.555787

SCHÄFER, F., BREUER, M., DURST, F., 2009a. The dynamics of the transitional flow over a backward-facing step. J Fluid Mech 623, 85–119. https://doi.org/DOI: 10.1017/S0022112008005235

SCHÄFER, F., BREUER, M., DURST, F., 2009b. The dynamics of the transitional flow over a backward-facing step. J Fluid Mech 623, 85–119. https://doi.org/DOI: 10.1017/S0022112008005235

Schmid, P.J., 2010. Dynamic mode decomposition of numerical and experimental data. J Fluid Mech 656, 5–28.

Schmidt, E., Grigull, U., 1989. Properties of water and steam in SI-units. 0-800/sup 0/C, 0-1000 bar.

Schmidt, O.T., Colonius, T., 2020. Guide to Spectral Proper Orthogonal Decomposition. AIAA Journal 58, 1023–1033. https://doi.org/10.2514/1.J058809

Schmidt, S.J., 2015. A low Mach number consistent compressible approach for simulation of cavitating flow.

Schnerr, G.H., Sezal, I.H., Schmidt, S.J., 2008. Numerical investigation of three-dimensional cloud cavitation with special emphasis on collapse induced shock dynamics. Physics of Fluids 20, 40703. https://doi.org/10.1063/1.2911039

Sezal, I.H., 2009. Compressible Dynamics of Cavitating 3-D Multi-Phase Flows.

Shahab, M.F., Lehnasch, G., Gatski, T.B., Comte, P., 2011. Statistical Characteristics of an Isothermal, Supersonic Developing Boundary Layer Flow from DNS Data. Flow Turbul Combust 86, 369–397. https://doi.org/10.1007/s10494-011-9329-0

Shehadi, E., 2018. Large Eddy Simulation of Turbulent Flow over a Backward-Facing Step. IT NV - 18009. Department of Information Technology, Mathematics and Computer Science, Disciplinary Domain of Science and Technology, Uppsala University.

Shi, L., Yu, Z., Jaworski, A.J., 2010. Vortex shedding flow patterns and their transitions in oscillatory flows past parallel-plate thermoacoustic stacks. Exp Therm Fluid Sci 34, 954–965. https://doi.org/https://doi.org/10.1016/j.expthermflusci.2010.02.012

Shie Mannor, Dori Peleg, Reuven Rubinstein, 2005. The cross entropy method for classification, in: ICML '05: Proceedings of the 22nd International Conference on Machine Learning. pp. 561–568.

Simpson, R.L., 1989. Turbulent Boundary-Layer Separation. Annu Rev Fluid Mech 21, 205–232. https://doi.org/10.1146/annurev.fl.21.010189.001225

Smeltzer, B.K., Rømcke, O., Hearst, R.J., Ellingsen, S.Å., 2023. Experimental study of the mutual interactions between waves and tailored turbulence. J Fluid Mech 962, R1. https://doi.org/DOI: 10.1017/jfm.2023.280

Song, S., Eaton, J.K., 2004. Flow structures of a separating, reattaching, and recovering boundary layer for a large range of Reynolds number. Exp Fluids 36, 642–653. https://doi.org/10.1007/s00348-003-0762-2

Stella, F., 2017. Characterisation of a turbulent separation over a ramp : entrainment and scaling laws. Université d'Orléans.

Stella, F., Mazellier, N., Kourta, A., 2017. Scaling of separated shear layers: an investigation of mass entrainment. J Fluid Mech 826, 851–887. https://doi.org/DOI: 10.1017/jfm.2017.455

Stiperski, I., Katul, G.G., Calaf, M., 2021. Universal Return to Isotropy of Inhomogeneous Atmospheric Boundary Layer Turbulence. Phys Rev Lett 126, 194501. https://doi.org/10.1103/PhysRevLett.126.194501

Structural Modeling, 2006. , in: Large Eddy Simulation for Incompressible Flows: An Introduction. Springer Berlin Heidelberg, Berlin, Heidelberg, pp. 209–279. https://doi.org/10.1007/3-540-26403-5_7

TAO, B.O., KATZ, J., MENEVEAU, C., 2002. Statistical geometry of subgrid-scale stresses determined from holographic particle image velocimetry measurements. J Fluid Mech 457, 35–78. https://doi.org/DOI: 10.1017/S0022112001007443

Teng, M., Piomelli, U., 2022. Instability and Transition of a Boundary Layer over a Backward-Facing Step. Fluids 7. https://doi.org/10.3390/fluids7010035

Toro, E.F., 2009. The Method of Godunov for Non—linear Systems, in: Toro, E.F. (Ed.), Riemann Solvers and Numerical Methods for Fluid Dynamics: A Practical Introduction. Springer Berlin Heidelberg, Berlin, Heidelberg, pp. 213–235. https://doi.org/10.1007/b79761_6

Toro, E.F., 1992. The weighted average flux method applied to the Euler equations. Philosophical Transactions of the Royal Society of London. Series A: Physical and Engineering Sciences 341, 499–530.

Towne, A., Schmidt, O.T., Colonius, T., 2018. Spectral proper orthogonal decomposition and its relationship to dynamic mode decomposition and resolvent analysis. J Fluid Mech 847, 821–867. https://doi.org/DOI: 10.1017/jfm.2018.283

Trummler, T., 2021. Numerical investigations of cavitation phenomena. Technische Universität München.

VOLINO, R.J., SCHULTZ, M.P., FLACK, K.A., 2009. Turbulence structure in a boundary layer with two-dimensional roughness. J Fluid Mech 635, 75–101. https://doi.org/DOI: 10.1017/S0022112009007617

Vreman, B., Geurts, B., Kuerten, H., 1995. A priori tests of large eddy simulation of the compressible plane mixing layer. J Eng Math 29, 299–327. https://doi.org/10.1007/BF00042759

Wang, C., Zhang, M., 2023. Dynamics of cavity structures and wall-pressure fluctuations associated with shedding mechanism in unsteady sheet/cloud cavitating flows. Flow 3, E9. https://doi.org/DOI: 10.1017/flo.2023.2

Wang, J., Huang, G., Lu, W., Sullivan, P.E., 2020. Dynamic mode decomposition analysis of flow separation in a diffuser to inform flow control strategies. J Fluids Eng 142, 021502.

Wang, L., Hejcik, J., Sunden, B., 2007. PIV Measurement of Separated Flow in a Square Channel With Streamwise Periodic Ribs on One Wall. J Fluids Eng 129, 834–841. https://doi.org/10.1115/1.2742723

Wang, L., Lu, X.-Y., 2012. Flow topology in compressible turbulent boundary layer. J Fluid Mech 703, 255–278. https://doi.org/DOI: 10.1017/jfm.2012.212

Wang, Z., Cheng, H., Ji, B., 2021. Numerical investigation of condensation shock and re-entrant jet dynamics around a cavitating hydrofoil using a dynamic cubic nonlinear subgrid-scale model. Appl Math Model 100, 410–431. https://doi.org/https://doi.org/10.1016/j.apm.2021.08.001

Weiss, J., Mohammed-Taifour, A., Schwaab, Q., 2015. Unsteady Behavior of a Pressure-Induced Turbulent Separation Bubble. AIAA Journal 53, 2634–2645. https://doi.org/10.2514/1.J053778

Welch, P.D., 1967. The use of fast Fourier transform for the estimation of power spectra: A method based on time averaging over short, modified periodograms. IEEE Transactions on Audio and Electroacoustics 15, 70–73.

Winklhofer, E., Kull, E., Kelz, E., Morozov, A., 2001. Comprehensive hydraulic and flow field documentation in model throttle experiments under cavitation conditions, in: International Conference on Liquid Atomization and Spray Systems. Zurich, Switzerland.

Wu, B., Li, S., Cao, S., Yang, Q., Zhang, L., 2020. Numerical investigation of the separated and reattaching flow over a 5:1 rectangular cylinder in streamwise sinusoidal flow. Journal of Wind Engineering and Industrial Aerodynamics 198, 104120. https://doi.org/https://doi.org/10.1016/j.jweia.2020.104120

Wu, W., Meneveau, C., Mittal, R., 2020. Spatio-temporal dynamics of turbulent separation bubbles. J Fluid Mech 883, A45. https://doi.org/DOI: 10.1017/jfm.2019.911

Xun, Q.-Q., Wang, B.-C., 2016. Hybrid RANS/LES of turbulent flow in a rotating rib-roughened channel. Physics of Fluids 28, 075101. https://doi.org/10.1063/1.4954248

YASSINE ALOUINI, 2021. All the segmentation metrics [WWW Document]. released under the Apache 2.0 open source license.

Yu, H., Goldsworthy, L., Brandner, P.A., Garaniya, V., 2017. Development of a compressible multiphase cavitation approach for diesel spray modelling. Appl Math Model 45, 705–727. https://doi.org/https://doi.org/10.1016/j.apm.2017.01.035

Zalesak, S.T., 1979. Fully multidimensional flux-corrected transport algorithms for fluids. J Comput Phys 31, 335–362. https://doi.org/https://doi.org/10.1016/0021-9991(79)90051-2

Zhang, G., Zhang, D., Ge, M., Petkovšek, M., Coutier-Delgosha, O., 2022. Experimental investigation of three distinct mechanisms for the transition from sheet to cloud cavitation. Int J Heat Mass Transf 197, 123372. https://doi.org/https://doi.org/10.1016/j.ijheatmasstransfer.2022.123372

ZHOU, J., ADRIAN, R.J., BALACHANDAR, S., KENDALL, T.M., 1999. Mechanisms for generating coherent packets of hairpin vortices in channel flow. J Fluid Mech 387, 353–396. https://doi.org/DOI: 10.1017/S002211209900467X

Appendix A. Post-Processing, Treatment, and Analysis

The flow was simulated for a total duration of 1.5 milliseconds, with 3000 time snapshots captured at intervals of 5e-7 seconds. Statistical stationarity was achieved after the initial 400 time steps (2e-4 seconds).

Considering the large amount of data, a specific subdomain ($0 \leq \tilde{x} \leq 10$) was used for data analysis. This region is of prime interest since the coherent structures within the shear layer are the focus (for both cases, the same mask and parameters were used).

Spanwise averaged two-dimensional average fields, which represent the average flow behavior across the channel depth of $|z^*| \leq 1/3$ (z^* was the nondimensionalized z with respect to the half depth of the channel), were obtained for the subdomain. As discussed in the 'Three Dimensional effects' section, three-dimensional effects are minimal in this region, and fluctuations have negligible spanwise variations.

The data analysis procedures utilized in the Results sections are included for each subsection below:

1. Characteristics of the Mean Flow

Measurement of the RRI and thickness of the shear layer (δ_ω):

In this study, the mean flow RRI is identified by either the isoline U=0 on the mean streamwise velocity field or the set of points where the backflow coefficient γ is equal to 0.5 (γ being defined as the fraction of time during which the flow moves downstream can be calculated easily as the fraction of positive grid values for x components of U) (Stella, 2017; Stella et al., 2017).

The vorticity thickness is defined as (Stella et al., 2017):

$$\delta_\omega = (U_{max} - U_{min})/(\partial U/\partial y)max$$

where U_{max} and U_{min} are the maximum and minimum streamwise mean velocity values at each specific horizontal distance from the step, respectively.

Two-point autocorrelation:

Two-point autocorrelation for the streamwise velocities component in x-y plane is given as:

$$R_{xx}(x_{ref}, x_{ref} + \Delta x) = \frac{\langle u(x_{ref})u(x_{ref} + \Delta x)\rangle}{\langle u(x_{ref})u(x_{ref})\rangle}$$

where x_{ref} is the reference coordinate, and Δx is the distance between the reference coordinate and other location within the computational domain. u is the fluctuating velocity field (both streamwise and cross-streamwise components were used in the calculations). The angle bracket represents the ensemble averaging over all time slots. Different reference coordinates are adopted along the shear layer to capture spanwise vortical structures within this region.

2. Spectral Analysis

Pre-multiplied power spectral density (PSD): The sampling interval was $\tilde{t} = \frac{TU_\infty}{H} = 288$ with a sampling rate of $\frac{f_s H}{U_\infty} = 10.67$. The Welch method with Hanning window was utilized to compute pre-multiplied PSD for a total of 11 equal-length segments in time with 50% overlap (Hu et al., 2019; NA and MOIN, 1998). Each segment comprises 512 samples, and the resulting frequency range $St_h = \frac{fH}{U_\infty} = 0.021 \sim 5.33$.

Spectral coherence: the spectral coherence for two statistically stationary signals $x(t)$ and $y(t)$ was obtained using the following expression (used for reversed flow and average pressure over the step):

$$\mathbf{C_{xy}(f)} = \frac{\left|\mathbf{P_{xy}(f)}\right|^2}{\mathbf{P_{xx}(f)P_{yy}(f)}}, \qquad \mathbf{0 \le C_{xy}(f) \le 1}$$

where $P_{xy}(f)$ represents cross-PSD between x(t) and y(t), and $P_{xx}(f)$ is PSD value for x(t). Spectral coherence is used for the calculation of cross-PSD between normalized values of average pressure over the step and reversed flow.

Cross-correlation for phase delay estimation:

The phase delay is estimated by finding the time lag at which the cross-correlation function between the two signals reaches its peak. The Cross-correlation for two discrete signals x(t) and y(t) is given as:

$$\mathbf{R_{xy}(\tau)} = \sum_{\mathbf{t}=-\infty}^{\infty} \mathbf{x(t)y(t+\tau)}$$

where $\boldsymbol{\tau}$ is the time lag between two signals. To improve the accuracy of the phase delay estimation, especially for signals with different magnitudes, the signals are normalized by their maximum values and centered by subtracting their means before performing the cross-correlation (Hertz and Azaria, 1985).

Spatio-temporal correlation:

Spatio-temporal correlation for the fluctuating pressure field is found as (Weiss et al., 2015):

$$R_{pp}(\Delta x, \Delta t) = \frac{\langle p'(x_{ref}, t_{ref}) p'(x_{ref} + \Delta x, t_{ref} + \Delta t) \rangle}{p'_{rms}(x_{ref}) p'_{rms}(x_{ref} + \Delta x)}$$

3. Modal Analysis:

SPOD:

The details about the theory and derivation of this technique are provided in the literature(Schmidt and Colonius, 2020; Towne et al., 2018). From the mathematical point of view, SPOD modes represent the eigenvectors of cross-spectral density matrix at each frequency, and the eigenvalues indicate the energy associated with that specific mode and frequency. Considering that the focus is on the pressure and velocity fluctuations, the workflow proposed by He et al.(He et al., 2021) was adopted in the calculations, where the SPOD was implemented to decompose the solution vector containing the pressure, velocity components and entropy as $q = [p, U, V, W, \Delta s]^T$, along with the weight vector of $Wg = \left[\frac{1}{\gamma \bar{p}}, \bar{\rho}, \bar{\rho}, \bar{\rho}, \frac{(1-\gamma)\bar{p}}{\gamma R^2}\right]$ which is defined based on the total disturbance energy to quantify the energy associated with disturbances in the flow. A weight matrix Wg was used to scale different flow variables, and the definition of Wg influences the physical meaning of SPOD mode energy, which stands for the energy content of each mode.

In the framework of SPOD, the solution vector q can be decomposed to modes at various frequencies as:

$$q(\mathbf{X}, t) = \sum_{j=1}^{\infty} \hat{q}_j(\mathbf{X}) \exp(i2\pi f_j t) + c.c. \quad (30)$$

$$= \sum_{j=1}^{\infty} \sum_{k=1}^{N_b} a_j^k \phi_j^k(\mathbf{X}) \exp(i2\pi f_j t) + c.c. \quad (31)$$

where $i = \sqrt{-1}$, and $c.c.$ is the complex conjugate counterpart. Equation (30) represents the Fourier transform of q. Fourier transformation was performed using the Welch

method with overlapped window(Welch, 1967), which allows ensemble averaging over multiple realizations. The Fourier transform coefficient for j_{th} frequency ($\hat{q}_j(\mathbf{X})$) was decomposed to expansion coefficients a_j^k and POD modes ϕ_j^k. POD modes were calculated from eigenvectors of cross spectral density matrix (by considering the weight coefficients) and were orthonormal to each other so that $\phi_j^m(\mathbf{X})\left[\phi_j^n(\mathbf{X})\right]^T = \delta_{mn}$. Considering orthonormality of POD modes, the contribution of mode $\phi_j^k(\mathbf{X})$ to the total disturbance energy was determined using the eigenvalues of the cross spectral density matrix, which could be expressed based on the expansion coefficient as $\lambda_j^k = \left|a_j^k\right|^2$.

The details about the parameters used in the present SPOD analysis are included in Table A1. Considering the large amount of data, a specific subdomain ($0 \leq \tilde{x} \leq 10$) was used for SPOD calculations. This region is of prime interest since the coherent structures within the shear layer are the focus of this study (for both cases, the same mask and parameters were used).

Table A 1. Parameters related to the SPOD calculations.

Variables	*Number of Grid points of the Mask*	*Number of Snapshots*	*Sampling Frequency (St_h)*	*Number of Frequencies*	*Number of Overlapped Snapshots*	*Number of Blocks (Modes)*
$\mathbf{p, U, V, U, \Delta s}$	2,959, 200	3000	5.33	256	128	22

Appendix B. Visualization and Data Processing

Void fraction measurements were conducted for analyzing the hydrodynamic cavitation characteristics obtained from the experimental results and for the comparison with the numerical results. For this purpose, cavitating flow images are collected by a double-shutter high-speed (CMOS) camera (Phantom v310, a trademark of Vision RESEARCH). The camera was placed 250 mm from the image plane, and illuminations were made using an optic fiber light source. The image acquisition was performed with time interval of $133\mu s$ and exposure time of 6.93 μs. The image resolution was 720×1280 with 2.7 $\mu m\, px^{-1}$ optical magnification. 3500 series of sequential images with the same contrast and brightness were used for data processing and analysis. Previous studies(Bilu et al., 2014) demonstrated a correlation between the grey level value in images and the void fraction value. Based on this correlation, we utilized the grey level value as a proxy for void fraction values in our experimental results.

To accurately estimate void fraction in images containing surface defects on the device surface, we adopted a deep learning approach using the DeepLabv3+ neural network(Chen et al., 2018). Traditional thresholding techniques proved ineffective due to their sensitivity to surface imperfections. DeepLabv3+'s ability to handle complex image backgrounds and learn robust feature representations made it a viable approach for accurate void fraction segmentation. Each initial image and its corresponding mask were segmented into overlapping patches of 320×320 pixels with a 50% overlap to capture fine details and to avoid edge artifacts. This resulted in 21 image-mask pairs per initial image. To standardize input for the network, all patches were resized to 256×256 resolution. Image labels were generated using Labkit from the ImageJ software for supervised learning. Subsequently, 50 randomly selected images (1050 patches) were labeled and further divided into 90% training and 10% testing sets, which ensured sufficient data for robust model training and performance evaluation.

Patches of images and their corresponding masks were used as inputs and targets for the deep learning models. Pixel-wise softmax was applied to the output logits to compute the probability of each class in each pixel (Although segmentation for multiple classes was possible, two classes of void fraction and background were considered in this study).

Multiclass cross-entropy loss function(Shie Mannor et al., 2005) was employed to penalize any deviation from the target value, and Adam with weight decay (AdamW) optimizer(Loshchilov and Hutter, 2019) was selected for the optimizing procedure.

In addition to the loss function, three more metrics, namely, mean IOU (average over classes), accuracy and F1 score (harmonic mean of precision and recall), were implemented to evaluate and compare the performance of the networks for the segmentation task(YASSINE ALOUINI, 2021). Furthermore, batch sizes of 2 and 280 number of epochs were considered during the training of the networks. The performances of the network on training and test data in the last epoch are provided in Table S.1, which represents an acceptable performance of the network in segmentation task.

Table B 1. Training and test segmentation results using DeepLabv3+ neural network.

Training				*Test*			
Loss	Accuracy score	F1 score	mIOU	Loss	Accuracy score	F1 score	mIOU
0.0087	0.996	0.996	0.954	0.007	0.996	0.996	0.959

Following the training and optimization process, we deployed the trained network to segment a set of 3500 collected images. These images were then used for void characterization. For each image, we isolated the pixels associated with the void fraction segments. Subsequent to this, we normalized these pixel values shown by $I(i,j)$ (related to the pixel value for 8-bit grayscale images) based on the maximum pixel value (255 for the white color). This normalization process allowed us to assign a range of values from 0 to 1 to each void pixel, instead of using the binary 0/1 values. This new range of values better captures changes in vapor concentration within the corresponding region. In the next section, some results of void fraction along with comparisons with numerical results are provided.

An alternative method for void fraction estimation that was implemented in our study is as follow. the void fraction was determined by correlating the grayscale values from 2D images captured by a high-speed camera with the actual void fraction, a method supported by prior research (Bilu et al., 2014; Wang and Zhang, 2023). The analysis proceeded using these grayscale values. Each frame from the high-speed imaging was treated as an intensity matrix (A(t, x, y)), where (t) denotes the time index, and (x) and (y) represent the row and column indices, respectively. The intensity within this matrix ranges from 0 (representing black) to 255 (representing white).

Given that the brightness and contrast of the images remained consistent throughout the high-speed capture, aligning with findings from earlier studies(Bilu et al., 2014; Wang and Zhang, 2023), we inferred that the intensity of cavitation (the density of bubbles per pixel) could be proportionally estimated from the grayscale levels of each image. However, it's important to note that the background also exhibits some degree of greyness, potentially leading to inaccuracies in calculating the void fraction for areas deemed defective. To mitigate this, we subtracted the background contribution from each snapshot matrix to minimize errors.

Considering the significant disparity in dimensions between the depth of our device (60 μm) and the width of the channel (400 μm), we anticipated minimal variation in vapor concentration along the depth axis. Consequently, we disregarded these depthwise variations in our calculations. Therefore, the mean and variance of void fraction can be estimated as:

$$\bar{\alpha}(x,y) = \frac{1}{Nt}\sum_{t=0}^{Nt} I(t,x,y)$$

$$var(\alpha(x,y)) = \frac{1}{Nt}\sum_{t=0}^{Nt}\left(I(t,x,y) - \bar{\alpha}(x,y)\right)^2$$

where $I(t,x,y)$ is the subtracted and normalized grey level intensity of pixel at (x,y) location which belongs to the time step t. This value was obtained by subtracting the background intensity and then normalizing by the maximum possible pixel value (typically 255 for 8-bit grayscale images). The number of time snapshots used for data analysis was 10000 in all cases, except the Case II with 1500-time snapshots.

The frequency characteristics of cavitation regimes (Cases III and IV) were evaluated using the pre-multiplied power spectral density (PSD) at specific streamwise locations along the region of maximum void fraction fluctuation (α'_{rms}) pathway. For all the cases, the sampling interval was $T = 0.125\ s$ with a sampling rate of $f_s = 8e4\ Hz$. The Welch method with Hanning window was utilized to compute pre-multiplied PSD for a total of 39 equal-length segments in time with 50% overlap(Hu et al., 2019; NA and MOIN, 1998). Each segment comprised 512 samples, and the resulting frequency range was $St_h = \frac{fH}{U_0} = 4e-4 \sim 0.2$.

A method similar to Allan et al. (Allan et al., 2023), was employed to quantify bubble nuclei from high-speed camera images. First, the background subtraction and normalization were performed on the grayscale images. This process removed background noise and ensured consistency across images. For each cavitation regime, a 3D matrix was created, with two spatial dimensions representing bubble location and a third dimension representing time. A threshold intensity value (10% of maximum pixel intensity) was used to identify potential void regions (areas with vapor bubbles) within each pixel. The matrix was then segmented into void and non-void regions. Void regions were subdivided into disconnected groups (groups without shared pixels). Subsequently, in each time frame, connected groups smaller than a threshold size (25 μm in each direction) were considered as potential nuclei. Notably, a single group within the 3D matrix could track the movement and evolution of a single bubble over time. Finally, the spatial 2D domain was discretized into subdomains with a size of $100\mu m \times 100\mu m$. The average RMS of the number of nuclei within each subdomain were calculated. This approach could provide information about both the average and fluctuating characteristics of the nuclei distribution.